NASA Contractor Report 198416

Numerical Prediction of Turbulent Oscillating Flow and Heat Transfer in Pipes With Various End Geometries

Kirk LeRoi Oseid
University of Minnesota
Minneapolis, Minnesota

December 1995

Prepared for
Lewis Research Center
Under Grant NAG3–1024

National Aeronautics and
Space Administration

NUMERICAL PREDICTION OF TURBULENT OSCILLATING FLOW AND HEAT TRANSFER IN PIPES WITH VARIOUS END GEOMETRIES

A Thesis

Submitted to the Faculty of the Graduate School

of the University of Minnesota

by

Kirk LeRoi Oseid

in Partial Fulfillment of the Requirements

for the Degree of

Doctor of Philosophy

October 1993

ACKNOWLEDGMENTS

Producing this thesis has given me a great deal of satisfaction as it marks the end of a long, frustrating and in the end very satisfying effort. Four years ago I had only a basic understanding of numerical methods. While my interest in Computational Fluid Dynamics and heat transfer had peaked, I had little opportunity to perform this type of work on a productive and professional level. It became obvious that formal graduate studies were required to provide me with the credibility needed to practice in this field. I would like to thank my advisor, Dr. Suhas V. Patankar, for providing the guidance necessary to study such complex topics. Perhaps even greater thanks are in order to Dr. Patankar for taking me on as an advisee in the first place. I worked for some months before fully appreciating this facet of my good fortune.

I also thank Dr. Terry Simon, director of the experimental oscillating flow research at the University of Minnesota, for his encouragement and interest in my work, and for providing access to his own oscillating flow and heat transfer library.

Dr. James Hodges, whose fascination with fluid dynamics and heat transfer was infectious, is responsible for my own interest in these topics.

I am indebted to John Chai for the generous assistance he offered me during the course of my degree program at the University of Minnesota.

The facilities and computing resources of the Minnesota Supercomputer Institute are gratefully acknowledged. I hope always to have similarly comfortable surroundings and modern equipment available to me in the future.

Special thanks are in order to my parents and parents-in-law for their enthusiastic support during my studies. Their faith in me has far surpassed my own.

My greatest thanks are reserved for my wife Mary. She shared my commitment to return to school and cheerfully accepted the role of provider. Her love and encouragement are present in this dissertation.

Contents

List of Figures

NOMENCLATURE

A_r	amplitude ratio, $\frac{X_{max}}{L}$ or $\frac{Re_{max}D}{2LVa}$
c_f	skin friction coefficient
c_p	specific heat at constant pressure
c_μ, c_1 - c_6	turbulence model constants
D	pipe diameter
f_μ, f_1, f_2	low Reynolds number functions
G	production term in turbulence transport equations
h	heat transfer coefficient
hp	horsepower
i	$\sqrt{-1}$
J_o	Bessel function of the first kind, order zero
k	turbulent kinetic energy or thermal conductivity
k_t	turbulent thermal conductivity
ℓ	mixing length
L	pipe length
Nu	Nusselt number
p	mean pressure
Pr	molecular Prandtl number, $\frac{\mu c_p}{k}$
Pr_t	turbulent Prandtl number, $\frac{\mu_t c_p}{k_t}$
q	heat flux
r	radial coordinate direction
R	pipe radius, coefficient in RNG k-ϵ model
Re	Reynolds number, $\frac{\rho U_m D}{\mu}$
Re_t	turbulent Reynolds number, $\frac{\rho k^2}{\mu \epsilon}$

ρ	density
σ_k, σ_ϵ	Prandtl numbers for k, ϵ
τ	shear stress or nondimensional time
ϕ	phase shift
χ	nondimensional length
ω	angular velocity of the bulk flow oscillation

Superscripts

$*$	redefined value
$'$	fluctuating part
$\overline{\ }$	average quantity

Subscripts

b	bulk value
c	critical value for transition
fd	fully developed
i, j	coordinate directions in index notation
in	inlet conditions
m	mean quantity
max	maximum value
t	turbulent quantity
w	value at the wall
0	limiting value

Re_y	turbulent Reynolds number, $\frac{y\rho\sqrt{k}}{\mu}$
S	mean rate of strain
t	time
T	temperature
TI	turbulence intensity
u	mean axial velocity component
u^+	dimensionless velocity, $\frac{u}{u_\tau}$
u_τ	friction velocity, $\sqrt{\frac{\tau_w}{\rho}}$
U_b	bulk flow velocity
v	mean radial velocity component
Va	dimensionless frequency of oscillation, $\frac{\rho\omega D^2}{4\mu}$
x_i	axial coordinate direction
X_{max}	amplitude of bulk fluid axial displacement, $\frac{2U_{m,max}}{\omega}$
y	distance from the wall
y^+	dimensionless distance from the wall, $\frac{yu_\tau}{\nu}$

Greek symbols

δ_{ij}	Kronecker delta function
ϵ	dissipation rate
η	ratio of turbulent to mean strain time scale
θ	crank angle
Θ	dimensionless temperature
μ	dynamic viscosity
μ_t	turbulent viscosity
μ_{eff}	effective viscosity, $\mu + \mu_t$
ν	kinematic viscosity, μ/ρ

Chapter 1

Introduction

Unsteady flow is present in man, machine and nature. The flow of blood in arteries and capillaries in the human body is pulsatile - composed of a mean flow superposed with an oscillating component. The tides that wash in and out of rivers, harbors and estuaries are unsteady flows with very long periods of oscillation. Many engineering devices employ pulsatile and oscillating flow. Pulsating flow is defined here as a periodic flow with a net displacement of fluid over each flow cycle. Oscillating flow is defined as a periodic flow with a zero mean over each cycle. The subject of this thesis is oscillating flow and heat transfer in pipes which make up the heater and cooler sections of the NASA Space Power Research Engine (SPRE) currently under development. This engine uses the Stirling cycle as the thermal energy converter in a power plant for future space applications. The information presented in this thesis will of course be applicable to the design of many types of machinery which employ oscillating flow and heat transfer.

1.1 Invention of the Stirling Engine

What is known today as the Stirling engine was first proposed by Reverend Robert Stirling in his patent application of 1816. This closed air-cycle engine was expected

to compete with the steam engine, which was a crude, inefficient and dangerous device at that time. Other air-cycle engines had been proposed, but none included Stirling's *economizer,* referred to nowadays as the regenerator. This single component raised the efficiency of the device to the point where it could run on its own power, a feat that many contemporary engine designs could not accomplish. Stirling recognized that heat could be captured within the regenerator during expansion, and then absorbed back into the working fluid later in the cycle. This physical insight is notable, since Carnot's technique of heat engine analysis would not be formalized until 1824. An engine of this design was used for a short time in 1818 to drive a quarry pump, before the iron heater vessel failed under thermal stress and oxidation.

After this, Robert Stirling's attentions were directed increasingly toward the church, leaving the younger brother James, himself a trained engineer, to pursue further development of the engine. The next significant Stirling engine was built in 1828, employing a small auxiliary compressor to raise the air pressure and thereby increase the efficiency. James noted that the engine produced about 20 hp upon startup, but that the power fell off as the engine warmed. Apparently in the absence of knowledge of Carnot's recent work, Stirling reasoned that cooling must be applied to the engine in order that the "requisite difference of temperature" be maintained on opposite ends of the regenerator. Cooling was not addressed in Robert's original patent. A water-cooled engine was built in the 1830's to test the design. A patent for the water-cooling feature was granted in 1840.

Perhaps the first commercially successful Stirling engine was installed at the Dundee Foundry in 1841. The water-cooled engine produced 21 hp with an efficiency of about 6.5%, similar to the available steam engines. James had by this time also reconfigured the firebox in order to eliminate direct radiant heating of the engine

and thereby reduce the thermal stresses imposed on the heater vessel. Uniform heating was obtained by carefully directing the flue gases to flow around the heater. This engine was unable to satisfy the needs of the growing foundry, and was replaced in 1843 by a double-acting version of 45 hp and 18% efficiency. No steam engine of the time, nor any air-cycle engine of the nineteenth century could compete with this efficiency. Nevertheless, the engine was replaced by a steam engine some three years later after a series of heater failures which idled the foundry on three separate occasions.

By the middle of the nineteenth century the steam engine had become a reliable and reasonably efficient engine to power the industrial revolution. Most large power requirements during this period were met by steam engines. Many low power closed air-cycle engines were proposed and offered commercially during the end of the nineteenth century and running well into the twentieth. At low power, these engines could compete with steam in terms of efficiency (typically on the order of 1%), and were much simpler and cheaper to build and operate at a time when electricity was not widely available. These small engines may well have kept the spirit of the Stirling engine design alive during a period when other engines obtained dominance.

1.2 Renaissance of the Stirling Engine

The steady improvement of the steam engine, the development of reliable internal combustion engines and the widening distribution of electric power eliminated all commercial Stirling-type engines by the mid 1930's. Shortly thereafter the design was rekindled by a company seeking to increase the market for it's own radio equipment. Philips Company of the Netherlands sought to devise a power source that would enable them to sell radios in parts of the world where electric power was not yet available over a conventional distribution grid. The *external combustion* Stirling

engine was considered as a means of providing electric power and was preferred over storage batteries, which would eventually require recharging and were heavy and difficult to transport. The Stirling engine offered several advantages over other heat engines, including quiet operation and the ability to run on poor fuels. The Philips team was able to build and run a 16 watt engine by 1938. This was the first in a long series of engines built by or in association with Philips. By 1950, Philips was able to manufacture 150 generator sets of 200 watt capacity. This was closest any of the engines came to commercial success. (On a related note, Stirling refrigerators developed by Philips were commercially successful for cryogenic cooling and gas liquefaction.) The Philips engines were tested in household fans, boats, self-propelled lawn mowers, cars and buses. An artificial heart pump and several stationary engines were also tested. The pistons of the Philips engine designs were connected by linkages, being referred to as *kinematic* engines. Philips abandoned Stirling engine research in 1979. Theirs was by far the longest development effort. A history of the Philips Stirling engine projects, along with the early history of Stirling engines, is given in the very thorough text of Hargreaves (1991), from which much of the preceding discussion has been drawn.

The Philips kinematic engines were never commercially successful for a number of reasons, including

- inadequate lubrication of the pistons
- gradual fouling of the regenerator
- inadequate life of the seals used in various locations
- poor heat transfer into the hot end of the engine

These issues highlight the difficulties involved in bringing the otherwise simple Stirling engine into common use.

1.3 The Stirling Engine in Space

The space race began in 1957 with the launch of Sputnik, providing further motivation to develop the Stirling engine. General Motors and Philips had by 1959 produced a 3 kW generator set driven by a solar-powered Stirling engine. The hot end of the engine would be heated by liquid metal circulating through a solar collector array. The single-cylinder engine used a rhombic drive mechanism and a centrifugal oil circulation system to provide lubrication under microgravity. The engine met the design power specification, but was overshadowed by the development of photo-voltaic cells, which provided sufficient power to satisfy the newly available low-power solid-state electronics.

The manned space station project being developed by NASA will require significantly more power than the simple satellites of the sixties. The engine used for this space power application must not suffer from any of the limitations of the kinematic engine, and must have a considerable useful life with (preferably) zero maintenance. One means of eliminating some of the problems mentioned above is to use a *free-piston* design. In this design the displacer and power pistons are not rigidly connected, but instead communicate with one another through pressure forces transmitted by the working fluid. An advantage of this configuration is the tendency for the frequency of operation to be fixed by the natural frequency of the displacer piston, a parameter which the engine designer controls. Varying load levels are satisfied in a very natural way by self-induced changes in piston strokes and phase angle (West, 1986). As a free-piston engine, journal bearings are not used, so mechanical friction occurs only between the pistons and cylinders. The "loading"

on these surfaces is symmetrical and negligible in the microgravity environment. As a result, the engine requires no lubrication (other than that provided by the working fluid). Fouling problems are thereby also eliminated. The entire volume of working fluid can be hermetically sealed into the engine casing such that reciprocating and rotating shaft seals are eliminated. Insuring adequate heat transfer from the heat source to the working fluid remains as a design challenge, providing motivation for the present research. Details of the mathematical models used to design free-piston Stirling engines are found in Walker and Senft (1985). An overview of the Stirling SPRE development program is given by Dochat (1990). Recent SPRE test results obtained at NASA Lewis Research Center are discussed in Cairelli, et al. (1991). Optimization of the SPRE design is taking place in a somewhat empirical fashion, with adjustments to various components being considered or tested (Wong, et al. 1992). Improved understanding of the flow and heat transfer in oscillating flow would minimize these expensive hardware design iterations.

1.4 Other Stirling Engine Applications

Several ongoing Stirling engine development efforts will be discussed briefly in this section. They give some indication of the breadth of applications of the Stirling engine.

Detroit Diesel Corporation and Stirling Thermal Motors Inc. are jointly building a 4-cylinder kinematic engine producing 25 kW at 1800 RPM (Bennethum, et al. 1991). The engine uses a variable angle swashplate drive to provide power control. The crankcase is pressurized to reduce the demand on the reciprocating shaft seals. A more conventional and reliable rotating seal is used on the output shaft. The engine proposes to solve many of the interminable problems associated with kinematic Stirling engines, including lubrication, regenerator contamination

and seal life. Cost control efforts have resulted in an engine which is anticipated to be competitive with diesel engines of similar size. The modular design allows the same power unit to be applied to portable and marine generator sets, hybrid electric vehicles, solar conversion and refrigeration.

Free piston Stirling engines are also being considered for earth-bound applications. Mechanical Technology Inc. has considerable experience with free-piston engines (Goldwater, 1990). These engines are being considered for residential cogeneration, heat pumps, unmanned submersibles and hybrid electric vehicles. In the later application a low-powered Stirling engine would drive a sealed linear generator and act as a range extender for a battery powered vehicle. The size, weight and cost of available generators has fallen significantly in recent years. De Graaff (1991) argues for the use of a free-piston Stirling engine and sealed linear generator set as the sole power source for electric vehicles, given the weight of currently available storage batteries.

Stirling Technology Company, Sandia National Laboratory and others have cooperated to design a 25 kW solar power converter system (Wallace, et al. 1991). This system uses a free-piston Stirling engine, but drives a conventional rotary induction generator. The power pistons of this engine act directly as a hydraulic pump. A separate hydraulic motor couples the engine to the generator. Besides the Stirling engine and collector, most components of the system are commercially available products. The design operating life of the Stirling engine itself is 60000 hours, a figure presently possible only through the use of the free-piston configuration.

The free-piston Stirling engine can also be configured with "pistons" of water (Fauvel, et al. 1990). Such an engine is referred to as a Fluidyne. In this arrangement, the addition of heat to the Stirling cycle can be used to pump water. This system can be applied in irrigation systems in areas of the world where conventional

pumping engines and fuels are prohibitively expensive.

Many of the papers referenced above are found in the proceedings of the Intersociety Energy Conversion Engineering Conference, which meets annually. This forum includes Stirling engines and related technologies, and is often the first publication to present these papers.

1.5 Literature Survey of Oscillating Flow and Heat Transfer

This thesis considers methods of improving the modeling of friction and heat transfer in Stirling engine performance codes. The literature survey will be restricted to those papers which offer guidance for modeling flow and heat transfer under conditions which are similar to those in the heater and cooler sections of Stirling engines. Turbulence modeling has been shown to be a possible limiting feature of heat transfer predictions and will receive close attention before heat transfer papers themselves are reviewed. This literature survey updates the thorough survey of Koehler (1990) and extends the scope to include heat transfer in oscillating flow.

1.5.1 Laminar Oscillating Flow

1.5.1.1 Experiments

Fully developed laminar oscillating flow was first studied experimentally by Richardson and Tyler (1929), who used a crank-driven piston-cylinder to produce flow of nearly sinusoidal bulk variation. They observed that the peak in the velocity profile moved towards the pipe wall at sufficiently high rates of oscillation. Gaver and Grotberg (1986) measured the axial velocities in a tapered channel with oscillating flow and summed the cycle-averaged flow. They found one steady streaming cell on each side of the symmetry plane for moderate oscillation rates, and two cells

on each side at higher rates. The steady streaming is predicted by theory and is observed in acoustic studies.

1.5.1.2 Analytical and Numerical Solutions

The analytic solution corresponding to the Richardson and Tyler flow was formulated by Sexl (1930). Uchida (1956) evaluated Sexl's solution for pulsatile (non-zero mean) flow. The velocity gradient was used to evaluate the work required to maintain the pulsating flow, and the dissipation within the flow. The dissipation is found to be higher than that of steady flow at the same mean flow rate. Drake (1965) obtained a series solution using separation of variables for oscillating flow in a rectangular channel. The peak in the axial velocity was found to occur near a corner, in agreement with the previously quoted work of Richardson and Tyler. Iguchi, et al. (1992) solved the laminar flow in the entrance region of a square duct, finding good agreement with their experimental results, and proposed an expression for approximating the length of the entrance region.

1.5.2 Transitional and Turbulent Oscillating Flow

Until recently, relatively few papers on turbulent oscillating flow have been available. Unlike the laminar case, analytic studies are not possible and laboratory and numerical experiments are difficult and expensive. Many of the experimental studies provide only qualitative results describing the flow patterns and turbulent structure. Numerical studies often suffer from a lack of data suitable for validation of the models. A handful of experiments have been performed recently to support development of the SPRE engine. This effort was deemed necessary to improve the predictions of the available engine design codes. These whole-engine design codes were tuned to duplicate test data. It was originally assumed that the poor perfor-

mance of the models was due to underprediction of viscous flow losses (Tew, el al 1990). The design codes were then tuned by artificially augmenting the friction loss coefficients. In fact, adjustments to the codes cannot be indiscriminately applied to the flow losses alone: thermodynamic losses also result from seal leakage and heat losses through the pistons and cylinders. Moreover, the distribution of these losses varies from one engine design to another. Fundamental research on the important components that make up the Stirling engine is required in order to accurately characterize each source of losses.

1.5.2.1 Experiments

Park and Baird (1970) observed the decay of oscillations in a u-tube manometer and established criteria for the critical Reynolds number (R_c) for transition based on the oscillation rate. End-effects were observed to produce transition at a lower R_c in short tubes, while flows that were laminar over most of the oscillating flow cycle tended to have higher R_c . In the later cases, the laminar flow may not be able to respond and transition might not occur before the next flow reversal. Chan and Baird (1974) measured the overall rate of energy dissipation in an oscillating liquid column and deduced the wall friction. The wall shear was significantly higher than for the corresponding steady flow laminar boundary layer. They hypothesize that the flow is intermittently turbulent, but note that the transition from laminar to turbulent flow must be more gradual than for steady flow. The critical Reynolds number for oscillating flow in straight pipes was measured by Sergeev (1966). Similar results were obtained by Hino, et al. (1976) and Ohmi, et al. (1982).

Tu and Ramaprian (1983) studied sinusoidally pulsed turbulent flows at a fairly high mean Reynolds number of 50000. When the pulsations matched the characteristic frequency of the turbulence (3.5 Hz), the time mean flow was found to deviate

from steady flow. The turbulence assumed a nearly constant value throughout the cycle. At lower pulsation rates the turbulence was nearly absent during acceleration. The law of the wall was violated in all cases during some portion of the cycle.

Seume (1988) performed experiments to observe the behavior of oscillating flow during transition. The test rig consisted of a long straight pipe connected to a piston-cylinder driven by a scotch yoke mechanism. The scotch yoke provides sinusoidal piston motion. The length-to-diameter ratio (L/D) of the pipe was 60, matching the heater tubes of SPRE. The test fluid was atmospheric air. Data on fluid velocity and rms fluctuations was taken using hot film anemometry over a variety of operating conditions. This allowed for quantitative analysis of the structure of the flow throughout the flow cycle at several locations within the pipe. Two transition mechanisms were identified. In the first mechanism, fluid within the pipe remains laminar, but turbulent fluid from outside the pipe is drawn in and swept downstream. The passage of this turbulent slug is detected by the instrumentation as transition. Once the slug passes, the fluid may or may not revert to laminar flow, depending on local conditions. In the second transition mechanism, the boundary layer grows in the normal fashion. At a sufficient velocity, transition may occur if local instabilities become large. Like previous researchers, Seume found that laminar low prevailed during accelerating portions of the cycle. Transition occurred very near the peak flow rate, with turbulent conditions lasting through most of the decelerating portions of the cycle.

Friedman (1991) continued the work of Seume, taking detailed measurements at the same operating point as the SPRE heater tubes. Single hot-wire anemometry was used to collect data on the mean and rms fluctuations of the axial velocity. Cross-wire anemometry was used for the mean and rms fluctuations of the radial velocity component and one Reynolds stress component $\overline{-u'v'}$. This data was used

to test the ability of the present numerical models to predict the damping effects of acceleration and the convection of a turbulent slug, as will be discussed in chapter 4.

Fishler and Brodkey (1991) performed visualization experiments on oscillating flow under operating parameters similar to those in arteries of humans and large animals. (This parametric range includes that of the SPRE engine heaters and coolers.) The flow was driven through a long straight pipe by a scotch yoke and piston. The experiment employed trichloroethylene as the fluid, which was doped with magnesium oxide particles with a maximum diameter of about 20 micron. Data collection took the form of high-speed film, shot from a camera which was mounted on a sliding carrier driven by the same scotch yoke. The particle motions recorded thus represent the deviation from laminar, rectilinear flow. The films were studied to obtain qualitative information about the state of the flow. In most cases, turbulence was observed only during the decelerating parts of the flow cycle.

Simon, et al. (1992) have proposed a set of empirical transition criteria for oscillating pipe flow. The result is cast in a form suitable for use in one dimensional engine simulation codes. The criteria determine when transition will occur based on crank angle, distance from the inlet, peak flow rate and oscillation rate. The criteria are based on experimental data. Once transition is predicted to occur, a steady flow friction coefficient at the instantaneous flow rate is to be applied.

1.5.2.2 Numerical Solutions

Koehler (1990) modeled oscillating flow in straight pipes and examined the ability of the Lam-Bremhorst low Reynolds number k-ϵ model to predict transition and subsequent relaminarization. The model was able to predict both transition and relaminarization, but the response was too fast. Koehler used derived inlet bound-

ary conditions for the turbulence quantities, and felt that this may have produced some of the discrepancy. The use of experimentally derived values was expected to provide better performance, although this was left for future work.

Mankbadi and Mobark (1991) used a standard k-ϵ model with wall functions to test the ability of the model to account for unsteady effects. They recommend a dimensionless oscillation rate as the criterion for applicability of the turbulence model for unsteady flows. They note that a low Reynolds number model may be more appropriate than a standard model using wall functions.

Ahn and Ibrahim (1992) computed oscillating, incompressible flow in a pipe under conditions similar to SPRE. The standard, high-Reynolds number k-ϵ turbulence model of Launder and Spalding (1974) was employed for turbulence closure. The high-Reynolds number k-ϵ model was found to be inadequate for transitional cases (with modest values of Re_{max}). The behavior improved for cases with lower rates of oscillation (quasi-steady behavior). In the case of high Re_{max}, the results followed closely the steady correlation at the corresponding instantaneous Reynolds number. This may be an artifact of the wall functions boundary condition.

Ibrahim (1993) is, at the time of this writing, employing a novel means of modeling transition. The approach taken is to model the flow as laminar until such time as a set of transition criteria are satisfied. A k-ϵ turbulence model is then activated. Early results show good agreement with the experimental data of Friedman (1991). The transition criteria are based on the work of Simon, et al. (1992).

1.5.2.3 Turbulence Modeling

The effects of turbulence largely determine the friction and hence the pressure drop within the tubes of the Stirling engine heaters and coolers. From a computational perspective, the heat transfer problem cannot be solved until the flow is understood.

Attention will thus focus on finding an accurate or at least adequate turbulence model of oscillating flow before heat transfer results are obtained.

For complex flows, it is desirable to employ a turbulence model that requires no a priori knowledge of the turbulent structure of the flow field. This rules out the use of the mixing-length and one equation turbulence models (to be discussed in chapter 2). The next class of turbulence models, in order of complexity, is the two equation models. The most common model of this class is the k-ϵ model. Launder and Spalding (1972) discuss the early development of this type of turbulence model, which employs modeled transport equations for the turbulent kinetic energy and the dissipation rate. These two values are used to devise an "effective" viscosity. In their so-called standard form, the k-ϵ models are used only for regions where the flow is fully turbulent, with wall functions used to provide a link to the wall. To provide more generality, the so-called low Reynolds number version of the k-ϵ model was devised, first by Jones and Launder (1972). This model used damping functions on the turbulent viscosity and dissipation equation sink term. Additional terms were also added to the kinetic energy and dissipation equations to facilitate the application of boundary conditions and also to avoid singularities in the dissipation equation at the wall. The authors expressed the hope that further development would provide a way to avoid such terms, which are not physically based. Many subsequent low Reynolds number k-ϵ models continued to use damping functions to avoid singularities and force the turbulent viscosity to zero at the wall. Additional terms in the kinetic energy and dissipation equations are sometimes used in combination with the damping functions.

One model which employs no additional terms is the low Reynolds number k-ϵ turbulence model of Lam and Bremhorst (1981). Damping functions are applied to the turbulent viscosity and to the sink term of the dissipation equation. Another

function is applied to the source term to boost the dissipation rate near the wall and hence force the kinetic energy to zero. This and other low Reynolds number models are reviewed by Patel, et al. (1985).

While the low Reynolds number k-ϵ models have been able to predict, at least qualitatively, the relaminarization of steady flows subjected to favorable pressure gradients, the opposite is true for decelerated flows. These flows are subject to separation, which the models typically underpredict. Hanjalic and Launder (1980) trace the problem to an insufficient dissipation rate, giving rise to a too high turbulent viscosity. This provides excessive damping, often preventing separation. They added the irrotational component of the strain rate to the source term which appears in both the kinetic energy and dissipation equations. However, the term was preceded by a larger coefficient in the dissipation equation. Rodi and Scheuerer (1986) used this model and compared its performance with that of the Lam-Bremhorst model and a one equation model. The modified model performed well when subjected to adverse pressure gradient flows. The one equation model, with an empirically prescribed length scale, also performed well.

Thangam and Speziale (1992) have recomputed the backward facing step problem in an effort to find the cause of errors due to the use of the k-ϵ model. They found that since the separation point is well defined for this problem, wall functions could be used without ill effect. They were able to reduce the error in the reattachment length to 12% by use of a sufficiently fine grid. Additionally, by incorporating an anisotropic eddy viscosity model, the error was reduced to only 3%. The anisotropic treatment appears to add considerably to the complexity of the model.

A recent low Reynolds number k-ϵ model by Yang and Shih (1992) uses only one damping function, applied to the the turbulent viscosity. An additional term is

added to the dissipation equation, as was done in the Jones and Launder model, and the time scale in the dissipation equation is redefined to eliminate the singularity as the wall is approached. The time scale k/ϵ is augmented by the addition of the Kolmogorov time scale $\sqrt{\nu/\epsilon}$ which is negligible in the fully turbulent region, but has physical significance very near the wall, based on similarity arguments.

Mansour, et al. (1989) computed turbulent channel flows using direct numerical simulation. The results were processed and used as a data base against which to compare the performance of low Reynolds number k-ϵ models. Budgets of the various terms in the kinetic energy equation demonstrate that the pressure diffusion is negligible in comparison to other terms at all locations within the boundary layer. The profiles of kinetic energy and dissipation rate are found to be very dependent on the form of the damping functions used for the turbulent viscosity and the dissipation equation. A modified damping function for the dissipation equation source term is tested and found to produce better agreement with the direct numerical simulation data.

Alternate forms of two equation models have been proposed using other variables from which to derive the length scale. Wilcox (1988) presented a k-ω model where the frequency of turbulent eddies $\omega = \epsilon/k$ is given by a modeled transport equation. Speziale, et al. (1990) propose a k-τ model, where the turbulent time scale τ is the inverse of ω. They argue that the transport equation for τ can be solved subject to natural, as opposed to contrived, boundary conditions, and that the limiting form of the turbulent time scale at the wall contains only viscous terms. The resulting profile for τ is shown to be almost linear near the wall, eliminating the numerical stiffness found in the k-ϵ models.

Multiple time scale models have been proposed by Kim and Chen (1989), Chen and Singh (1990), Kim (1990, 1991, 1992), Liou and Shih (1993) and others. These

models propose to divide the spectrum of energy-containing eddies into two or more (usually two) ranges. Transport equations for the kinetic energy and energy transfer rate (dissipation) within each scale are solved to emulate the cascade of energy from large, energy-containing eddies to the small eddies, where dissipation occurs.

A new type of k-ϵ model based on Renormalization Group Theory is presented by Yakhot and Smith (1992). The method uses spectral averaging to close the transport equations for turbulent kinetic energy and dissipation. A new feature of the model is an additional source term in the dissipation equation which is responsive to rapid strains. The models of Kim (1992) and Yakhot and Smith (1992) will be considered in detail in chapter 2.

1.5.3 Heat Transfer

1.5.3.1 Experiments

Liao, et al. (1985) reported a decrease in the heat transfer coefficient in turbulent pulsating flow. Their results conflict with those of some previous workers, but the increase or decrease seems to be dependent on frequency and amplitude parameters. Available data covers wide ranges on the parameter map.

Dec and Keller (1989) measured the heat transfer from the wall of a pulse combustor tailpipe. They observed Nusselt numbers as much as 2.5 times higher than those corresponding to steady flow at the same bulk flow rate. The degree of enhancement increased linearly with pulsation frequency. Recently, Dec, et al. (1992) reviewed the literature and observed the trends in heat transfer enhancement or decrement due to pulsations. They found that flows with small amplitude pulsations produced relatively little effect on the heat transfer, with most researchers reporting slight decreases. Flows with large amplitude pulsations, such that flow reversal occurred periodically, produced enhancements by as much as a factor of 5.0

over the corresponding steady flow heat transfer.

Smith, et al. (1992) are currently building a test rig for oscillating flow, pressure, and heat transfer measurements. The rig is designed to cover the wide range of operating parameters that occur in Stirling engine heaters, coolers and regenerators.

Tang and Cheng (1993) used their experimental data and multivariate statistical analysis to produce correlations for the cycle-averaged Nusselt number for heat transfer between a pipe and oscillating air flow. The correlations give the Nusselt number as a function of Re_{max}, Va and A_r. The data were taken on a test rig consisting of a copper pipe with $L/D = 54$, with sinusoidally varying bulk flow. Data reduction was performed by combining thermocouple measurements of inlet and outlet bulk temperatures with the known, uniform heat flux and the first law of thermodynamics to produce Nu results without direct temperature gradient measurements. Variations on the statistical methods are discussed, and one of three correlations is recommended on the basis of minimum error and the ability to reproduce the steady flow correlation in the limit as Va tends to zero. The results cannot be extended to other fluids.

Heat transfer in oscillating flow is being studied experimentally by Simon and Qiu (1993) at the time of this writing. They have found the Nusselt number variation over the cycle to be quite complicated. The experimental test geometry is similar to that of the present numerical study, but subtle differences prevent direct comparison of results. Simon and Qiu use an expansion ratio of 3.33. The ratio used in the present numerical work is 2.0. Moreover, the thin brass outer walls of the expansion/contraction end regions in the experiment are cooled by a jacket of circulating, chilled water. The flush-square shoulders of the end regions are essentially adiabatic. The numerical model uses adiabatic outer walls on the expansion and contraction regions with heated shoulders. As a result, the experimental data

show a pronounced front of cool fluid entering and passing down the pipe. This is substantially different than the numerical model, in which the end regions act as a store of heated fluid which is drawn into the pipe after flow reversal, producing gradual variations of temperature.

1.5.3.2 Analytic and Numerical Solutions

Faghri, et al. (1979) performed an analytic study of heat transfer in periodically developed pulsating laminar flow without area change, and found that the heat transfer was enhanced by the unsteady convection superposed on the steady flow component. The degree of enhancement increased with the frequency of the pulsation. Siegel (1987) and Zhang and Kurzweg (1991) computed the axially enhanced heat transfer in laminar oscillating channel and pipe flow, respectively. They found that the axial heat transfer can be much larger than in heat pipes. This occurs at relatively high oscillation rates, so the the degree of convective transport is negligible.

Yakhot, et al. (1987) modeled the heat transfer in turbulent pipe flow using a expression for the turbulent Prandtl number Pr_t which depends on the ratio of turbulent to molecular viscosity. In this way Pr_t is allowed to take values which vary across the boundary layer. The expression is based on the work of Yakhot and Orszag (1986). Good agreement was obtained for fluids with widely varying Prandtl numbers.

Heat transfer from gas to cylinder walls is modeled by Lee (1983) and Jeong (1991) under conditions of oscillating pressure. These simplified analytic studies consider reciprocating machines where the heat transfer is driven by the temperature gradient produced by oscillating gas pressure in a piston-cylinder arrangement. The use of a complex Nusselt number correlation is recommended to account for the

phase lag between the wall heat flux and the bulk fluid temperature. This mechanism is different from the heat transfer which occurs due to convection within pipes subjected to oscillating flow. Nevertheless, the use of the complex Nusselt number for heaters and coolers subjected to oscillating flow has been proposed. This thesis will demonstrate that the complex Nusselt number correlation is inappropriate for oscillating flow.

Ibrahim, et al. (1991) noted that heat transfer results differed when using the incompressible and thermally expandable fluid assumptions. The difference between thermally expandable and compressible models was slight.

Cho and Hyun (1990) modeled the flow and heat transfer in laminar pulsating pipe flow. They found that the cycle-averaged friction coefficient differed little from the steady case, but the average Nusselt number behavior was more complex. The heat transfer was increased over the steady value for intermediate values of the oscillation rate, but decreased for lower and higher rates.

Ibrahim, et al. (1992) modeled the flow and heat transfer in oscillating pipe and channel flows, and over blunt bodies. They found the local friction factors and Nusselt numbers were often an order of magnitude higher than the corresponding steady flow values, in the vicinity of an area change. The variation of the fluid temperature was found to lag behind the flow variation.

Chapter 2

The Mathematical Representation of the Problem

This chapter will provide an overview of the equations used to represent the physical problem in a well-posed mathematical form. Laminar flow is considered first. Turbulent flow will be considered later. Gas flows typically have negligible body forces. In the absence of gravity this condition will be satisfied exactly.

2.1 Laminar Flow

Incompressible laminar pipe flow and heat transfer is governed by the axisymmetric Navier-Stokes and energy equations

$$\frac{\partial u}{\partial x} + \frac{1}{r}\frac{\partial}{\partial r}(rv) = 0 \tag{2.1}$$

$$\rho\frac{\partial u}{\partial t} + \rho u\frac{\partial u}{\partial x} + \rho v\frac{\partial u}{\partial r} = -\frac{\partial p}{\partial x} + \frac{\partial}{\partial x}\left(\mu\frac{\partial u}{\partial x}\right) + \frac{1}{r}\frac{\partial}{\partial r}\left(r\mu\frac{\partial u}{\partial r}\right) \tag{2.2}$$

$$\rho\frac{\partial v}{\partial t} + \rho u\frac{\partial v}{\partial x} + \rho v\frac{\partial v}{\partial r} = -\frac{\partial p}{\partial r} + \frac{\partial}{\partial x}\left(\mu\frac{\partial v}{\partial x}\right) + \frac{1}{r}\frac{\partial}{\partial r}\left(r\mu\frac{\partial v}{\partial r}\right) - \mu\frac{v}{r^2} \tag{2.3}$$

$$\rho\frac{\partial T}{\partial t} + \rho u\frac{\partial T}{\partial x} + \rho v\frac{\partial T}{\partial r} = \frac{\partial}{\partial x}\left(\frac{k}{c_p}\frac{\partial T}{\partial x}\right) + \frac{1}{r}\frac{\partial}{\partial r}\left(r\frac{k}{c_p}\frac{\partial T}{\partial r}\right) \tag{2.4}$$

Equations (2.1) through (2.4) are solved using the SIMPLER algorithm of Patankar (1980). Koehler (1990) provides further details about the numerical procedure. Results are presented in chapters 3 and 5 for the laminar flow and heat transfer solutions, respectively.

2.2 Turbulent Flow

Numerical modeling of turbulent flow is a research topic in itself. The purpose of this thesis is not to develop new turbulence modeling techniques, but rather to employ available methods to study the behavior of oscillating flows. Certain limitations on the degree of involvement in turbulent flow modeling must be imposed. For the most part, currently available models are used, with consideration given to the possibility of making modest modifications to these models only when warranted.

The frequency of turbulent fluctuations in the Stirling engine components is far higher than the bulk flow oscillation frequency. This allows us to take advantage of the Reynolds-averaging procedure, wherein the Navier-Stokes equations are averaged over a period of time which is long relative to the turbulent fluctuation time scale, but shorter than the bulk flow oscillation time scale. This technique provides a set of unsteady transport equations for the turbulent flow variables.

The convection and diffusion of heat dominate in this application, so compression work, pressure diffusion and viscous heating effects are not included in the energy equation. The variables used below will be considered to be the mean part unless otherwise noted.

Incompressible turbulent pipe flow is governed by the axisymmetric Navier-Stokes and energy equations

$$\frac{\partial}{\partial x_j}(u_j) = 0 \tag{2.5}$$

$$\frac{\partial}{\partial t}(\rho u_i) + \frac{\partial}{\partial x_j}(\rho u_i u_j) = -\frac{\partial p}{\partial x_i} + \frac{\partial}{\partial x_j}(\tau_{ij} - \rho\overline{u_i' u_j'}) \tag{2.6}$$

$$\frac{\partial}{\partial t}(\rho c_p T) + \frac{\partial}{\partial x_j}(\rho c_p T u_j) = \frac{\partial}{\partial x_j}\left(k\frac{\partial T}{\partial x_j} - \rho c_p \overline{T' u_j'}\right) \tag{2.7}$$

The eddy viscosity concept is used for turbulence closure. The turbulent stresses for incompressible flow are modeled as

$$-\rho\overline{u_i' u_j'} = \mu_t\left(\frac{\partial u_i}{\partial x_j} + \frac{\partial u_j}{\partial x_i}\right) - \frac{2}{3}\rho k \delta_{ij} \tag{2.8}$$

The normal turbulent stresses are conveniently grouped with the pressure. The redefined pressure is stated as

$$P = p + \frac{2}{3}\rho k \tag{2.9}$$

For the temperature, the turbulent stresses are modeled as

$$-\rho c_p \overline{T' u_j'} = \frac{\mu_t c_p}{Pr_t}\frac{\partial T}{\partial x_j} \tag{2.10}$$

The turbulent Prandtl number Pr_t is assigned the uniform value of 0.9, which is a typical value found in figure 12-9 of Kays and Crawford (1980) and produces good results for steady turbulent pipe flow. This treatment simplifies the solution of turbulent heat transfer and eliminates the need to specify a variation of Pr_t. The turbulent Prandtl number does in fact rise as the wall is approached, but the turbulent viscosity tends to zero at the same time.

Once turbulence closure is applied, the governing transport equations will be solved in their axisymmetric forms shown below in equations (2.41) through (2.44). Means of closing the equations will now be discussed.

2.2.1 Turbulence Modeling

2.2.1.1 The Mixing-Length Model

The eddy viscosity concept requires a means of specifying the field values of the turbulent viscosity μ_t. Numerous techniques have been proposed for this purpose,

beginning with the mixing length theory of Prandtl (discussed in White (1974)). This technique assumes that turbulent transport is analogous to molecular transport, and the correlation is fashioned after the kinetic theory of gases. Kinetic theory states that the gas viscosity is proportional to the product of the density, mean free path and the acoustic velocity: $\mu \propto \rho \ell v_a$. Prandtl sought a similar expression for the turbulent viscosity that would produce a turbulent shear expression with the same form as the molecular shear. In a simple laminar shear flow, we have

$$\tau = \mu \frac{\partial u}{\partial y} \tag{2.11}$$

For the turbulent stress, the desired form is thus

$$\tau_t = \mu_t \frac{\partial u}{\partial y} \tag{2.12}$$

The turbulent viscosity was then assumed to take the form

$$\mu_t = \rho \ell^2 \left| \frac{\partial u}{\partial y} \right| \tag{2.13}$$

where ℓ is the so-called *mixing length.* The mixing length was determined empirically, and was found to depend on the distance from the wall.

The mixing length model has proven to be quite reliable in certain well-defined flow situations such as fully-developed pipe flow. For more general flow geometries, specifying ℓ is difficult or impossible. Alternate methods of computing μ_t are required, especially when transport and unsteady effects are present.

2.2.1.2 The One-Equation Models

The next level of complexity in turbulence modeling is to generate a transport equation for one or more turbulence quantities and express μ_t as a function of these quantities. Depending on the number of transport equations employed, these

techniques are referred to as one- or two-equations turbulence models. Prandtl (discussed in Schlichting (1979)) derived a one-equation model based on the transport equation for turbulent kinetic energy. The turbulent kinetic energy is defined as $k = \frac{1}{2}(\overline{u'^2} + \overline{v'^2} + \overline{w'^2})$. Bradshaw, et al. (discussed in Schlichting (1979)) derived a one-equation model based on the transport equation for turbulent shear stress, which in turn was derived from the turbulent kinetic energy equation. These transport equations can be derived by manipulating the Navier-Stokes equations.

In Prandtl's model the turbulent viscosity is considered to be proportional to the product of a velocity scale and a length scale

$$\mu_t \propto U_{scale} L_{scale}. \tag{2.14}$$

The velocity scale is taken as

$$U_{scale} \propto k^{\frac{1}{2}} \tag{2.15}$$

The length scale in this case is essentially the mixing length. Bradshaw's model contained a more complicated expression for the length scale which was designed specifically for the computation of turbulent boundary layer flow.

These models are capable of accounting for the convection of turbulent kinetic energy, but the difficulty in specifying the length scale for general flows remains. The length scale can be inferred from experimental data, but this reduces the scope of the model to flows of the same type as the data. A model which requires no data is desired.

2.2.1.3 The Two-Equation Models

A model in which the turbulence length scale is also determined from a transport equation would be free of the limitations of the mixing length and of the

one-equation models. Such models were proposed by Kolmogorov, Harlow and Nakayama (1967), and Spalding (all discussed in Launder and Spalding (1972)). Kolmogorov proposed a transport equation for the frequency of turbulent fluctuation $k^{\frac{1}{2}}/\ell$ as a means of specifying the length scale. The model could not be tested in 1942 for lack of adequate computing resources. Harlow and Nakayama used the transport equation for the dissipation rate $k^{\frac{3}{2}}/\ell$ as the second equation. Spalding used a transport equation for the square of the frequency of turbulent fluctuation, so the method was similar to that of Kolmogorov. Like Harlow and Nakayama, most subsequent use of two-equation models has focused on the use of the dissipation rate to represent the length scale. This is especially convenient since ϵ is required in the sink term of the kinetic energy equation. These models are referred to as k-ϵ turbulence models. The transport equations for k and ϵ (or any of the other variables) can be derived from the Navier-Stokes equations. The procedure is detailed in McComb (1990).

It is worth noting that the dissipation is defined as

$$\epsilon = \nu \overline{\left(\frac{\partial u_i'}{\partial x_j} + \frac{\partial u_j'}{\partial x_i} \right) \frac{\partial u_i'}{\partial x_j}} \tag{2.16}$$

The early k-ϵ models considered only those regions of the flow where the turbulence was isotropic. The isotropic part of the dissipation is

$$\epsilon = \nu \overline{\frac{\partial u_i'}{\partial x_j} + \frac{\partial u_j'}{\partial x_i}} \tag{2.17}$$

This distinction is of no consequence except near walls where damping occurs preferentially, producing anisotropy. This will have some consequence when attempts are made to extend the model to near-wall regions.

The length scale can be determined once the turbulent kinetic energy dissipation rate ϵ is known. The length scale is given by

$$L_{scale} \propto \frac{k^{\frac{3}{2}}}{\epsilon} \tag{2.18}$$

Just as in Prandtl's model, the turbulent viscosity is

$$\mu_t \propto \frac{k^2}{\epsilon} \tag{2.19}$$

The first successful k-ϵ models were capable of computing the turbulence variables only in the equilibrium regions, that is, where the generation and destruction rates of turbulence are equal. These are also referred to as the fully turbulent regions. Near-wall regions which are not in equilibrium are the viscous sublayer and the Van Driest layer (discussed in Schlichting (1979)). In the viscous sublayer, the presence of the wall damps the turbulent fluctuations to the extent that turbulent transport is negligible relative to laminar diffusion. In the Van Driest layer, the turbulence is actually intermittent, but the time averaged turbulence may be approximated by an exponential decay of turbulence as the edge of the viscous sublayer is approached. The so-called *wall functions* were used to bridge the viscous sublayer and the Van Driest layer. This technique is essentially a means of projecting boundary conditions out to the fully turbulent region where the transport equations are valid. Wall functions are discussed at length in Patankar and Spalding (1967).

Wall functions are not strictly applicable for low-speed, unsteady or separated flows (Patel, et al. 1985). For oscillating flow, the velocity profile varies rapidly with time near flow reversal. A turbulence model which depends on wall functions is clearly unsuited for this situation. This shortcoming of the k-ϵ model was recognized early on, and efforts to extend the model were made by several investigators. The general approach was to modify the existing k-ϵ model, now referred to as the High Reynolds Number (HRN) or Standard k-ϵ model. The goal was to modify the model in such a way that the governing transport equations could be integrated directly to the wall, eliminating the need for wall functions entirely. This family of models is referred to as the Low Reynolds Number (LRN) models. Several LRN k-ϵ turbulence

models are reviewed in Patel, et al. (1985).

Previous work on oscillating pipe flow performed by Koehler (1990) showed that the LRN k-ϵ model of Lam and Bremhorst (1981) was capable of predicting the turbulent structure in oscillating flow. This model was used extensively in the present research, so a detailed description will be given. The results obtained with the model will be presented later in this work.

The Lam-Bremhorst model provides low Reynolds number functions (f_1, f_2) that allow the dissipation equation to be integrated to the wall. This eliminates the need to specify wall functions to bridge the viscous sublayer. The turbulent viscosity is damped (f_μ) so that it approaches zero at solid walls. The modeled turbulent kinetic energy and dissipation rate transport equations used in this model are

$$\frac{\partial}{\partial t}(\rho k) + \frac{\partial}{\partial x_j}(\rho u_j k) = \frac{\partial}{\partial x_j}\left(\left(\mu + \frac{\mu_t}{\sigma_k}\right)\frac{\partial k}{\partial x_j}\right) + \rho G - \rho\epsilon \tag{2.20}$$

$$\frac{\partial}{\partial t}(\rho \epsilon) + \frac{\partial}{\partial x_j}(\rho u_j \epsilon) = \frac{\partial}{\partial x_j}\left(\left(\mu + \frac{\mu_t}{\sigma_\epsilon}\right)\frac{\partial \epsilon}{\partial x_j}\right) + c_1 f_1 \rho G \frac{\epsilon}{k} - c_2 f_2 \rho \frac{\epsilon^2}{k} \tag{2.21}$$

The production term G is $\frac{\mu_t}{\rho}S$, where the strain rate in axisymmetric coordinates is given by

$$S = 2\left(\frac{\partial u}{\partial x}\right)^2 + 2\left(\frac{\partial v}{\partial r}\right)^2 + 2\left(\frac{v}{r}\right)^2 + \left(\frac{\partial u}{\partial r} + \frac{\partial v}{\partial x}\right)^2 \tag{2.22}$$

The turbulent viscosity is given by

$$\mu_t = \rho f_\mu c_\mu \frac{k^2}{\epsilon} \tag{2.23}$$

The following constants are adapted without change from the standard k-ϵ model of Launder and Spalding (1974)

$$c_\mu = 0.09 \quad c_1 = 1.44 \quad c_2 = 1.92 \quad \sigma_k = 1.0 \quad \sigma_\epsilon = 1.3 \tag{2.24}$$

The low Reynolds number functions f_μ, f_1 and f_2 are given by

$$f_\mu = (1 - exp(-0.0163R_y))^2 \left(1 + \frac{20}{R_t}\right) \tag{2.25}$$

$$f_1 = 1 + \left(\frac{0.055}{f_\mu}\right)^3 \tag{2.26}$$

$$f_2 = 1 - exp(-R_t^2) \tag{2.27}$$

The low Reynolds number functions approach unity in the fully turbulent region, so the model is functionally identical to the standard k-ϵ model in that region. Two modest modifications, in the form of upper and lower limits to the f_μ function, were employed to enhance performance of the model in transitional cases. The value of f_μ is not allowed to take values above 1.0. This is a physically reasonable restriction. Furthermore, when R_t is below 200, f_μ is not allowed above $0.5 + 0.0025R_t$. These modifications are based on the work of Schmidt and Patankar (1988), who found that when f_μ is allowed to become too large during intermediate iterations, turbulence is damped excessively and transition cannot be predicted. For this study, a lower limit of 0.02 was also imposed on f_μ. The selection of this value is somewhat arbitrary, but allowing f_μ to approach zero was found to prevent transition. A similar lower limit was imposed by Zhu and Liu (1991), who used the Lam-Bremhorst model and found that transition is prevented when f_μ is allowed to become too small. Upon arriving at a converged solution, none of these modifications are actually invoked. They simply help prevent the solution from running astray at early stages in the iterative procedure.

The Lam-Bremhorst model has been used successfully in the present work. Some deficiencies were noted, as discussed later in this thesis, and it was decided to investigate the use of alternate turbulence models. One alternate modeling procedure

is the multiple time scale approach discussed by Hanjalic, et al. (1980). This procedure divides the turbulence energy spectrum into two or more ranges, and solves modeled transport equations for the turbulence variables within each range. This provides a means of modeling the cascade of turbulence energy from the large scale, energy containing eddies to the smallest scales, where viscous dissipation occurs. Convenience dictates the use of only two scales. Two-equation turbulence models of the k-ϵ type take no account of the cascade effect, and therefore depend more heavily on model constants to provide agreement with experimental results.

2.2.1.4 A Multiple Time Scale Model

A two-scale LRN turbulence model was proposed by Kim (1992), and was applied to the present research. In this model, pairs of transport equations are solved for each range. The large scale turbulence variables are called the production range kinetic energy (k_p) and the energy transfer rate (ϵ_p). The small scale variables are the transport range kinetic energy (k_t) and the dissipation rate (ϵ), which represents the same dissipation rate as that of the k-ϵ models. The sum of the large and small scale kinetic energies is equivalent to the turbulence kinetic energy of the k-ϵ models.

The k_p and ϵ_p transport equations used in this model are

$$\frac{\partial}{\partial t}(\rho k_p) + \frac{\partial}{\partial x_j}(\rho u_j k_p) = \frac{\partial}{\partial x_j}\left(\left(\mu + \frac{\mu_t}{\sigma_k}\right)\frac{\partial k_p}{\partial x_j}\right) + \rho G - \rho\epsilon_p \tag{2.28}$$

$$\frac{\partial}{\partial t}(\rho \epsilon_p) + \frac{\partial}{\partial x_j}(\rho u_j \epsilon_p) = \frac{\partial}{\partial x_j}\left(\left(\mu + \frac{\mu_t}{\sigma_\epsilon}\right)\frac{\partial \epsilon_p}{\partial x_j}\right) + \frac{\rho}{k_p}\left(c_1 G^2 + c_2 G\epsilon_p - c_3 f_{\epsilon_p}{\epsilon_p}^2\right) \tag{2.29}$$

The production term G is the same as that used in the k-ϵ models.

The k_t and ϵ transport equations are

$$\frac{\partial}{\partial t}(\rho k_t) + \frac{\partial}{\partial x_j}(\rho u_j k_t) = \frac{\partial}{\partial x_j}\left(\left(\mu + \frac{\mu_t}{\sigma_k}\right)\frac{\partial k_t}{\partial x_j}\right) + \rho\epsilon_p - \rho\epsilon \tag{2.30}$$

$$\frac{\partial}{\partial t}(\rho\epsilon) + \frac{\partial}{\partial x_j}(\rho u_j \epsilon) =$$
$$\frac{\partial}{\partial x_j}\left(\left(\mu + \frac{\mu_t}{\sigma_\epsilon}\right)\frac{\partial \epsilon}{\partial x_j}\right) + \frac{\rho}{k_t}\left(c_4 {\epsilon_p}^2 + c_5 \epsilon_p \epsilon - c_6 f_\epsilon \epsilon^2\right) \tag{2.31}$$

The model constants are given as

$$c_\mu = 0.09 \quad c_1 = 0.21 \quad c_2 = 1.32 \quad c_3 = 1.84 \quad c_4 = 0.32 \quad c_5 = 1.21$$
$$c_6 = 1.65 \quad \sigma_k = 0.75 \quad \sigma_\epsilon = 1.15 \tag{2.32}$$

The low Reynolds number functions are given by

$$f_{\epsilon_p} = 1 - exp(-R_y) \tag{2.33}$$

$$f_\epsilon = 1 - 0.13exp(-R_y) \tag{2.34}$$

$$f_\mu = \frac{1 - exp\left(-\beta_1\sqrt{R_y} - \beta_2 R_y - \beta_3 {R_y}^2\right)}{1 - exp(-\beta_4 R_y)} \tag{2.35}$$

with

$$\beta_1 = 0.005 \quad \beta_2 = 0.001 \quad \beta_3 = 0.00011 \quad \beta_4 = 0.14 \tag{2.36}$$

The turbulent viscosity is given by

$$\mu_t = \rho f_\mu c_\mu \frac{k^2}{\epsilon_p} \tag{2.37}$$

where $k = k_p + k_t$.

The performance of this model in oscillating flow was very similar to that of the Lam-Bremhorst k-ϵ model. The details are presented in chapter 4.

2.2.1.5 A Renormalization Group Model

Another turbulence model to consider for possible application to oscillating flow is the renormalization group (RNG) k-ϵ model. The derivation of this model begins

with the exact transport equations for k and ϵ, but closure is obtained not through modeling of the higher order terms, but through the RNG theory, which employs spectral averaging to obtain expressions for the turbulent viscosity and the source terms of the k and ϵ equations. RNG theory can be considered a model-building method for many different types of problems involving lack of exact closure. A version of the RNG k-ϵ model which is appropriate for high Reynolds number applications is presented by Yakhot and Smith (1992).

The RNG closure produces three source/sink terms in the ϵ-equation. The first two have the same form as those used in the standard k-ϵ models; only the coefficients differ. Yakhot and Smith consider the RNG-based closure for these two terms to be exact. This is a striking result, and a tribute to earlier workers who had only their intuition to guide them in selecting the proper form for closure.

The new term in the RNG-based ϵ-equation has no formal closure, but Yakhot and Smith (1992) propose a form which contains one adjustable constant. This term is responsible for rapid-strain response and has no counterpart in the standard k-ϵ models.

The RNG k-equation takes the same form as in the standard k-ϵ models. The RNG ϵ-equation is:

$$\frac{\partial}{\partial t}(\rho\epsilon) + \frac{\partial}{\partial x_j}(\rho u_j \epsilon) = \frac{\partial}{\partial x_j}\left(\left(\mu + \frac{\mu_t}{\sigma_\epsilon}\right)\frac{\partial \epsilon}{\partial x_j}\right) + c_1 \rho G \frac{\epsilon}{k} - c_2 \rho \frac{\epsilon^2}{k} - \frac{c_\mu \eta^3 \left(1 - \frac{\eta}{\eta_0}\right)}{1 + \beta \eta^3}\frac{\epsilon^2}{k} \tag{2.38}$$

The ratio of turbulent to mean strain time scales $\eta = Sk/\epsilon$. The fixed point (limiting) ratio for high Reynolds number is $\eta_0 = 4.38$. The value $\beta \approx 0.012$ is tuned to give good agreement with the experimental value of the von Karman constant. The other coefficients are

$$c_\mu = 0.0845 \quad c_1 = 1.42 \quad c_2 = 1.68 \quad \sigma_k = 0.719 \quad \sigma_\epsilon = 0.719 \tag{2.39}$$

The values of c_μ, c_1, c_2, σ_k, σ_ϵ and η_0 are all established by means of the RNG theory. Only β is adjusted to obtain agreement with experimental results. The turbulent viscosity is given by

$$\mu_t = \rho c_\mu \frac{k^2}{\epsilon} \tag{2.40}$$

The RNG k-ϵ model was tested for steady pipe flow in the high Reynolds number form presented above. The model produced an improvement in the radial distribution of turbulent viscosity, relative to the Lam-Bremhorst model, but the difference was slight. The model was not applied to oscillating flow due to the limitations of the wall function method discussed in section 2.2.1.3 above.

Modifications to create a low Reynolds number RNG k-ϵ model are discussed briefly by Yakhot and Orszag (1986). This author was unable to find a complete presentation of the LRN RNG k-ϵ model in the literature. Instead, the HRN version discussed above was modified with the addition of the f_1 and f_2 low Reynolds number functions from the Lam-Bremhorst model to the first two source terms of the ϵ-equation. The last term was modified slightly to prevent unnatural behavior. The function f_μ from Lam-Bremhorst was added to the turbulent viscosity expression. The details of these modifications and the results will be discussed in detail in chapter 4.

2.2.1.6 Other Turbulence Models

Turbulence is in fact a convective process. The eddy viscosity models take account of the effect of turbulence on the mean flow by attributing the turbulent transport to the "turbulent viscosity." In other words, the convective turbulent transport is modeled as an enhanced diffusive transport. It is believed that turbulent flow behaves according to the Navier-Stokes equations (2.1) through (2.4): the same equations

used to model laminar flow. The differences between solutions for laminar and turbulent flows using these equations are the small spatial scales and unsteady nature of turbulent flow. Resolving turbulent flow at the scale of the smallest structures is possible, but only at great cost. This type of turbulent flow computation is usually referred to as Direct Numerical Simulation (DNS). The required grid spacings and time steps used in DNS are so small as to make routine computations of turbulent flow impractical. The method has been of great utility in producing data sets for subsequent statistical analysis, which has led to a better understanding of the structure of turbulence. The review paper of Moin (1990) provides a discussion of the DNS method and the related Large Eddy Simulation method.

The Reynolds-averaged Navier-Stokes equations, which are closed by the eddy viscosity treatment in this thesis, can also be closed by solving transport equations for the second order stress terms of equations (2.6) and (2.7). However, transport equations for the second order terms contain third order correlations: this so-called *turbulence closure problem* requires that we truncate, at some level, our effort to derive stress transport equations. The Reynolds Stress models (RSM) are obtained by expressing the third order correlations in terms of the mean flow field. This also provides a natural means of accounting for the anisotropy of complex turbulent flows. RSM models have been successful in capturing some flow phenomena that are missed by the eddy viscosity models. Notable examples are the secondary flow in square ducts and flows with rotation. However, the number of transport equations to be solved is increased significantly relative to eddy viscosity models, even when algebraic truncations are applied. There also exists the issue of whether to apply wall functions or integrate the governing equations to the solid walls. Launder (1989) points out that the development and testing of LRN stress models lags well behind that of the eddy viscosity models. For these reasons, RSM models have not

been used for this thesis research.

2.2.2 The Mean Flow

Once the field values of μ_{eff} $(= \mu + \mu_t)$ are available, the time averaged Navier-Stokes and energy equations can be solved. The incompressible, axisymmetric forms of these equations are

$$\frac{\partial u}{\partial x} + \frac{1}{r}\frac{\partial}{\partial r}(rv) = 0 \tag{2.41}$$

$$\rho\frac{\partial u}{\partial t} + \rho u\frac{\partial u}{\partial x} + \rho v\frac{\partial u}{\partial r} = -\frac{\partial P}{\partial x} + \frac{\partial}{\partial x}\left(\mu_{eff}\frac{\partial u}{\partial x}\right) + \frac{1}{r}\frac{\partial}{\partial r}\left(r\mu_{eff}\frac{\partial u}{\partial r}\right) + \frac{\partial}{\partial x}\left(\mu_{eff}\frac{\partial u}{\partial x}\right) + \frac{1}{r}\frac{\partial}{\partial r}\left(r\mu_{eff}\frac{\partial v}{\partial x}\right) \tag{2.42}$$

$$\rho\frac{\partial v}{\partial t} + \rho u\frac{\partial v}{\partial x} + \rho v\frac{\partial v}{\partial r} = -\frac{\partial P}{\partial r} + \frac{\partial}{\partial x}\left(\mu_{eff}\frac{\partial v}{\partial x}\right) + \frac{1}{r}\frac{\partial}{\partial r}\left(r\mu_{eff}\frac{\partial v}{\partial r}\right) + \frac{\partial}{\partial x}\left(\mu_{eff}\frac{\partial u}{\partial r}\right) + \frac{1}{r}\frac{\partial}{\partial r}\left(r\mu_{eff}\frac{\partial v}{\partial r}\right) - 2\mu_{eff}\frac{v}{r^2} \tag{2.43}$$

$$\rho\frac{\partial T}{\partial t} + \rho u\frac{\partial T}{\partial x} + \rho v\frac{\partial T}{\partial r} = \frac{\partial}{\partial x}\left(\left(\frac{k}{c_p} + \frac{\mu_t}{Pr_t}\right)\frac{\partial T}{\partial x}\right) + \frac{1}{r}\frac{\partial}{\partial r}\left(r\left(\frac{k}{c_p} + \frac{\mu_t}{Pr_t}\right)\frac{\partial T}{\partial r}\right) \tag{2.44}$$

Equations (2.41) through (2.43) are solved sequentially along with the turbulence transport equations using the SIMPLER algorithm of Patankar (1980). Coupling enhancement is employed to speed the convergence of the solution of the turbulence transport equations. Coupling enhancement is a minor modification to the sequential solution procedure which solves the pair of strongly coupled k- and ϵ-transport equations several times before proceeding to solve the next variable in the sequence. Since constant fluid properties are assumed, the heat equation (2.44) is solved after a converged flow solution is obtained. Details of the solution procedure are found in Koehler (1990).

The oscillating flow and heat transfer problem is solved over the domain shown in figure 2.1. Figure 2.1 also shows representative control volumes over which the discretized equations were solved (only alternate control volume faces have been shown). The grid is refined near the walls of the domain to resolve the steep velocity gradients. A somewhat coarser grid is acceptable near the axis and in regions remote from the expansion/contraction.

The inflow boundary conditions are used to create an oscillating flow. The axial velocity component at the inflow is specified as

$$U_{b,in} = U_{b,max} sin(\omega t) \tag{2.45}$$

This boundary condition is applied to the left end of the domain if $sin(\omega t)$ is positive, and to the right end when it is negative. The radial velocity component is set to zero at the inlet. A zero axial gradient boundary condition is used at the outlet end for all variables. The no-slip condition is applied to the velocity components at all walls. A symmetry condition is used at the axis for all variables.

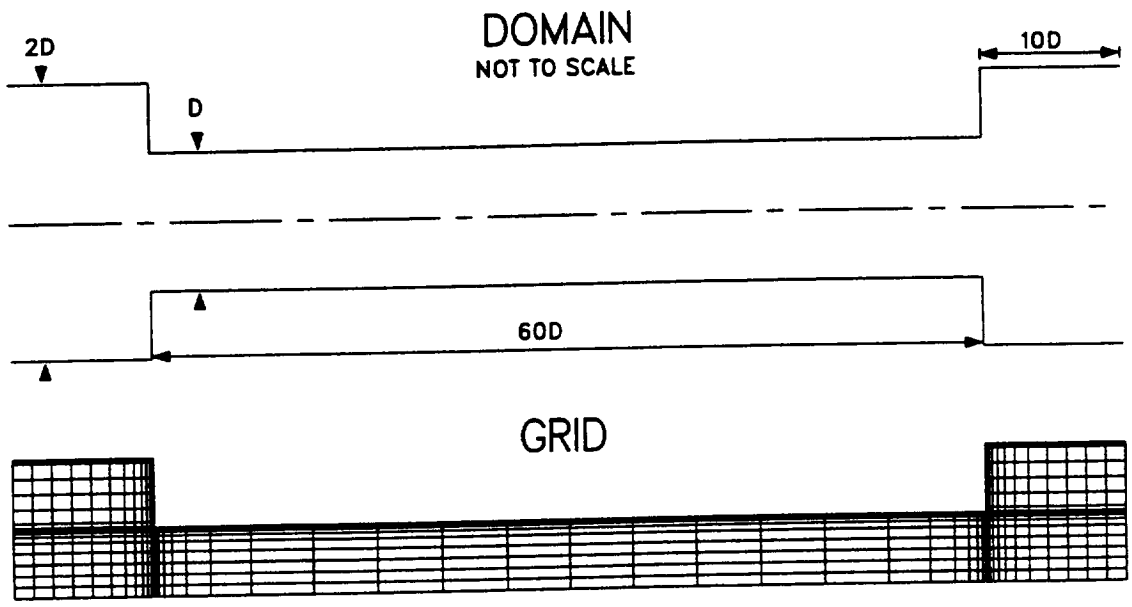

Figure 2.1: Axisymmetric domain geometry and computational grid for pipe with expansion/contraction ends.

Chapter 3

The Laminar Flow Solution

In this chapter the flow solution for laminar pipe flows will be presented. Fully developed pipe flow will be defined and some results will be shown to demonstrate the concept of fully developed flow and to verify the performance of the computer program. Oscillating pipe flow will be considered next. Analytic solutions are available under certain conditions: these will be studied and compared with the computer program results.

3.1 Fully Developed Pipe Flow

The concept of fully developed flow is used to distinguish between entrance flows and flows which are well downstream of a pipe inlet. In engineering flows, the entrance region may be only a small fraction of the total pipe length. In these cases, piping systems can be designed with reasonable accuracy using pressure drop and heat transfer correlations which are based on fully developed flow data. When necessary, corrections may be applied later in those cases where entrance effects are deemed significant. Incropera and DeWitt (1985) give the length of the entrance region (the hydrodynamic development length) for laminar flow as

$$\left(\frac{x}{D}\right)_{fd} \approx 0.05Re \tag{3.1}$$

Beyond this point the flow is fully developed. The flow is considered to be laminar when the Reynolds number is less than about 2300.

The defining concept of fully developed flow is the absence of axial dependence. All terms in the momentum equation which involve axial gradients are thus zero. For incompressible laminar flow without body forces, the axial momentum equation in axisymmetric coordinates then reduces to

$$0 = -\frac{dp}{dx} + \frac{d}{dr}\left(\mu \frac{du}{dr}\right) \tag{3.2}$$

The pressure gradient is a constant by the fully developed flow definition. Equation (3.2) can then be integrated twice to obtain the axial velocity profile. By applying the no-slip boundary condition at the pipe wall and the zero-gradient condition at the axis, the profile may be written as

$$u(r) = \frac{-dp/dx}{4\mu}\left(R^2 - r^2\right) \tag{3.3}$$

The velocity profile is parabolic in the radius. The elliptic flow solver employed for the present research must be able to reproduce this result at positions well downstream of the pipe inlet.

Figure 3.1 shows the numerical solution for the fully developed velocity profile using three different radial grids. The results were taken at the outlet of a straight pipe with a length of 500 diameters. A good solution can be obtained with a surprisingly coarse grid. Radial grids with 5, 10 and 20 uniform control volumes were used to produce the profiles in figure 3.1. The solution with only 5 control volumes is very reasonable, while the solution with 20 control volumes is indistinguishable from the exact solution to the resolution of this figure, serving to verify the computer program.

3.2 Oscillating Pipe Flow

The study will now be extended to the unsteady case where the bulk flow varies sinusoidally. The oscillating flow can be said to assume a *periodically developed* state after a sufficient number of flow cycles have been completed. Fully developed oscillating flow was first studied experimentally by Richardson and Tyler (1929). They observed that the peak in the velocity profile moved towards the pipe wall at sufficiently high rates of oscillation. The governing equations for this flow can be solved analytically for positions far removed from the pipe inlet. This solution is discussed below. The corresponding numerical results will then be compared to the analytic solution for verification.

3.2.1 Analytic Solution

The analytic flow solution corresponding to the Richardson and Tyler study was formulated by Sexl (1930). The separation of variables technique was used to obtain the axial velocity time- and radial-dependence given by the real part of

$$u(r,t) = \frac{K \exp i\omega t}{i\omega}\left[1 - \frac{J_o r\sqrt{-i\omega/\nu}}{J_o R\sqrt{-i\omega/\nu}}\right] \tag{3.4}$$

where

$$K \exp i\omega t = -\frac{1}{\rho}\frac{dp}{dx} \tag{3.5}$$

Figures 3.2 through 3.4 show the velocity profiles throughout the oscillating flow cycle given by equation (3.4) for $Va = 1$, 30 and 100. Notice that the Sexl solution is pressure gradient-driven. The crankangles of figures 3.2, 3.3 and 3.4 refer to the variation of the pressure gradient throughout the cycle. The most significant feature of oscillating flow is the increase in the wall velocity gradient, particularly at low flow rates. This creates an axial pressure gradient which is higher than that

of steady flow at the same Re. The pressure gradient is also out of phase with the bulk flow rate. The bulk flow lags the pressure gradient by 90° as Va becomes large. Figure 3.5 shows this phase shift as a function of Va.

3.2.2 Numerical Solution

A numerical model used to compute fully developed pipe flow can be extended to model unsteady flow by making the boundary flow rate vary with time. For this section, the computer program was set up to model a pipe with sudden expansion and contraction end regions. The domain geometry and grid are shown in figure 3.6. Figure 3.7 compares the axial velocity profiles of the Sexl analysis and the present study at the peak instantaneous flow rate with $Va = 30$, for which the velocity lags the pressure gradient by 73°. The agreement between the analytic and finite volume solutions is good, particularly near the wall, where the shear stress is computed. The numerical solution was obtained with only 16 control volumes across the pipe radius, and the profile used in figure 3.7 is taken at the axial middle of the pipe section, 25 diameters from either end.

Figures 3.8 through 3.10 show the axial velocity profile at the middle of the pipe at select crank angles during the flow cycle for $Va = 1$, 30 and 100. These crank angles refer to the variation of the bulk flow rate. The velocity profiles for low values of Va differ only slightly from the steady flow case, as shown in figure 3.8. The profiles are nearly identical for accelerating and decelerating flow. Compare the profiles of figure 3.8 for 58.7 and 121.3° crank angle, for instance. They are virtually indistinguishable. The velocity profiles become more complicated at higher oscillation rates, as seen in figures 3.9 and 3.10. The effect of oscillation is most apparent near flow reversal (crankangles of 180° and 360°). The momentum of the core fluid is relatively higher than that of the near-wall fluid, causing a recirculation

of fluid within the pipe, even though the bulk flow is instantaneously zero. After flow reversal the low-momentum fluid near the wall responds quickly to the axial pressure gradient, and accelerates ahead of the core fluid. In figure 3.9 the axial fluid does not take the the lead again until just after 90°. The peak in the velocity profile is off the axis for most of the flow cycle when the rate of oscillation is high, as seen in figure 3.10. In all oscillating cases, as the fluid decelerates the high-momentum core fluid flows at a sufficient rate to cause the near-wall fluid to reverse prior to bulk flow reversal. This is required by the incompressible continuity equation to ensure that the mass rate is constant at all sections along the pipe. At the middle of the pipe the next half-cycle is identical to the last, with all flow directions reversed.

The wall shear is phase shifted in time with respect to the bulk flow velocity in oscillating flow. Figure 3.11 shows the friction coefficient as it varies through the first half cycle at the midsection of the pipe for Va = 1, 30 and 100. Re_{max} is 2000 in each case. The steady flow friction coefficient at the corresponding instantaneous flow rate is shown for reference. At low rates of oscillation the friction coefficient differs little from the steady case (except near flow reversal). As the rate of oscillation increases the friction coefficient becomes generally higher during the accelerating portion of the cycle and lower during deceleration. During acceleration, the low-momentum fluid near the wall responds quickly to the pressure gradient, creating an enhanced wall velocity gradient and friction coefficient. During deceleration, the opposite effect occurs. The near-wall velocity reverses prior to bulk flow reversal, and the friction coefficient drops sharply to zero. Figure 3.11 has been prepared by using the signed values of the near-wall velocity to evaluate the wall shear stress. Though unusual, this treatment has been used to illustrate the near-wall flow reversal which occurs prior to the bulk flow reversal at 180° crank angle. The friction coefficient curves for the oscillating cases all pass through zero when the

near-wall flow reverses. In order to obtain the more conventional, unsigned friction coefficient, the negative portions of the curves may be simply mirrored across the abscissa.

The flow field is far more complicated within the end regions. Figures 3.12 through 3.14 show streamline plots in the left end region at select times during the cycle for the cases $Re_{max} = 2000$ and $Va = 1$, 30 and 100. Flow is to the right for crankangles between zero and 180° and to the left for the remainder of the cycle. For low values of Va the effects of oscillation are apparent during inflow only near flow reversal (see figure 3.12 for $Va = 1$, 180°), when the momentum of the core fluid causes a slight recirculation. In the second half of the flow cycle the momentum of the flow is sufficient to cause separation, which in turn traps a large portion of fluid within a recirculation zone. This recirculation zone is initiated during outflow and persists through a portion of the flow cycle, depending on Va. As Va is increased, less time is available for the growth of the recirculation zone. When the rate of oscillation is increased, the recirculation persists over a larger portion of the flow cycle. Figure 3.13 shows that the recirculation left over from the previous cycle is still relatively strong within the left end region at about 30°. This early in the cycle, the incoming flow is forced to move around the recirculating slug of fluid left over from the previous cycle. Eventually this slug is sheared apart and by about 120° the effect of oscillation is barely noticeable. During outflow, the center of the separation bubble remains slightly closer to the shoulder of the expansion (where it originates) relative to the $Va = 1$ case. When Va is increased to 100, the effects of oscillation are apparent throughout the flow cycle as shown in figure 3.14. During outflow the separation bubble is closer yet to the shoulder of the expansion.

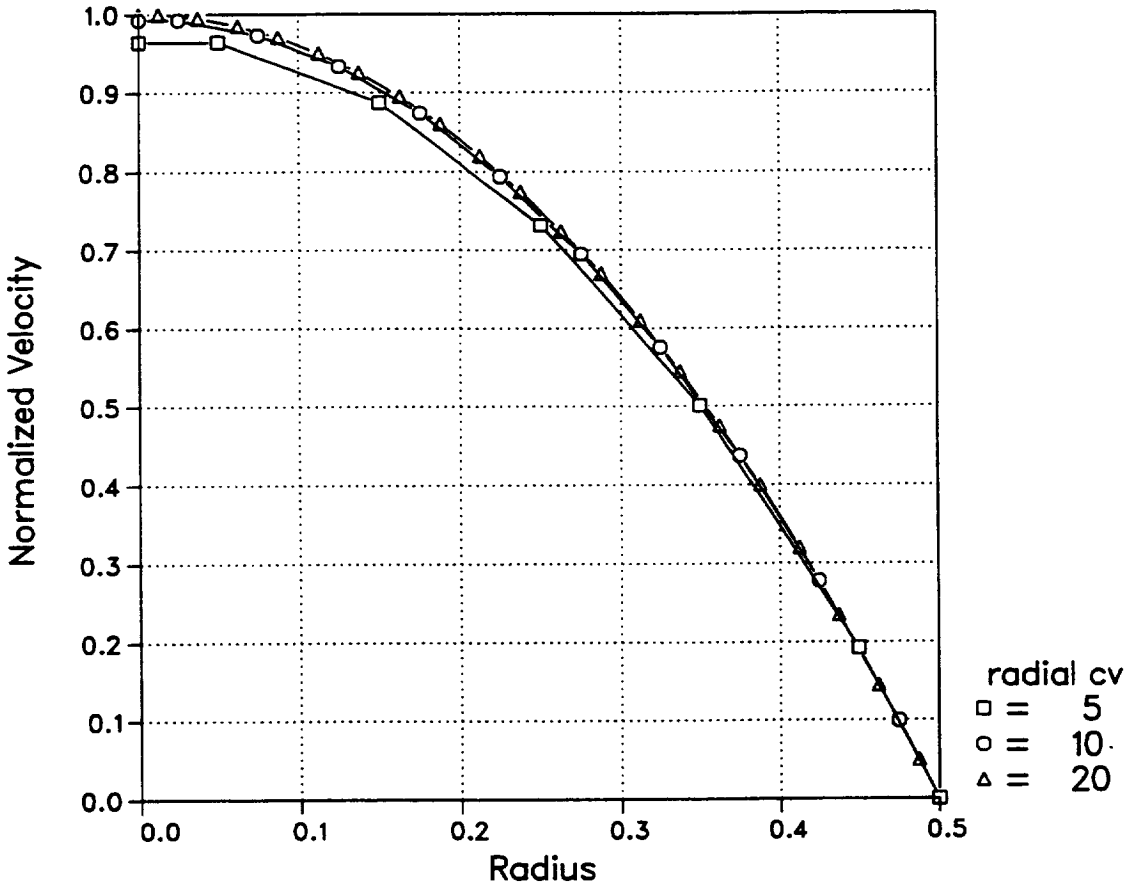

Figure 3.1: Fully developed velocity profiles given by the numerical solution for three grid densities.

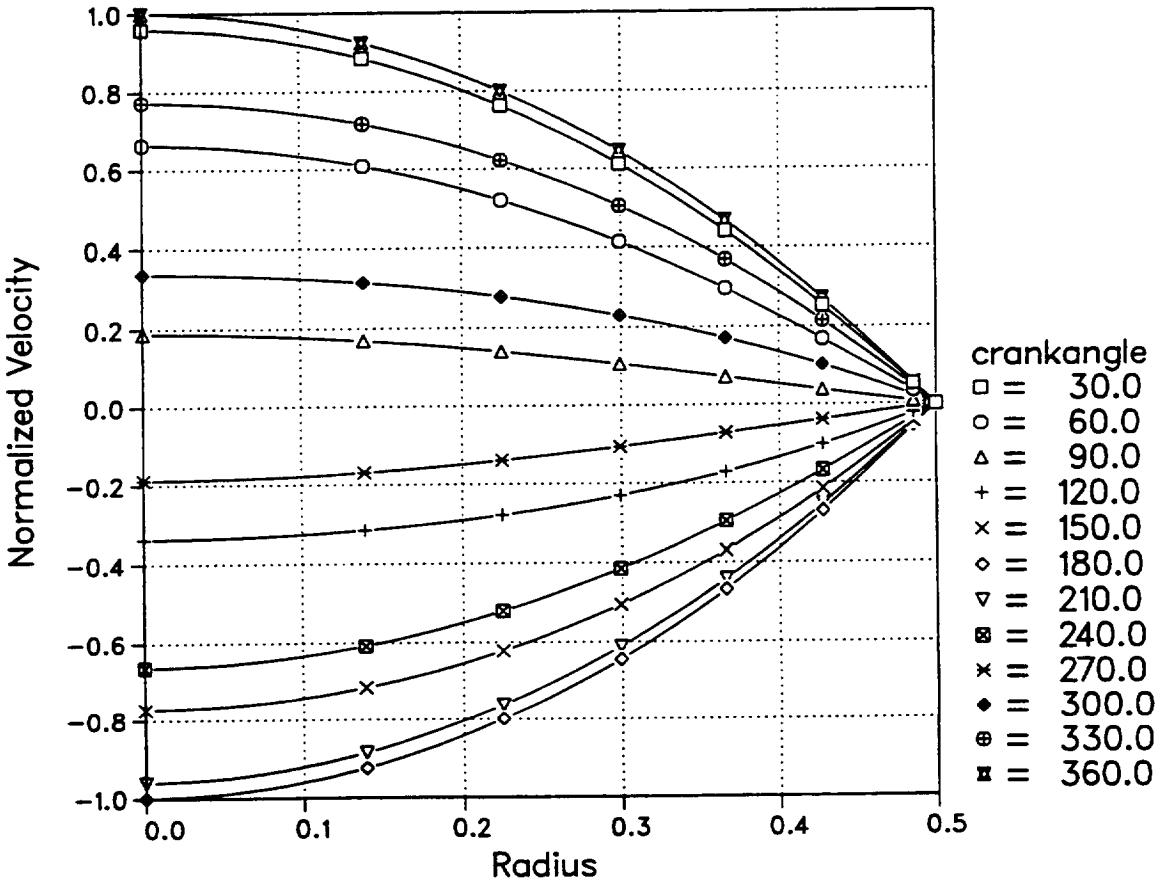

Figure 3.2: Velocity profiles throughout the oscillating flow cycle for $Va = 1$ as given by Sexl's analytic solution.

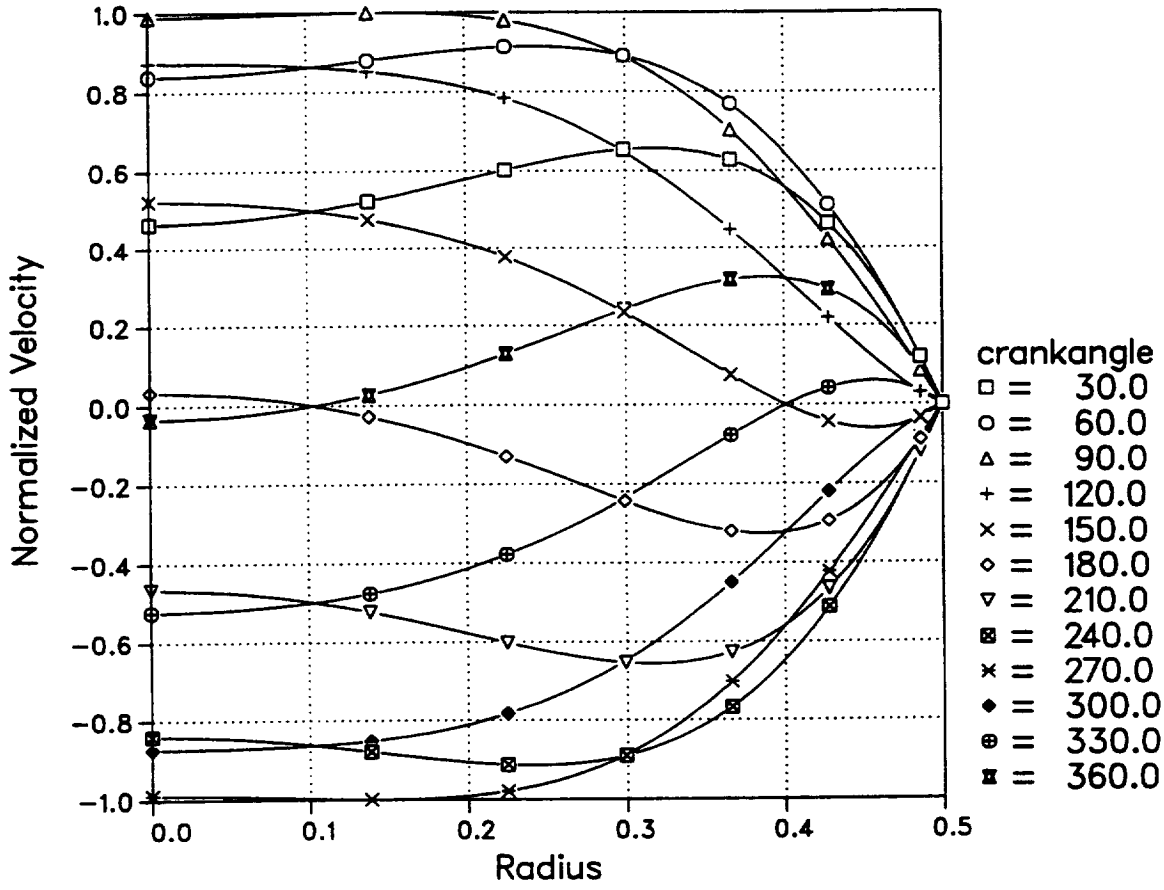

Figure 3.3: Velocity profiles throughout the oscillating flow cycle for $Va = 30$ as given by Sexl's analytic solution.

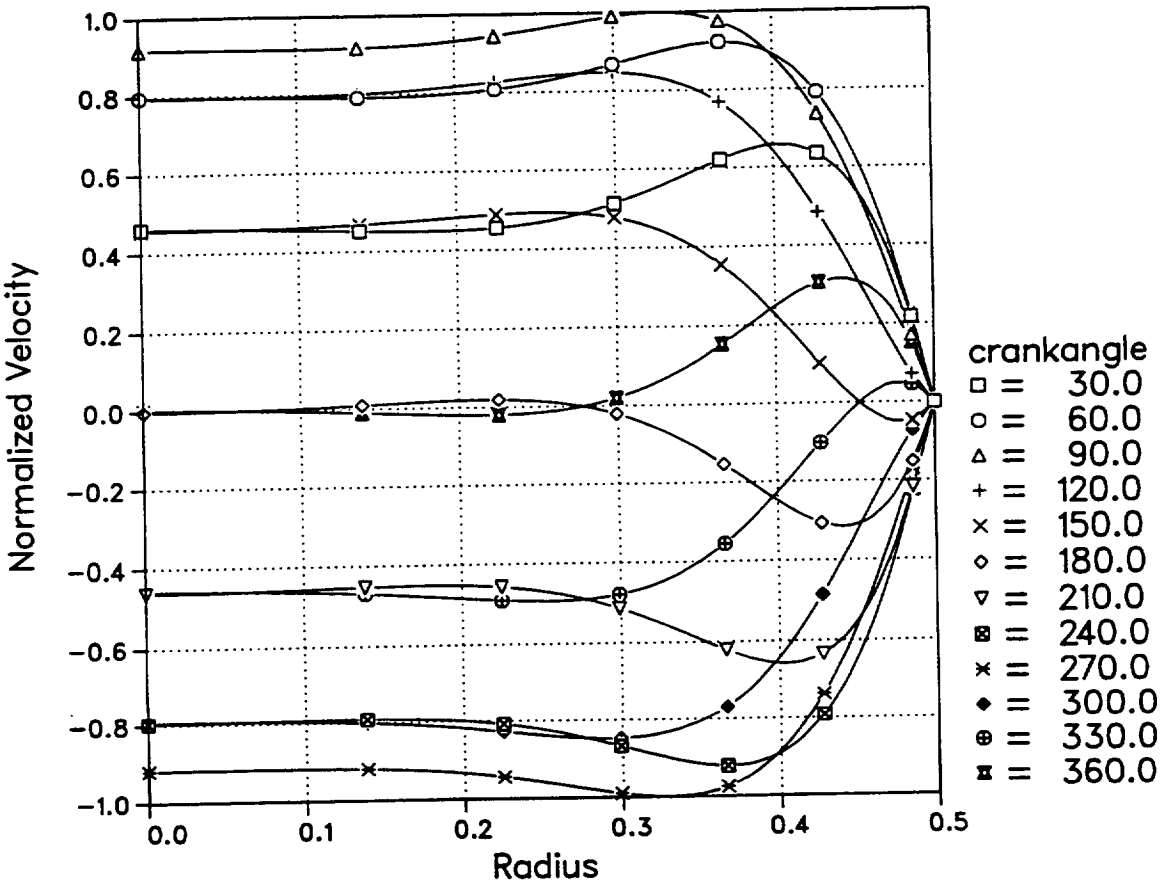

Figure 3.4: Velocity profiles throughout the oscillating flow cycle for $Va = 100$ as given by Sexl's analytic solution.

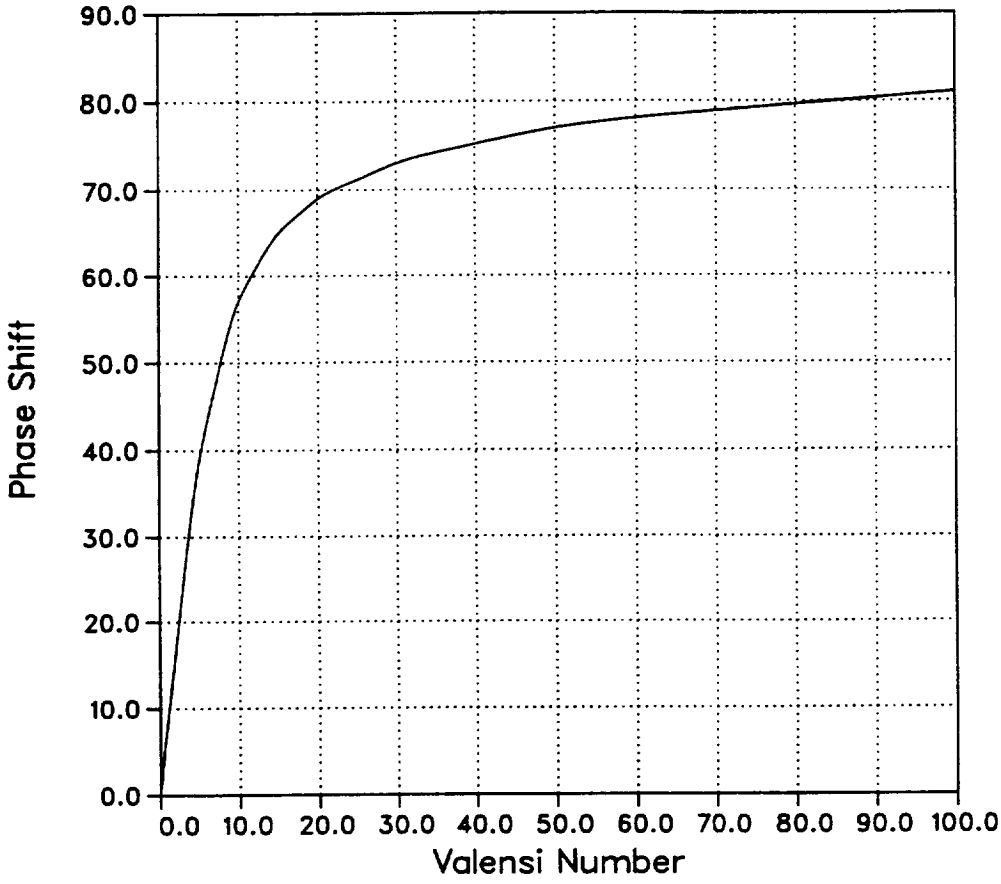

Figure 3.5: Variation of the bulk velocity-pressure gradient phase shift with Va.

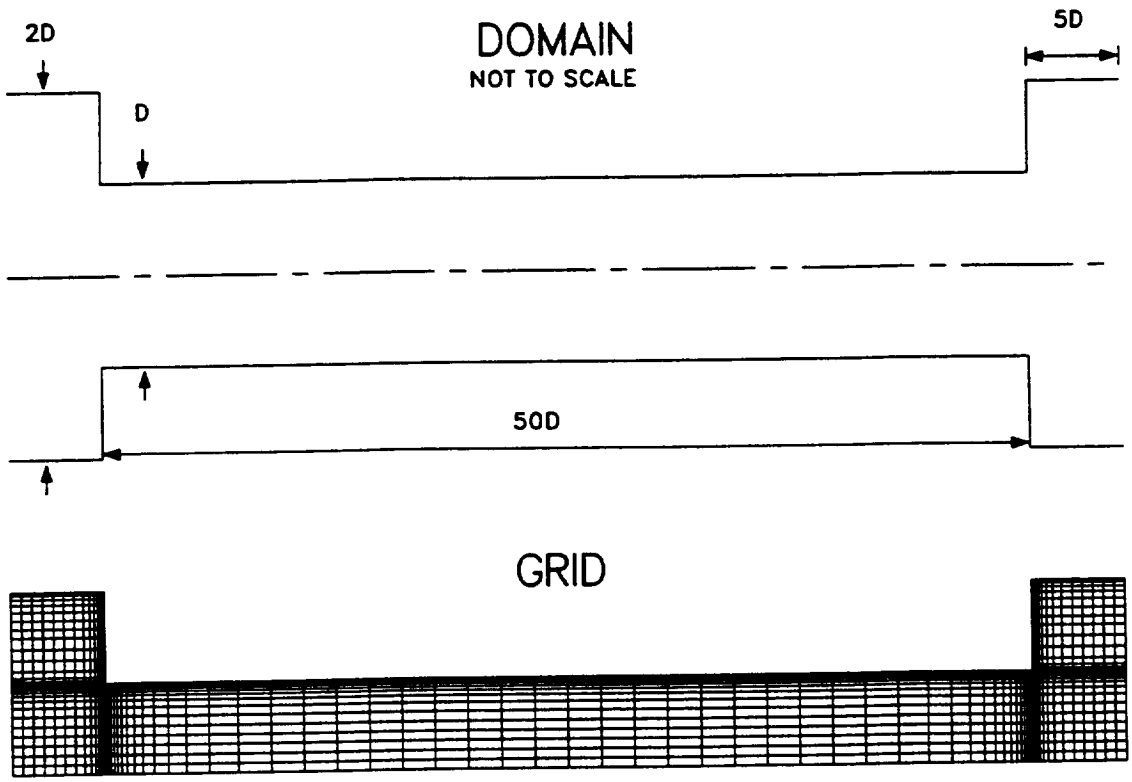

Figure 3.6: Axisymmetric domain geometry and computational grid for pipe with expansion/contraction ends.

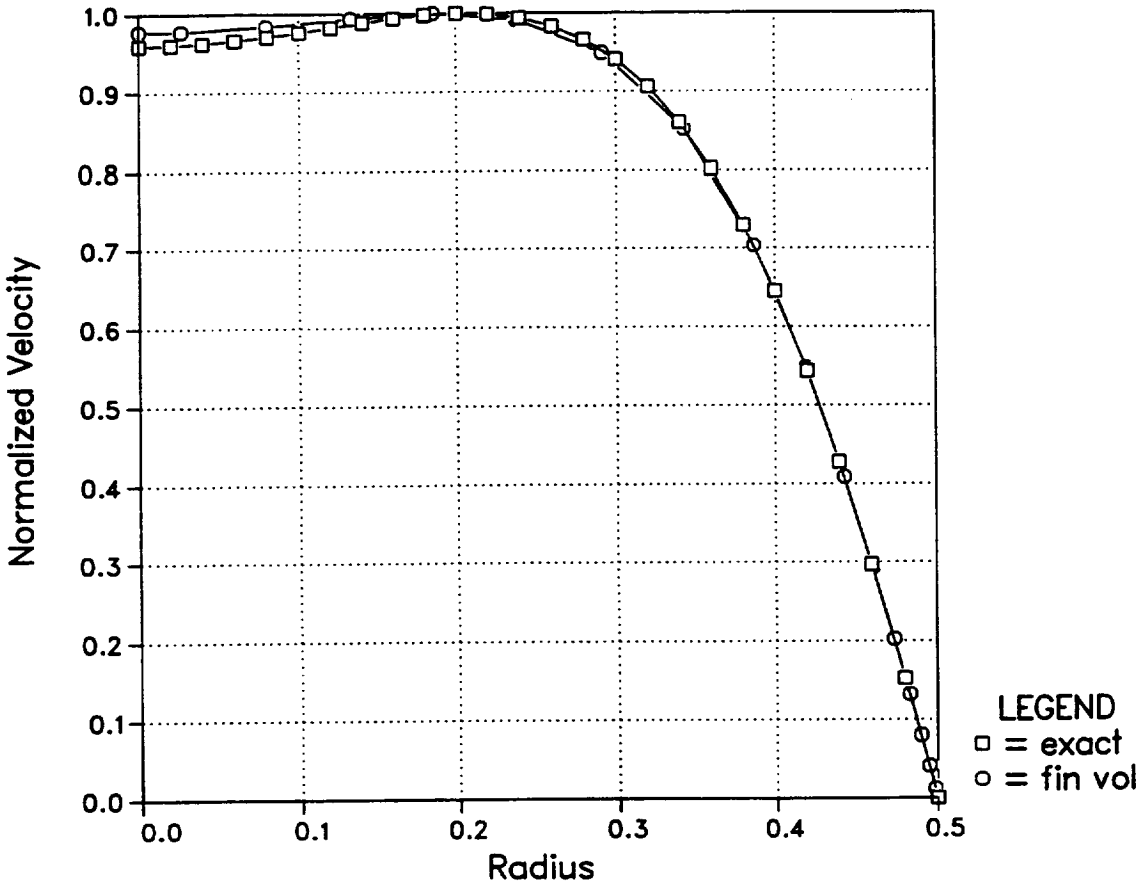

Figure 3.7: Comparison of exact and finite volume solution velocity profiles for Va = 30.

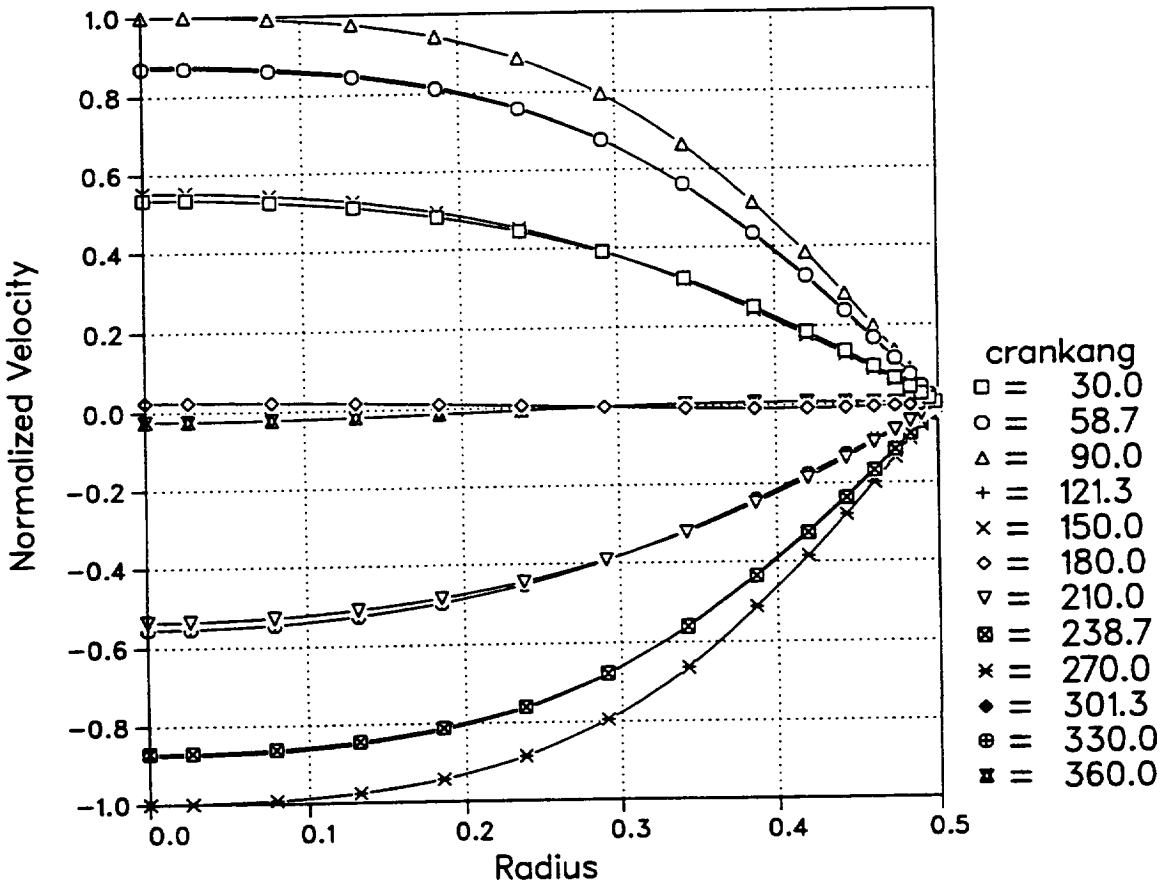

Figure 3.8: Velocity profiles at the pipe midlength at select times during the flow cycle for $Va = 1$.

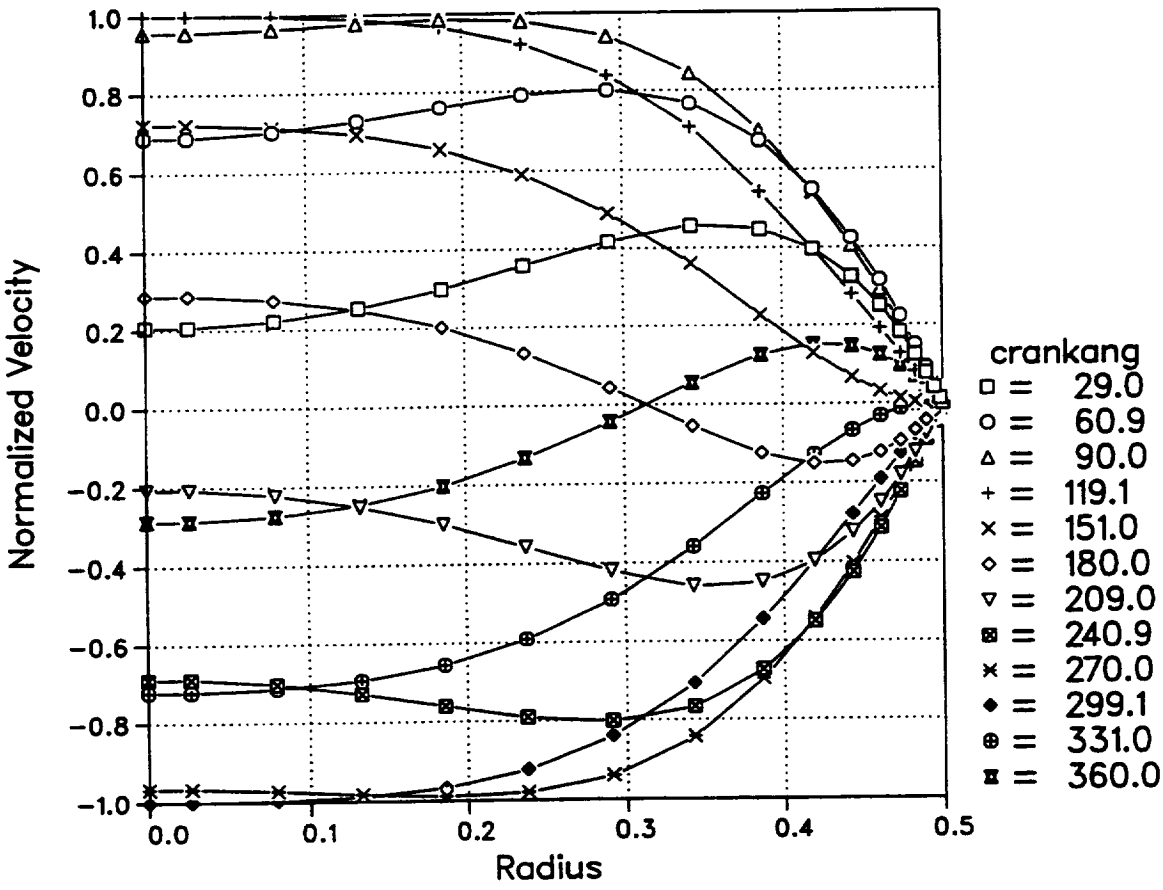

Figure 3.9: Velocity profiles at the pipe midlength at select times during the flow cycle for $Va = 30$.

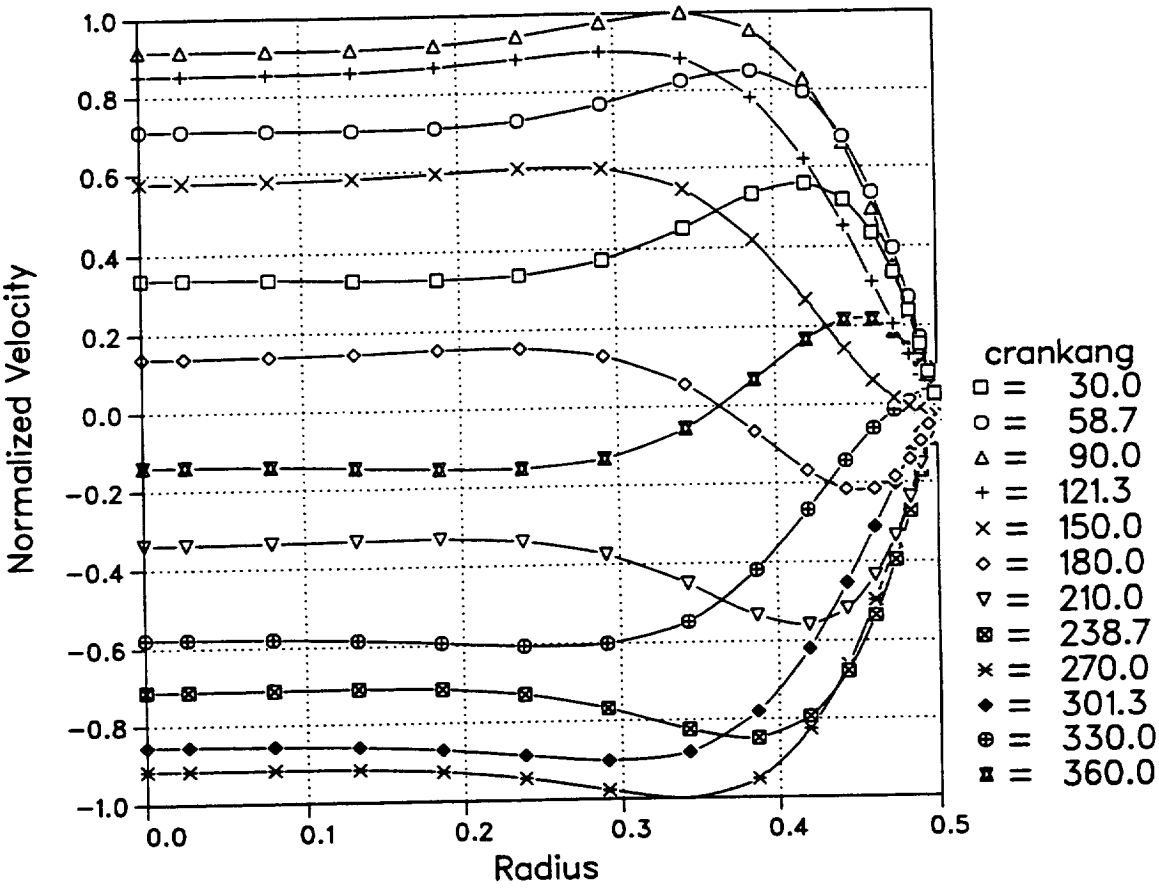

Figure 3.10: Velocity profiles at the pipe midlength at select times during the flow cycle for $Va = 100$.

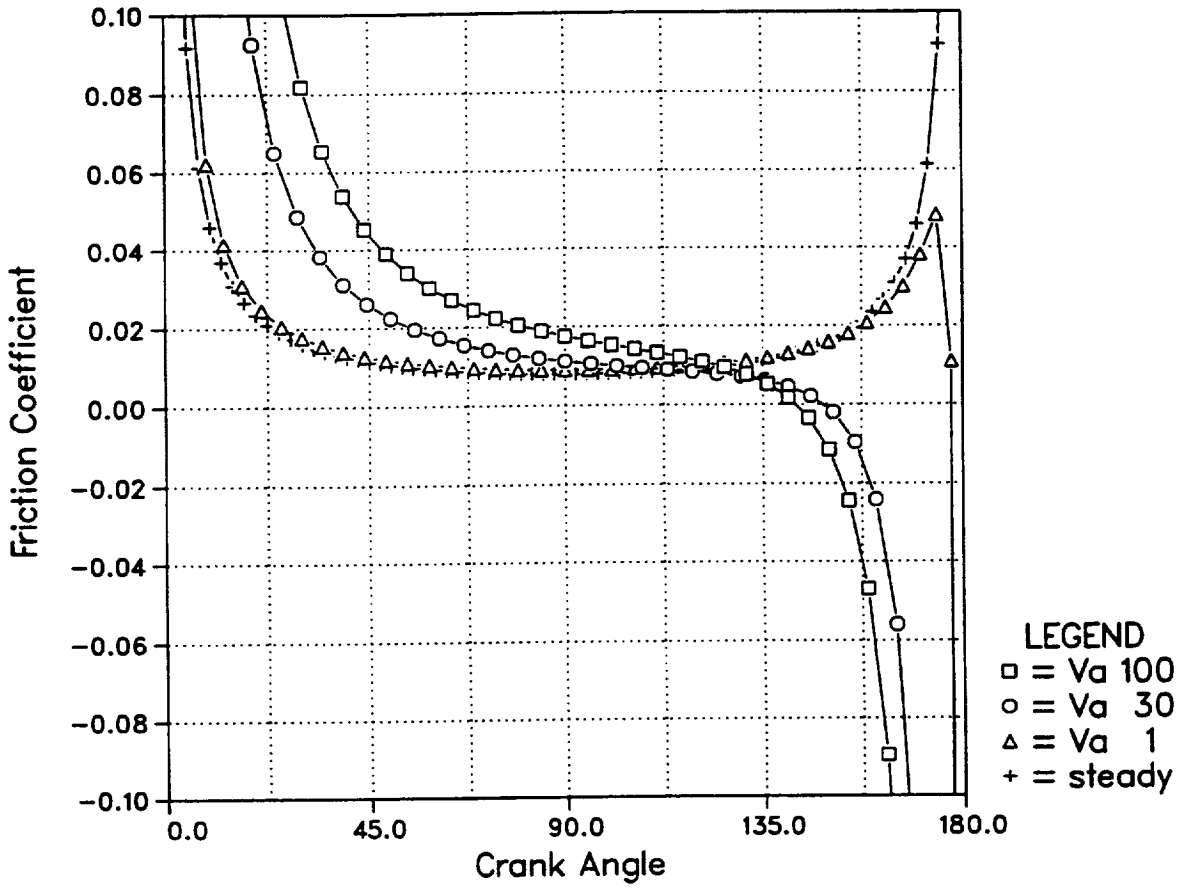

Figure 3.11: Friction coefficient variation at the pipe midlength during one half flow cycle for select Va.

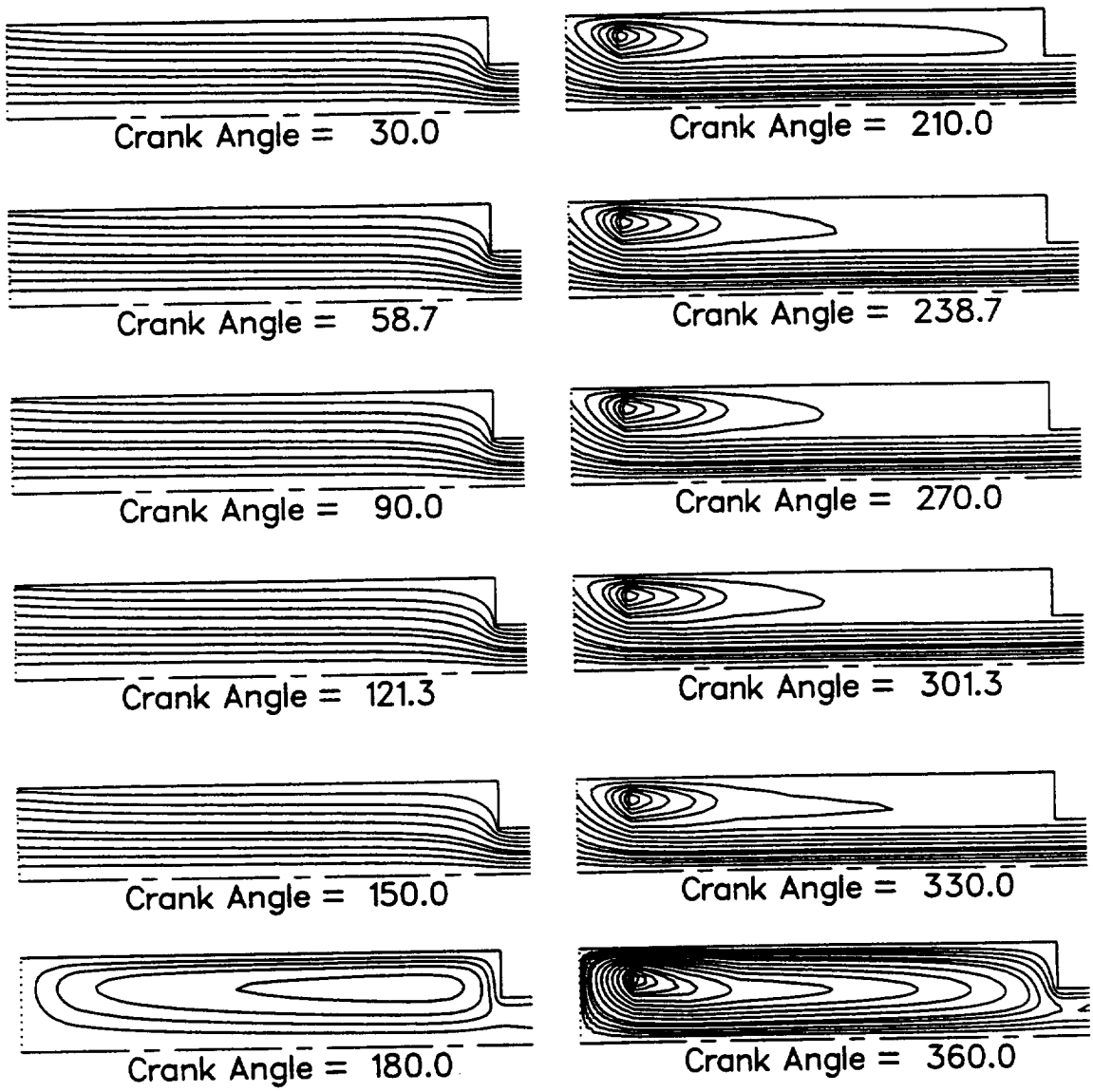

Figure 3.12: Streamlines within the left end region at select times during the flow cycle for $Va = 1$.

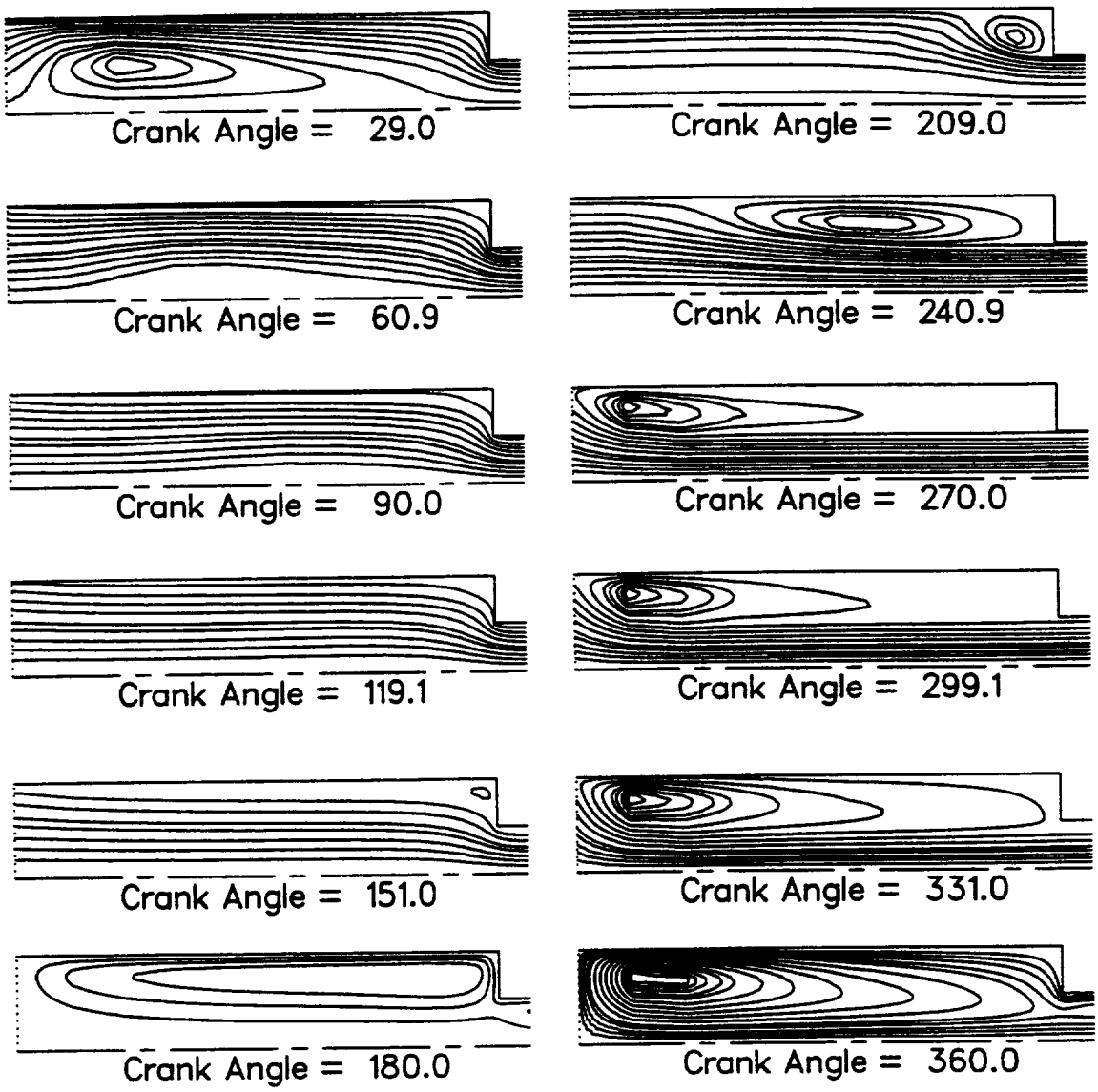

Figure 3.13: Streamlines within the left end region at select times during the flow cycle for $Va = 30$.

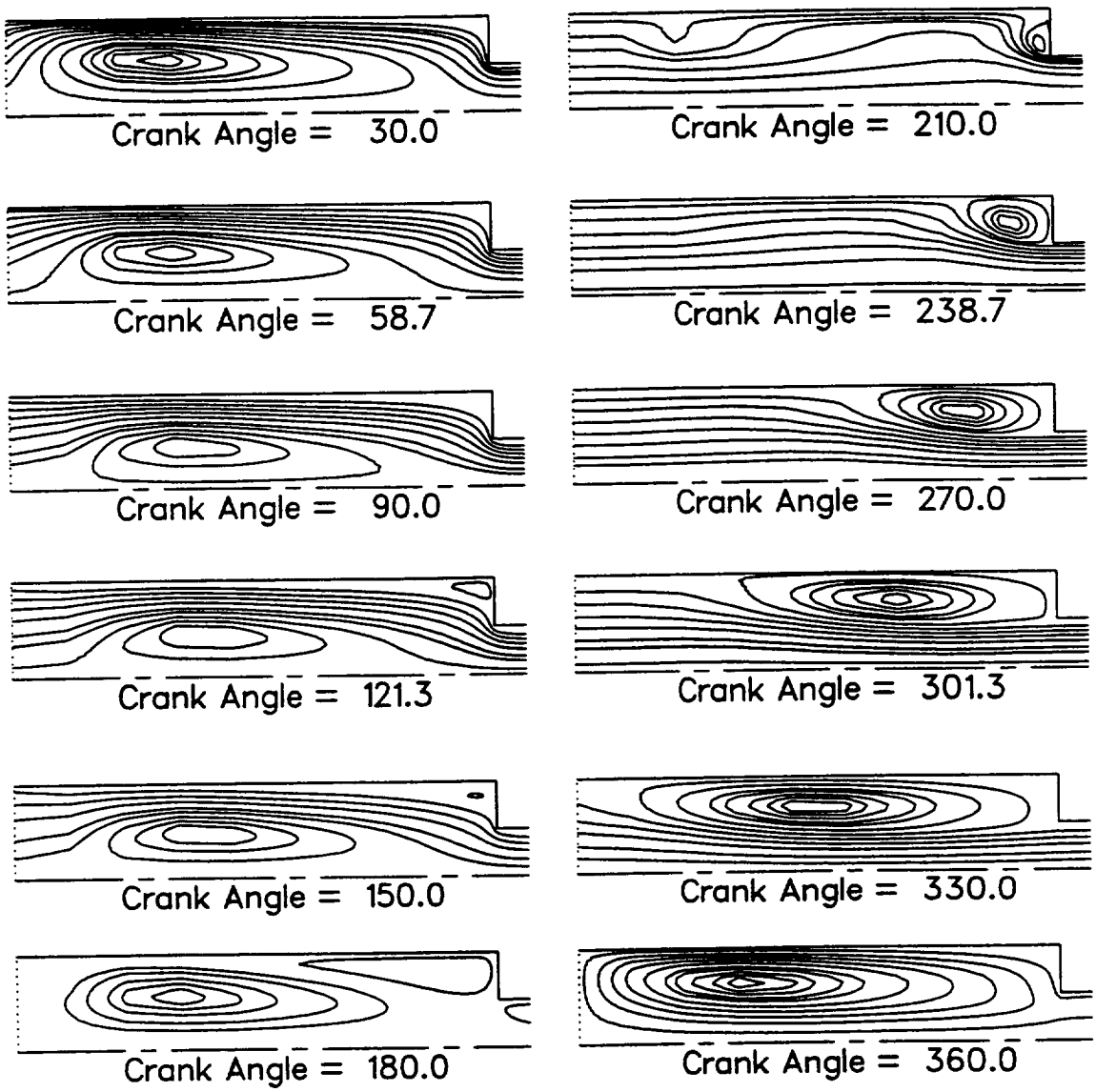

Figure 3.14: Streamlines within the left end region at select times during the flow cycle for $Va = 100$.

Chapter 4

The Turbulent Flow Solution

In this chapter the flow solution for turbulent flows will be presented. Fully developed results for pipe flow will be shown first, as a means of verifying the performance of the turbulence models. Results for oscillating flow will then be presented. Comparisons with the available experimental data will also be made, with points of agreement and discrepancies noted.

The operating conditions considered in this and following chapters are, unless otherwise noted, representative of the SPRE operating conditions. For SPRE, the maximum Reynolds number (Re_{max}) during the flow cycle is 12000. The oscillation rate is given by the Valensi number (Va), which is 80 for the SPRE design point.

Three different turbulence models were tested during the course of this work. Most of the results presented are based on the Lam-Bremhorst Low Reynolds Number (LRN) model. The two time scale model of Kim and the RNG model of Yakhot and Smith were also tested. The mathematical bases of these turbulence models were discussed in chapter 2.

4.1 Fully Developed Pipe Flow

The definition of fully developed flow does not depend on whether the flow is laminar or turbulent. The absence of axial variation in all the dependent variables is sufficient to satisfy the fully developed condition. The nature of turbulent flow, with enhanced cross stream transport, is such that fully developed conditions are typically established within only a few diameters of the pipe inlet. Incropera and DeWitt (1985) consider turbulent flow to be fully developed after 10 to 60 pipe diameters.

The increased cross stream transport which occurs in turbulent flow has a dramatic effect on the axial velocity profile. Relative to laminar flow, the velocity profile is flatter near the axis, and the velocity gradient at the wall is much steeper. As a result, the pressure gradient required to drive a turbulent flow is much larger than for laminar flow. Turbulent flows typically occur in piping systems when the Reynolds number is greater than about 2300.

The velocity profile for turbulent flow has been the subject of a great deal of experimental research. The measured profile can be fitted well using the so-called *law of the wall.* The flow can be divided into three regions, depending on the distance from the wall. Next to the wall, turbulent fluctuations are damped and the molecular diffusion dominates. This is referred to as the viscous sublayer. Far away from the wall, the effects of molecular diffusion are negligible in comparison with turbulent transport processes. This is called the fully turbulent region. Between these layers is a region where the flow is intermittently laminar or turbulent. Time averaging reveals that a gradual increase in turbulent activity occurs as this region is traversed from the viscous sublayer to the fully turbulent region. This is referred

to as the buffer region. For the viscous sublayer, the velocity profile is given by

$$u^+ = y^+ \tag{4.1}$$

where

$$u^+ = \frac{u}{u_\tau} \qquad \text{and} \qquad y^+ = \frac{y u_\tau}{\nu} \tag{4.2}$$

are the *wall coordinates* and

$$u_\tau = \sqrt{\frac{\tau_w}{\rho}} \tag{4.3}$$

is the friction velocity. In the fully turbulent region, the profile is fitted to the expression

$$u^+ = A \log y^+ + B \tag{4.4}$$

The form of this expression also suggests the name *log-linear* for this region. Schetz (1984) recommends $A = 5.6$ and $B = 4.9$ as the best fit through the available experimental data in the log-linear region. Equations (4.1) and (4.4) make up the law of the wall.

The performance of the computer model can be tested against the law of the wall profile. Figure 4.1 compares the computed velocity profile (in symbols) and the law of the wall (dashed lines). The agreement is good. The computed results are based on fully developed turbulent flow using the Lam-Bremhorst turbulence model at $Re = 50{,}000$. The grid is composed of 42 nonuniform grid points across the pipe radius, with near-wall grid points clustered tightly together. As is typical, the pipe flow profile shows a slight "wake" at the axis. The low Reynolds number functions of the Lam-Bremhorst turbulence model do a good job of fairing in the viscous sublayer and the log-linear regions.

Figure 4.2 compares the same predicted fully developed axial velocity profile with the experimental data of Laufer (1953). Alternate numerical data points are

plotted for clarity. The numerical curve is normalized against it's own peak value. The experimental data is normalized to match the bulk velocity of the numerical profile. The agreement is fair. The numerical model produces a somewhat flatter profile near the axis, and thus overpredicts the velocity closer to (but not at) the wall. This is a common deficiency of the k-ϵ model, due to a slightly overpredicted turbulent viscosity near the axis. The numerical model nevertheless produces the correct wall shear.

4.2 Oscillating Pipe Flow

As was done in chapter 3, the numerical model can be extended to oscillating flow by imposing a time-dependent velocity boundary condition. Oscillating flow in straight pipes was studied numerically by Koehler (1990). This thesis presents the results obtained when the model is extended to the case where expansion and contraction regions are applied to the ends of the pipe.

The motivation for modeling oscillating pipe flow with enlarged end regions is to observe what effect the end regions have on the flow within the pipe itself. Koehler specified a uniform axial inlet velocity for his numerical model. The boundary conditions for the turbulence quantities at the inlet to the straight pipe were derived. These boundary conditions were based on the assumption of isotropic turbulence, for which

$$k_{in} = \frac{3}{2}\left(TI\ U_{b,in}\right)^2 \tag{4.5}$$

is the definition of the turbulence intensity TI. The available data for fully developed turbulent pipe flow was then manipulated to produce an expression for the dissipation rate

$$\epsilon_{in} = \frac{1}{TI\ Re^{\frac{7}{8}}}\ \frac{k_{in}^2}{\nu} \tag{4.6}$$

This functional dependence on Re follows from the data, but the use of TI is somewhat arbitrary. This treatment requires that the flow be allowed several pipe diameters in which to develop before the results can be considered representative of pipe flow. The same turbulence boundary conditions are used in the present study, but the end regions provide a space in which the turbulence can adjust prior to reaching the pipe itself. Interesting flow features are also allowed to develop in the end regions. For instance, flow separation occurs when high momentum fluid flows into an expansion. Upon flow reversal, these features are expected to be swept back into the pipe, and their effect on the pipe flow can be observed.

The results for turbulent flow depend strongly on the values of Re and Va. For moderate values of these parameters, the flow is not turbulent throughout the entire cycle. Especially for low values of Va, the flow may be laminar for a considerable time near flow reversal, when the bulk flow rate is low. As Va increases, turbulent effects persist over a larger portion of the flow cycle. In this and following chapters we will refer to "turbulent oscillating flow" while recognizing that laminar and transitional flow will be present during part of the flow cycle.

4.2.1 Results for the Sudden Expansion/Contraction Ends

In this section the results for the pipe fitted with sudden expansion/contraction ends are considered. The Lam-Bremhorst turbulence model is used. The results are compared with the available experimental data.

Figures 4.3 through 4.6 show the axial velocity profiles at the pipe midlength at select times during the flow cycle for Va = 40, 60, 80 and 100. Re_{max} in each case is 12000. For moderate values of Va, the effect of oscillation is apparent only near bulk flow reversal. In figure 4.3 the circulation of flow at bulk flow reversal is small, but not negligible. Notice, however, that the profiles for crank angles of

58.7° and 121.3° are nearly indistinguishable. When Va is raised, the profiles for accelerating flow begin to differ from those of decelerating flow, particularly near the wall. Figure 4.6 shows that the profiles for 58.7° and 121.3° are different. The profile for 58.7° is somewhat laminar-like. The wall gradient is lower than that of the 121.3° profile. For $Va = 100$, the wall-near fluid at 58.7° has not yet made the full transition to turbulence. The profile at 121.3° shows a steeper wall gradient since the flow is turbulent at this point in the cycle. This effect of transition is not seen in the laminar case, and causes the turbulent flow to be more complicated than the laminar flow.

As was mentioned in chapter 2, the law of the wall is not generally applicable for oscillating flow. However, it is nonetheless instructive to observe the predicted axial velocity profile in wall coordinates. Figures 4.7 through 4.10 show the velocity profile in wall coordinates for $Va = 40$, 60, 80 and 100. The profiles are measured at 90° crank angle at the axial midlength of the pipe. The rate of change of the pressure gradient is modest at 90° crank angle and the end effects are insignificant 30 pipe diameters downstream of the inlet. Under these conditions, the velocity profile is expected to be at least qualitatively similar to the universal profile, and this is born out by the figures. Figure 4.9 also shows the experimental data of Friedman (1991) for the SPRE operating condition. These data differ from the universal profile, but the differences can be explained as an unsteady effect. Once transition has occurred, the velocity profile near the wall is expected to be steeper than for steady flow and the flow near the pipe axis is slightly slower. Figure 4.9 shows that the experimental velocities are indeed slower near the axis. The Lam-Bremhorst turbulence model apparently causes the velocity to follow the universal profile too closely, and thereby understates the unsteady effect.

The variation of the friction coefficient over the first half of the flow cycle is

shown in figures 4.11 through 4.14. These results are taken at the pipe midlength. The friction coefficient is defined as

$$c_f = \frac{\tau_w}{\frac{1}{2}\rho U_b^2} \tag{4.7}$$

This definition of c_f is undefined as the bulk flow rate approaches zero, in which case the definition would have no utility.

The Blasius friction coefficient correlation for steady flow at the corresponding instantaneous Reynolds number is also plotted on each figure for reference. Schlichting (1979) gives this correlation as

$$c_f = 0.0791 Re^{-0.25} \tag{4.8}$$

The modest Reynolds number dependence produces a rather flat curve over the cycle.

Figure 4.11 shows that the friction coefficient starts high and drops quickly during the early part of the flow cycle. This is indicative of the laminar nature of the flow at this point in the cycle. At about 25° crank angle the predicted friction coefficient drops below the corresponding steady flow value. The flow is still laminar-like at this point. At 35° the friction coefficient starts to rise up and meets the steady flow curve. This behavior is expected at low values of Va, for which the flow can be characterized as quasi-steady. As Va increases, the laminar behavior of the flow persists farther into the cycle. Figures 4.12, 4.13 and 4.14 show that transition is predicted at roughly 40°, 45° and 60°, respectively. In each case, the flow near the wall reverses prior to bulk flow reversal, causing the friction coefficient to drop sharply to zero before rising again and taking a laminar-like value.

The experimental friction coefficient for the SPRE operating condition based on Friedman's data is also shown on figure 4.13. Up to about 40° the agreement

between the predicted and measured friction coefficients is excellent. However, the experimental data continue to show laminar-like behavior up to nearly 90°. The experimental data were measured with a smooth nozzle entrance to the pipe, while the numerical results are based on a sudden contraction pipe entrance. Friedman (1991) states that the observed transition at this axial location coincides with the arrival of a slug of turbulent flow which was generated within the nozzle at the end of the previous flow cycle. This slug is then convected back into the pipe during the next cycle. This turbulent fluid may be responsible for the fact that the data for crank angles of 90° through 130° are above both the predicted and steady flow results. The traveling slug issue was investigated further by building a nozzle-ended numerical model and subjecting it to the SPRE operating condition. This model and the corresponding results will be discussed below.

A turbulent slug generated within the end region during outflow would not be expected to survive the intense shearing action which occurs at a sudden contraction after flow reversal. Apart from the traveling slug issue, the experimental data of figure 4.13 show that the turbulence within the pipe is damped by the acceleration of the fluid up to at least 80° crank angle. The numerical model predicts transition at about 45° crank angle, at which time the bulk flow Re is about 8500. The bulk flow Re passes 2300 at about 11° crank angle, showing that the model does reflect at least some degree of damping due to acceleration. It would be desirable to find a means of modifying the model to account for the experimentally observed degree of damping. Koehler (1990) proposed a modification to the dissipation rate transport equation (2.21) to account for the effects of acceleration and deceleration. The modification consists of adding an additional production term which is scaled by the instantaneous value of acceleration. The proposed term would take the form

$$\epsilon K_a \tag{4.9}$$

where

$$K_a = \frac{\mu}{\rho U_{b,max}^3} \frac{\partial}{\partial t}(U_b) \tag{4.10}$$

and U_b is given by $U_{b,max} sin(\omega t)$. The dissipation rate transport equation would then become

$$\frac{\partial}{\partial t}(\rho\epsilon) + \frac{\partial}{\partial x_j}(\rho u_j \epsilon) = \frac{\partial}{\partial x_j}\left(\left(\mu + \frac{\mu_t}{\sigma_\epsilon}\right)\frac{\partial \epsilon}{\partial x_j}\right) + c_1 f_1 \rho \frac{\epsilon}{k}(G + c_3 \epsilon K_a) - c_2 f_2 \rho \frac{\epsilon^2}{k} \tag{4.11}$$

The constant c_3 would be fitted against experimental data. The new term would thus augment the existing production term G.

The sinusoidal variation of the bulk velocity in the present research will produce an acceleration source term which is proportional to $cos(\omega t)$. Curve A of figure 4.15 shows the variation of $cos(\omega t)$ over the flow cycle. At the beginning of the cycle the flow is accelerating. The new source term would provide a positive contribution to the dissipation, resulting in the desired damping of turbulence. During the second quarter-cycle the contribution would change signs, amplifying turbulence during deceleration. However, the new source term contribution would be physically unrealistic during the second half cycle. The fluid itself is unaware of the coordinate direction. Regardless of the direction of flow, the fluid will sense "acceleration" whenever the magnitude of the axial velocity is increasing. In other words, the new dissipation rate source term should be positive in the third quarter-cycle and negative in the fourth. Curve B of figure 4.15 has the correct sign for the last half cycle.

The proposed modification to the dissipation rate equation given by equation (4.10) is physically unrealistic for oscillating flow. The combination of the behavior of curve A of figure 4.15 during the first half cycle and curve B during the second

would provide the correct sign. However, this treatment results in stepwise discontinuities in the source term contribution at each flow reversal. This is in itself physically unrealistic and would require further (ad hoc) modifications to correct. The additional modifications would create yet another source of uncertainty in the results. It seems that there is no straightforward means of applying an acceleration modification to the dissipation rate equation in the case of oscillating flow. This treatment will no longer be considered for the present research.

The streamlines within the left end region are shown in figures 4.16 through 4.19 for Va = 40, 60, 80 and 100. These figures show that pronounced unsteady effects are present near flow reversal in each case, and the unsteady effect persists over a larger fraction of the flow cycle as Va increases. The recirculation bubble within the end region during outflow is initiated shortly after 180°. The subplot for 210° crank angle in figures 4.16 through 4.19 clearly shows the effect of Va. As Va increases, less time is available for growth of the recirculation bubble. The bubble continues to grow as the flow cycle continues.

4.2.2 Results for Smooth Nozzle Ends

In this section we consider the results obtained from the smooth nozzle-ended model. The objective of this numerical test is to determine whether the Lam-Bremhorst turbulence model can predict the passage of a turbulent slug of fluid entering the pipe from the nozzle region. The smooth nozzle-ended pipe is not representative of the SPRE design, but was employed during the early stages of experimental oscillating flow research at the University of Minnesota. Seume (1988) used the smooth nozzles in an attempt to prevent large-scale separation at the inlet to the pipe and thereby concentrate attention on the fully developed features of oscillating flow. This approach was successful except for a small portion of the cycle immediately

following flow reversal. The divergence angle of the nozzle was too large to prevent separation during outflow. A recirculating bubble of fluid was trapped within the nozzle. Upon reversal, this relatively turbulent fluid was convected back into the pipe. The fluid entering the test section behind the slug had a low level of turbulence, since it had passed through a heat exchanger core which acted like a fine-scale flow straightener. This heat exchanger was intended to be used during later heat transfer experiments, and was included in the flow tests in order to ensure that consistent end conditions were employed during both the flow and heat transfer phases of the experiments. As the turbulent slug was swept through the pipe the instrumentation sensed the arrival at each probe location as transition. Depending on the probe location, the fluid would in some cases remain turbulent after the slug had passed, or would revert to laminar flow, depending on local conditions.

The geometry of the SPRE design will employ different end conditions. One end of the heater (and cooler) will be connected to a large plenum, with the other end close-coupled to the regenerator matrix. The plenum ends will behave as sudden expansion/contractions. Fluid entering from the plenum will experience intense acceleration and shearing. This will break up any large scale flow structures, rendering the flow in the pipe relatively insensitive to the flow structure in the plenum region. Fluid entering the pipes from the regenerator will have a nearly uniform axial velocity component, but the turbulence structure will be difficult to specify.

The traveling slug problem, though not directly applicable to the SPRE design, provides an opportunity to test the turbulence model employed for closure of the Navier-Stokes equations. Figure 4.20 shows the grid used to model the left nozzle end region. The length-to-diameter ratio of the pipe is 60, matching the Seume experiment. Each nozzle is 4 pipe diameters in length. The nozzle inlet diameter is 3.33 times that of the pipe. The nozzle contour is formed by two cubic functions.

The nozzle inlet boundary flow is used to create the flow oscillation.

Figure 4.21 shows the friction coefficient over the first half of the flow cycle, plotted along with the experimental data which was also plotted in figure 4.13, at the axial middle of the pipe. The results for the nozzle-ended model are essentially identical to those obtained with the expansion/contraction model. There is no evidence that a turbulent slug is convected into the pipe after flow reversal, or if it were it has dissipated before reaching the axial middle of the pipe.

4.2.2.1 Shortcomings of the Lam-Bremhorst Model

The results presented above point out two shortcomings of the Lam-Bremhorst turbulence model when applied to oscillating flow. First, the model fails to account for the full degree of damping which occurs as the flow is accelerated. Figure 4.13 compared the predicted and measured friction coefficients and showed that the model predicted transition too early. For the SPRE operating condition, the flow in the pipe passes through $Re = 2300$ at about 11^o crank angle. The Lam-Bremhorst turbulence model was able to delay transition to about 45^o, but this is still premature relative to the experimental results, for which transition did not occur until after 80^o crank angle. The second shortcoming is the inability of the model to predict the passage of a turbulent slug of fluid. This feature was demonstrated by the experimental results shown in figure 4.21.

At this stage in the research the two time scale model of Kim (1992) was considered to determine whether it would improve the predictions of the acceleration damping effect or the traveling turbulent slug. The details of this model where discussed in chapter 2.

4.2.3 Results of the Kim Model

In this section the results for the Kim model are compared with those of the Lam-Bremhorst model and the experimental data of Friedman (1991). Some general comparisons of the predictions of flow and turbulence quantities are first made. The transition to turbulence and the acceleration damping behavior of the models are compared next. Lastly, the ability of the model to predict a traveling slug of fluid ingested from the nozzle end after flow reversal is studied.

Figures 4.22 through 4.26 compare the results of the Lam-Bremhorst and Kim models at peak flow for the $Re_{max} = 12000$, $Va = 80$ case. The sudden expansion/contraction model results are used, with data taken at the axial middle of the pipe. Figure 4.22 shows the axial velocity profiles. The Kim result is not as flat as that of the Lam-Bremhorst model, but the wall gradients appear to be similar. The Kim velocity profile is slightly better than the Lam-Bremhorst result in that the velocity profile is not excessively flat (compare with figure 4.2).

Figure 4.23 shows the normalized turbulent viscosity profiles for the Lam-Bremhorst and Kim models. The Kim result is significantly higher except near the wall, where both models show a decay to zero. The Kim result is worse than Lam-Bremhorst. According to Schlichting (1979), the turbulent viscosity is expected to fall off near the axis, where turbulence production is low. Neither model produces a good distribution of turbulent viscosity near the axis.

Figure 4.24 shows the normalized turbulent kinetic energy profiles for the same condition. The Kim model predicts a substantially higher level at all locations except the wall. While the boundary condition forces both models to zero at the wall, the Kim model produces a far steeper gradient near the wall and a much larger overshoot.

Figure 4.25 shows the normalized dissipation rate profiles. In this case the Kim model produces significantly higher values at all radial positions.

Figure 4.26 shows the axial velocity profiles of the Lam-Bremhorst and Kim models plotted in wall coordinates. The experimental data of Friedman is also shown, along with the universal profile in dashed line. The three data sets represent the velocity profile at the axial middle of the pipe at the peak flow rate. The Lam-Bremhorst results follow the universal profile fairly closely. (The universal profile is based on steady flow.) Except at the axis, the Kim results do a good job of following the unsteady experimental data, at least for this instant in time.

Figure 4.27 shows the variation of the friction coefficient over the first half cycle for the Lam-Bremhorst and Kim models. The experimental results of Friedman and the steady flow results at the corresponding bulk flow rate are also shown. The Kim results follow the laminar-like behavior during the first 30° crank angle, but then become turbulent well before the experimental data and about 10° before the Lam-Bremhorst results. Moreover, the Kim results are significantly higher than all others through most of the remainder of the half cycle. The friction coefficient at 90° (peak flow) is very close to the experimental result, which explains the good velocity profile agreement shown by the Kim model in figure 4.26. Recall that the experimental velocity profile at 90° crank angle (figure 4.26) was influenced by the arrival of the turbulent slug. No traveling slug is expected when using the expansion/contraction geometry, so the close agreement between the Kim model and the experimental velocity profile results in figure 4.26 is fortuitous.

The presence of a traveling slug being carried into the pipe after flow reversal is inferred from experimental observations within the pipe section itself. Turbulence levels are seen to rise dramatically at a time consistent with the arrival of a slug traveling through the pipe at the bulk fluid velocity. No detailed experimental data

is available concerning the structure of turbulence generated within the nozzle during outflow. On the other hand, the numerical models provide detailed information about the distribution of all variables within the nozzle. This information can be studied to observe the ability of the model to predict the traveling slug effect. The Kim model was used to produce figures 4.28 through 4.33, which show surface plots of the turbulent viscosity within the right-end nozzle for several steps in time, beginning at flow reversal. In these figures, the pipe ends at an axial length of 64. The nozzle is represented by the area to the right. In figure 4.28, the bulk flow has come to rest. The turbulence within the nozzle results from separation which occurred during the previous quarter-cycle, for which flow was to the right. As the cycle continues, this turbulence, characterized in these figures by the turbulent viscosity, is expected to be convected back into the pipe (to the left). Figure 4.29 shows the turbulent viscosity in the nozzle at 2.5° after flow reversal. The bulk flow is moving into the pipe at $Re = 518$. The levels of turbulent viscosity have decayed slightly, but there is no evidence that the turbulent structure has been convected from the nozzle into the pipe. Figures 4.30 through 4.33 show the turbulent viscosity at approximately 5.7°, 9.2°, 13.0° and 17.1° crank angle after flow reversal, for which the instantaneous Reynolds numbers are 1187, 1926, 2709 and 3519, respectively. The turbulence in these figures is seen to decay in place, instead of being swept into the pipe. Similar flow visualizations based on the Lam-Bremhorst model (not shown) produced similar results. Both the Lam-Bremhorst and Kim models fail to ingest the turbulent slug after flow reversal.

A further test was performed to determine whether the Kim model can predict the passage of a turbulent slug. The flow behind a turbulence generating grid was considered. If the turbulence level at the plane of the grid is increased and then decreased in a stepwise fashion, the turbulence within the fluid passing downstream

of the grid should exhibit a slug flow behavior. This type of flow is spatially one-dimensional. Near-wall effects need not be modeled and there is no turbulence generation, so the results are a test of the convection and rate of dissipation of the turbulence. This test was also performed using the k-ϵ model for comparison.

Figure 4.34 shows the trajectory of the normalized turbulent kinetic energy downstream of a turbulence generating grid as produced by the Kim model. The length and time scales are also normalized using $k^{\frac{3}{2}}/\epsilon$ and k/ϵ, respectively. The inlet turbulence intensity is 2% initially, and this steady flow result is represented by the $\tau = 0.0$ curve. The inlet turbulence is then increased to 10% for the next five time steps before returning to the initial level. A slug of highly turbulent fluid is seen passing to the right after the inlet turbulence intensity is reduced, but this turbulence quickly dissipates while being convected downstream.

Figure 4.35 shows the same results for the k-ϵ model. For this model the turbulent slug persists slightly longer than in the case of the Kim model. For instance, the Kim model predicts a peak value of the normalized turbulent kinetic energy of about .0024 when $\tau = 2.48$, the first time step after the inlet turbulence intensity is reduced. At the same instant, the standard k-ϵ model predicts a peak turbulent kinetic energy of about .0027. It appears that two time scale model does not provide any possibility of improvement over the k-ϵ model with respect to the convection of a slug of turbulent fluid.

The RNG-based k-ϵ turbulence model was tested next for application to turbulent and transitional oscillating flow. The details of the High Reynolds Number (HRN) version of this model were discussed in chapter 2.

4.2.4 Results of the RNG Model

The RNG-based k-ϵ model of Yakhot and Smith (1992) has been tested to determine its suitability for the prediction of oscillating flow. The model was first tested on steady pipe flow using the HRN formulation. This model was not applied to oscillating flow due to the limitations of the wall function boundary conditions which were discussed in chapter 2. Since the details of the LRN form of the RNG model are not available in the literature, an attempt was made to formulate a low-Reynolds number RNG model by following the treatment of the Lam-Bremhorst model. The HRN RNG model was modified by applying the Lam-Bremhorst low Reynolds number functions to the turbulent viscosity equation (f_μ) and the first two source/sink terms of the dissipation equation (f_1 and f_2). These functions are given by equations (2.25) through (2.27). The turbulent viscosity is then given by

$$\mu_t = \rho f_\mu c_\mu \frac{k^2}{\epsilon} \tag{4.12}$$

The dissipation equation becomes

$$\begin{aligned}\frac{\partial}{\partial t}(\rho\epsilon) + \frac{\partial}{\partial x_j}(\rho u_j \epsilon) = \frac{\partial}{\partial x_j}\left(\left(\mu + \frac{\mu_t}{\sigma\epsilon}\right)\frac{\partial \epsilon}{\partial x_j}\right) \\ + c_1 f_1 \rho G \frac{\epsilon}{k} - c_2 f_2 \rho \frac{\epsilon^2}{k} - \frac{c_\mu \eta^3 \left(1 - \frac{\eta}{\eta_0}\right)}{1 + \beta\eta^3}\frac{\epsilon^2}{k}\end{aligned} \tag{4.13}$$

This new model was first applied to steady pipe flow for testing. The model tended to produce a gradual decay of turbulence, ultimately converging to a laminar-like solution. Since no damping function was applied to the last term, it was suspected to be the cause of the poor performance. This term has the ability to change sign, depending on the value of η, so further investigation was in order. For the purposes of this discussion, the last term will be referred to as the RNG coefficient multiplying $\frac{\epsilon^2}{k}$. The RNG coefficient is then

$$R = -\frac{c_\mu \eta^3 \left(1 - \frac{\eta}{\eta_0}\right)}{1 + \beta\eta^3} \tag{4.14}$$

To better understand the behavior of this term, its variation with η was first plotted as shown in figure 4.36. The RNG coefficient is negative for η less than 4.38 (η_0). This produces amplification of turbulence. For η greater than 4.38, the RNG coefficient causes damping of turbulence. To determine the variation of R and η across the pipe section, their values were processed from the results of a converged data set using the Lam-Bremhorst model. The data set is based on steady pipe flow at $Re = 12000$, and the results are taken at the end of a 100 diameter long pipe. Figure 4.37 shows the profile of η. The wall boundary condition for k forces η to zero at the wall. The modest turbulence activity near the axis produces a small value of η in that area. The value of η is highest in the turbulence-generation region. Figure 4.38 shows the profile of R across the pipe section. Clearly, R will tend to enhance turbulence over the bulk of the pipe cross section. However, near the wall the effect of R is to cause significant damping. The magnitude of R in this region is such that it dominates the dissipation equation, forcing the solution toward a laminar-like result. This behavior must be modified in order to produce a plausible LRN RNG model.

Several attempts were made to apply a damping function such as f_2 to R, but these efforts did not produce a well-behaved model. Finally, it was found that if the value of η were restricted, R would be bounded and the model would produce the desired level of turbulence. The treatment adopted here is to restrict η to values less than or equal to 4.0. This prevents R from contributing any turbulence damping behavior. While admittedly ad hoc, the model does produce good results for this steady pipe flow application. These results will now be discussed.

Figure 4.39 compares the axial velocity profiles of the LRN RNG and Lam-Bremhorst models for steady pipe flow at $Re = 12000$. The RNG model produces a slightly higher peak and a rounder shoulder. The Lam-Bremhorst model is flatter

due to a somewhat overstated turbulent viscosity near the axis. The turbulent viscosity is compared in figure 4.40 for the same operating conditions. The reduction in turbulent viscosity at the axis for the RNG model is caused by the coefficient R in the dissipation equation. Near the axis, this coefficient acts as a sink term in the dissipation equation. Since R goes to zero at the axis, dissipation is boosted. This is an improvement over the Lam-Bremhorst model. Since turbulence generation goes to zero at the axis, turbulent viscosity is expected to drop, and this is reflected in the data of Reichardt (1951). Figure 4.41 compares the kinetic energy profiles. These are essentially identical near the axis, with the Lam-Bremhorst model producing a slightly higher peak. Near the wall, however, the RNG model produces slightly higher values. Figure 4.42 shows the dissipation profiles. Once again the Lam-Bremhorst model produces a slightly higher peak, but the RNG model is somewhat higher near the axis, which produces the desired drop in turbulent viscosity. Figure 4.43 compares the velocity profiles in wall coordinates. The agreement between the models is good, with the RNG model producing a slightly higher "wake" near the axis.

Figures 4.44 through 4.47 compare the axial velocity, turbulent viscosity, kinetic energy and dissipation profiles of the LRN RNG and Lam-Bremhorst models for steady pipe flow at $Re = 100000$. The axial velocity profile of the Lam-Bremhorst model is even flatter relative to the LRN RNG model as compared to the $Re = 12000$ case as shown in figure 4.44. This is due to the increasing spread between the turbulent viscosities of the two models. For $Re = 12000$ the Lam-Bremhorst model produces a turbulent viscosity at the axis which is about 35% higher than the LRN RNG model. At $Re = 100000$, the spread is about 39%, as shown in figure 4.45. The kinetic energy profiles of the two models are quite similar at $Re = 100000$, as shown in figure 4.46. The LRN RNG model produces slightly smaller values near

the axis and the peak, and somewhat larger values very close to the wall, but the agreement is better than in the $Re = 12000$ case. For $Re = 100000$ the peak in the dissipation is very high and close to the wall, as shown in figure 4.47, from which it is difficult to distinguish between the LRN RNG and Lam-Bremhorst models. Figure 4.48 shows the comparison in the vicinity of the wall. Once again, the Lam-Bremhorst model produces a higher peak. The wall value of the dissipation is also higher in the Lam-Bremhorst model. Figure 4.49 compares the velocity profiles in wall coordinates. For $Re = 100000$ both models follow the universal profile closely. Again, the RNG model produces a slightly higher "wake" near the axis.

The LRN RNG model presented here does a good job reproducing the details of steady pipe flow. It remains to be seen whether the model offers any improvement in the prediction of oscillating pipe flow. As a test, the model was applied to a 100 diameter long straight pipe subjected to oscillating flow with $Re_{max} = 12000$ and $Va = 80$, the SPRE operating conditions. The model was reasonably well behaved, but produced results which are strikingly similar to those of the Lam-Bremhorst model. This may have been anticipated, given that the LRN form of the RNG model borrowed heavily from the Lam-Bremhorst model. Figure 4.50 shows the friction coefficient at the axial middle of the pipe over the first half cycle. The experimental and steady flow results are shown for reference. The LRN RNG results are virtually identical to those of the Lam-Bremhorst model (see figure 4.27).

The LRN RNG k-ϵ model tested above is not representative of the LRN version proposed by Yakhot and Orszag (1986). That model employed differential relations for the turbulent viscosity in the near-wall region. Details of the application of the model have not been published. Testing of the LRN RNG model of Yakhot and Orszag will have to wait until such time as this model becomes available.

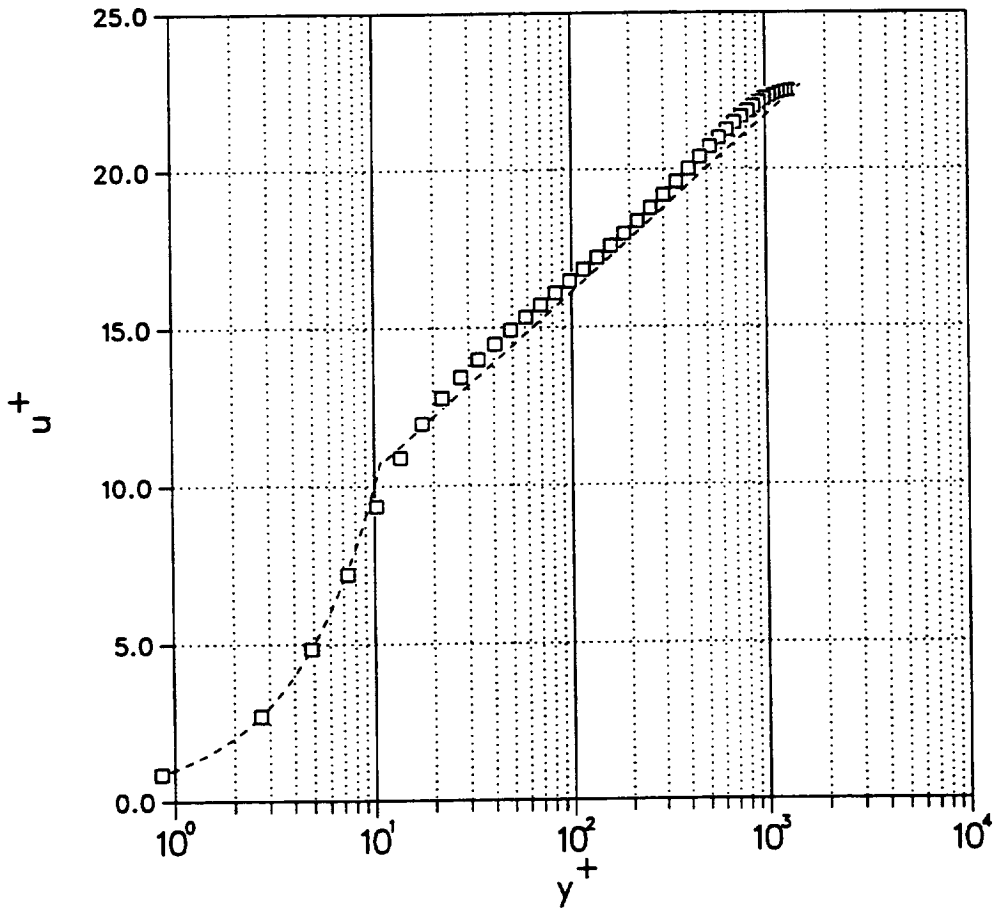

Figure 4.1: Velocity profile for fully developed pipe flow plotted in wall coordinates.

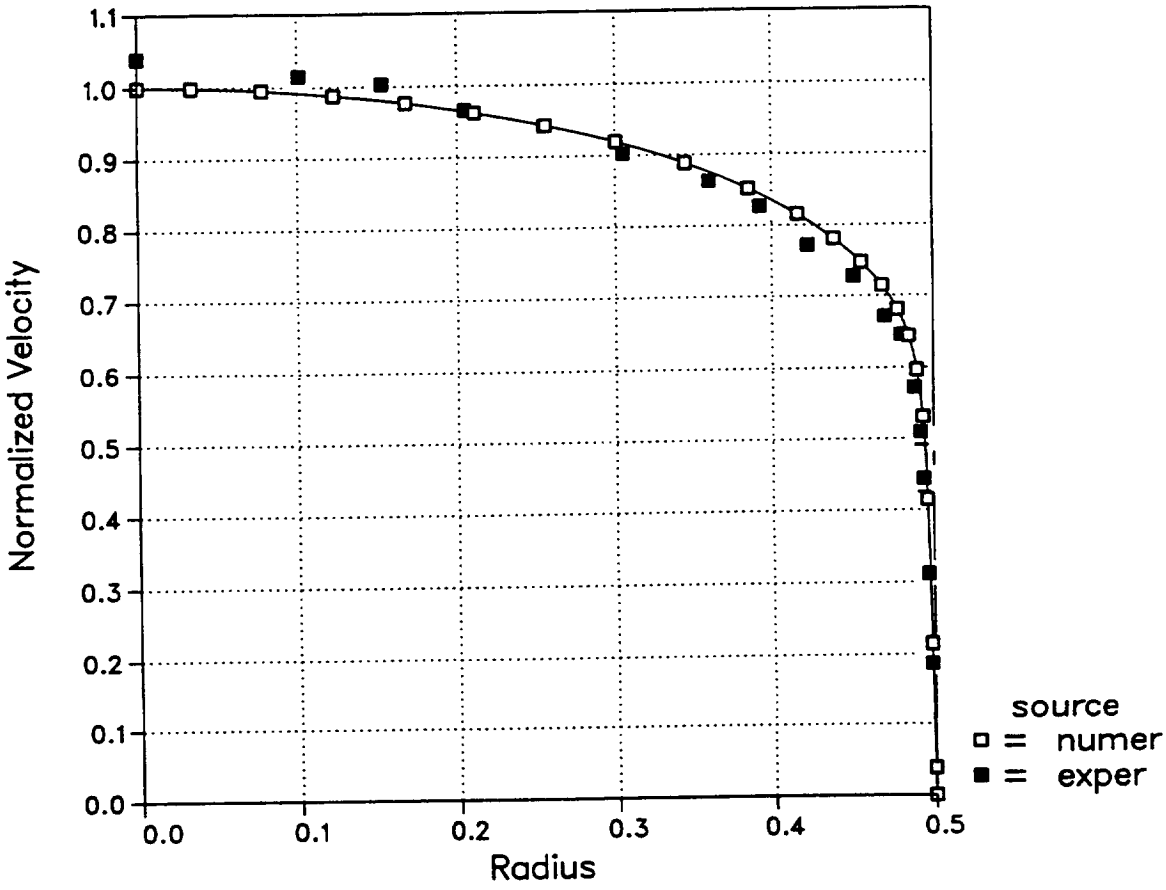

Figure 4.2: Comparison of experimental and numerical velocity profiles for fully developed pipe flow.

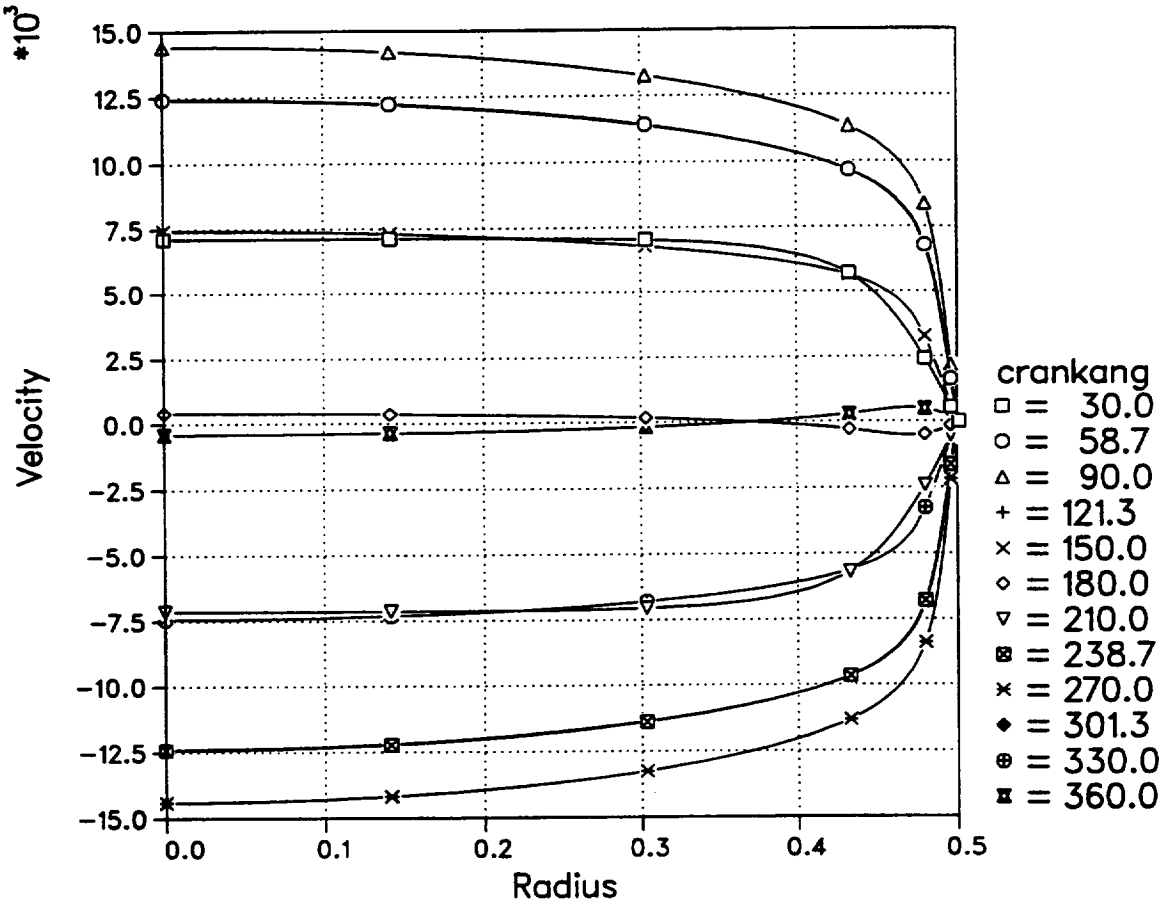

Figure 4.3: Velocity profiles at the pipe midlength at select times during the flow cycle for $Va = 40$.

C-2

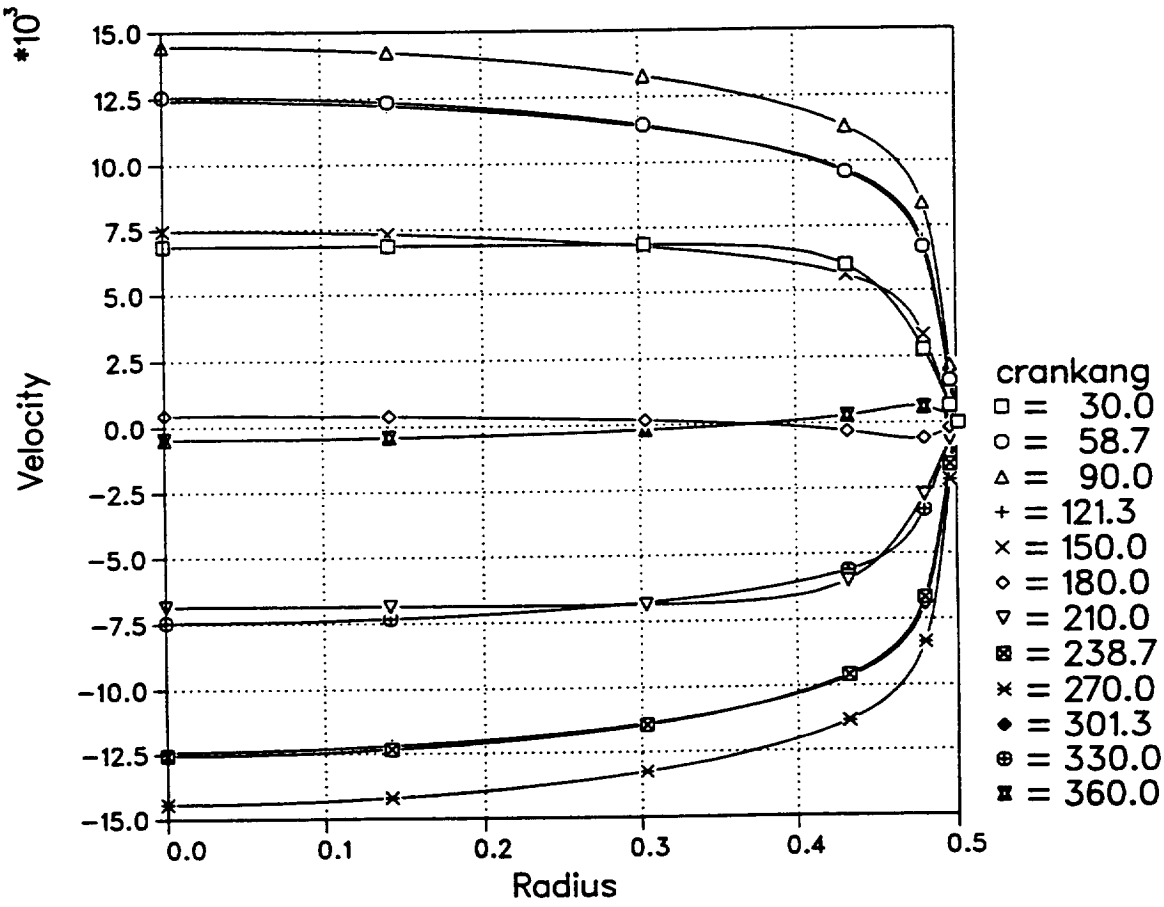

Figure 4.4: Velocity profiles at the pipe midlength at select times during the flow cycle for $Va = 60$.

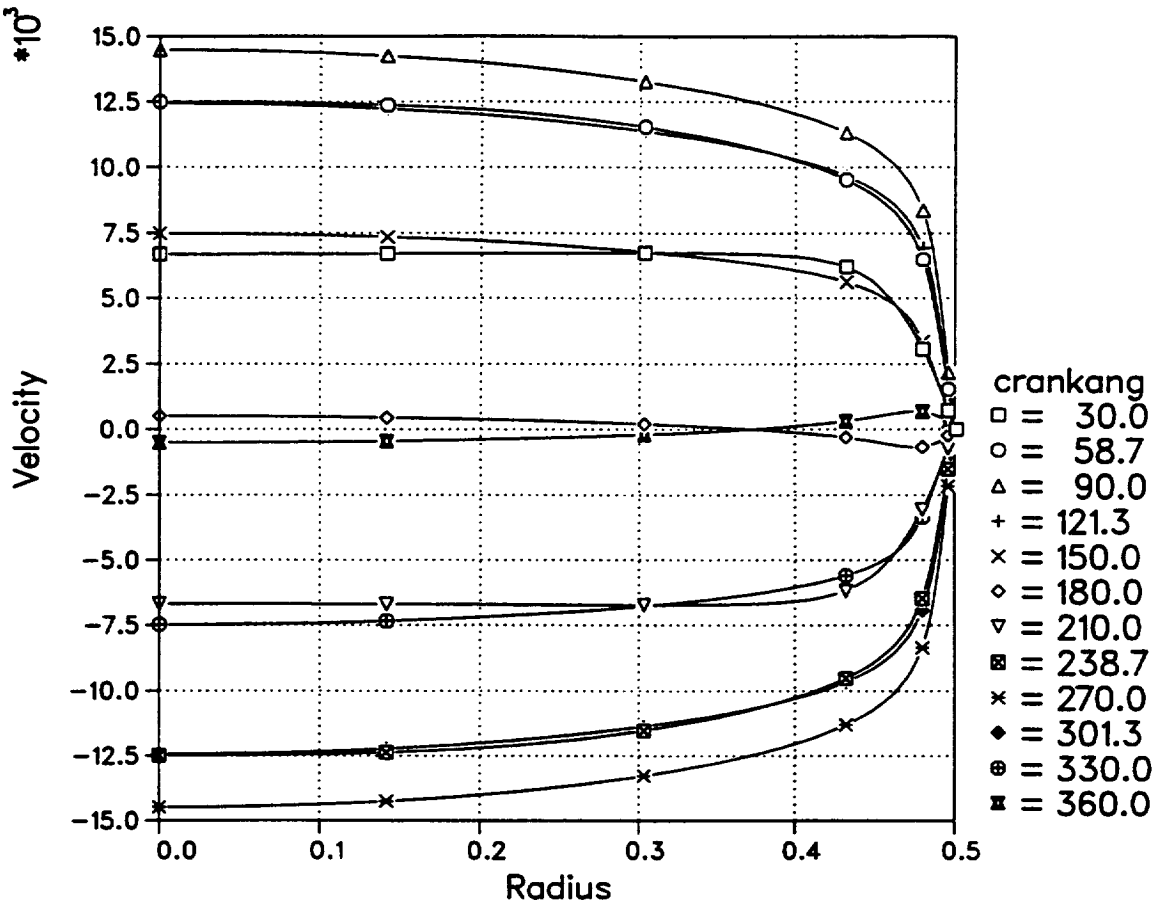

Figure 4.5: Velocity profiles at the pipe midlength at select times during the flow cycle for $Va = 80$.

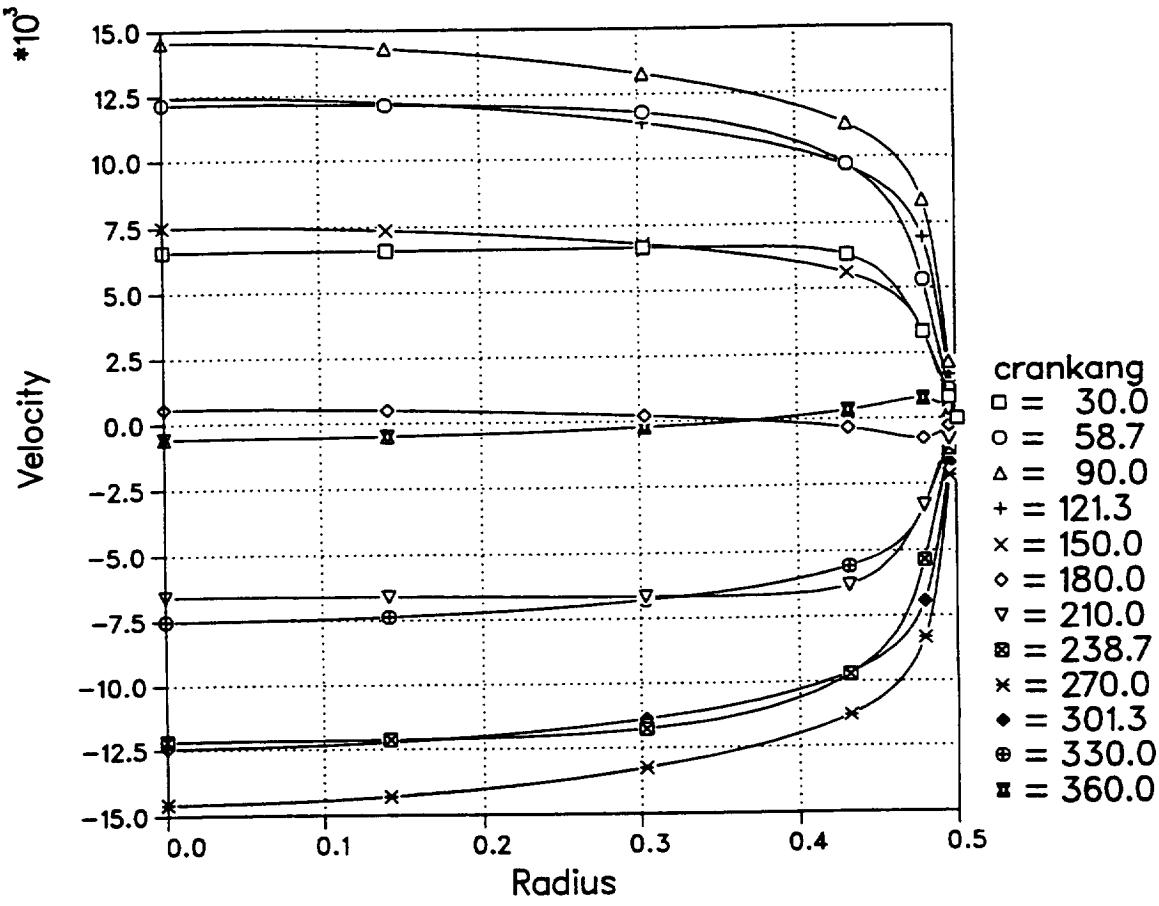

Figure 4.6: Velocity profiles at the pipe midlength at select times during the flow cycle for $Va = 100$.

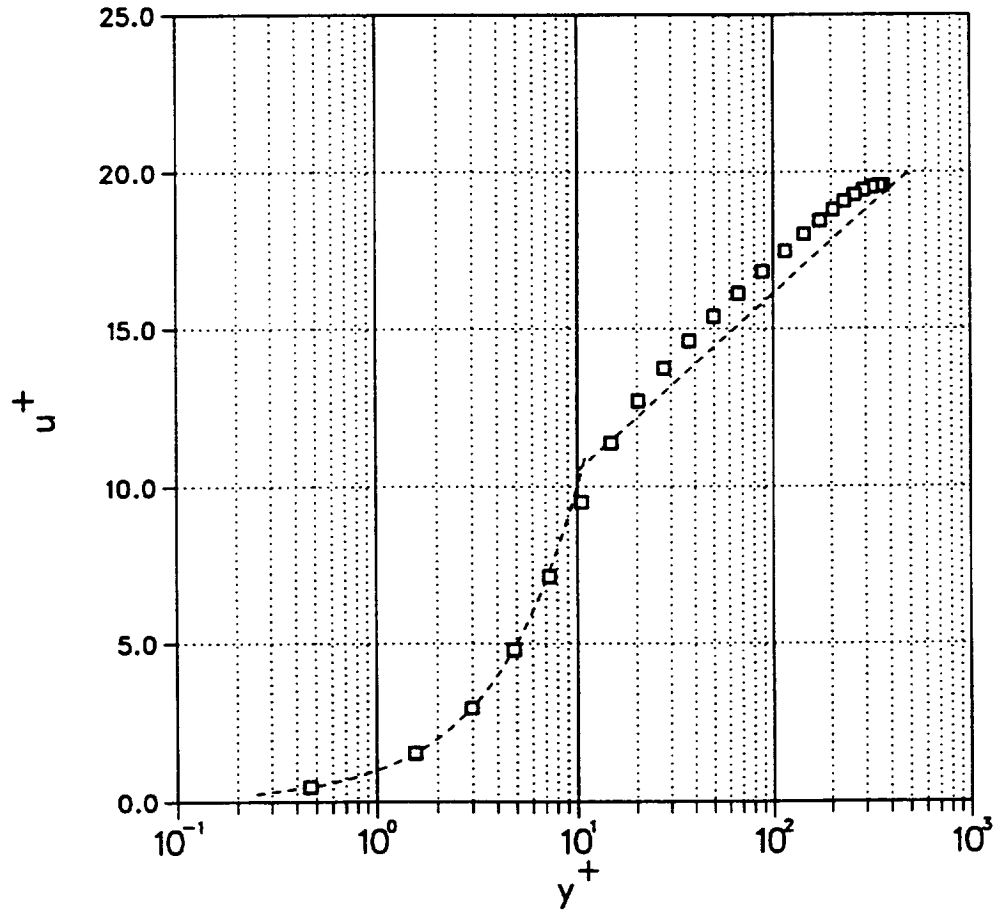

Figure 4.7: Velocity profile in wall coordinates at the pipe midlength for $Va = 40$.

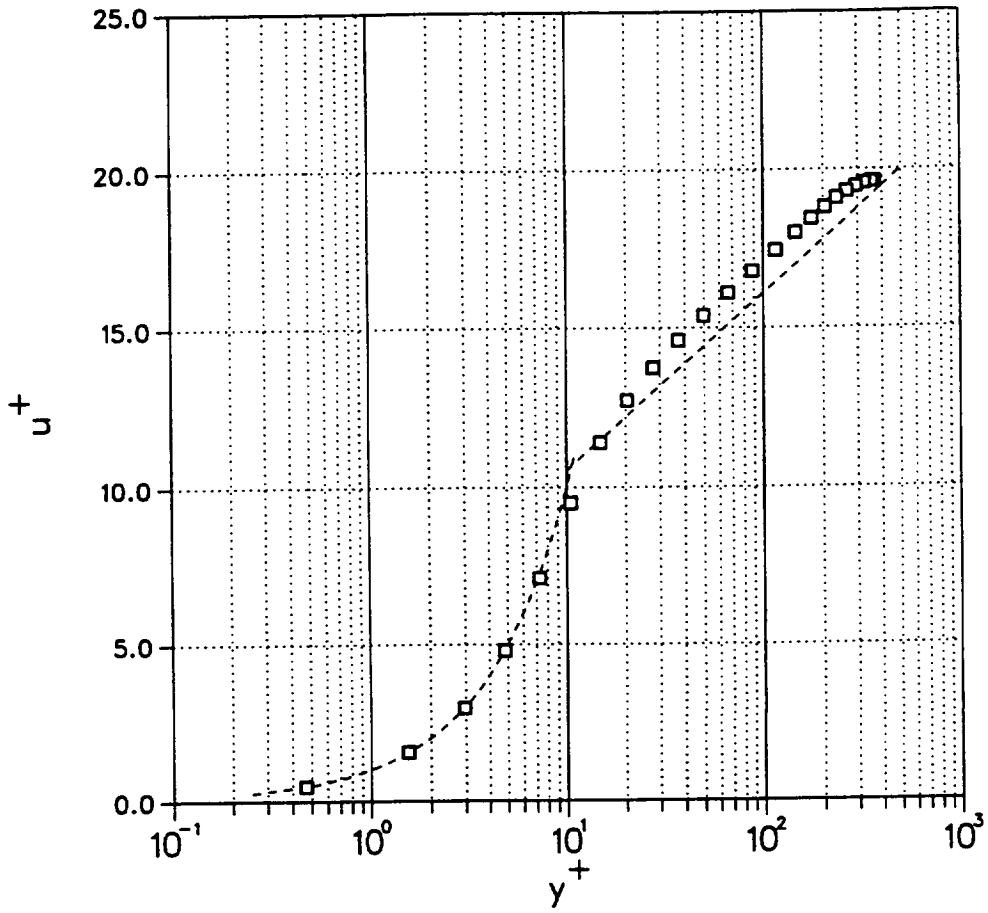

Figure 4.8: Velocity profile in wall coordinates at the pipe midlength for $Va = 60$.

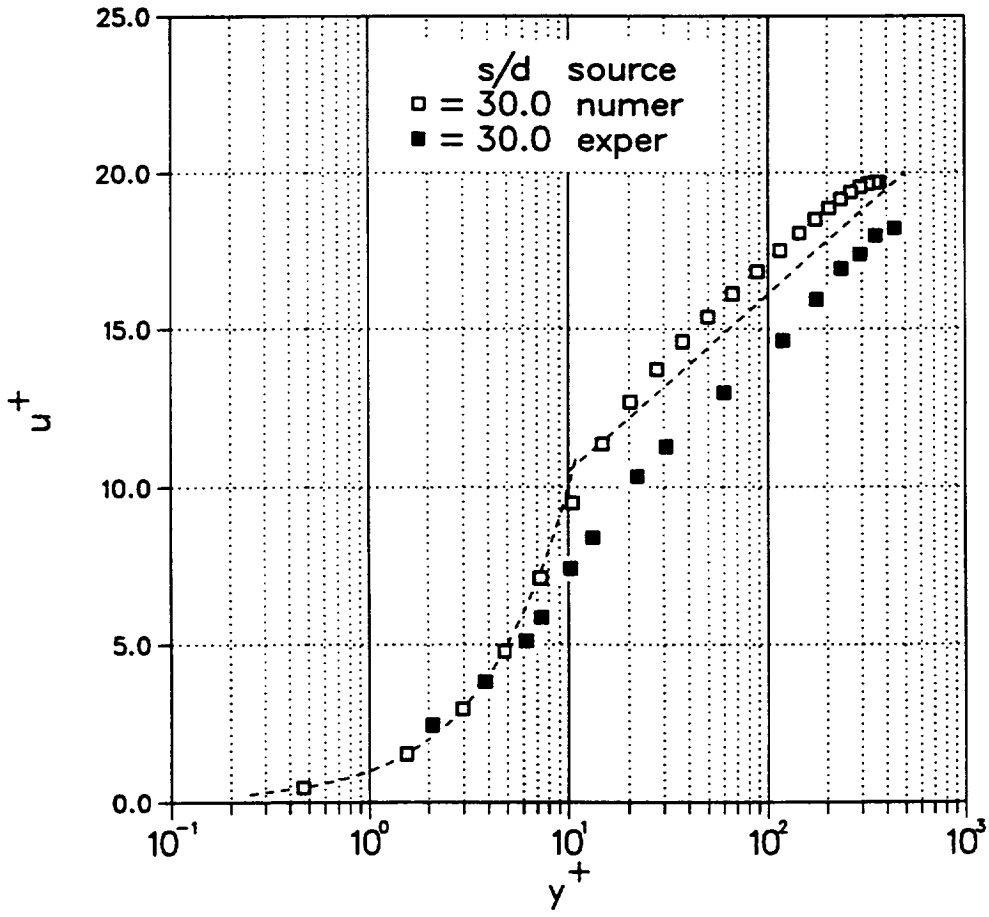

Figure 4.9: Velocity profile in wall coordinates at the pipe midlength for $Va = 80$.

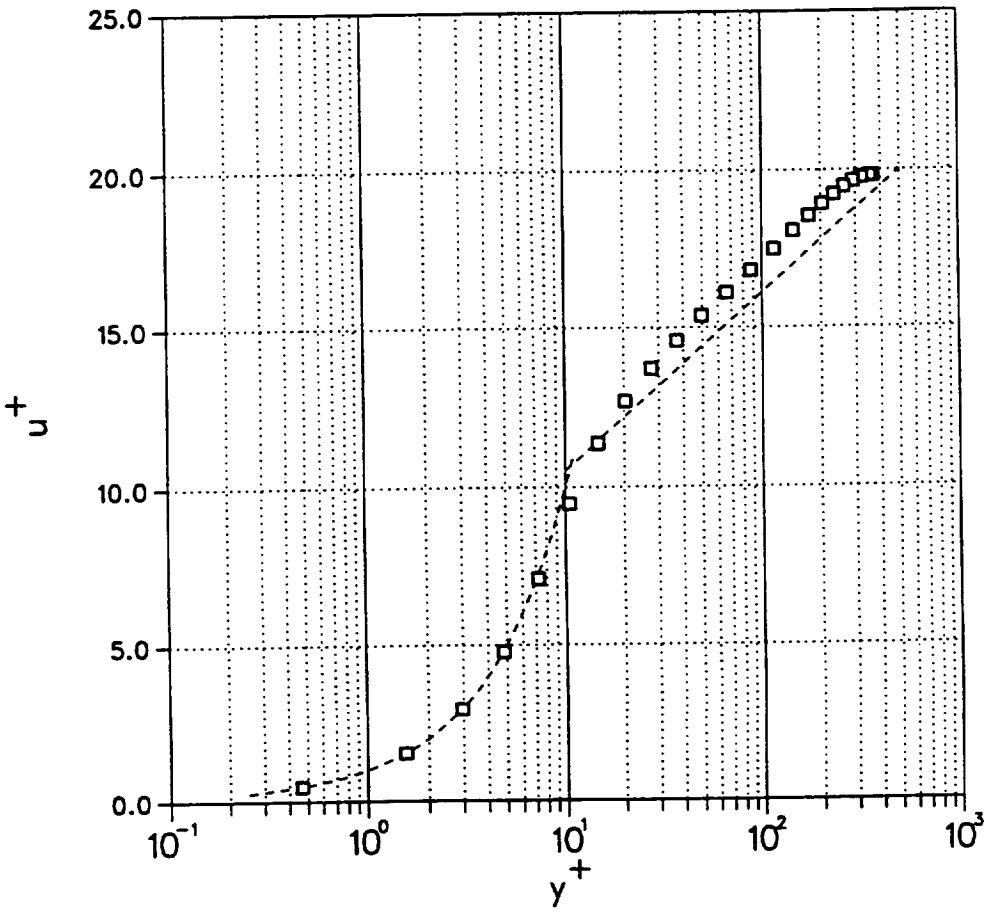

Figure 4.10: Velocity profile in wall coordinates at the pipe midlength for $Va = 100$.

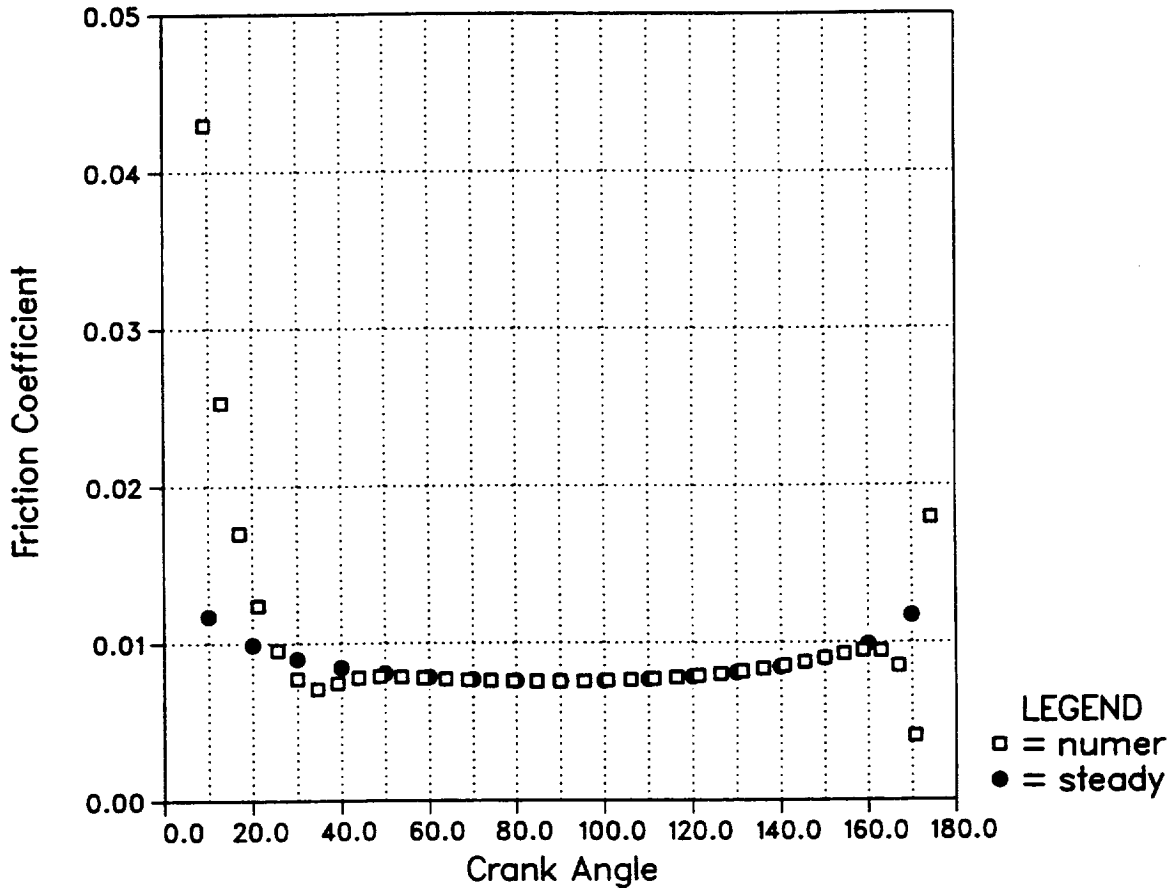

Figure 4.11: Friction coefficient over one half flow cycle at the pipe midlength for $Va = 40$.

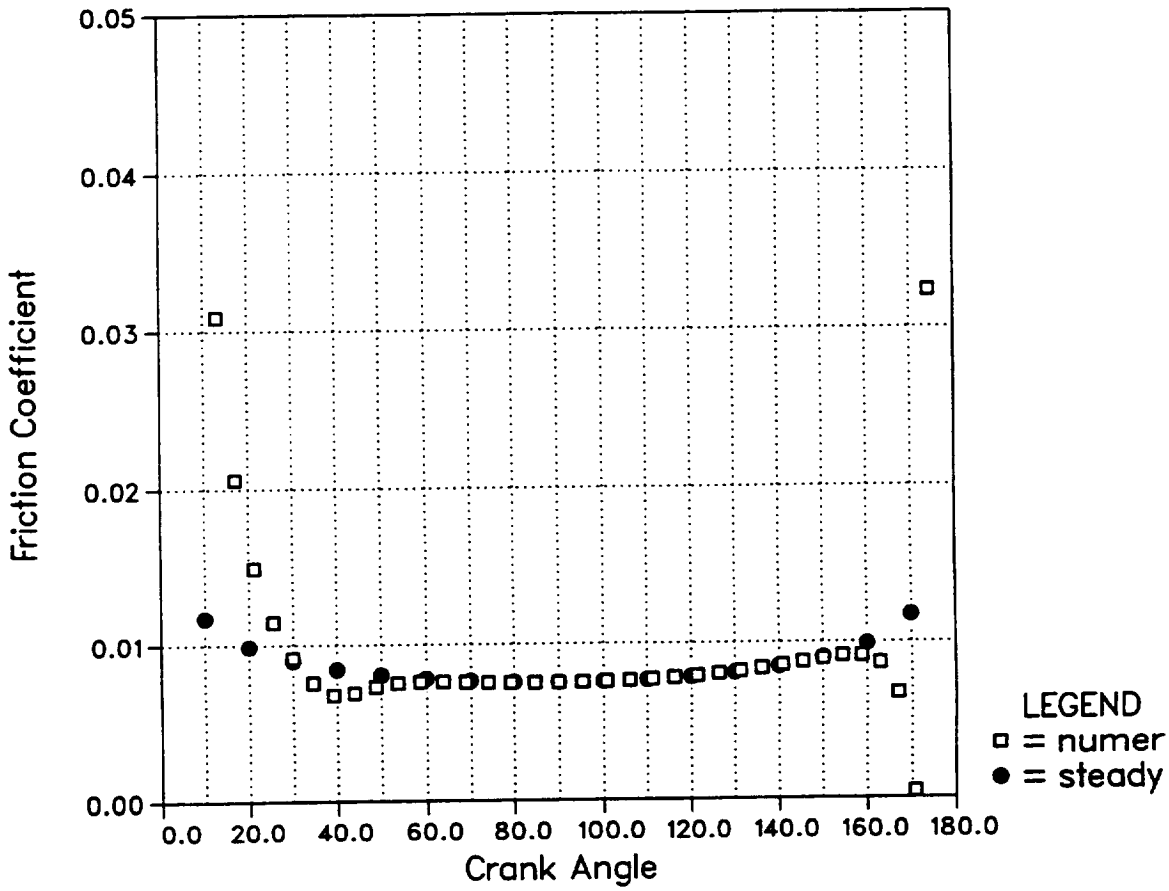

Figure 4.12: Friction coefficient over one half flow cycle at the pipe midlength for $Va = 60$.

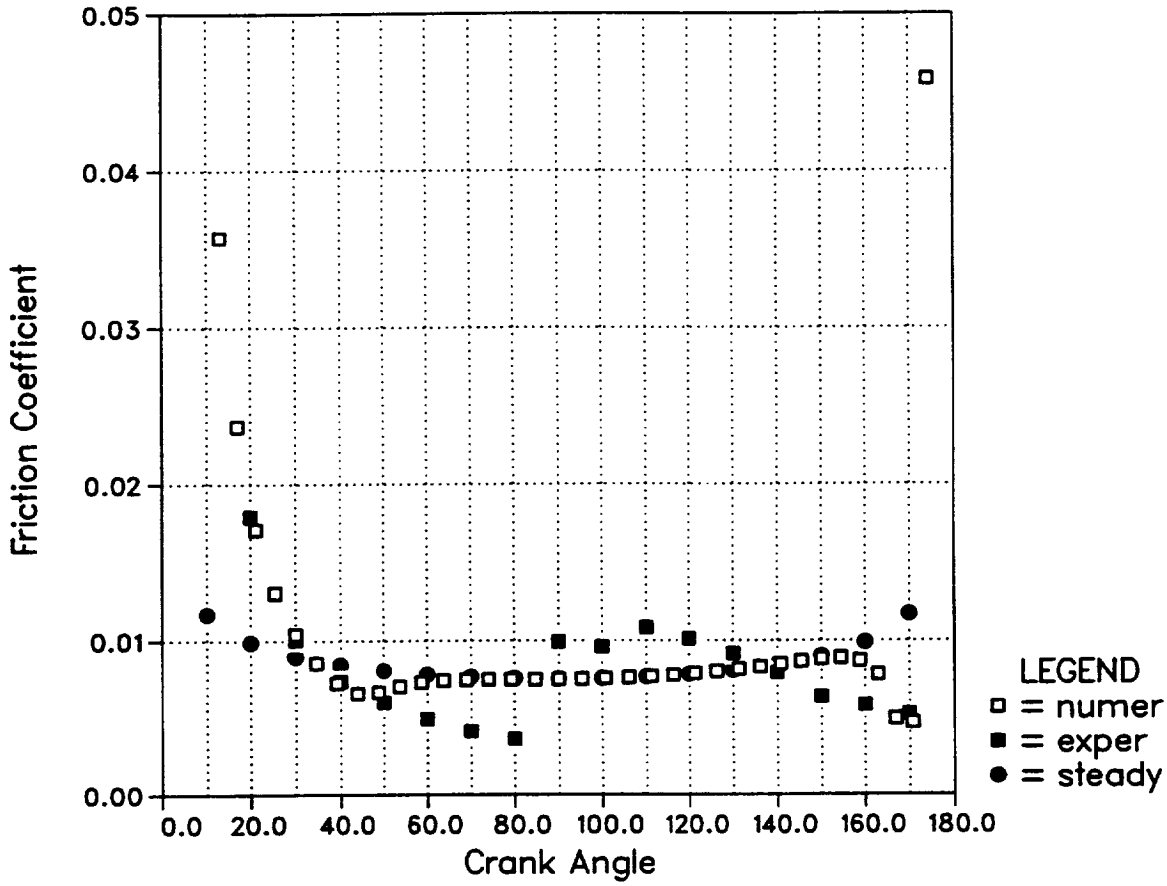

Figure 4.13: Friction coefficient over one half flow cycle at the pipe midlength for $Va = 80$.

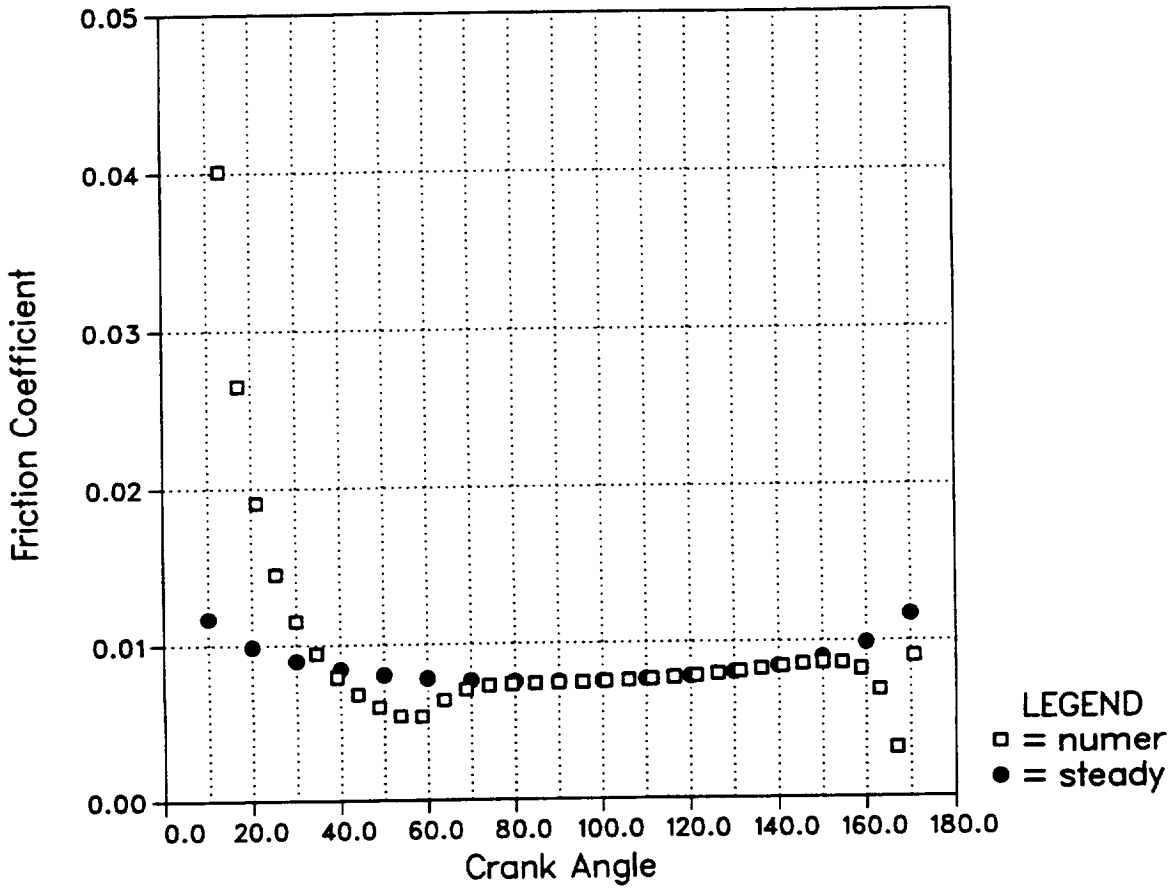

Figure 4.14: Friction coefficient over one half flow cycle at the pipe midlength for $Va = 100$.

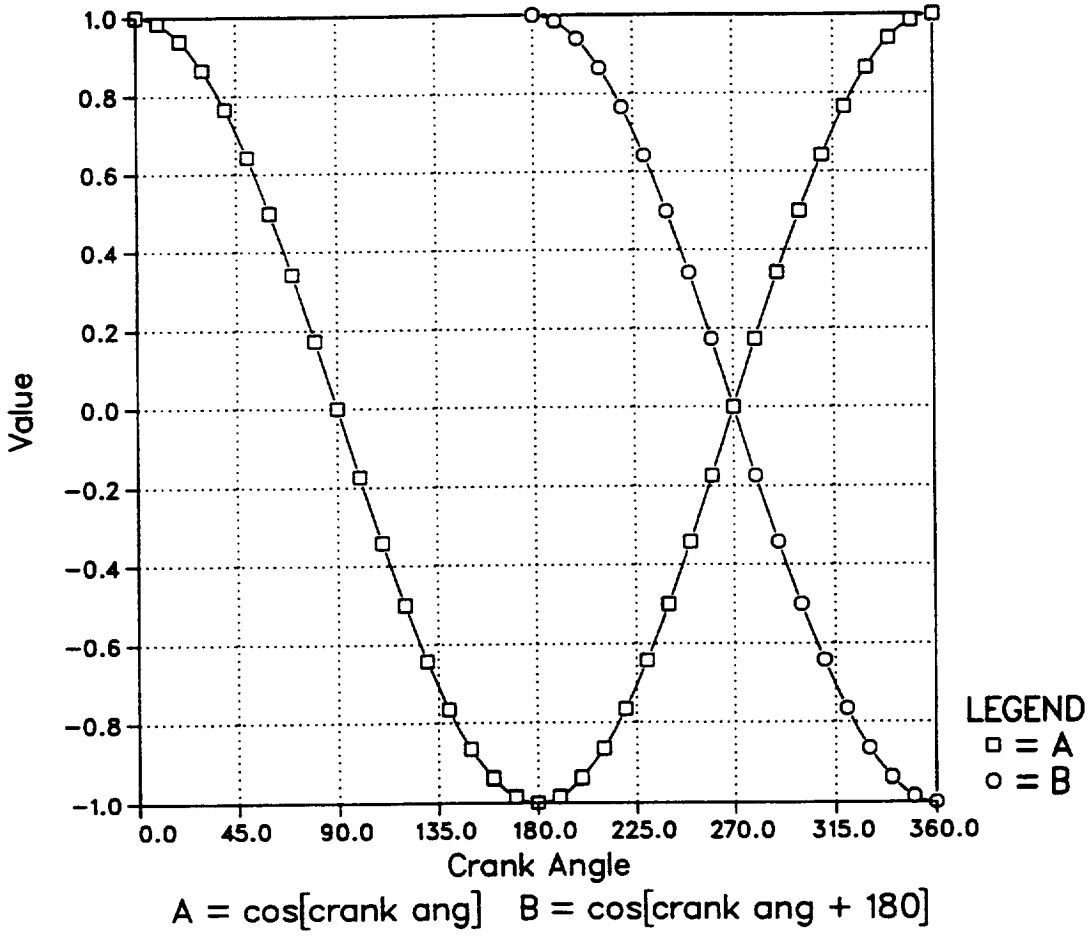

Figure 4.15: Variation of an acceleration source term for the dissipation equation, proposed by Koehler (1990).

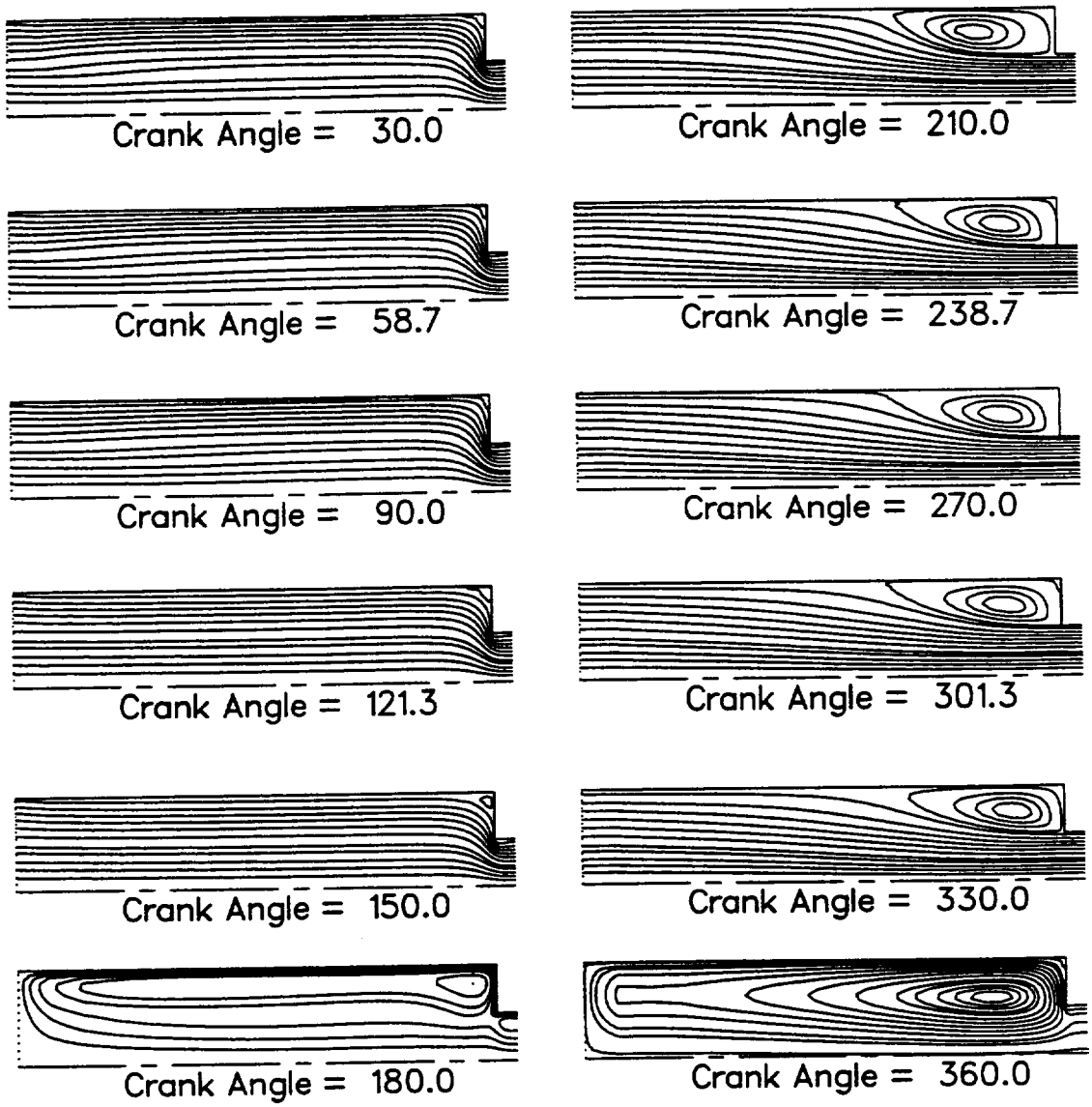

Figure 4.16: Streamlines within the left end region at select times during the flow cycle for $Va = 40$.

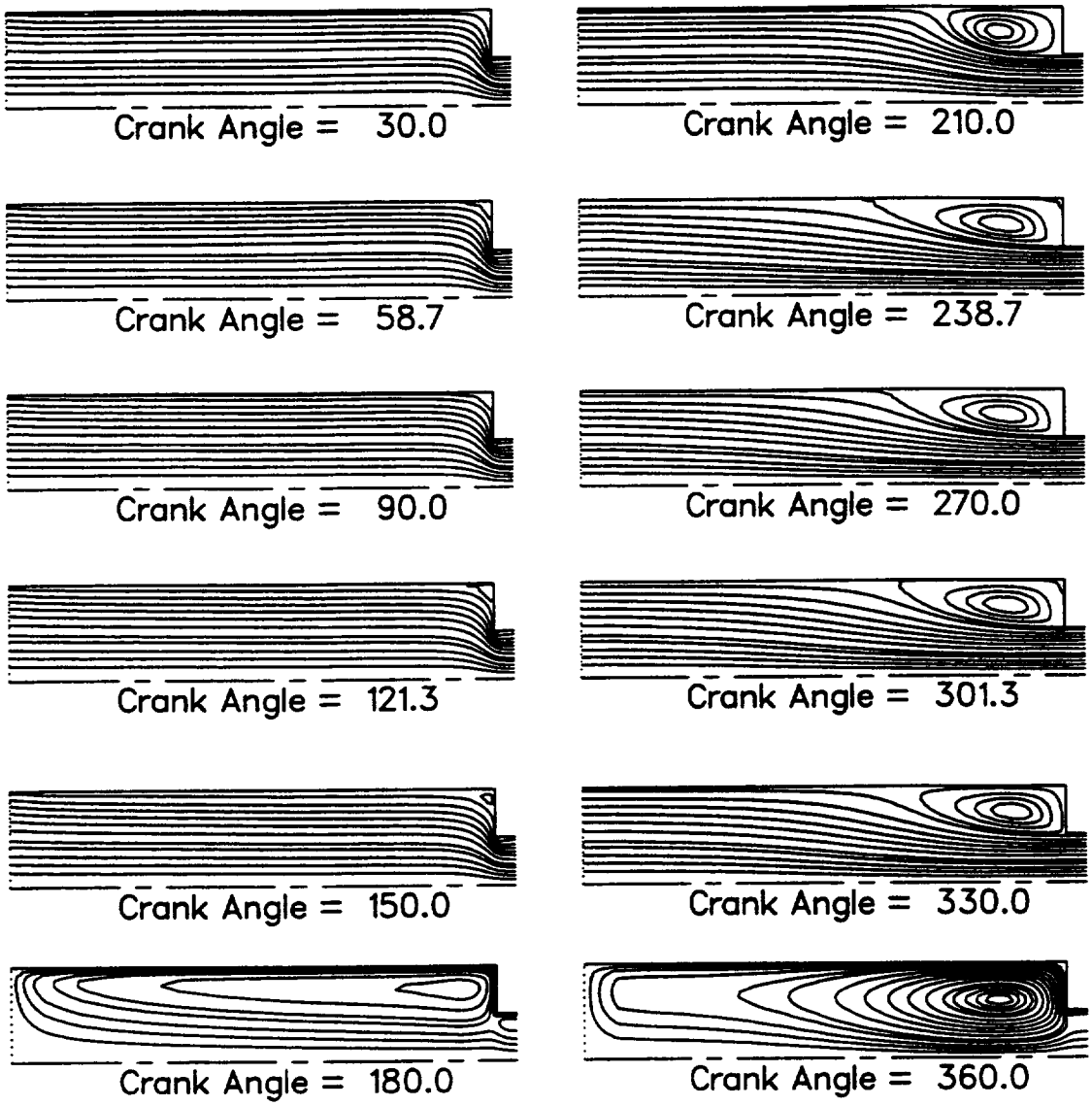

Figure 4.17: Streamlines within the left end region at select times during the flow cycle for $Va = 60$.

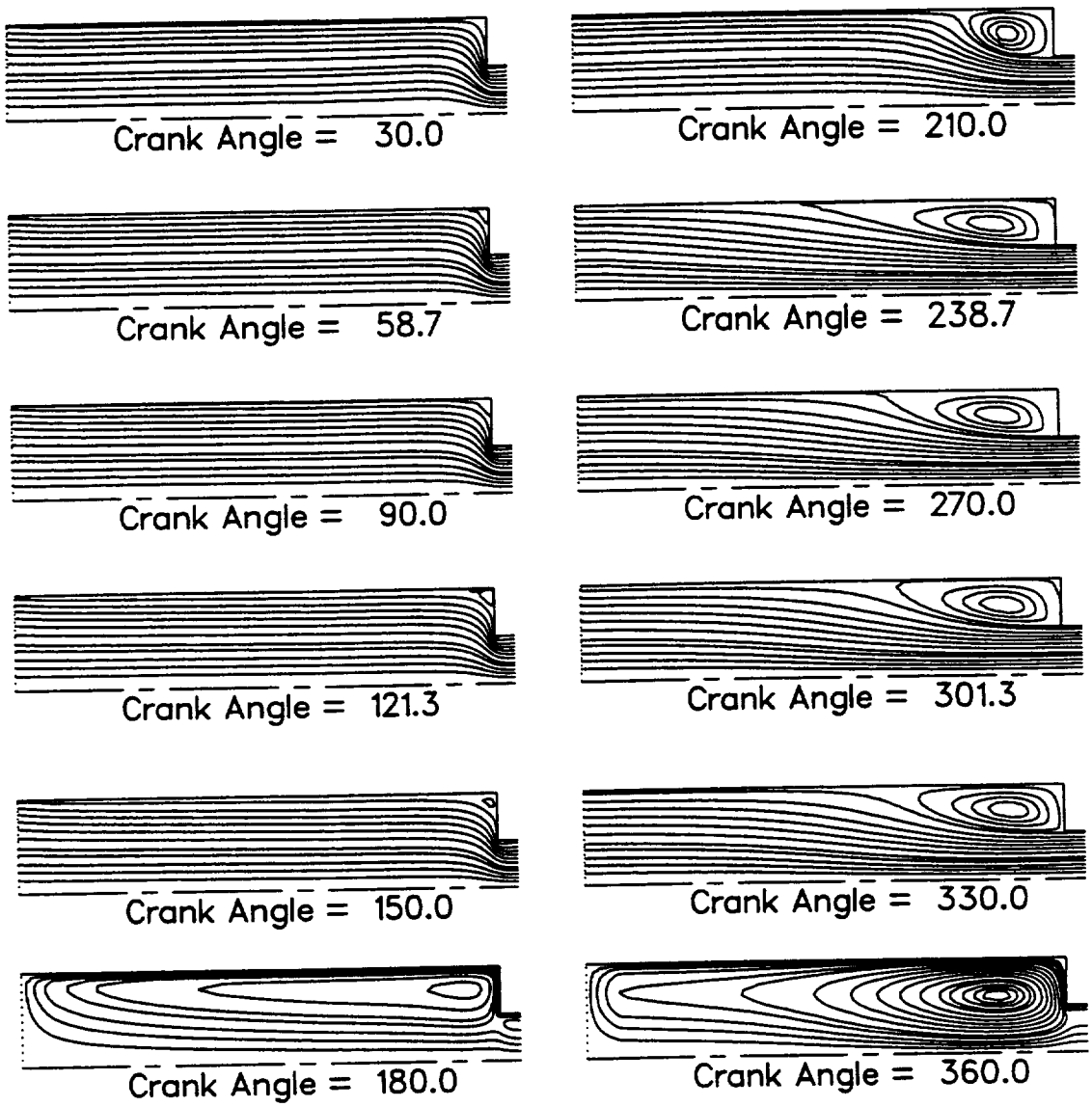

Figure 4.18: Streamlines within the left end region at select times during the flow cycle for $Va = 80$.

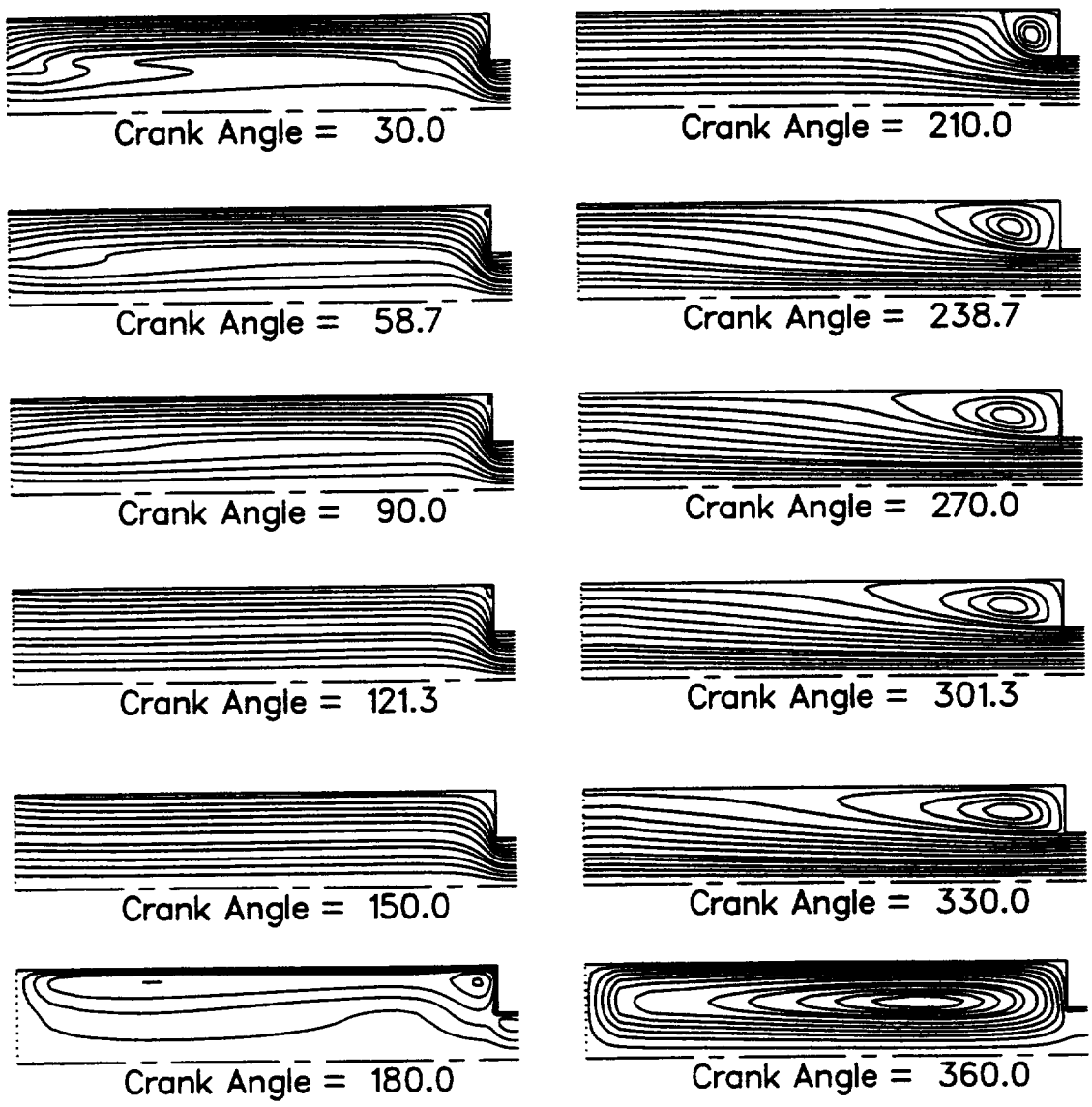

Figure 4.19: Streamlines within the left end region at select times during the flow cycle for $Va = 100$.

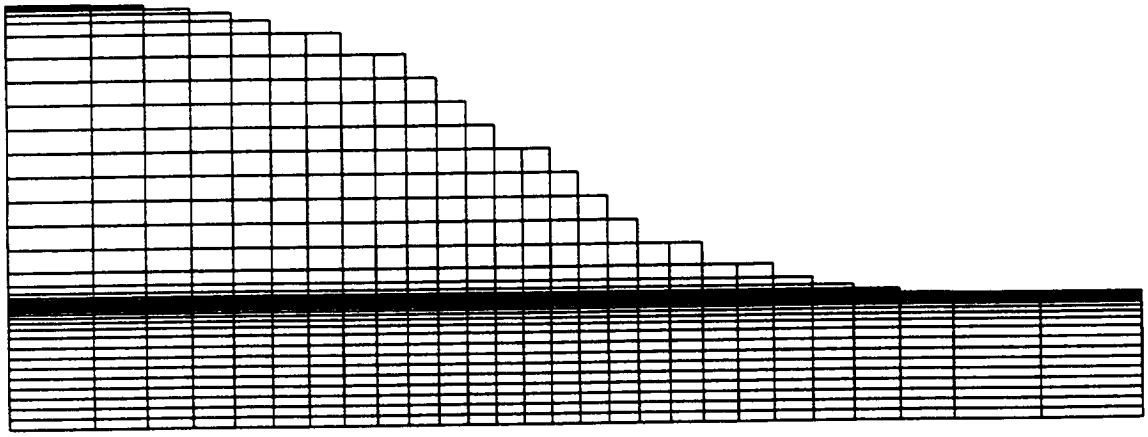

Figure 4.20: Grid for nozzle-ended model.

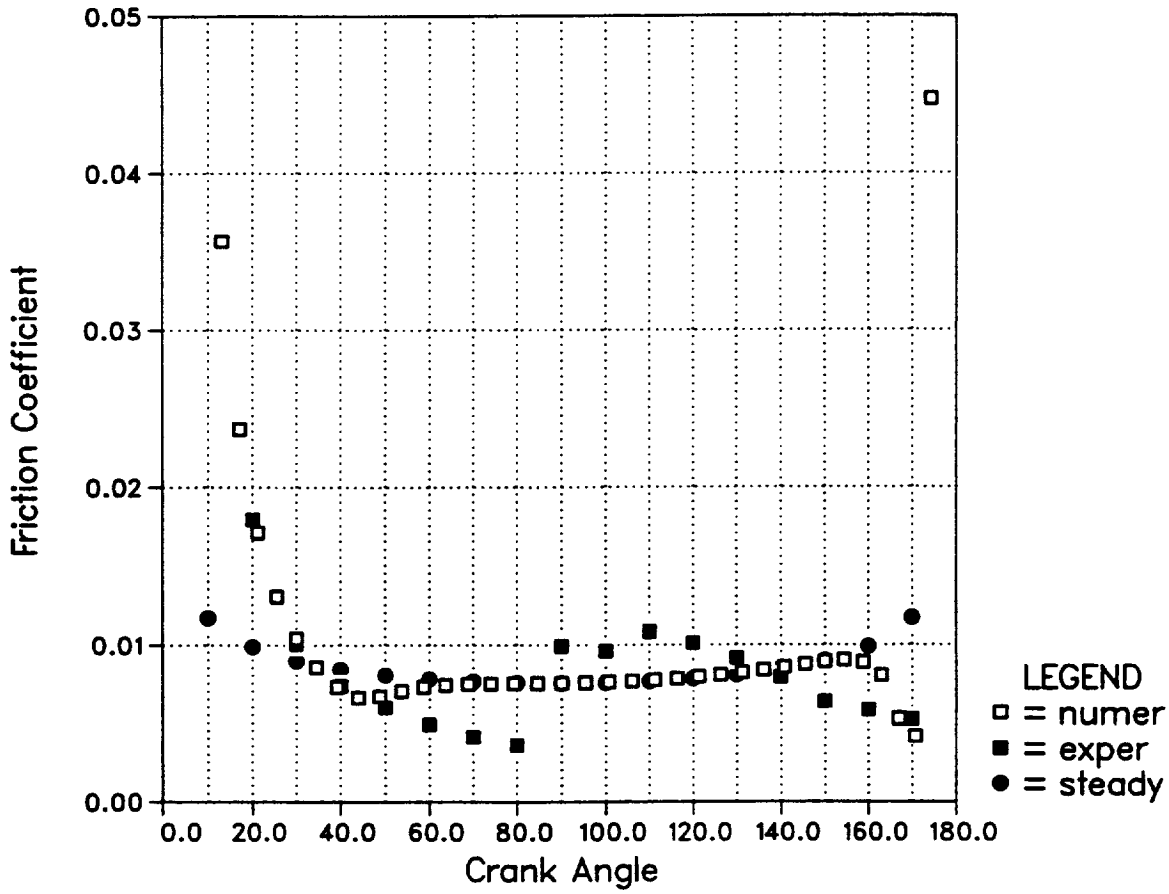

Figure 4.21: Friction coefficient during the first half of the flow cycle for the nozzle-ended model.

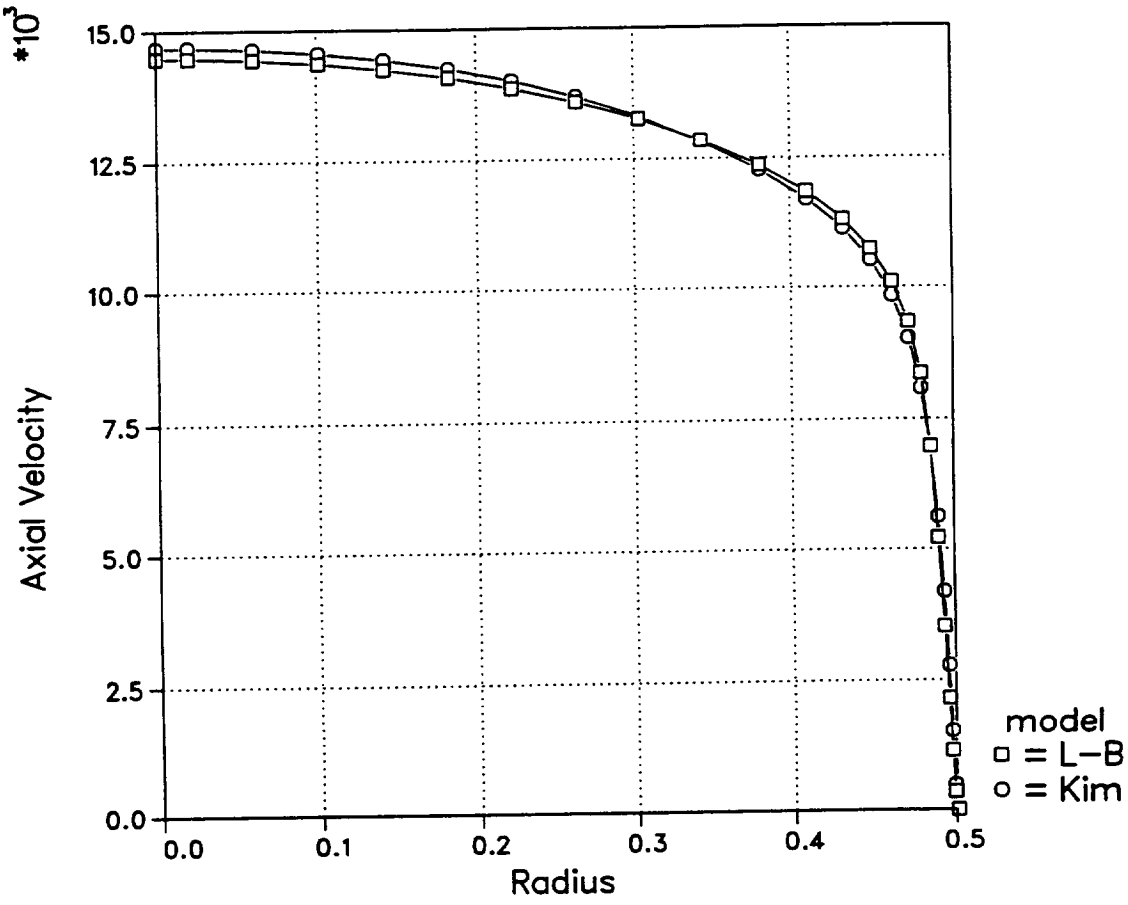

Figure 4.22: Axial velocity profiles obtained from the Lam-Bremhorst and Kim turbulence models.

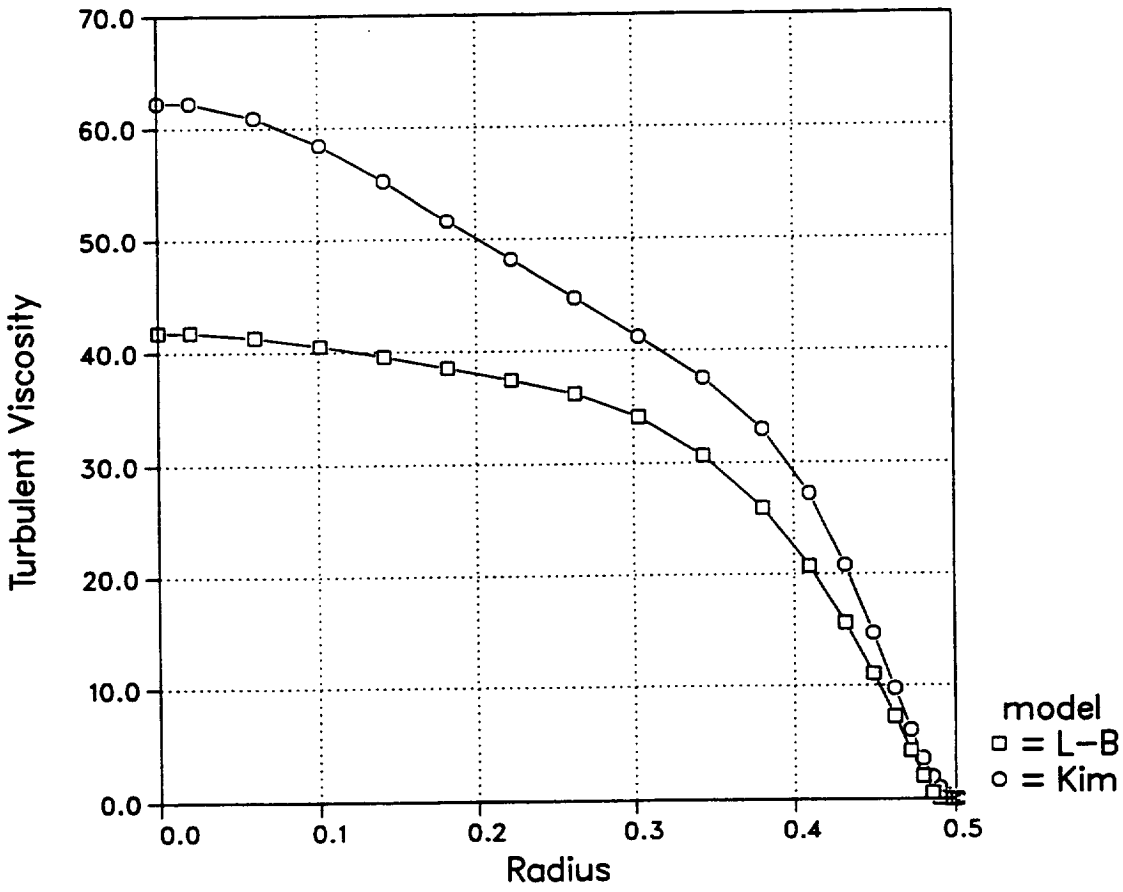

Figure 4.23: Normalized turbulent viscosity profiles μ_t/μ obtained from the Lam-Bremhorst and Kim turbulence models.

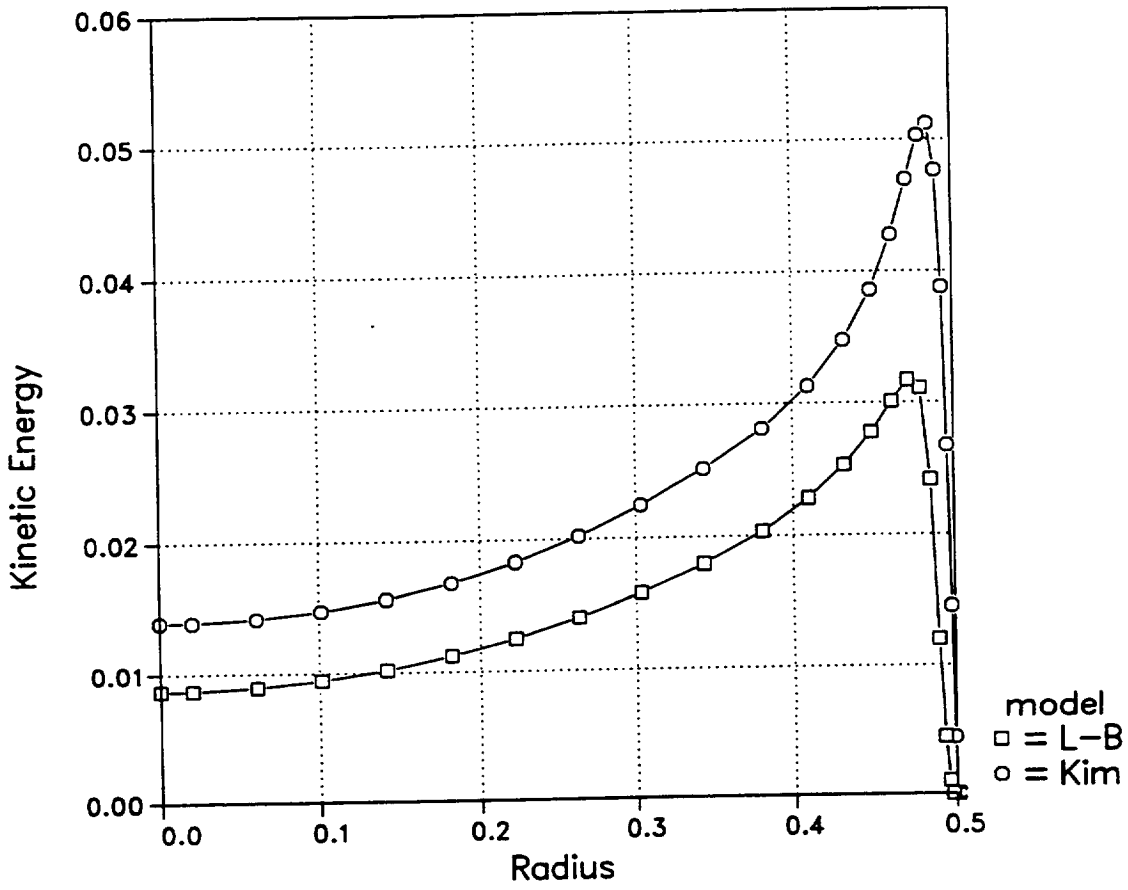

Figure 4.24: Normalized turbulent kinetic energy profiles $2k/U^2_{m,max}$ obtained from the Lam-Bremhorst and Kim turbulence models.

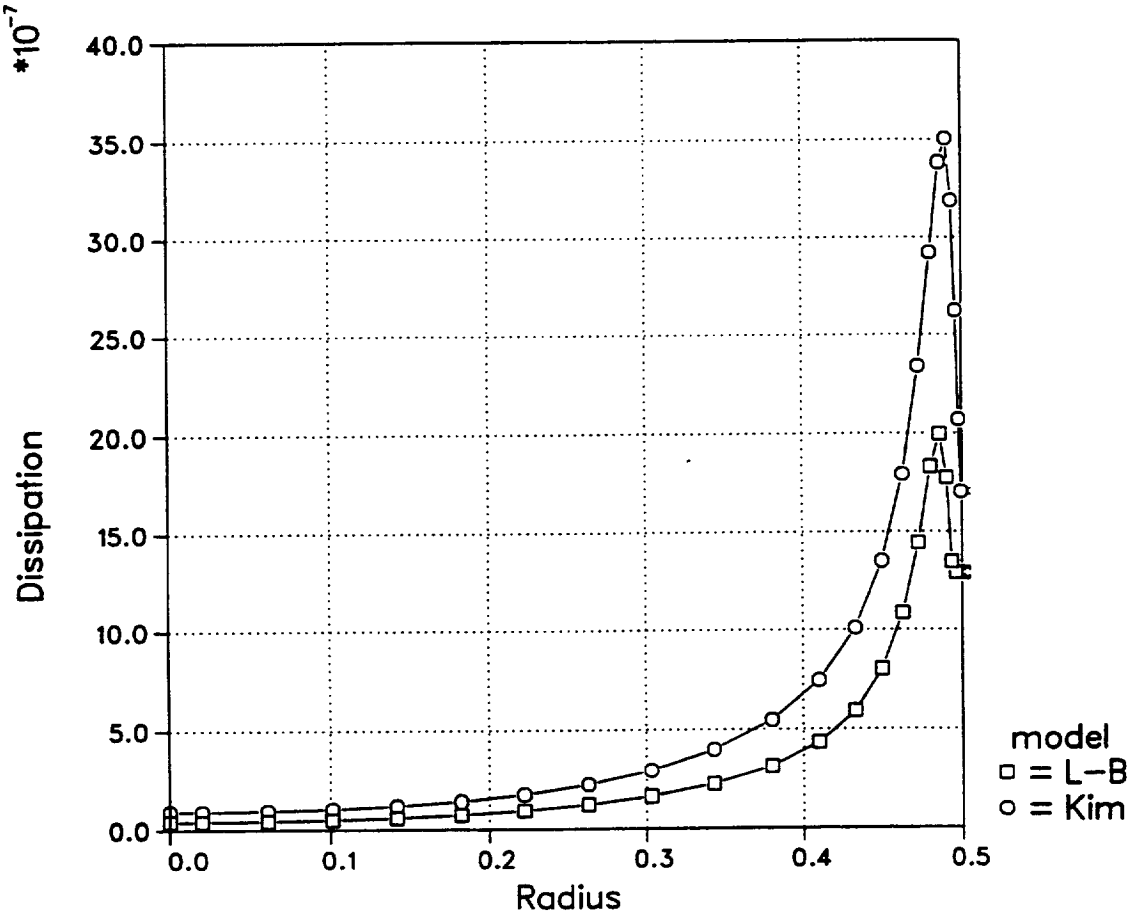

Figure 4.25: Normalized dissipation rate profiles $\epsilon\nu/U^4_{m,max}$ obtained from the Lam-Bremhorst and Kim turbulence models.

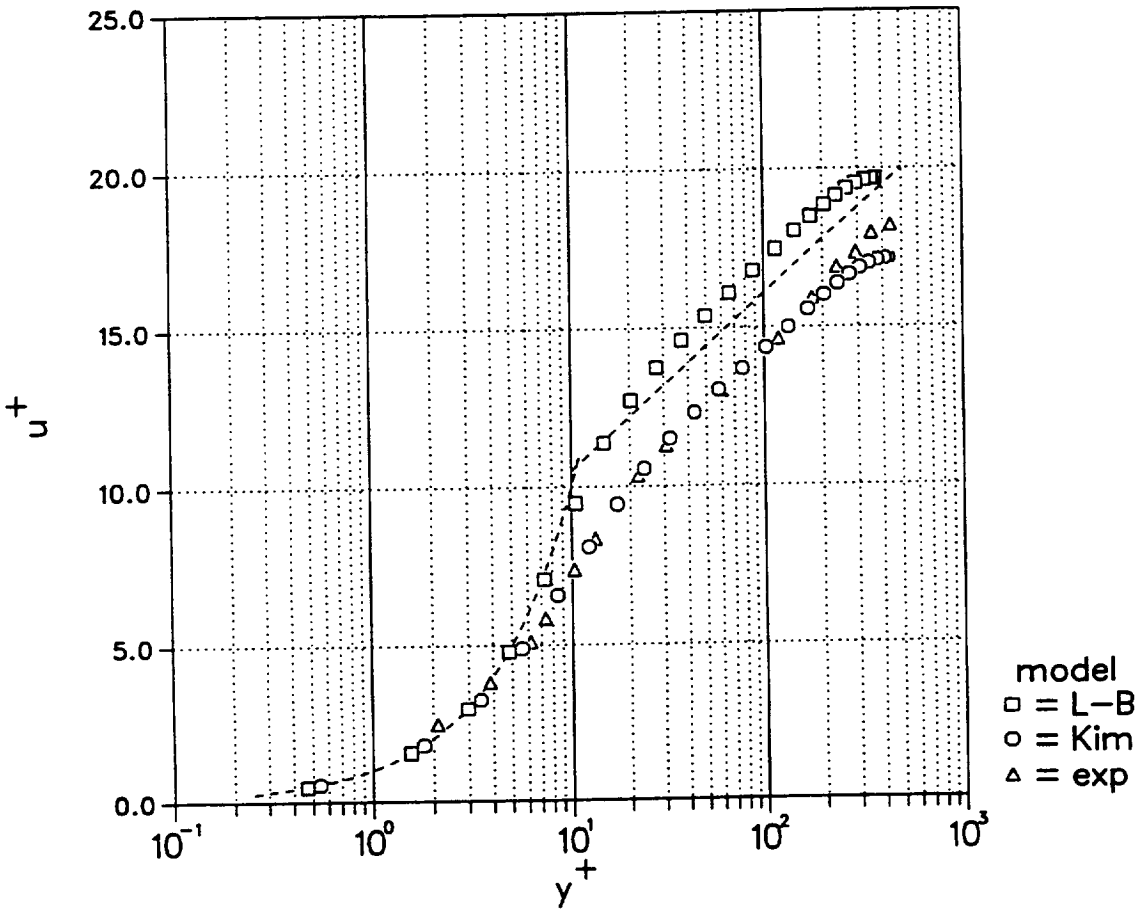

Figure 4.26: Axial velocity profiles in wall coordinates for the Lam-Bremhorst and Kim turbulence models. Experimental data and universal profile shown for reference.

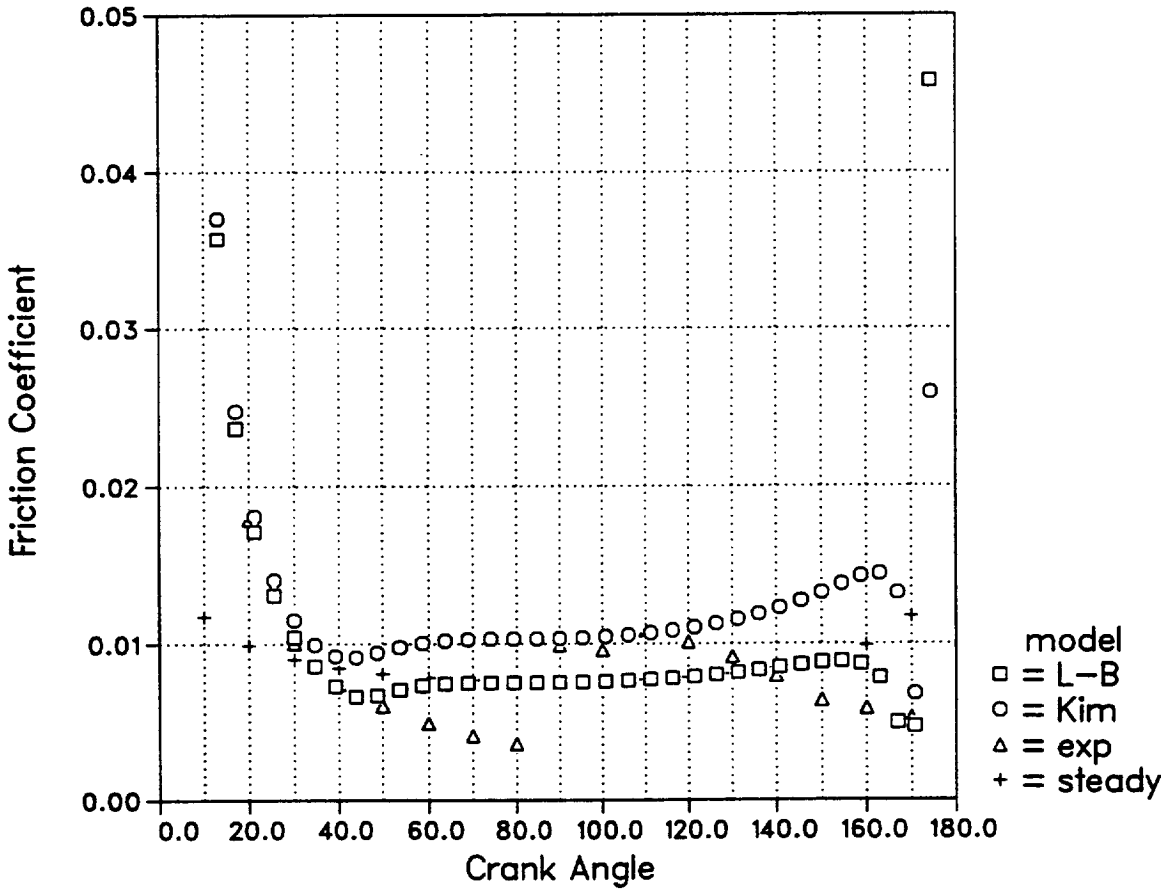

Figure 4.27: Friction coefficient over one half flow cycle at the pipe midlength for the Lam-Bremhorst and Kim turbulence models. Experimental data and steady flow results shown for reference.

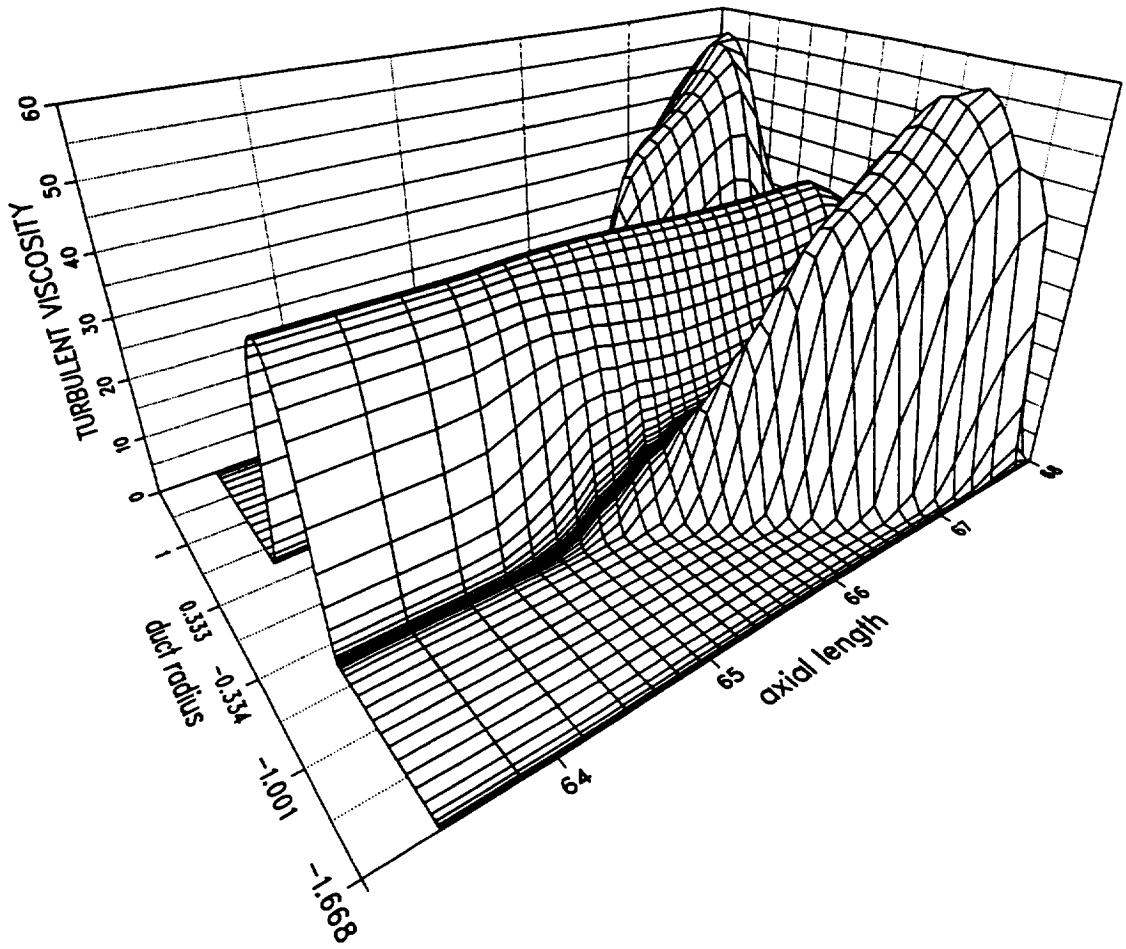

Figure 4.28: Turbulent viscosity within smooth nozzle end at flow reversal.

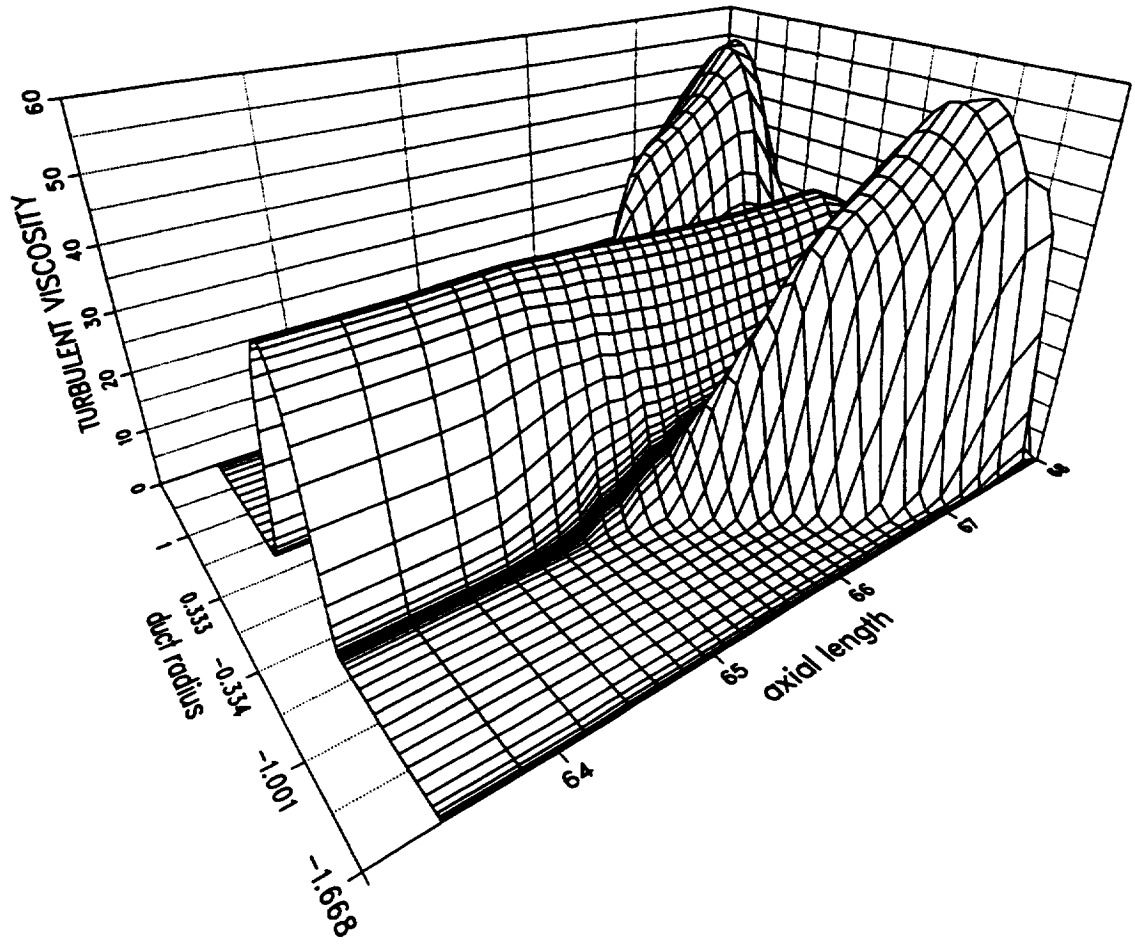

Figure 4.29: Turbulent viscosity within smooth nozzle end 2.5° after flow reversal.

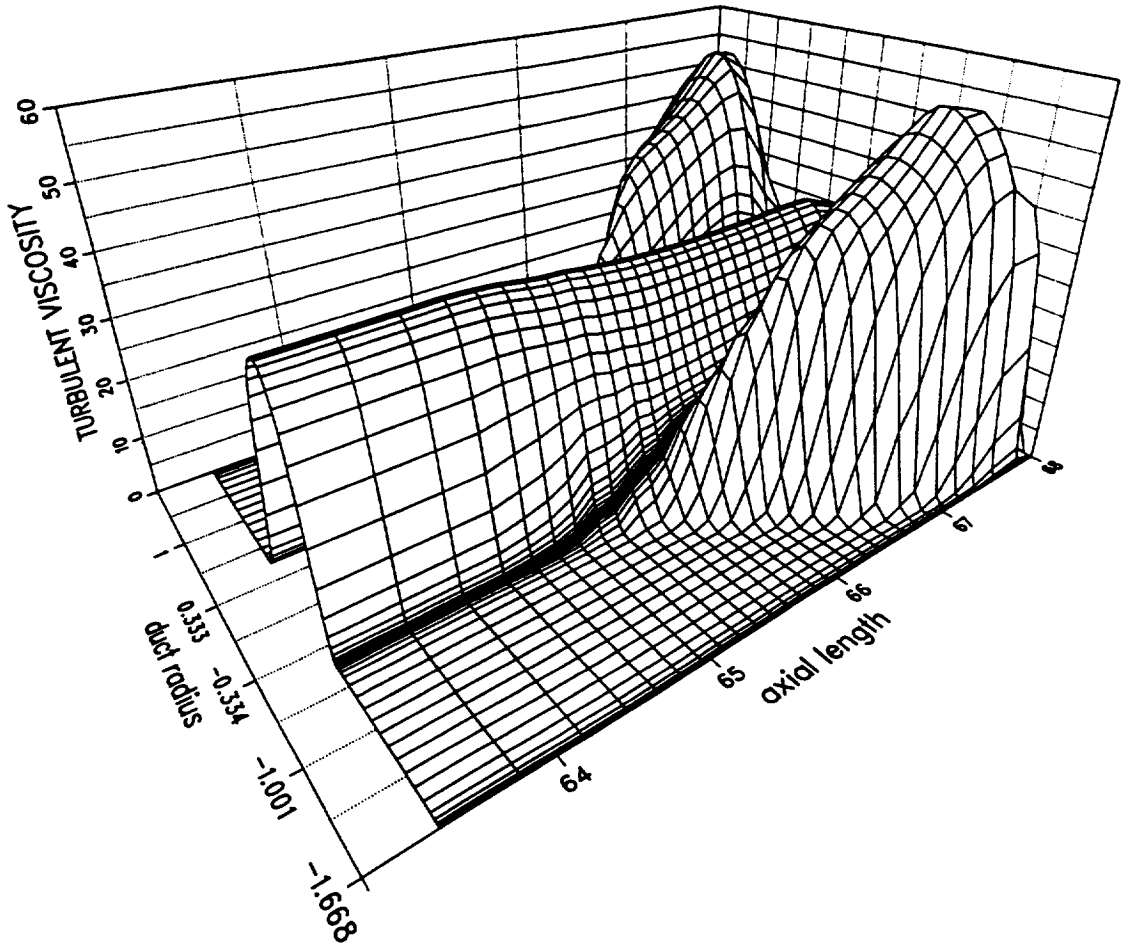

Figure 4.30: Turbulent viscosity within smooth nozzle end 5.7° after flow reversal.

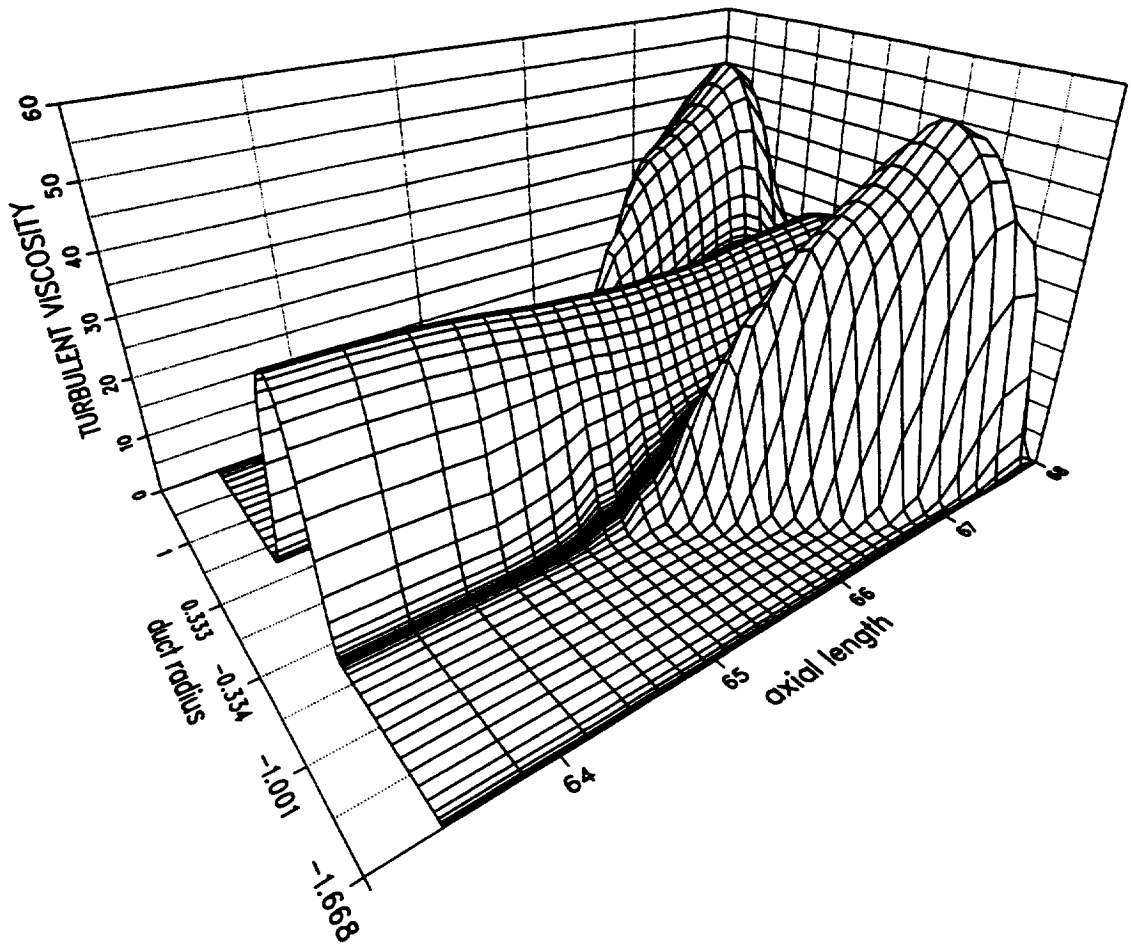

Figure 4.31: Turbulent viscosity within smooth nozzle end 9.2° after flow reversal.

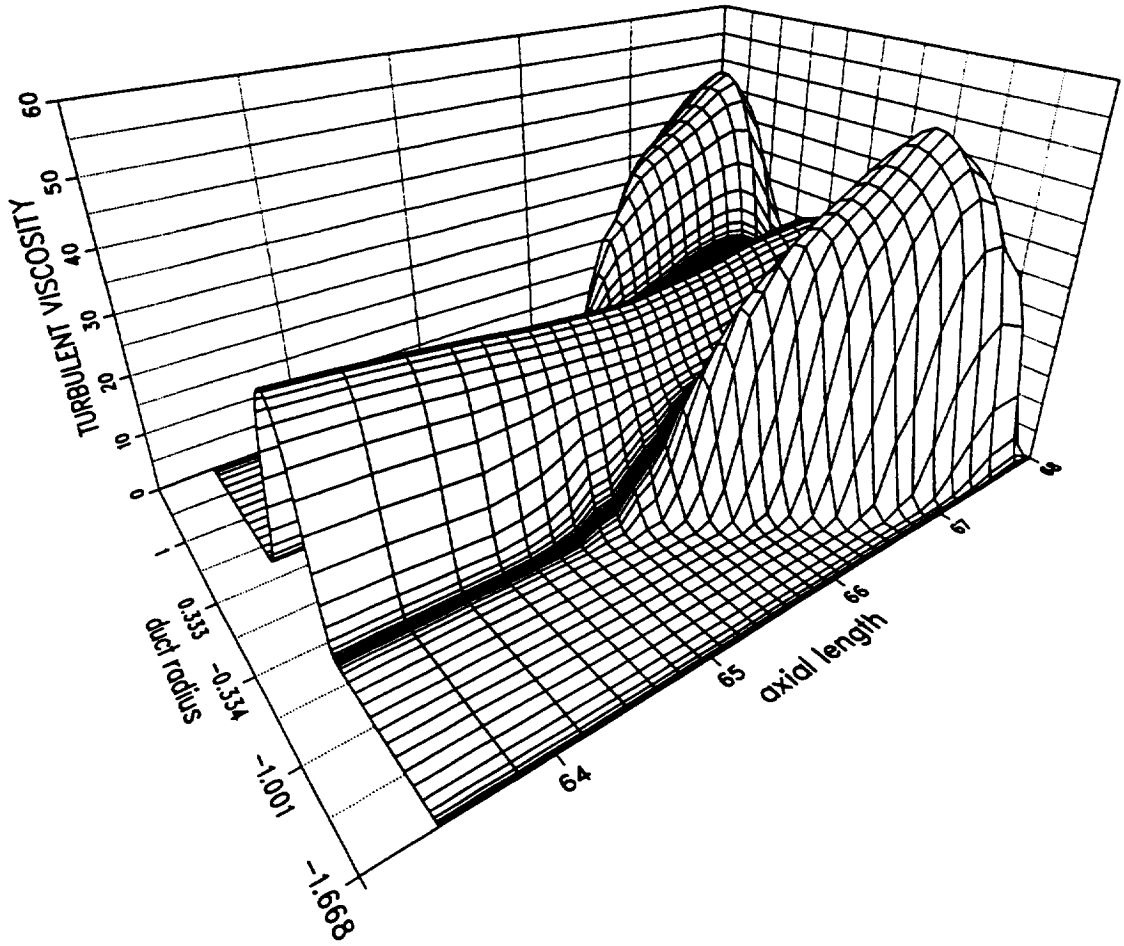

Figure 4.32: Turbulent viscosity within smooth nozzle end 13.0° after flow reversal.

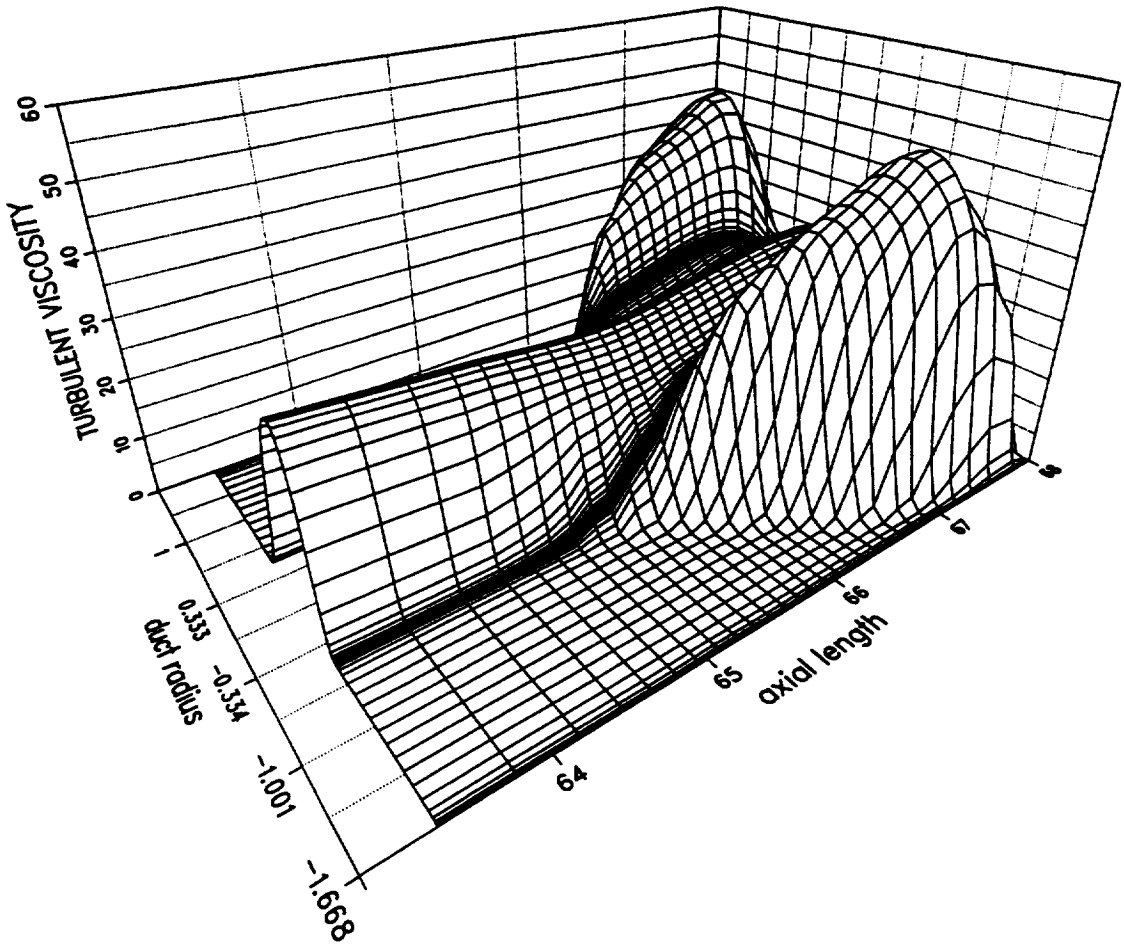

Figure 4.33: Turbulent viscosity within smooth nozzle end 17.1° after flow reversal.

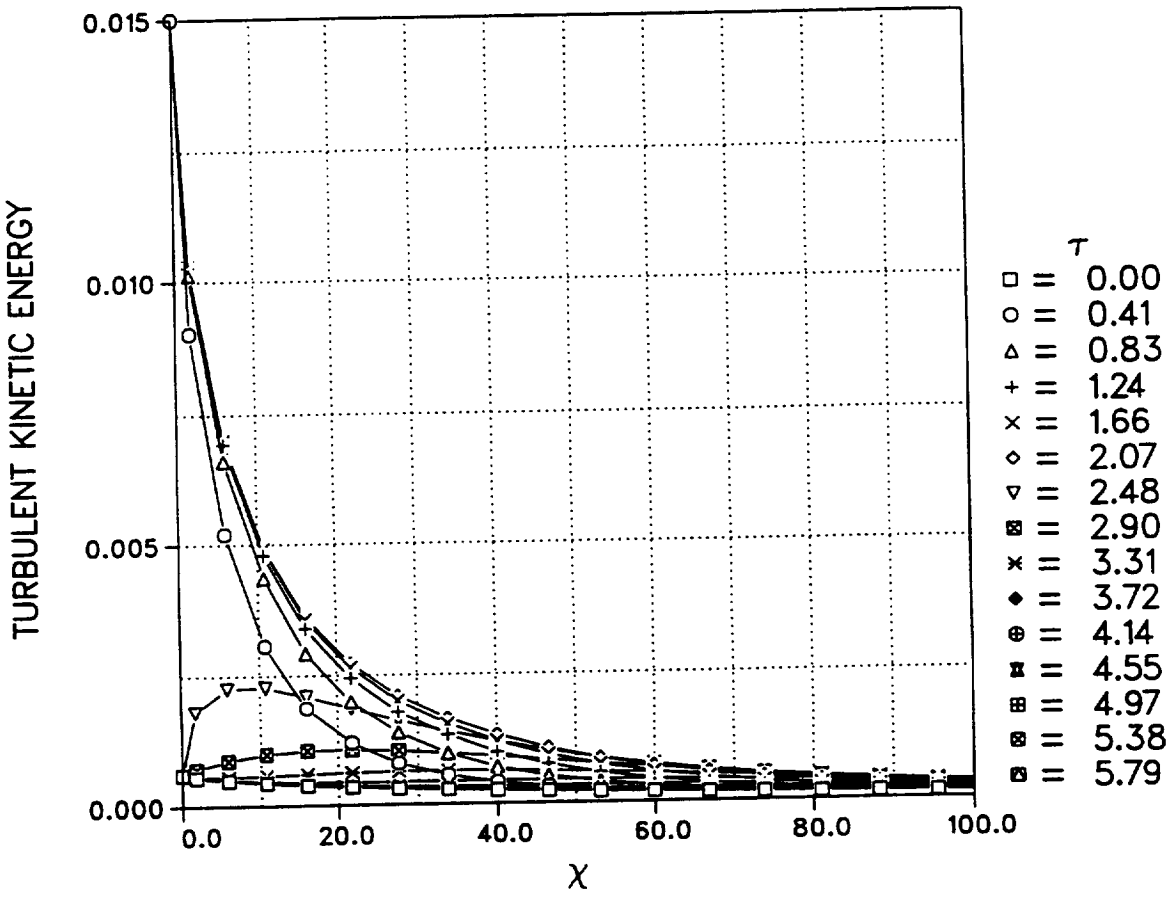

Figure 4.34: Normalized turbulent kinetic energy behind turbulence generating grid for Kim model.

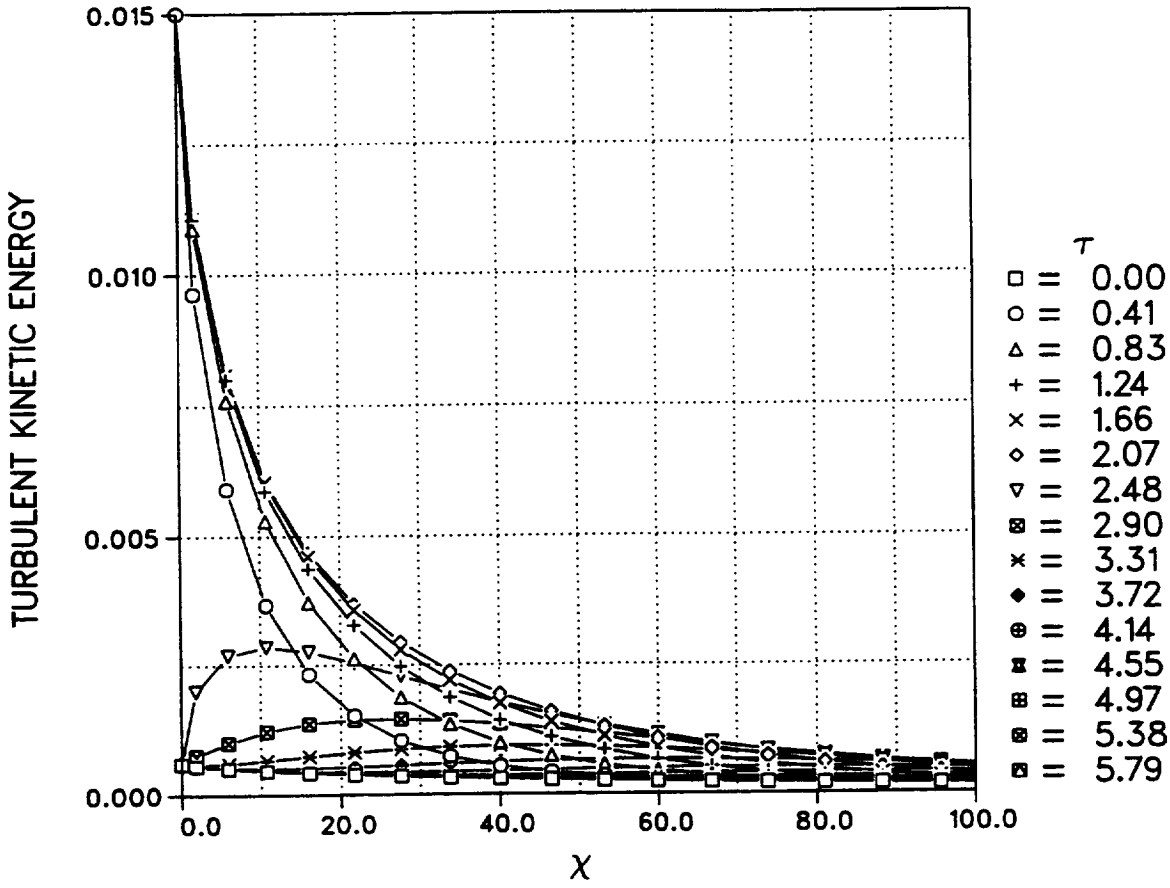

Figure 4.35: Normalized turbulent kinetic energy behind turbulence generating grid for Lam-Bremhorst model.

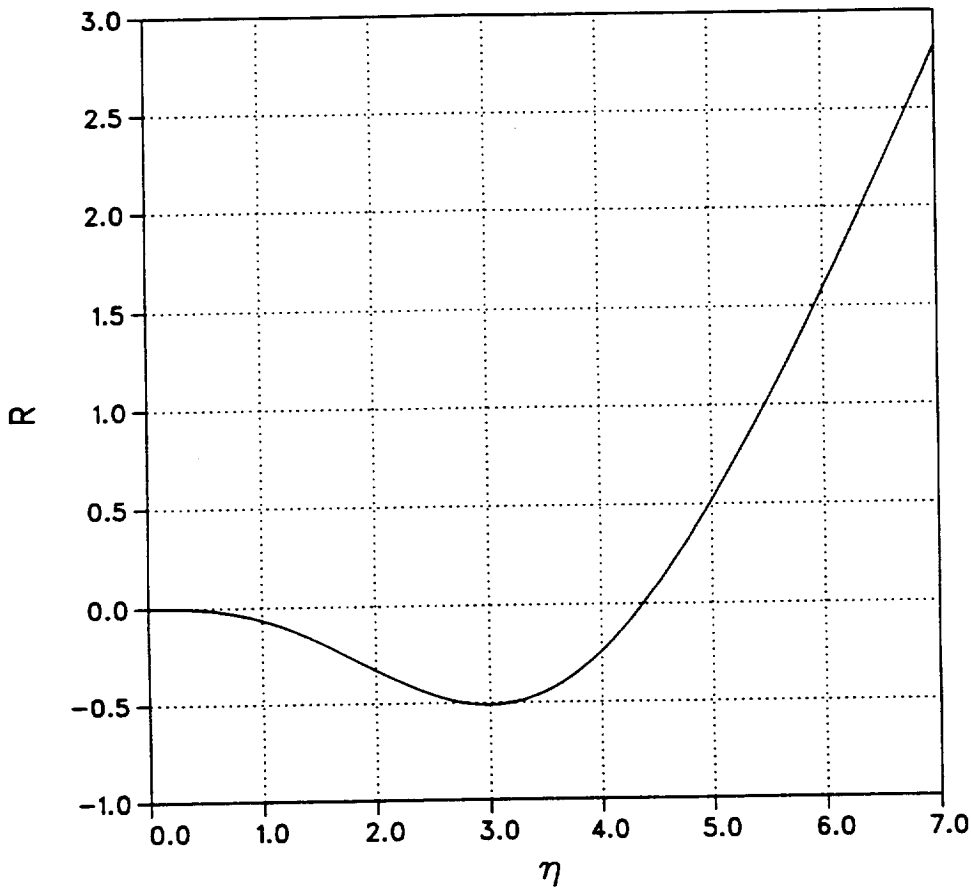

Figure 4.36: Variation of the RNG coefficient with η.

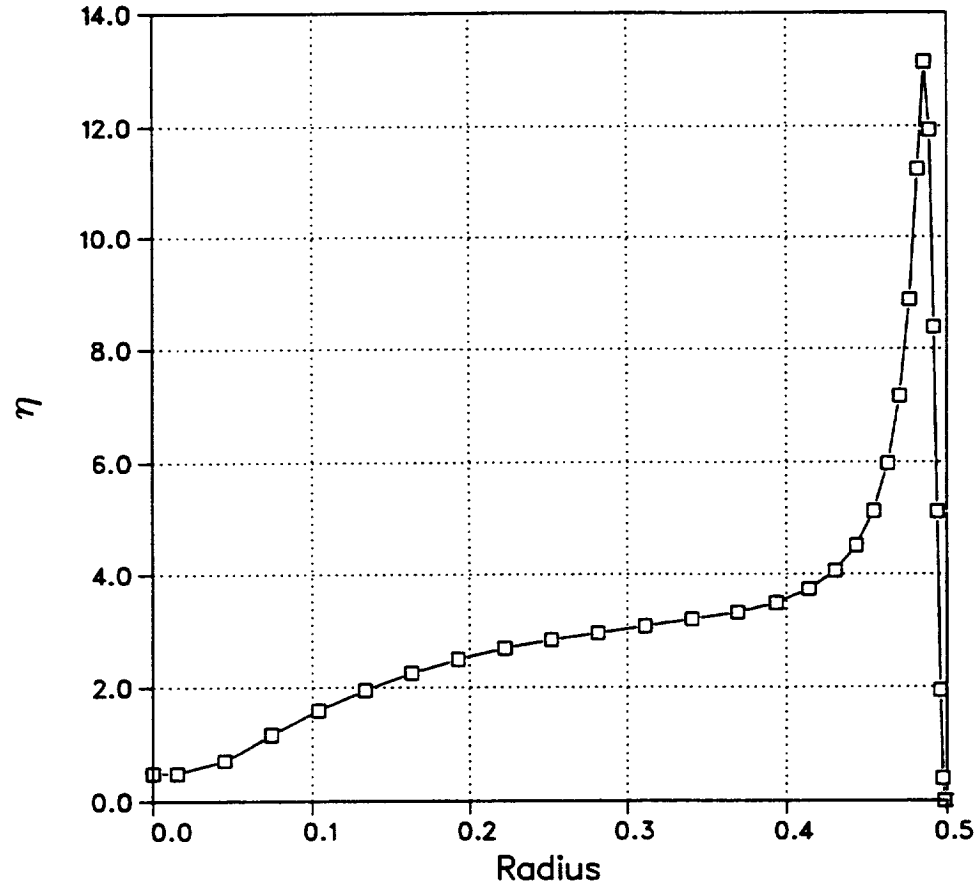

Figure 4.37: Profile of η for $Re = 12000$, based on the Lam-Bremhorst data set.

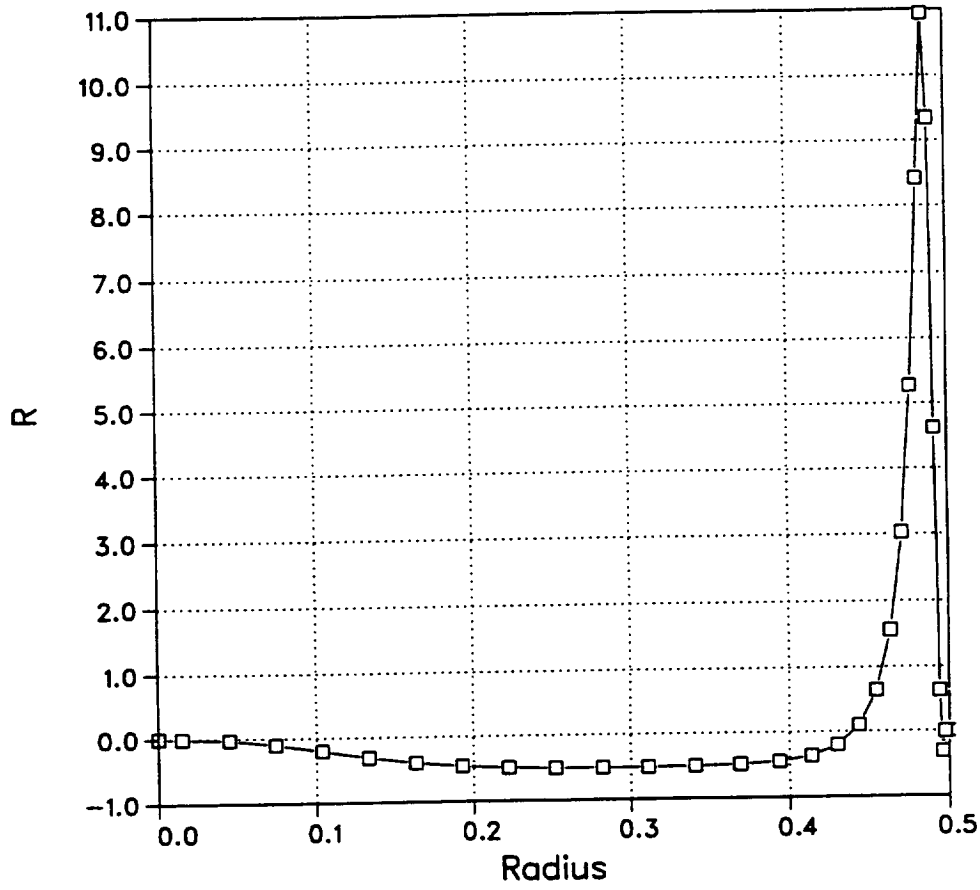

Figure 4.38: Profile of the RNG coefficient for $Re = 12000$, based on the Lam-Bremhorst data set.

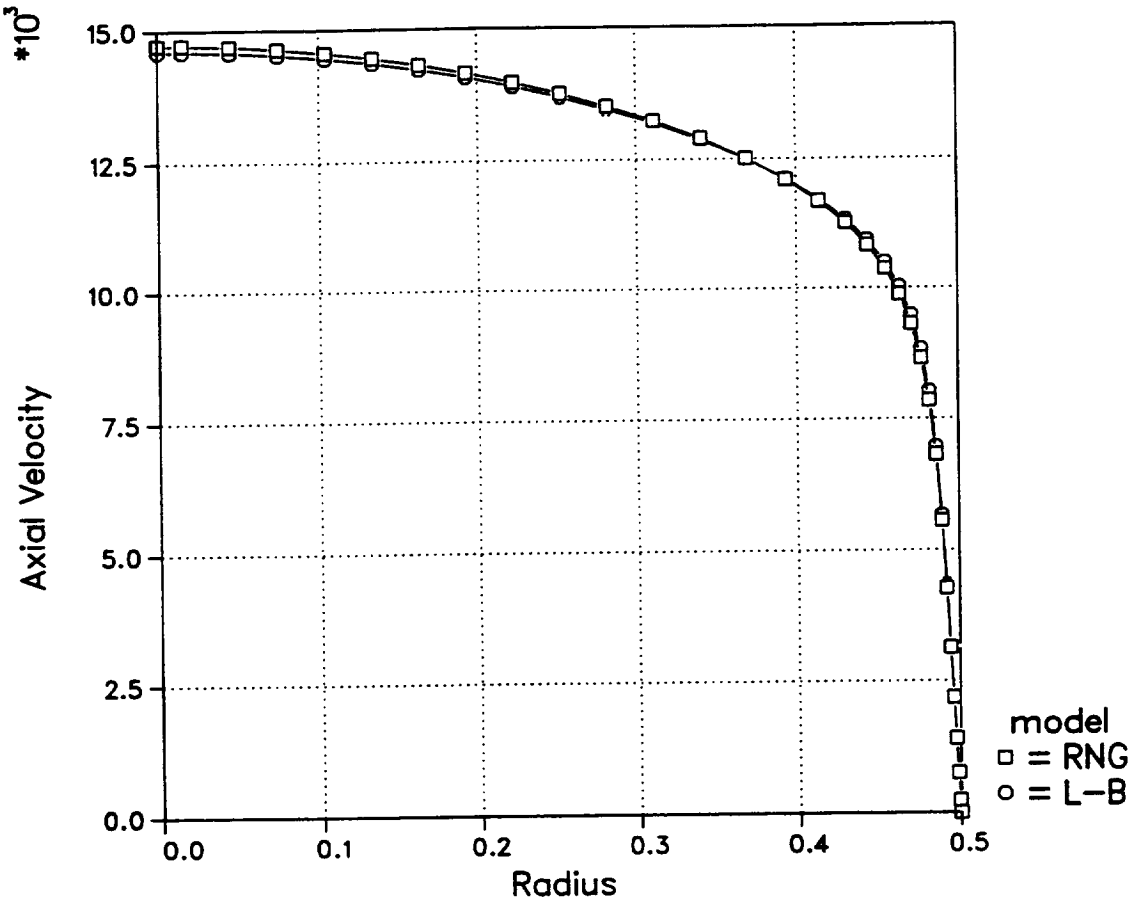

Figure 4.39: Comparison of the axial velocity profiles of the RNG and Lam-Bremhorst models for $Re = 12000$.

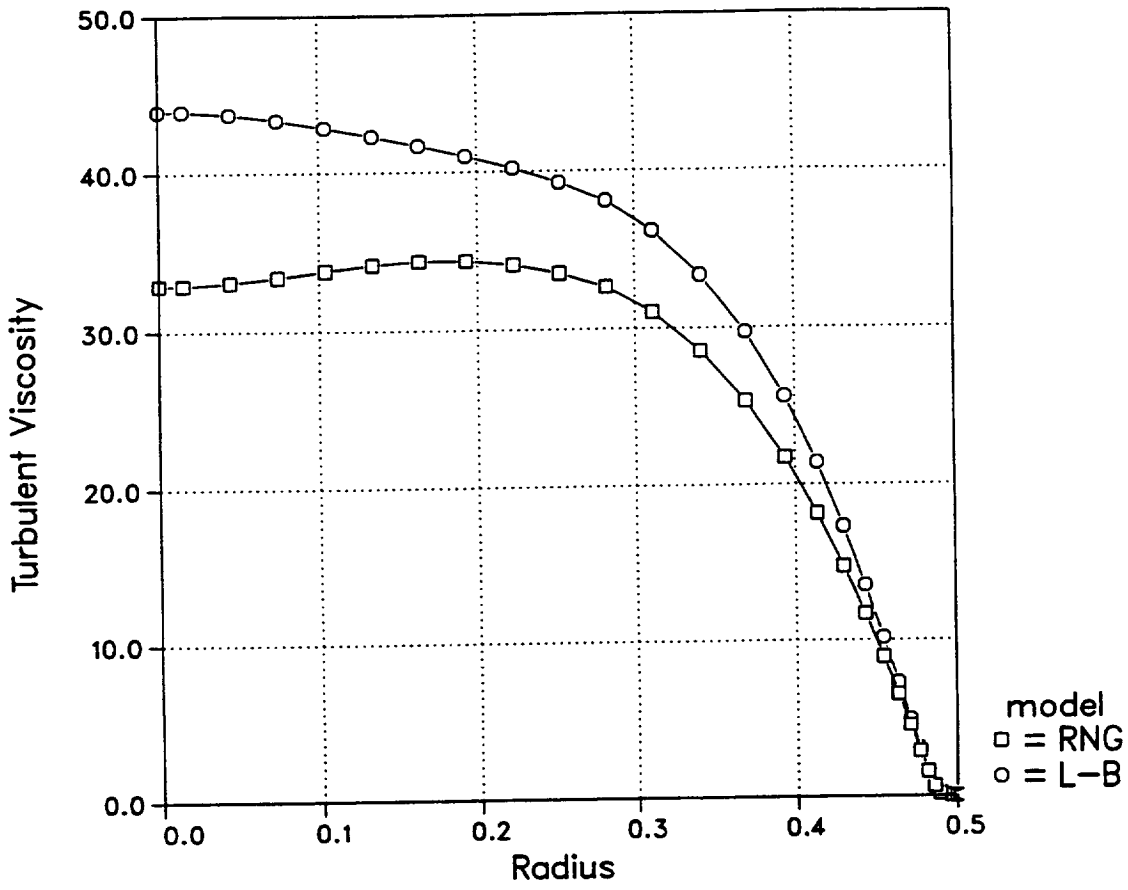

Figure 4.40: Comparison of the turbulent viscosity profiles of the RNG and Lam-Bremhorst models for $Re = 12000$.

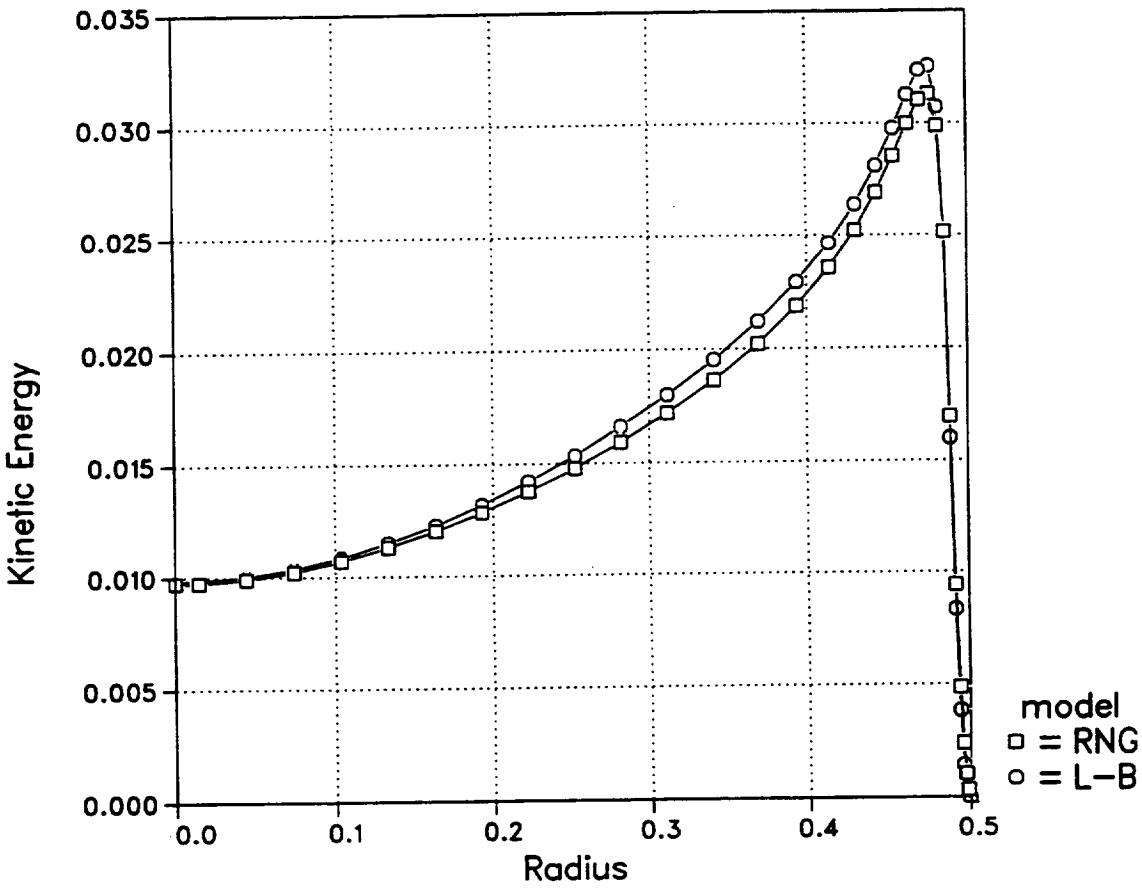

Figure 4.41: Comparison of the kinetic energy profiles of the RNG and Lam-Bremhorst models for $Re = 12000$.

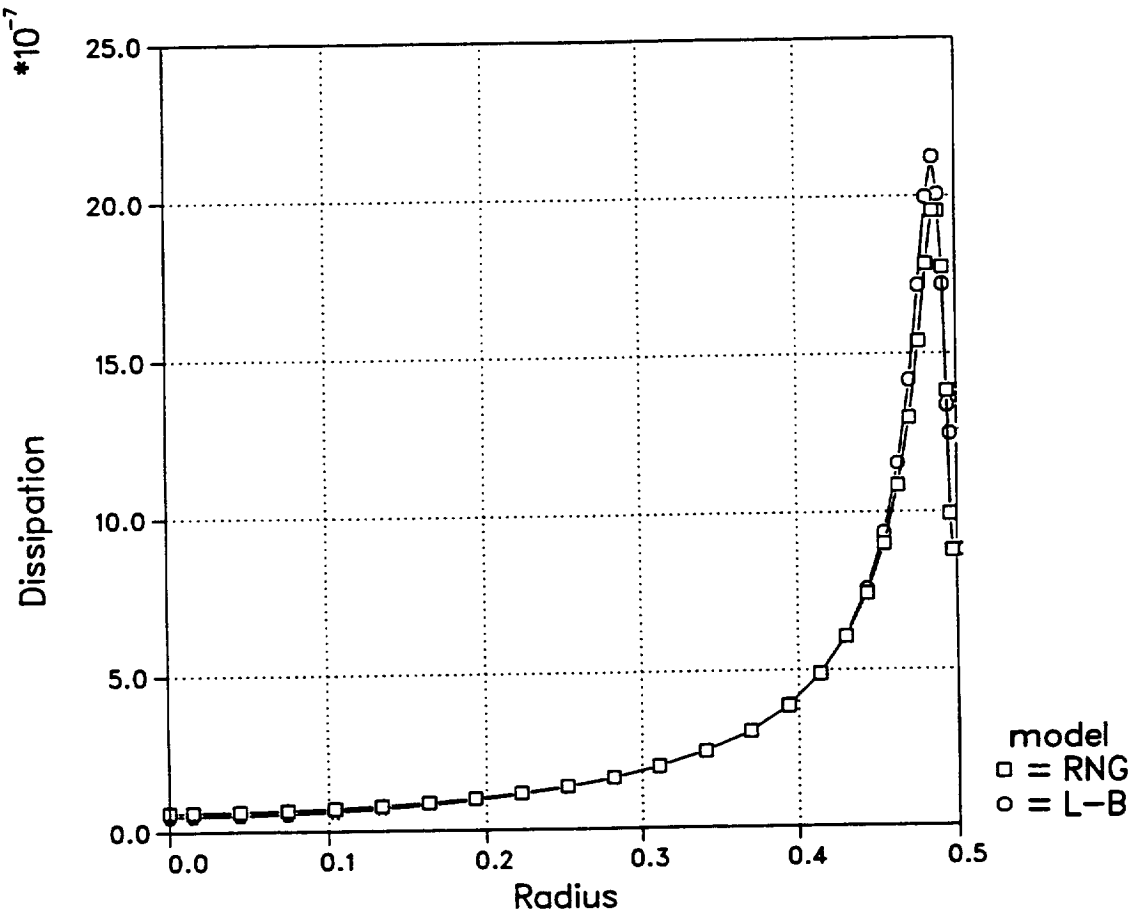

Figure 4.42: Comparison of the dissipation profiles of the RNG and Lam-Bremhorst models for $Re = 12000$.

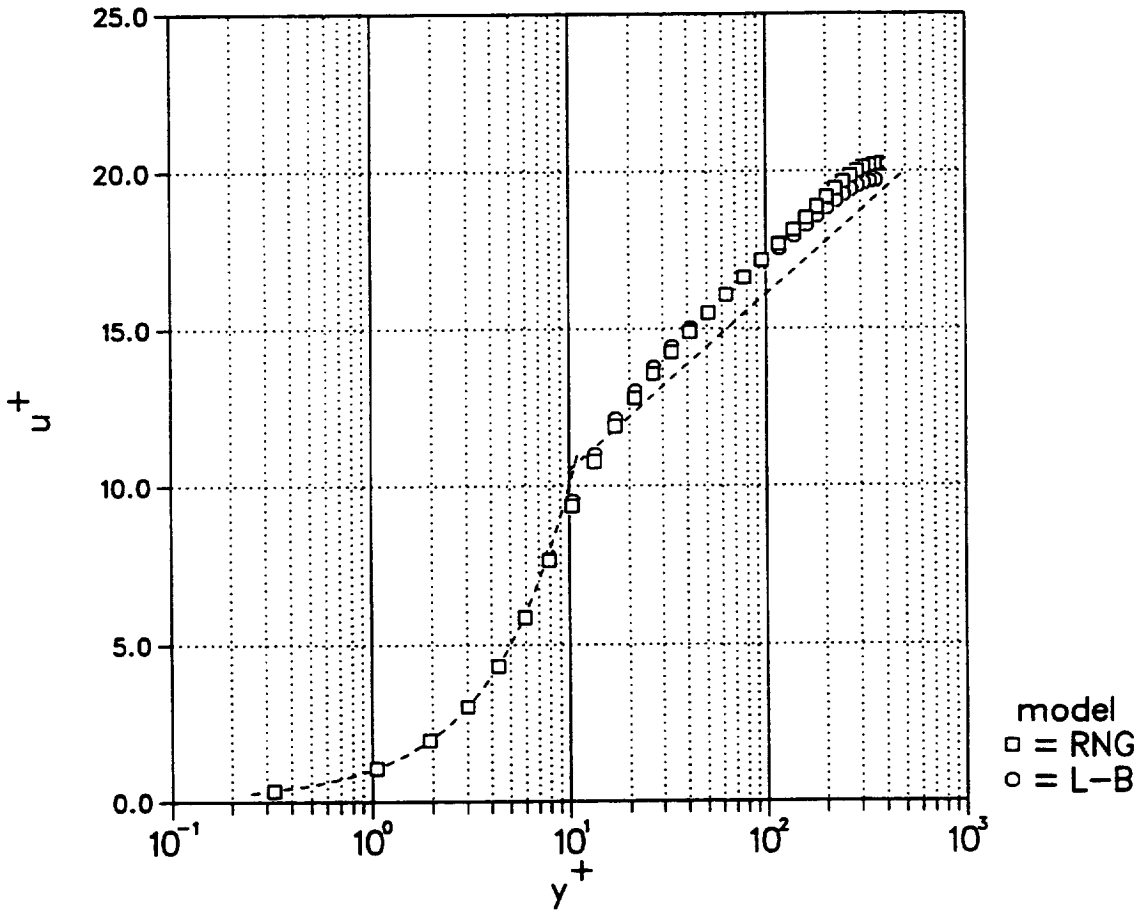

Figure 4.43: Comparison of the wall coordinate velocity profiles of the RNG and Lam-Bremhorst models for $Re = 12000$.

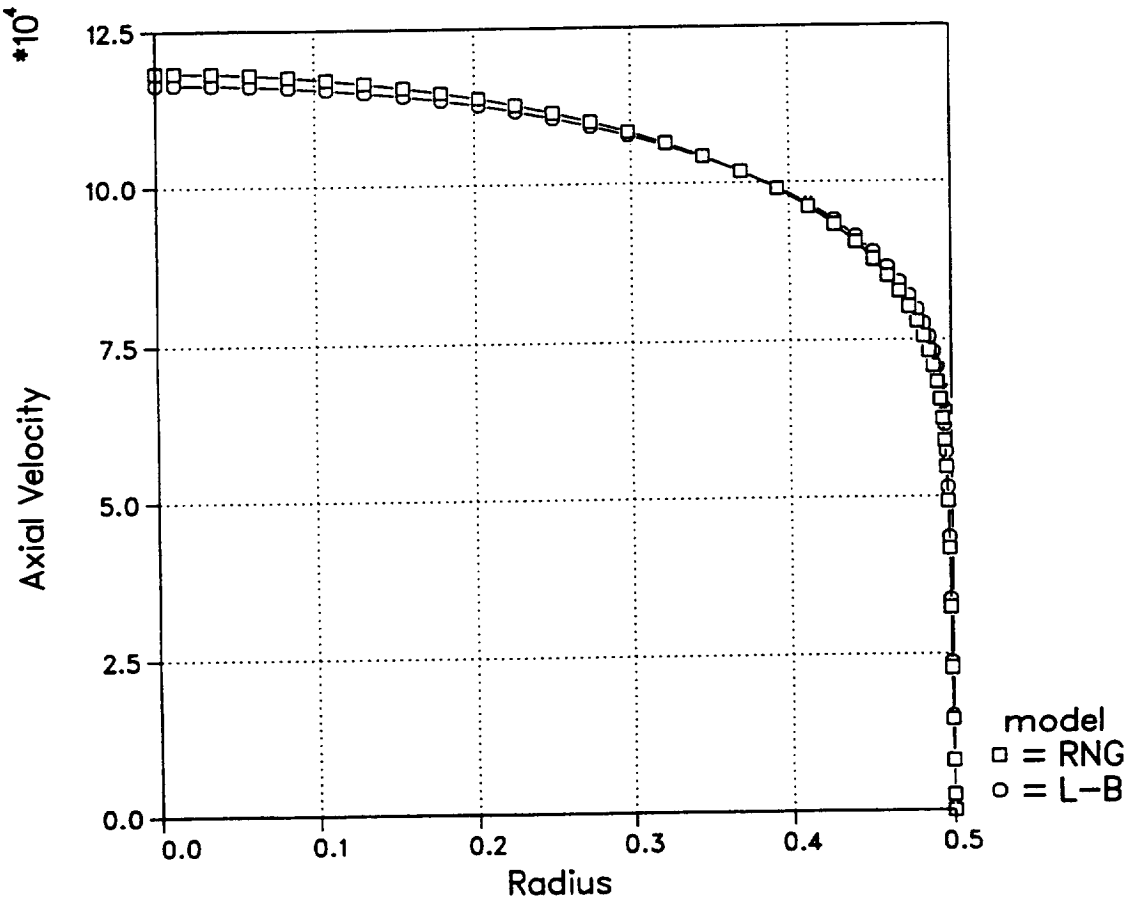

Figure 4.44: Comparison of the axial velocity profiles of the RNG and Lam-Bremhorst models for $Re = 100000$.

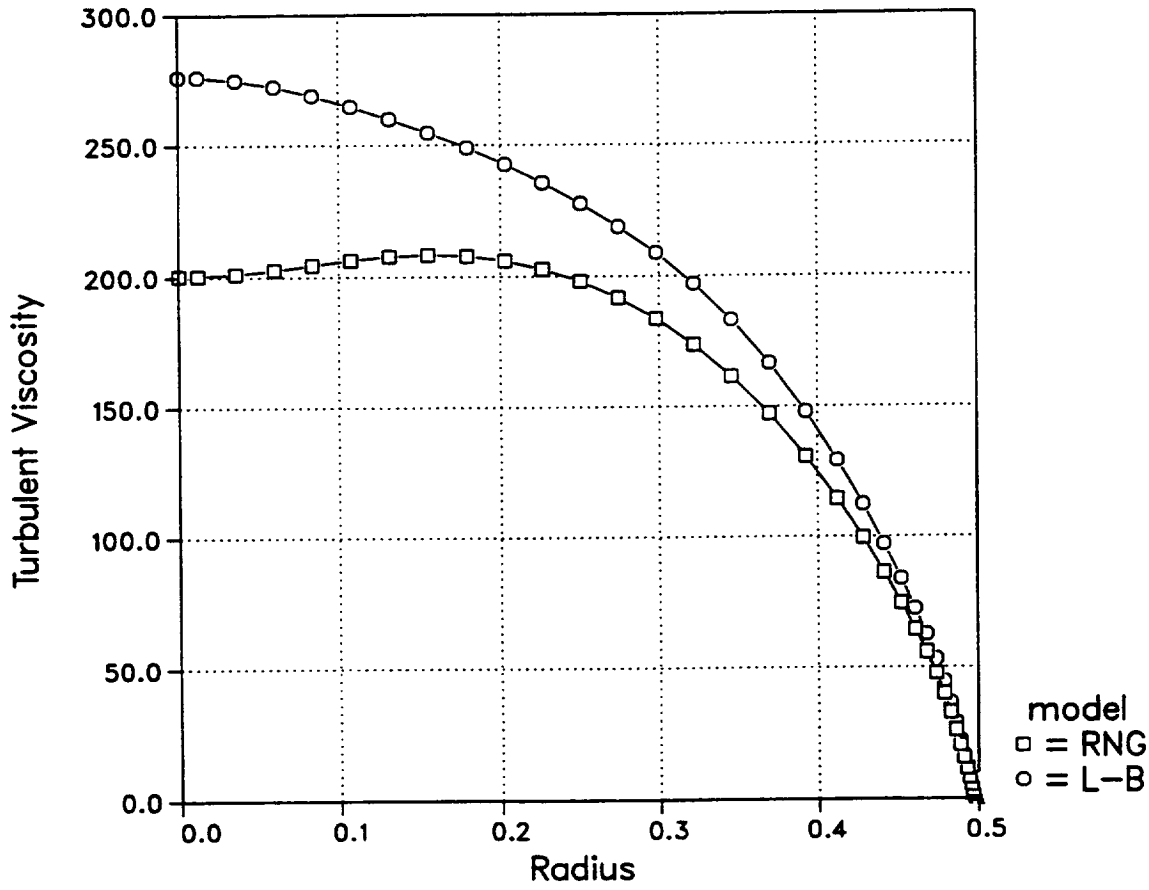

Figure 4.45: Comparison of the turbulent viscosity profiles of the RNG and Lam-Bremhorst models for $Re = 100000$.

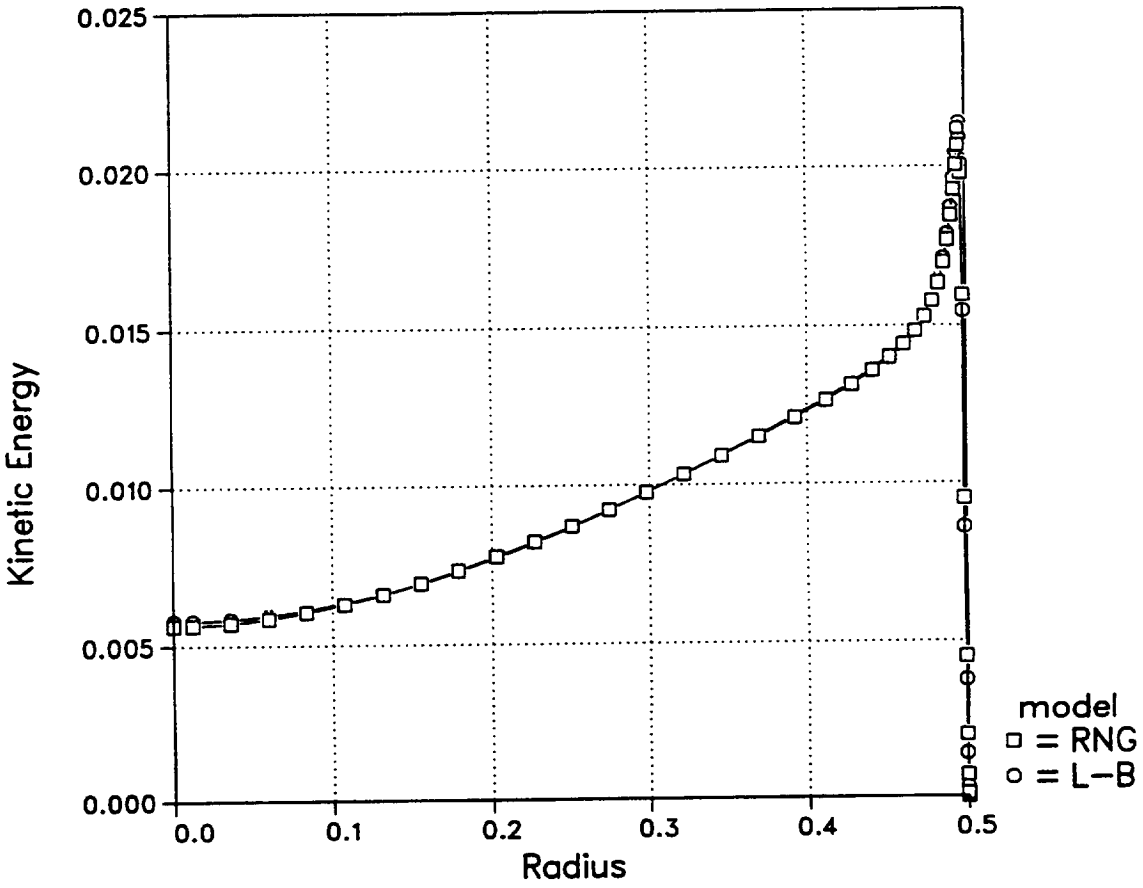

Figure 4.46: Comparison of the kinetic energy profiles of the RNG and Lam-Bremhorst models for $Re = 100000$.

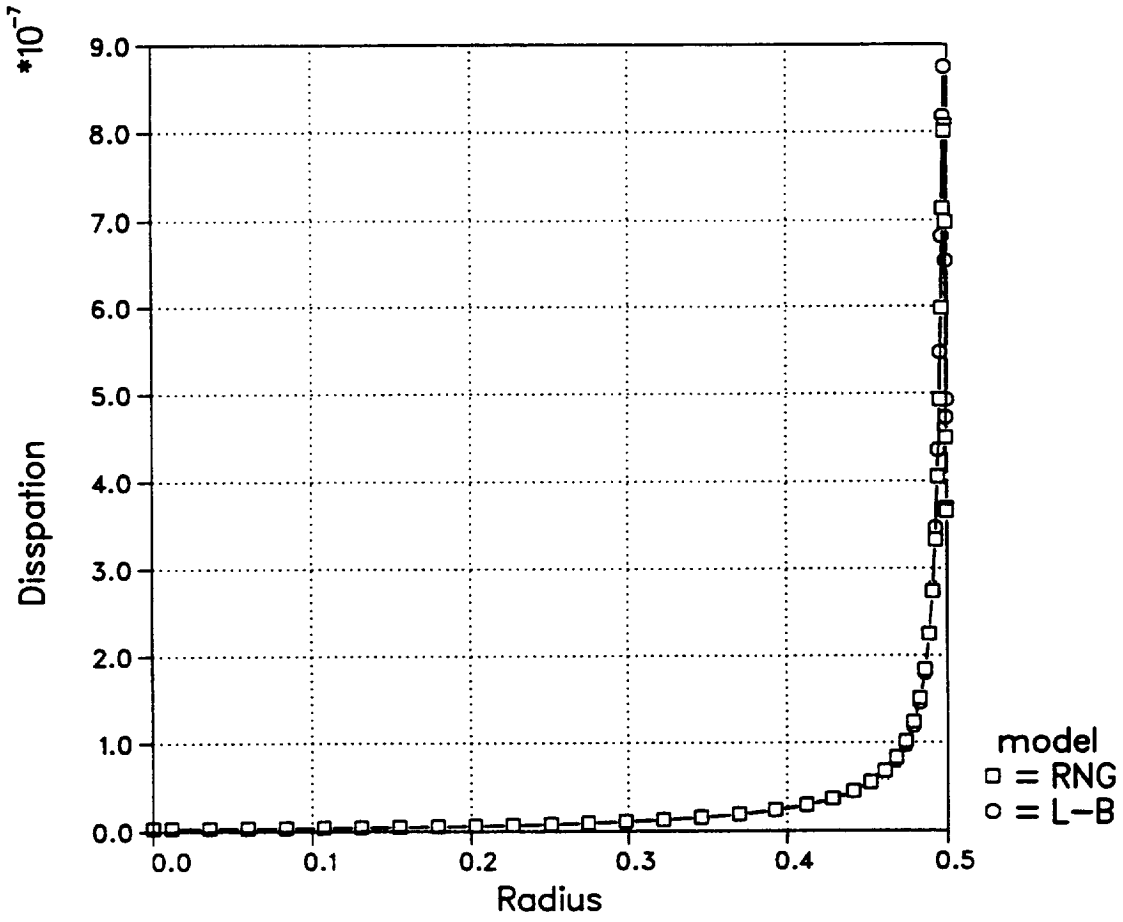

Figure 4.47: Comparison of the dissipation profiles of the RNG and Lam-Bremhorst models for $Re = 100000$.

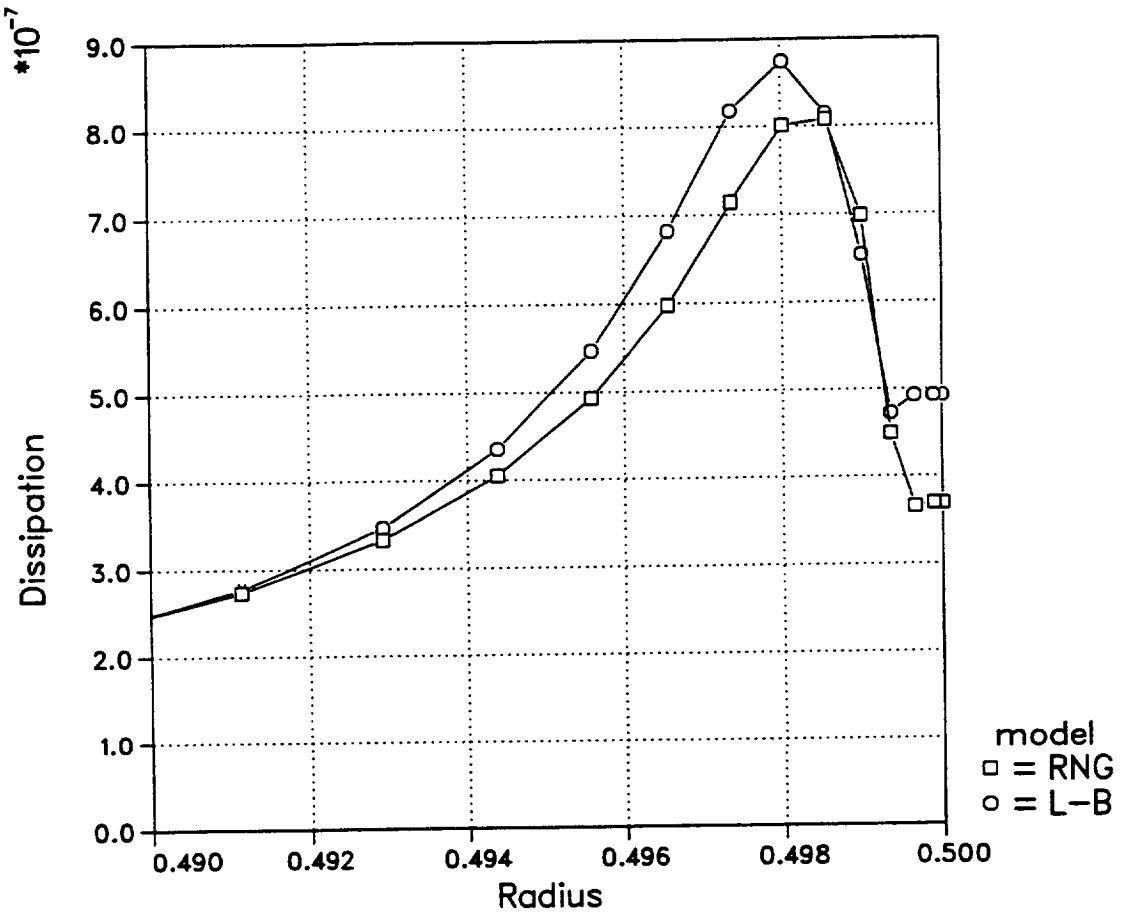

Figure 4.48: Near-wall comparison of the dissipation profiles of the RNG and Lam-Bremhorst models for $Re = 100000$.

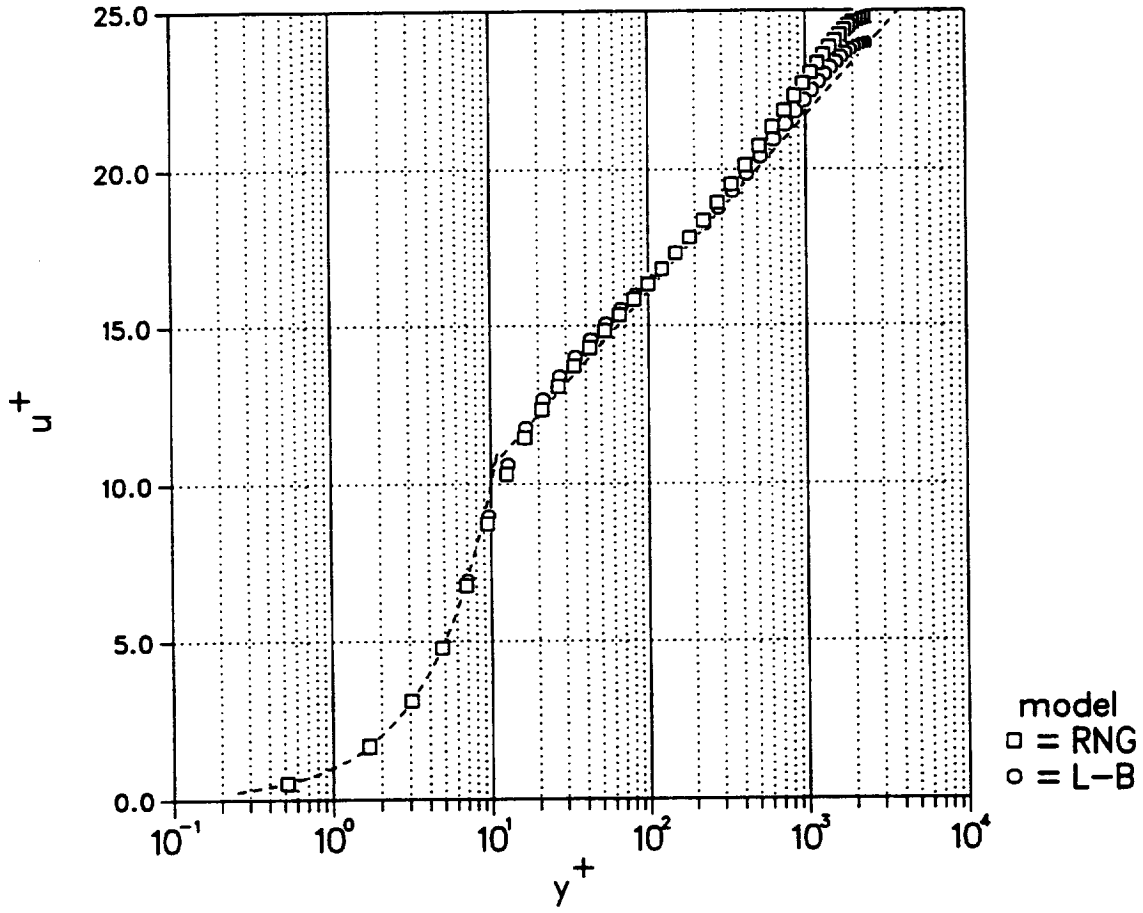

Figure 4.49: Comparison of the wall coordinate velocity profiles of the RNG and Lam-Bremhorst models for $Re = 100000$.

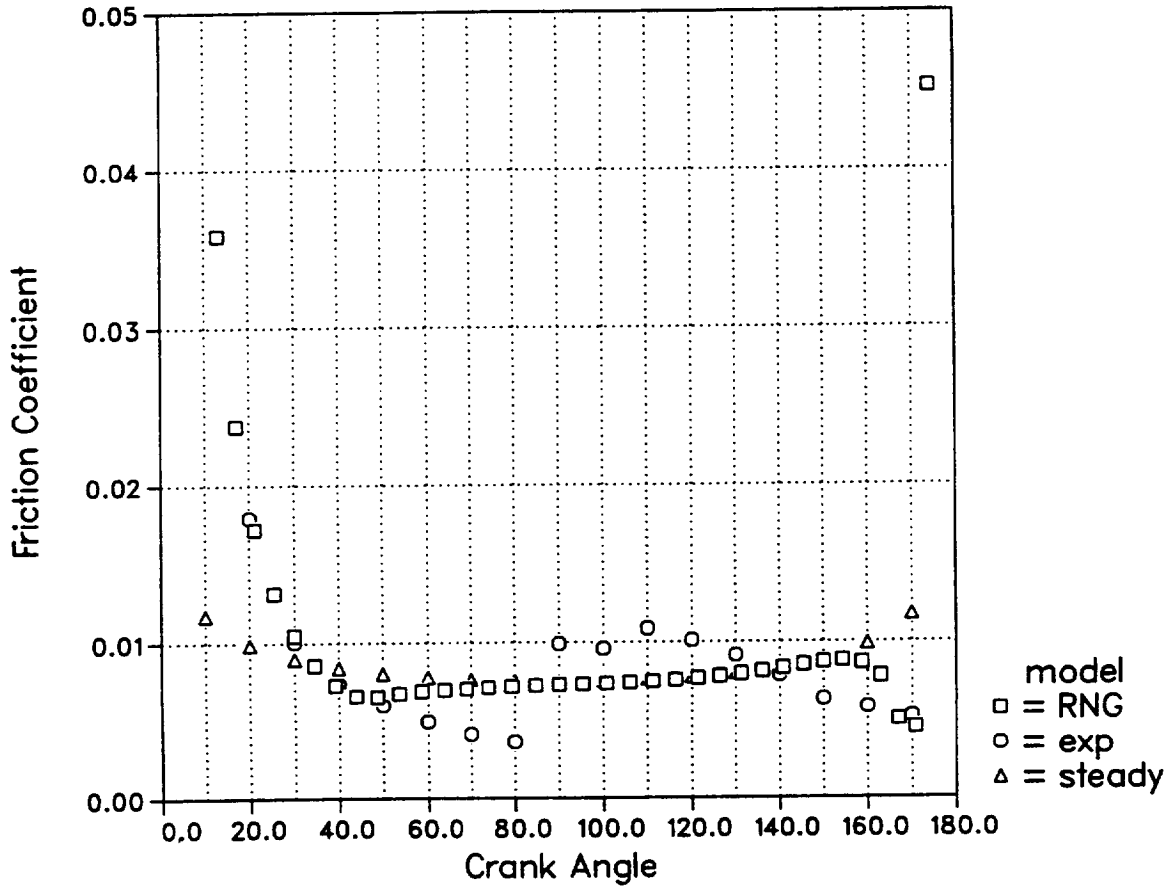

Figure 4.50: Friction coefficient over one half flow cycle at the pipe midlength for RNG model with $Re_{max} = 12000$, $Va = 80$.

Chapter 5

The Laminar Heat Transfer Solution

In this chapter the heat transfer results for laminar pipe flow will be presented. Fully developed results will be considered first as a means of verifying the computer model. The unsteady case will then be studied to determine the effect of flow oscillation on the heat transfer.

5.1 Fully Developed Laminar Heat Transfer

Fully developed laminar flow was considered in Chapter 3. In the case of constant property flow, the corresponding heat transfer problem can be solved conveniently once the flow solution is available. Two types of boundary conditions are commonly encountered in analytical heat transfer solutions: the fixed wall temperature and the prescribed wall flux. These limiting cases can be approximated in the laboratory by exposing the outer pipe wall to condensing steam or by wrapping the pipe with resistant heating wire. Most engineering systems may be approximated using one or the other method of heating, and in practice most situations lie somewhere between these limiting cases.

The fluid temperature will necessarily change in the axial direction when heat

transfer occurs between the pipe wall and the fluid. However, a thermally fully developed situation is said to occur when the following condition is satisfied

$$\frac{\partial}{\partial x}\left[\frac{T_w(x) - T(r,x)}{T_w(x) - T_b(x)}\right] = 0 \tag{5.1}$$

This condition may occur when the boundary condition is either a fixed wall temperature or a prescribed wall flux. Boundary conditions for thermally developed flows are described in detail in Sparrow and Patankar (1977).

The thermally fully developed laminar heat transfer problem can be solved analytically to determine the heat flow from the pipe inner wall to the fluid. When the local Nusselt number is defined as

$$Nu = \frac{hD}{k} \tag{5.2}$$

Incropera and DeWitt (1985) give the numerical values of

$$Nu = 3.66 \tag{5.3}$$

for the fixed wall temperature boundary condition, and

$$Nu = 4.36 \tag{5.4}$$

for the prescribed flux boundary condition.

The computer model was tested for heat transfer in laminar pipe flow to ensure that these values were produced. Figures 5.1 and 5.2 show the evolution of the Nusselt numbers for the fixed wall temperature and prescribed flux boundary conditions, respectively, for developing flow. Each Nusselt number has been normalized by the corresponding thermally fully developed value given above. The flow is uniform across the inlet plane, so both the flow and heat transfer solutions require some distance before becoming fully developed. Figures 5.1 and 5.2 show that the predicted Nusselt numbers do approach the analytical values after a certain development length. The hydrodynamic development length given by equation

(3.1) when $Re = 2000$ is 100 pipe diameters. The heat transfer solution should become thermally fully developed at some point after the flow solution. The computer predicted Nusselt numbers are very nearly fully developed after 100 pipe diameters, and are essentially equal to the fully developed values after 200 diameters. This serves to verify the heat transfer portion of the computer program.

5.2 Heat Transfer in Laminar Oscillating Pipe Flow

The fluid flow solution for laminar oscillating pipe flow was considered in chapter 3. In this section we consider the corresponding heat transfer solution. The heat transfer solution may be obtained by solving the energy equation (2.4) using the velocity field as an input.

The computer program was configured to model the heat transfer by setting the pipe wall and expansion/contraction shoulders to a fixed hot temperature. The outer diameter of the expansion/contraction regions is adiabatic. For the laminar runs the pipe was 50 diameters long and the expansion/contraction regions were each 5 diameters long. In the SPRE Stirling engine the heater pipe outer walls are bathed in a liquid metal reactor coolant. The metal pipe walls will have a thermal conductivity much higher than the working fluid. For these reasons the fixed temperature wall boundary condition was selected as a good approximation. The inlet fluid was assigned a cool temperature. Heat was thus transferred from the pipe and shoulder walls to the fluid, much as would be expected in a shell and tube heat exchanger.

The dimensionless temperature profiles at the axial middle of the pipe at select crank angles during the first half of the flow cycle are shown in figures 5.3 through 5.5 for $Va = 1$, 30 and 100. Figure 5.3 shows that the unsteady effect is slight for

this low oscillation rate. The temperatures at the middle of the pipe are highest when the flow rate is low and the residence time of the fluid within the pipe is high. As the flow increases the temperatures drop. At 90° crank angle the fluid near the axis has had little opportunity to heat up before reaching the middle of the pipe. During the second quarter of the flow cycle the fluid decelerates and the temperatures rise once again. The effect of oscillation is apparent in the difference in temperature levels during accelerating and decelerating phases of the flow cycle. Early in the first quarter of the flow cycle the fluid has been heated significantly during the previous flow reversal. In the next quarter cycle the fluid is cooler since the pipe has been flushed with cool incoming fluid flowing at relatively high speed through the pipe. If the oscillation rate were very low ($Va \ll 1$) the profiles for crank angles of 30.0° and 150° would be identical, as would the profiles for 58.7° and 121.3°.

The unsteady effects become more complicated when Va is increased to 30, as shown in figure 5.4. For this higher rate of oscillation the fluid near the middle of the pipe never reaches the ends during a complete flow cycle. In other words, cool fluid is never swept entirely through the pipe. The temperatures near the middle of the pipe are thus noticeably higher than in the $Va = 1$ case. The variation of temperature throughout the cycle is so complex that a lucid commentary is difficult to provide. This is caused by the complicated velocity profiles seen previously in figure 3.9. The variation of the velocity near the wall is ahead of, and near the axis is behind, that of the bulk flow.

The temperature profiles become very flat when Va is raised to 100, as shown in figure 5.5. The fluid particles at the axial middle of the pipe travel only a small axial distance during the course of a flow cycle.

The temperature contours within the pipe at select times during the first half

cycle are shown in figures 5.6 through 5.8 for $Va = 1$, 30 and 100. The radial dimension of each subplot has been stretched by a factor of 8 for clarity. The top of each subplot represents the pipe wall, where heat is introduced, while the bottom represents the pipe axis. The flow is from left to right in all subplots except the last, which represents bulk flow reversal. The temperature contours during the second half of the cycle are mirror images of those shown for the first. Figure 5.6 reveals temperature contours which are quasi-steady in nature. The cool incoming fluid is heated progressively as it passes through the pipe. The speed of the flow can be gauged by the length to which the cool incoming fluid penetrates into the pipe. At peak flow, for instance (90° crank angle), the lowest temperature contour meets the axis nearly three-quarters of the way through the pipe. For all other times the fluid is heated much sooner.

The temperature distribution is more complicated when the oscillation rate increases. Figure 5.7 shows the contours for $Va = 30$. Two interesting features deserve attention in the first subplot of figure 5.7. First is the complicated distribution at the left end of the pipe for 29° crank angle. This is caused by the recirculation which was set up in the left end region during the previous cycle. At that time, a bubble of heated fluid was trapped in the end region. When the present cycle started, the slow moving incoming fluid was forced to climb around the bubble. Compare with figure 3.13. As a result, the coolest fluid enters the pipe at a radius between the wall and the axis. The second feature is the presence of cooler fluid at the right end of the pipe. This fluid was swept into the pipe during the end of the last cycle, and has had less time to be heated relative to the fluid near (but not at) the left end. This effect becomes more pronounced as the oscillation rate increases.

The temperature contours for $Va = 100$ are shown in figure 5.8. The situation is qualitatively similar to the $Va = 30$ case, but the fluid is much warmer. Also, the

warmest fluid along the pipe length is located near the axial middle. In fact, this very warm fluid never reaches the end of the pipe, a feature which is characterized by the amplitude ratio of the bulk fluid motion A_r. At this high rate of oscillation the amplitude ratio is only 0.2, showing that a fluid particle moving at the bulk fluid velocity would be displaced in the axial direction a distance of only two-tenths of the pipe length during the course of a flow cycle.

The cycle-averaged variation of the dimensionless bulk temperature is shown in figure 5.9 for $Va = 1$, 30 and 100. This type of figure is suggestive of the axial diffusion of heat which is driven by the axial temperature gradient. Figure 5.9 shows that the axial bulk temperature gradient is modest for $Va = 1$, and thus the axial heat transfer is largely by convection. The temperatures at the pipe ends are higher than T_{in} since the expansion and contraction regions hold a volume of heated fluid. The relative effectiveness of diffusion increases with the rate of oscillation. The axial temperature gradient is larger when Va is increased to 30, as required in order to move heat along the pipe axis in the face of diminished convection. This effect is even more pronounced when Va is increased to 100 and A_r is only 0.2. The contribution of convective heat transfer is small under these conditions, so the axial transport of heat becomes dominated by gradient diffusion.

The Nusselt number variation along the pipe wall at select crank angles during the first half of the flow cycle is shown in figures 5.10 through 5.12 for $Va = 1$, 30 and 100. The flow is from left to right. Each curve is normalized by the Nusselt number for fully developed laminar heat transfer with a constant wall temperature boundary condition ($Nu_{fd} = 3.66$). For low Va , the flow and heat transfer problem is quasi-steady. The variation of the Nusselt numbers shown in figure 5.10 is similar to that of figure 5.1. The developing temperature field near the pipe entrance creates a Nusselt number well above the fully developed value. The Nusselt number

then drops and levels off as the end effect diminishes. The hydrodynamic (and heat transfer) development length increases with Re, so the level of Nu depends slightly on the crank angle (bulk flow rate). The only unusual feature of figure 5.10 is the fact that the curves of Nu are lower during the first quarter of the cycle. For instance, the curve for 30° crank angle is lower than for 150°. This hysteresis is caused by the oscillating flow effect. The wall heat flux is low after flow reversal due to the extensive heating of the near-wall fluid which occurred while the flow rate was low, during the previous flow reversal. During the second quarter of the cycle the near-wall temperature is lower as a result of the significant convection of cool incoming fluid. This effect will also be seen in figure 5.16 below.

Oscillation has a more complicated effect on the relative level of Nu during the cycle as Va increases. For crank angles early in the cycle, the near-wall flow responds quickly to the imposed pressure gradient, creating a large velocity gradient, as shown previously in figure 3.9 for a moderate Va of 30. This in turn increases the temperature gradient and Nu. This effect is quite pronounced for x/D greater than about 15 when $Va = 30$, as shown in figure 5.11. Later in the cycle the gradients at the wall are lower. For $Va = 30$, flow reversal at the wall occurs at a crank angle near 149°, and the heat transfer is lowest at that time.

When Va becomes large, thermal convection diminishes in comparison to diffusion. The bulk fluid motion is restricted, and A_r is low. For large Va , a fluid particle near the middle of the pipe will never be swept out of the pipe, but will instead shuttle back and forth over a short distance. As a result, this fluid will reach a temperature closer to that of the wall. The heat flux and Nu are thus lowest near the middle of the pipe. This effect is shown in figure 5.12 for $Va = 100$.

The variation of the axial-averaged Nu ($\overline{Nu}$) over the entire cycle is shown in figures 5.13 through 5.15 for $Va = 1$, 30 and 100. There are two cycles of heat

transfer in each flow cycle since the heat transfer does not depend on the axial direction of flow. The Nusselt number is normalized against Nu_{fd}. Figure 5.13 shows the time variation of $\overline{Nu}$ when Va is low. When the flow rate is large, the entire length of the pipe falls within the developing region and $\overline{Nu}$ is higher than Nu_{fd}. The developing region takes up a smaller fraction of the pipe when the flow rate is low, and $\overline{Nu}$ approaches Nu_{fd}. The rapid variation near bulk flow reversal is an unsteady effect caused by circulation of fluid within the pipe. This effect diminishes shortly after flow reversal (20° and 200° crank angle) as the bulk flow increases and once again dominates the heat transfer.

The circulation effect becomes more prominent as Va increases. Figure 5.14 reflects the fact that near-wall flow reversal begins earlier and is significant over a larger portion of the cycle when $Va = 30$. This effect continues to increase with Va as shown in figure 5.15, for which $Va = 100$.

The Nusselt number used thus far is defined as

$$Nu = \frac{hD}{k} \tag{5.5}$$

The heat transfer coefficient was defined as

$$h = \frac{q}{T_w - T_b} \tag{5.6}$$

where q is the local heat flux from the wall to the fluid, T_w is the wall temperature, and T_b is the local bulk fluid temperature. The term local refers to a quantity whose value depends on axial position.

This definition of Nu is common for steady flow heat exchanger design, for which T_b is used in place of the free-stream temperature (T_∞) used for external flows.

The bulk (velocity-area weighted) temperature for incompressible, constant property flow has been defined here as

$$T_b = \frac{\int |u(r)|\, T\, r\, dr}{\int |u(r)|\, r\, dr} \tag{5.7}$$

where $r\,dr$ is a differential flow area and $u(r)$ is the axial velocity component. The absolute value of velocity is used since the scalar T_b is sensitive only to the magnitude of the flow. This definition also applies at flow reversal. Without the use of the absolute value the T_b definition would produce $Nu = 0$ when the bulk velocity becomes zero.

Figures 5.16 through 5.18 show the phase relationship between flux, T_w - T_b , and Nu over one flow cycle at the axial middle of the pipe for Va = 1, 30 and 100. This type of comparison serves to further illuminate the complicated features of this unsteady flow and heat transfer problem. The sudden jump in Nu near flow reversal has been discussed above. The underlying variation of flux and T_w - T_b are seen clearly in figure 5.16. As flow reversal approaches, the temperature difference drops faster than the flux, boosting Nu . At this low oscillation rate the flow is quasi-steady, but the flux and temperature difference do not have the same trends throughout the cycle. Except for a short period following flow reversal, the flux tends to rise later than the temperature difference during accelerating portions of the cycle and fall sooner during decelerating portions. This behavior was discussed above in conjunction with figure 5.10 and tends to keep Nu slightly lower during acceleration. Note that the variation of the flux and temperature difference at low oscillation rate bear some resemblance to the absolute value of a sinusoid. The flux and temperature difference both peak at nearly the same instant as the flow, and reach their minima together only shortly after the flow.

The variation of the flux and temperature difference become more complicated as Va increases. Figure 5.17 shows that the flux and temperature difference lag behind the flow, peaking at about 156° and 165°, respectively, for Va = 30. The heat flux variation is vaguely sinusoidal, though it rises faster during deceleration than it falls during acceleration. The variation of the temperature difference is

particularly complex due to the combination of phase shift and flow reversal effects. The situation becomes more complicated yet when $Va = 100$, as shown in figure 5.18. Here the heat flux lags the flow by 90° and the variation appears nearly sinusoidal.

Figures 5.16 through 5.18 consider the heat transfer behavior only at the axial middle of the pipe. At this point the end effects are small when the flow is low and symmetric in any case. The heat transfer behavior is even more complicated when viewed at positions away from the middle of the pipe. Figure 5.19 shows the variation at a position 10.8 diameters from the left end of the pipe for $Va = 1$, the same operating condition used in figure 5.16. At this position the heat transfer is significant during the first half of the cycle, when the left end of the pipe is the entrance. During the second half the left end is closer to the outlet, so the heat transfer is closer to the fully developed case. The differences in heat transfer behavior between the first and second halves of the flow cycle only become larger as either end of the pipe is approached.

One of the objectives of the present research is to reduce the unsteady 2-D heat transfer behavior in oscillating pipe flow into a more manageable form that can be incorporated into spatially 1-D Stirling engine performance codes. The temporal and spatial variation of Nu seen in figures 5.10 through 5.19 is far too complicated to reduce to a form such as

$$Nu = Nu(x, t) \tag{5.8}$$

It would be desirable to devise some means of simplifying the Nu expression so that its behavior can be expressed by a simple correlation. The unsteady and flow reversal effects discussed above produce a complicated variation of T_b, and this is the most ill-behaved part of the Nu definition. The use of T_b may not even be

desirable from the perspective of the engine performance modeler. The detailed variation of T_b through space and time will not be known a priori, but would be required in order to compute the total heat transfer between the fluid and pipe wall. The inlet and outlet fluid temperatures will be available from the performance code to be used (iteratively) as an input to the heat transfer calculation. It is proposed instead that the temperature difference T_w - T_{in} be used in the definition of the heat transfer coefficient given by equation (5.6). This will produce a variation of Nu which is identical to that of the flux, since T_w - T_{in} is a constant. The resulting redefined Nusselt number will be referred to as Nu^*.

Removing the T_b dependence eliminates some of the complications due to the oscillating flow effect. The end effects remain to be dealt with. We have seen that the end effects are significant, but they can be accounted for implicitly by the use of axial averaging. The final correlation for Nu would then be restricted to a given L/D ratio but would still be a function of time. This is acceptable for the purpose of building a Stirling engine performance code once the heat exchanger tube has been selected. (Cost, weight, configuration and space constraints may be just as important as the heat transfer performance.) When the redefined Nusselt number is averaged over the length of the pipe ($\overline{Nu^*}$) we find the behavior shown in figures 5.20 through 5.22.

Figure 5.20 shows the predicted variation of $\overline{Nu^*}$ over one flow cycle for Va = 1. The prediction is shown in square symbols. A curve fit is also plotted using the equation

$$\overline{Nu^*} = 4.0 * |sin(crank\ angle - 5°)| + 0.5 \tag{5.9}$$

Both the numerical prediction and the curve fit have a cycle-averaged $\overline{Nu^*}$ of 3.04. The curve fit was established by adjusting the amplitude, phase shift (relative to

the bulk flow) and vertical offset to produce the same cycle-averaged value and the best qualitative agreement with the computed curve. The form of the curve fit (5.9) is acceptable whenever Va is less than 5.

Figure 5.21 shows the variation of $\overline{Nu^*}$ over one flow cycle for $Va = 30$. For this case the following sinusoidal curve fit was selected

$$\overline{Nu^*} = 0.32 * sin\,(2 * (crank\ angle - 90°)) + 2.24 \tag{5.10}$$

The cycle-averaged value is 2.24.

Figure 5.22 shows the variation of $\overline{Nu^*}$ over one flow cycle for $Va = 100$. The curve fit is given by

$$\overline{Nu^*} = 0.13 * sin\,(2 * (crank\ angle - 69°)) + 1.43 \tag{5.11}$$

The cycle-averaged value is 1.43.

Figures 5.20 through 5.22 show that, unlike the conventionally defined Nusselt number, $\overline{Nu^*}$ decreases with increasing Va. This clearly illustrates the reduced effectiveness of axial convective transport as the oscillation rate increases. At very high rates of oscillation the axial transport is primarily due to diffusion which has been enhanced through interaction with the oscillating flow field. Zhang and Kurzweg (1991) refer to this condition as *enhanced axial heat transfer*. The axial heat flux under these conditions may be substantially larger than in the case of pure conduction, but will nevertheless be smaller than if steady pipe flow were allowed to occur.

The variation of the amplitude, mean and phase shift (relative to the bulk flow) of $\overline{Nu^*}$ with Va is shown in figure 5.23. This figure may be used as a means of interpolating the laminar $\overline{Nu^*}$ correlation (equations (5.10) or (5.11)) for oscillation rates in the range $5 \leq Va \leq 100$.

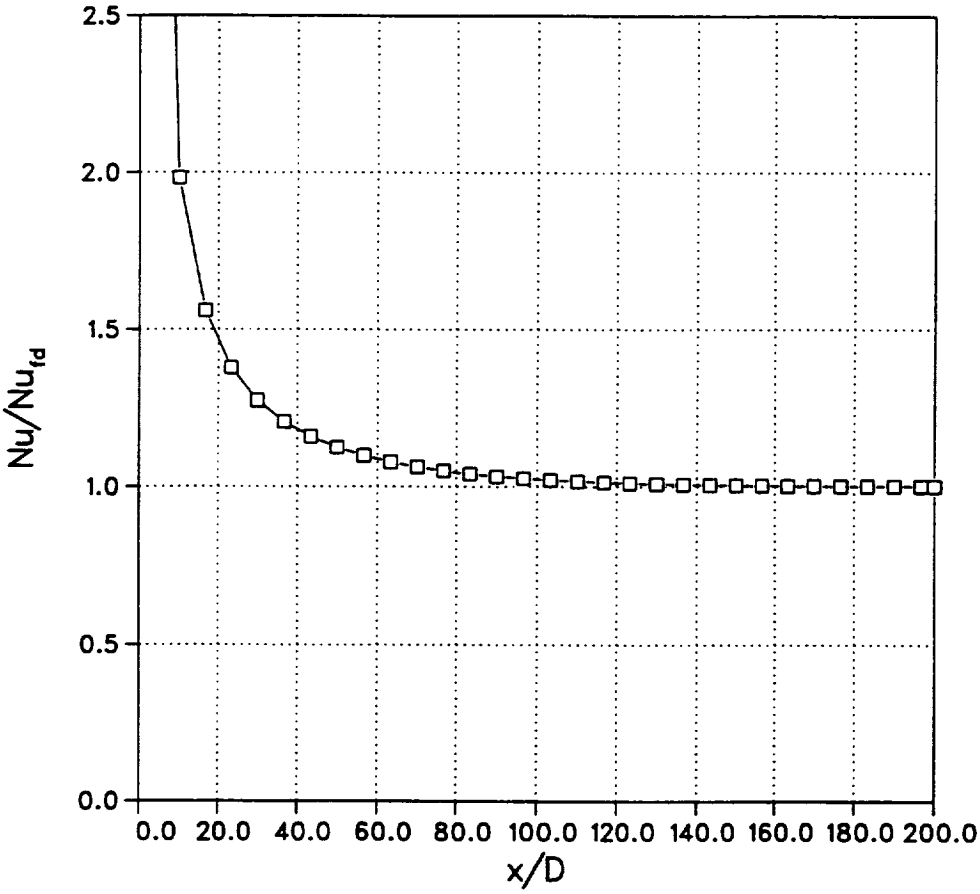

Figure 5.1: Development of the Nusselt number along the pipe length for a fixed wall temperature boundary condition.

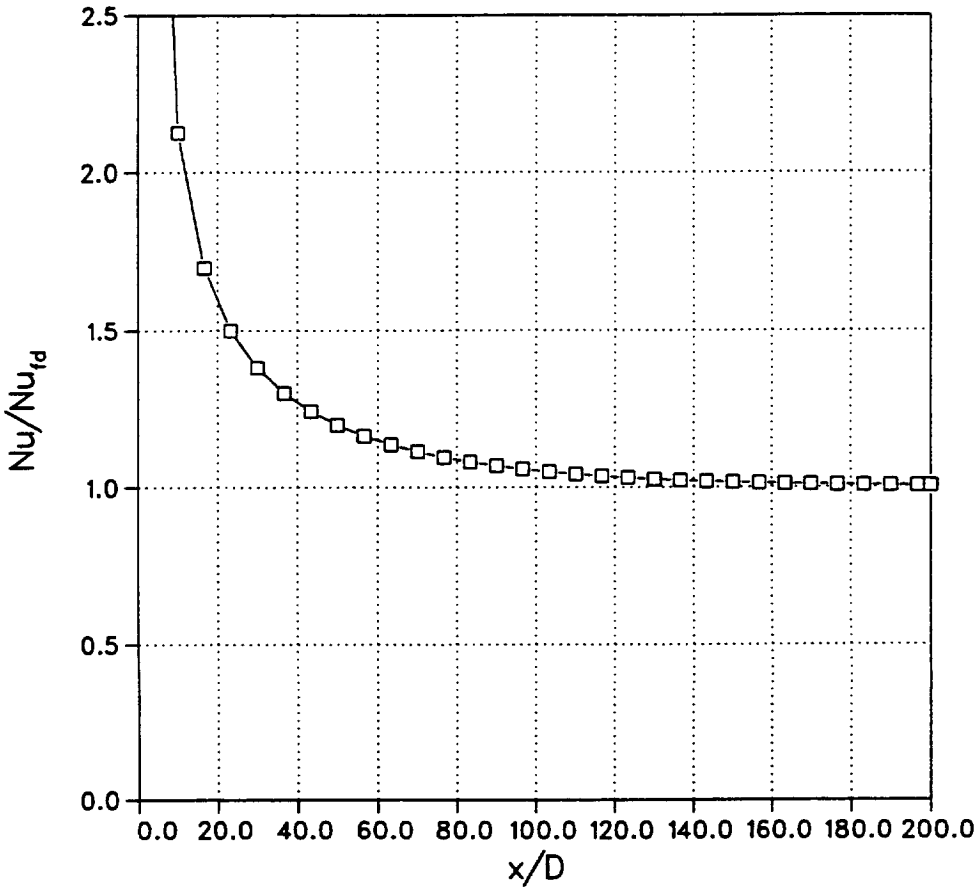

Figure 5.2: Development of the Nusselt number along the pipe length for a prescribed flux boundary condition.

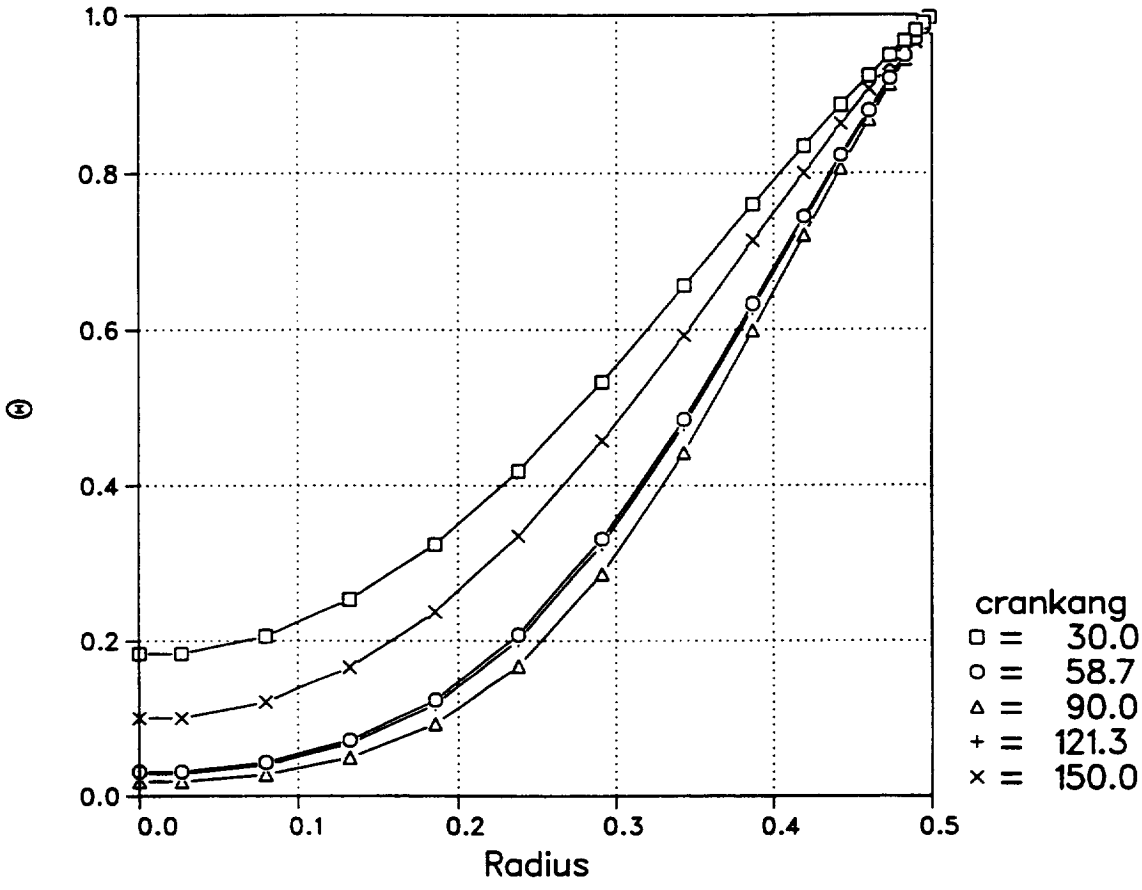

Figure 5.3: Temperature profiles at the axial middle of the pipe for $Va = 1$.

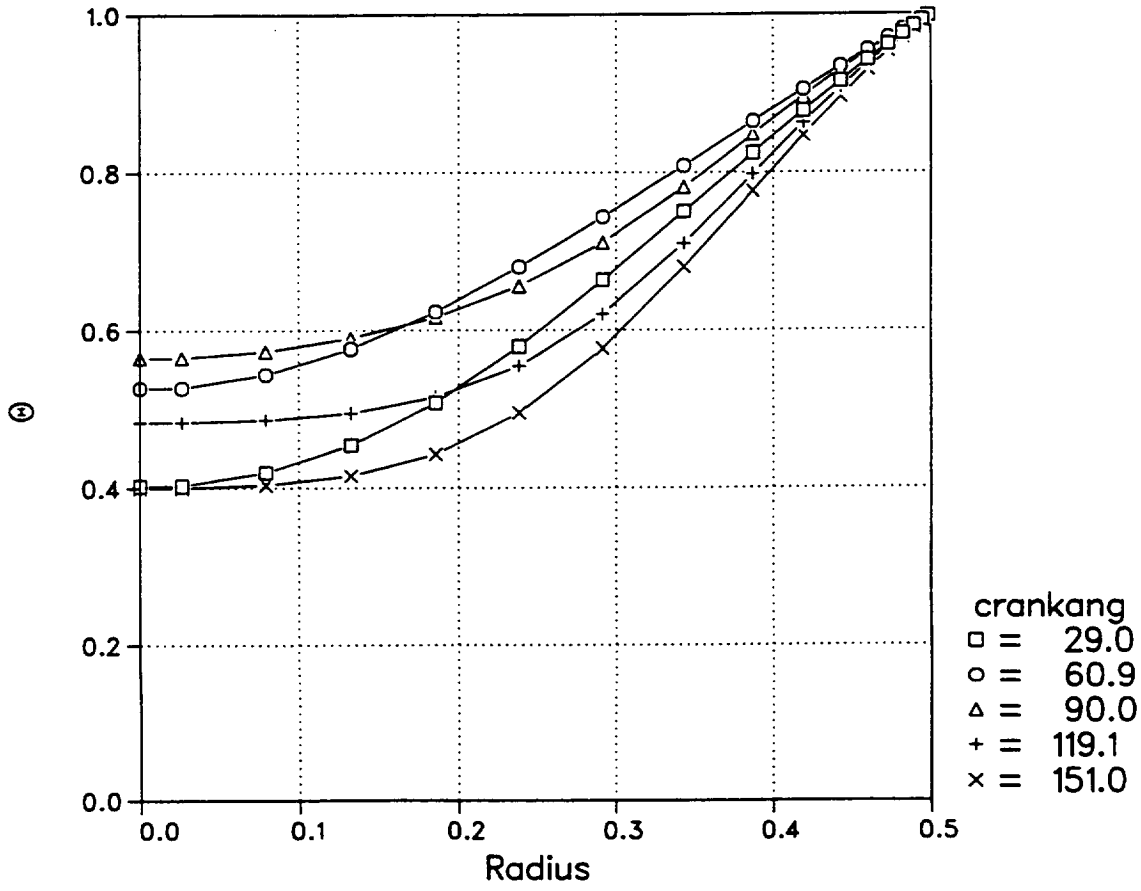

Figure 5.4: Temperature profiles at the axial middle of the pipe for $Va = 30$.

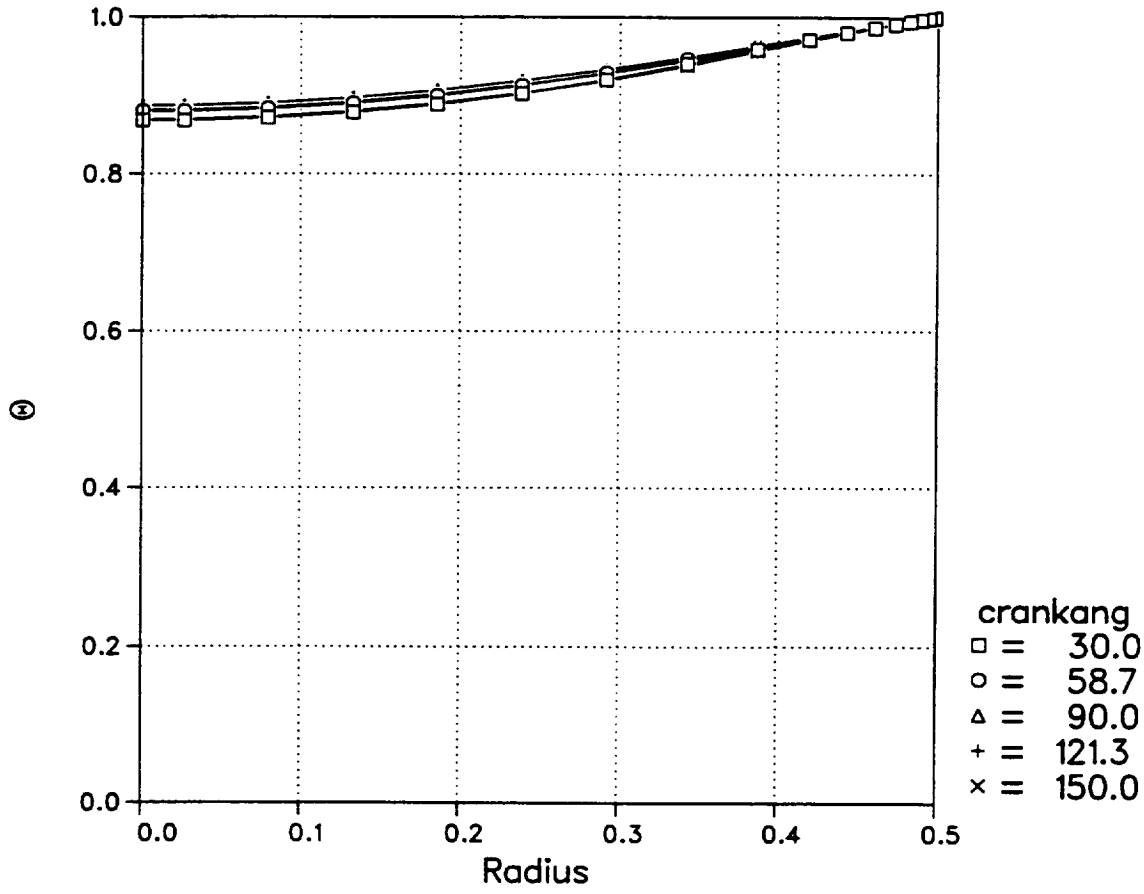

Figure 5.5: Temperature profiles at the axial middle of the pipe for $Va = 100$.

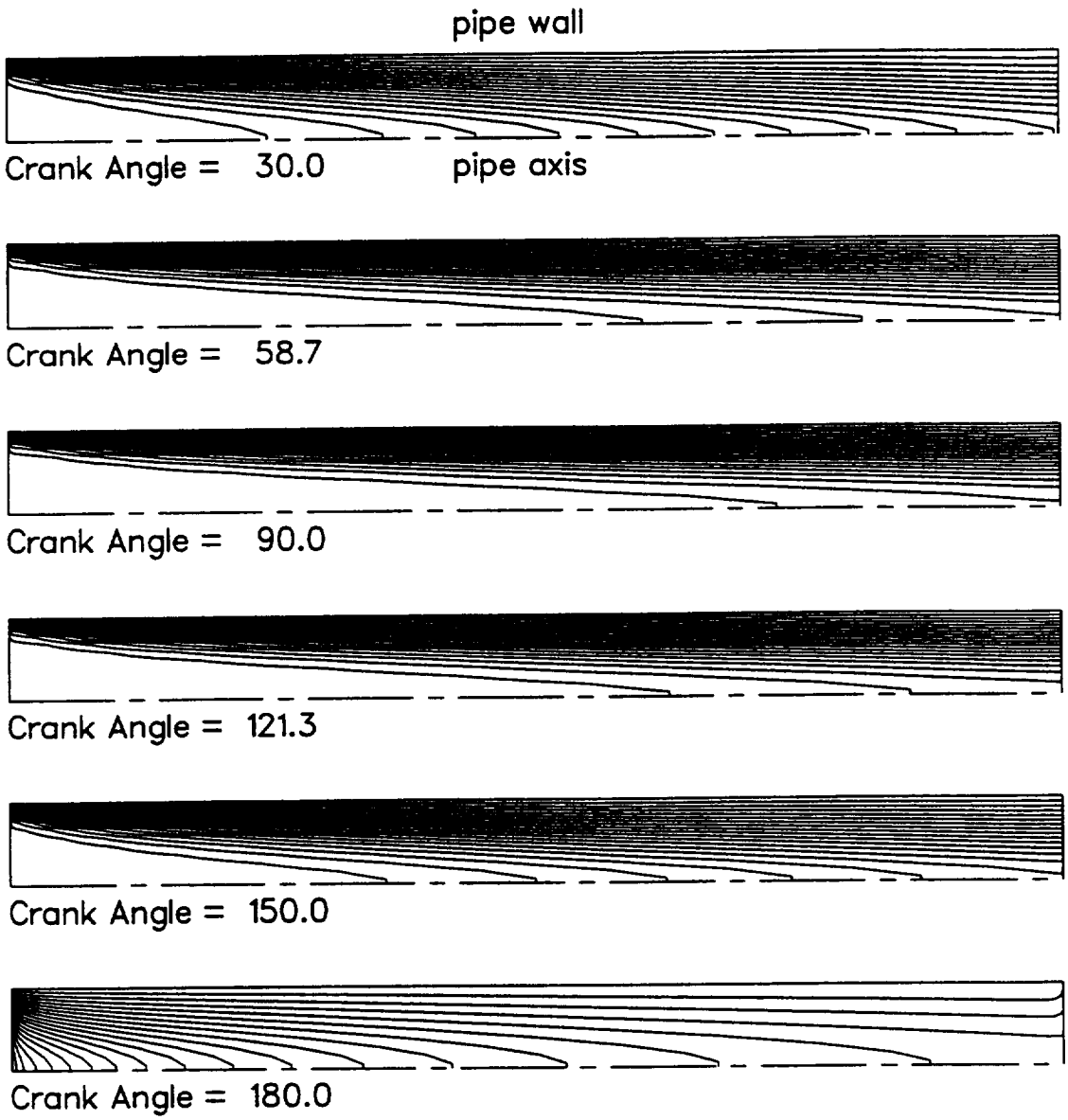

Figure 5.6: Temperature contours within pipe during first half cycle for $Va = 1$.

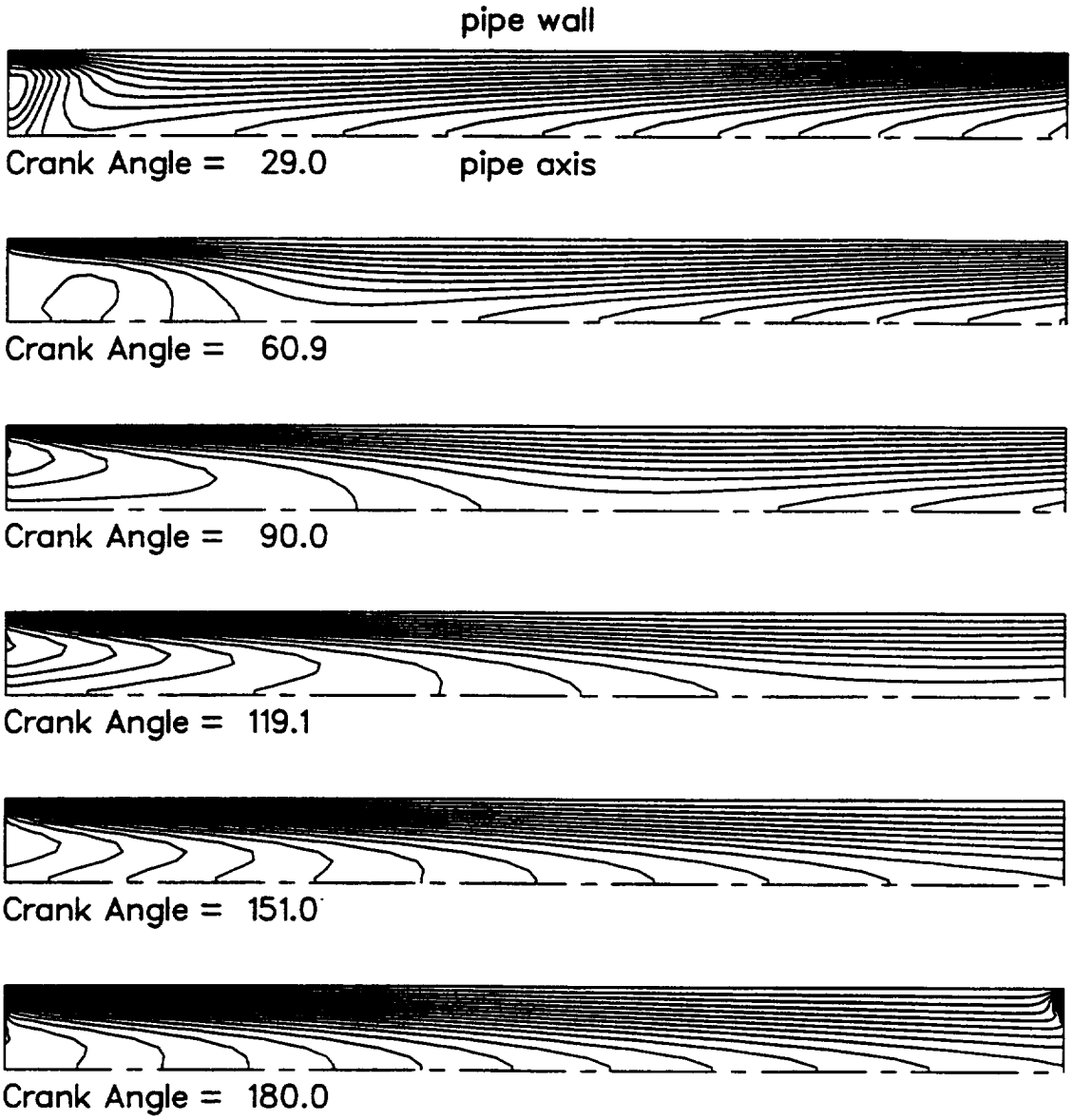

Figure 5.7: Temperature contours within pipe during first half cycle for $Va = 30$.

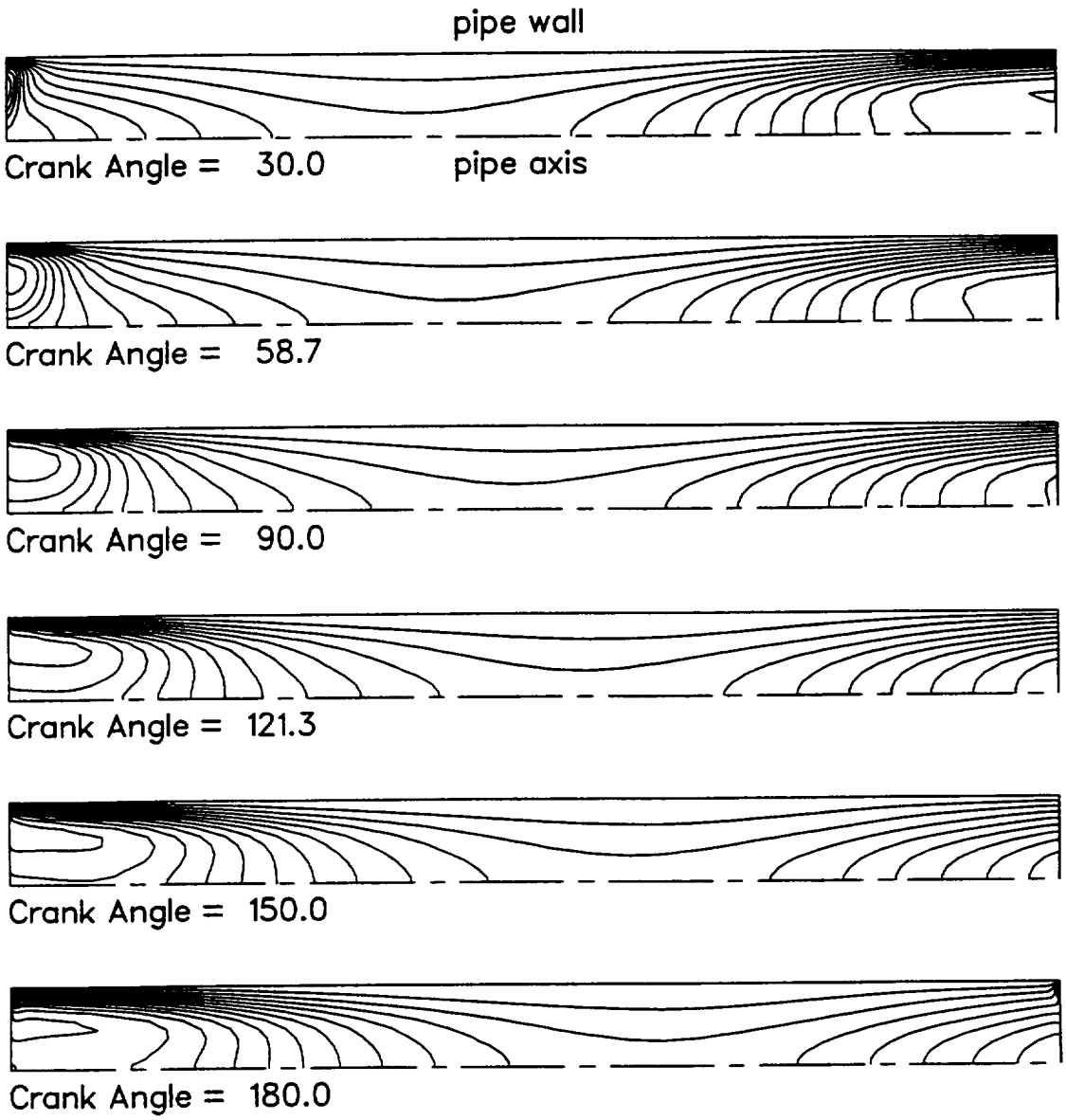

Figure 5.8: Temperature contours within pipe during first half cycle for $Va = 100$.

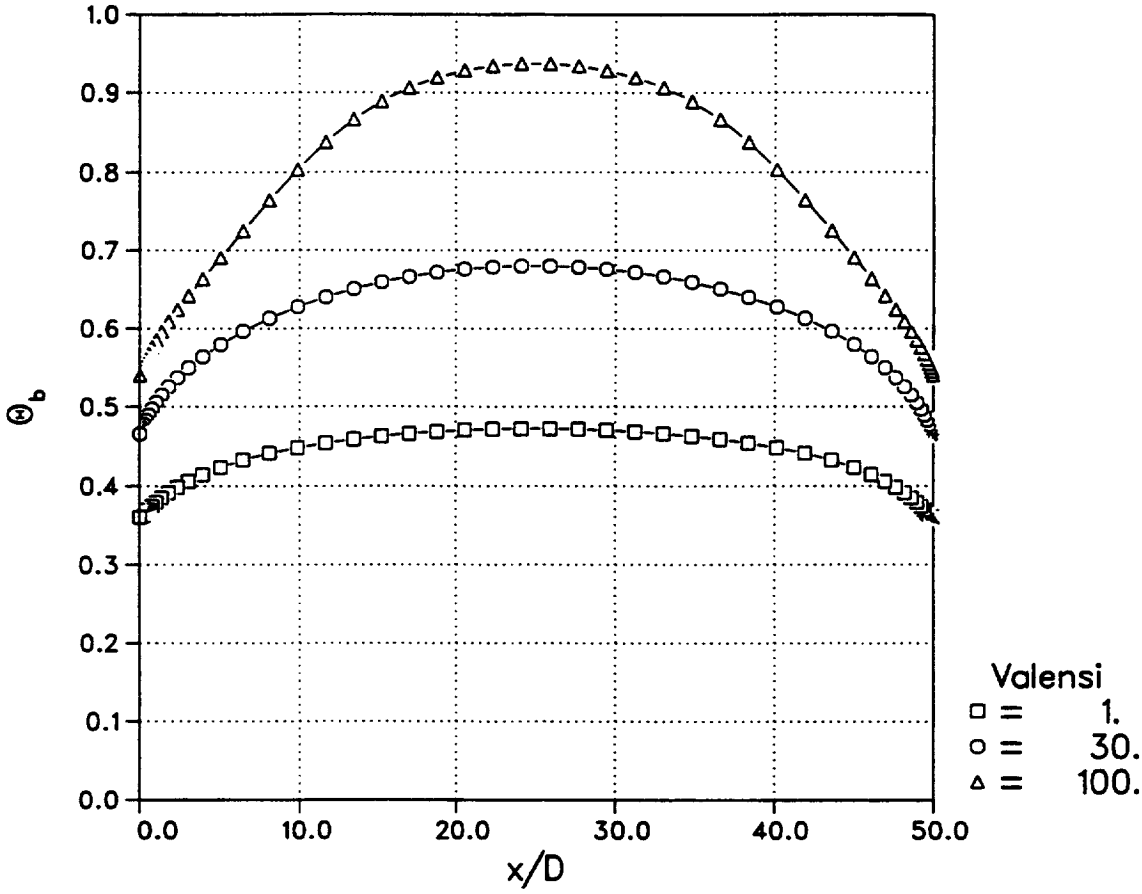

Figure 5.9: Cycle-averaged dimensionless bulk temperature for $Va = 1$, 30 and 100.

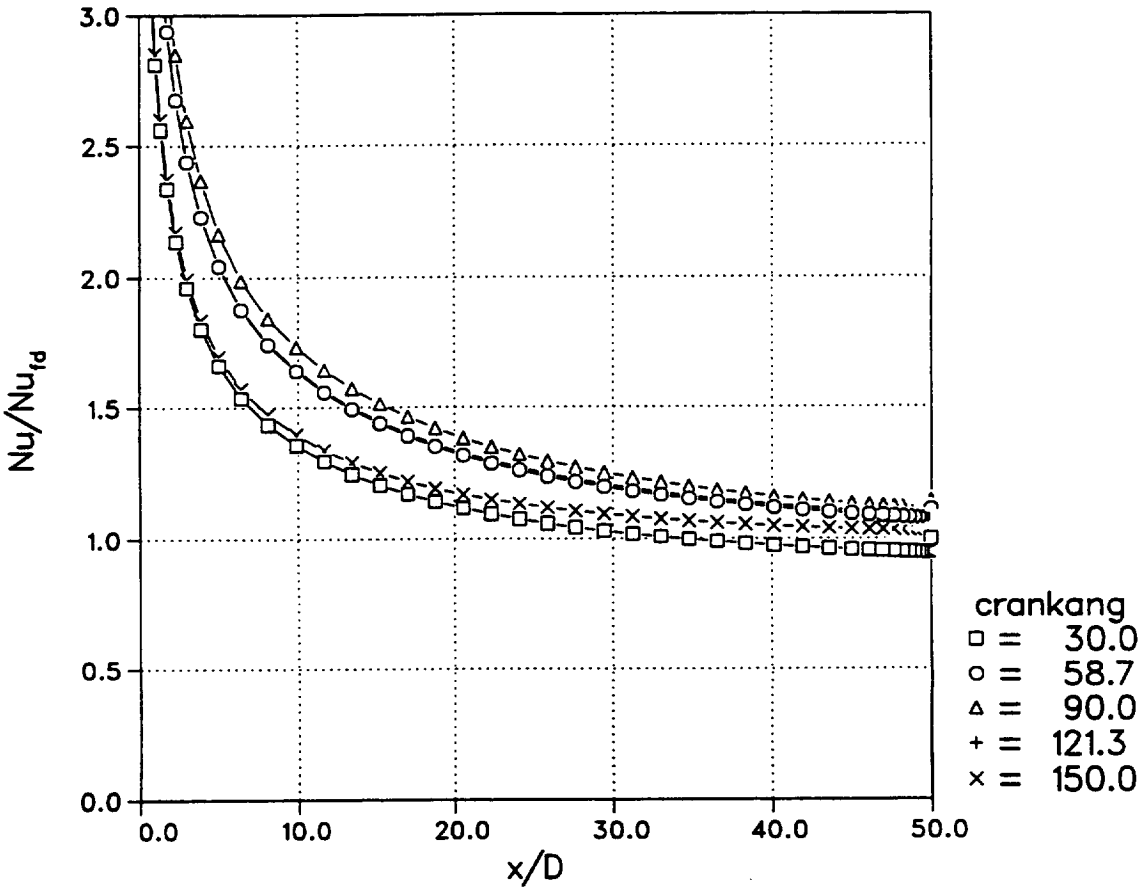

Figure 5.10: Nusselt number versus axial position during the first half cycle for Va = 1.

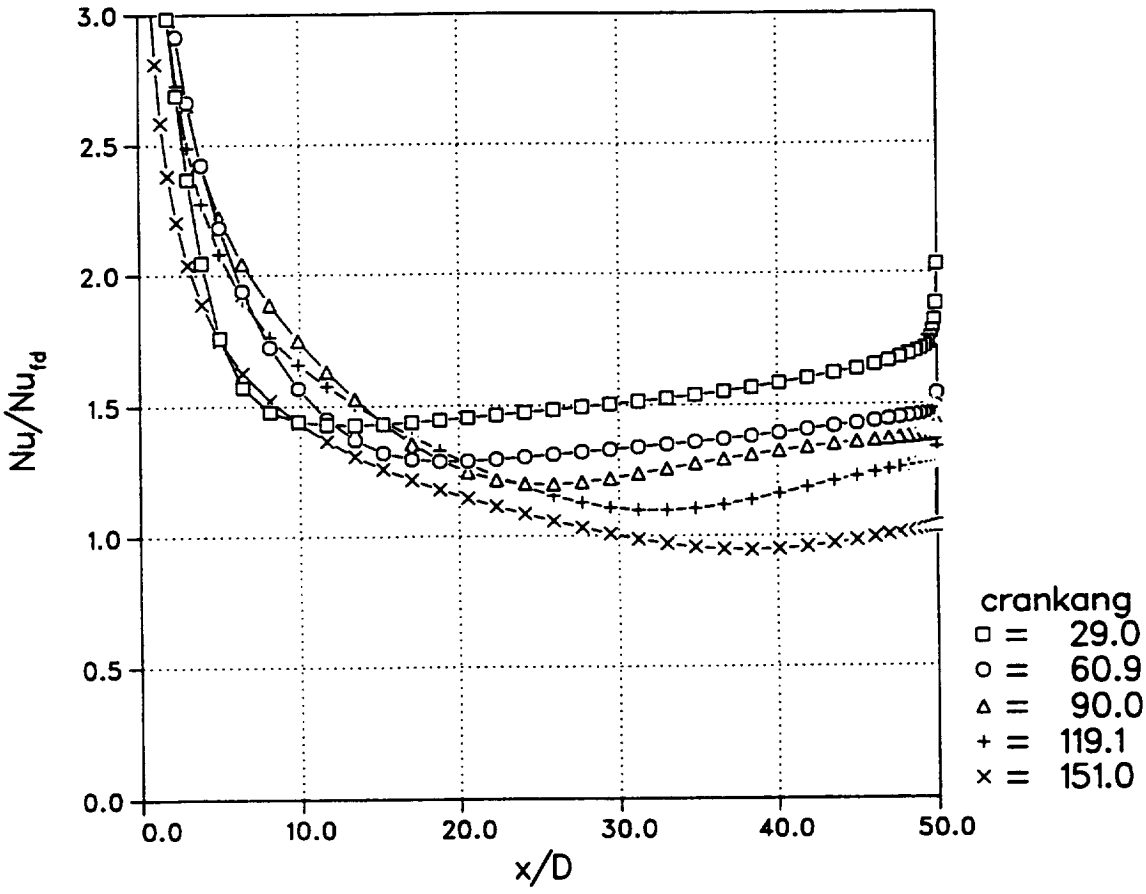

Figure 5.11: Nusselt number versus axial position during the first half cycle for Va = 30.

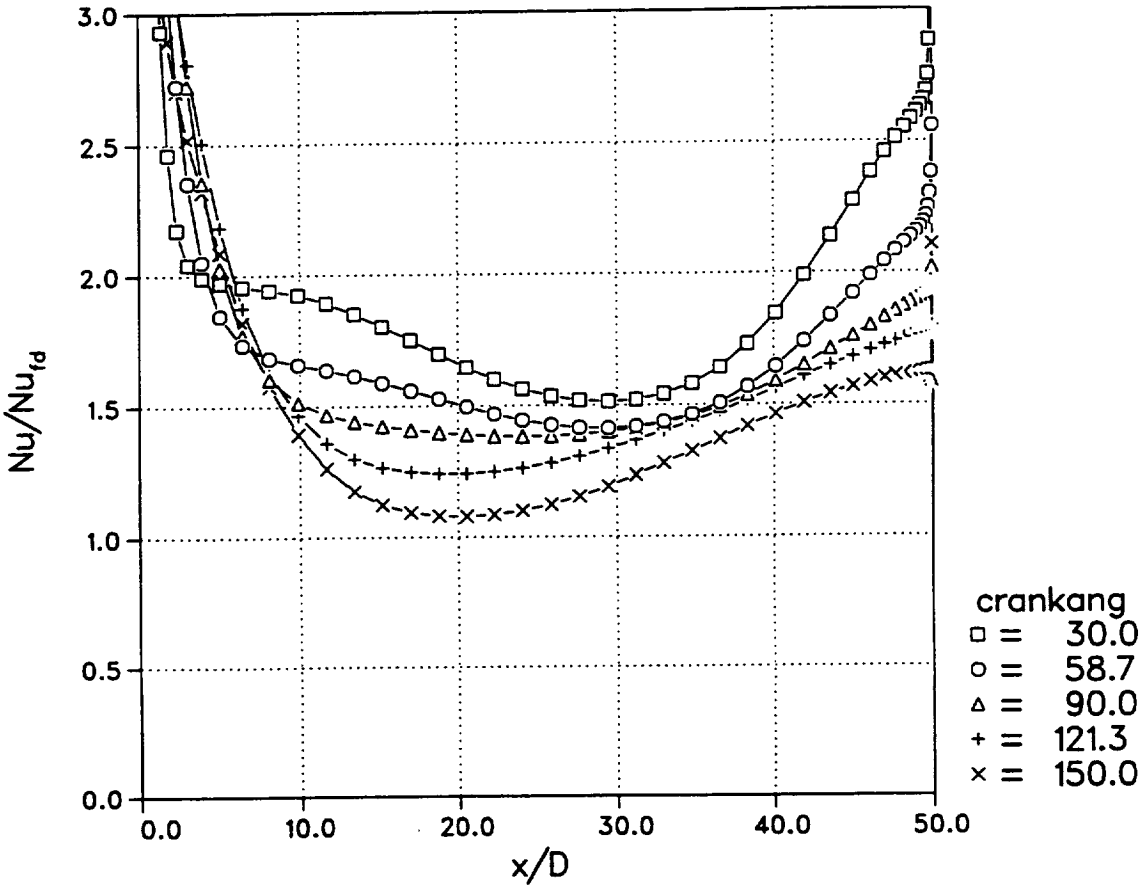

Figure 5.12: Nusselt number versus axial position during the first half cycle for Va = 100.

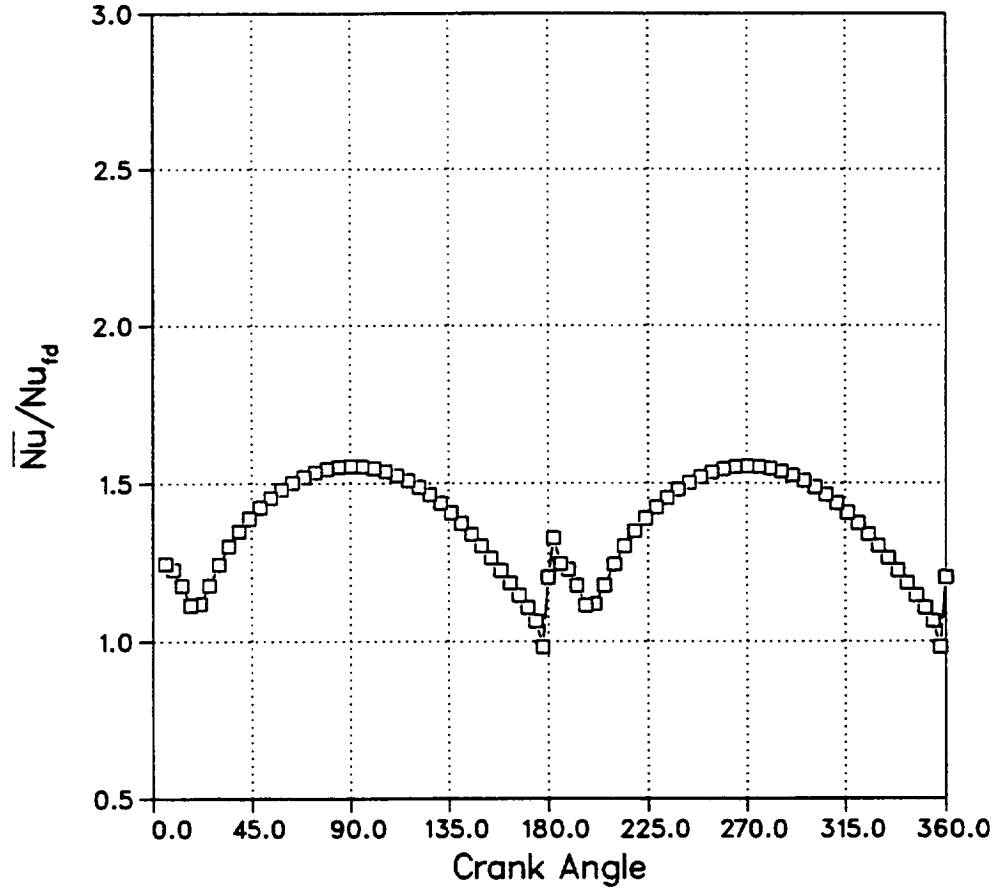

Figure 5.13: Axial-averaged Nusselt number variation during the cycle for $Va = 1$.

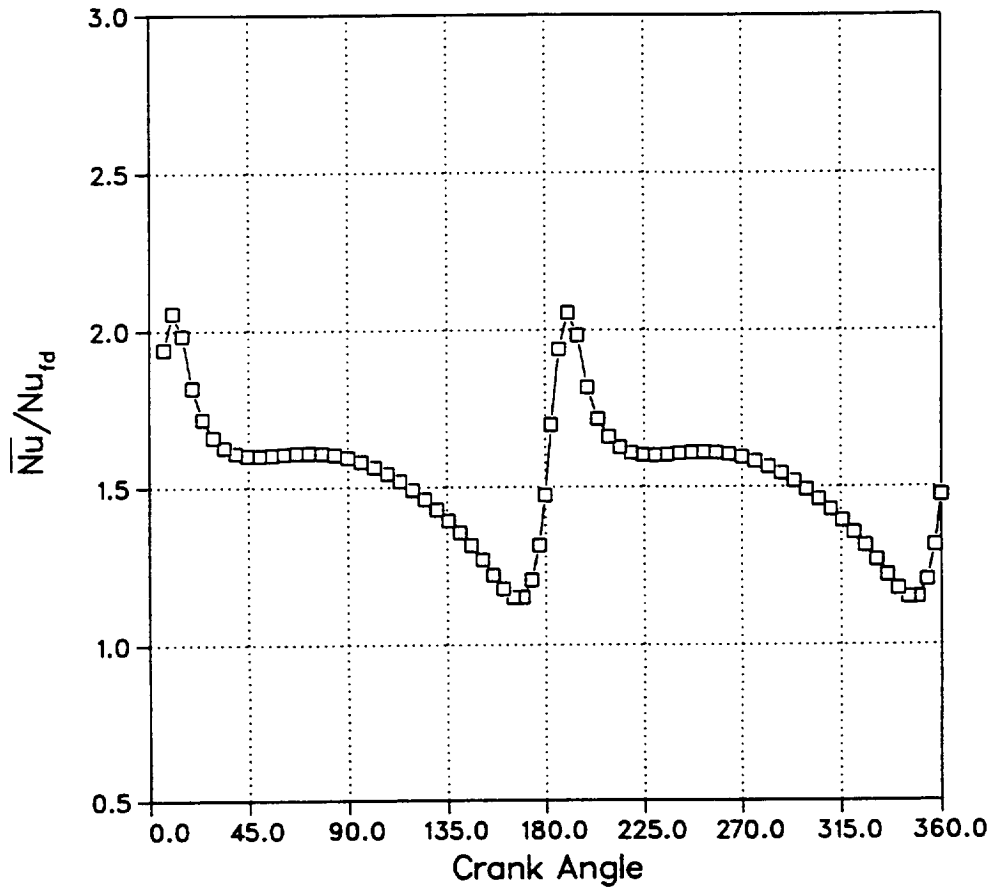

Figure 5.14: Axial-averaged Nusselt number variation during the cycle for $Va = 30$.

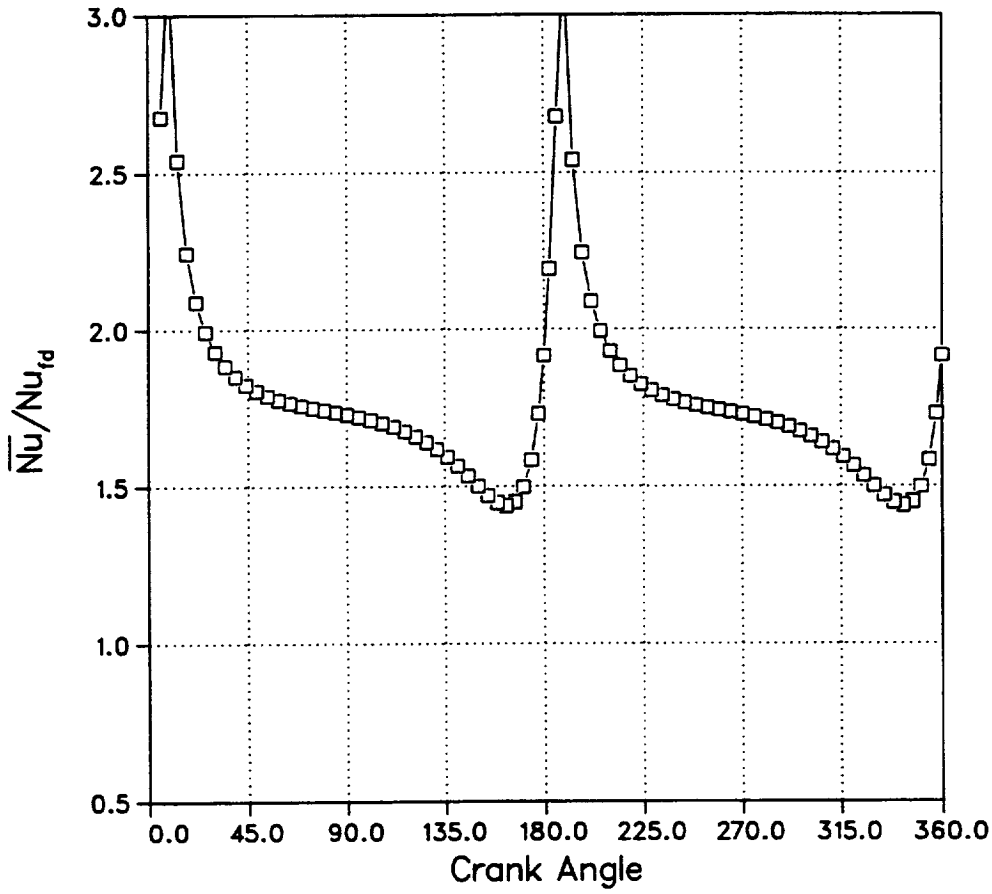

Figure 5.15: Axial-averaged Nusselt number variation during the cycle for $Va = 100$.

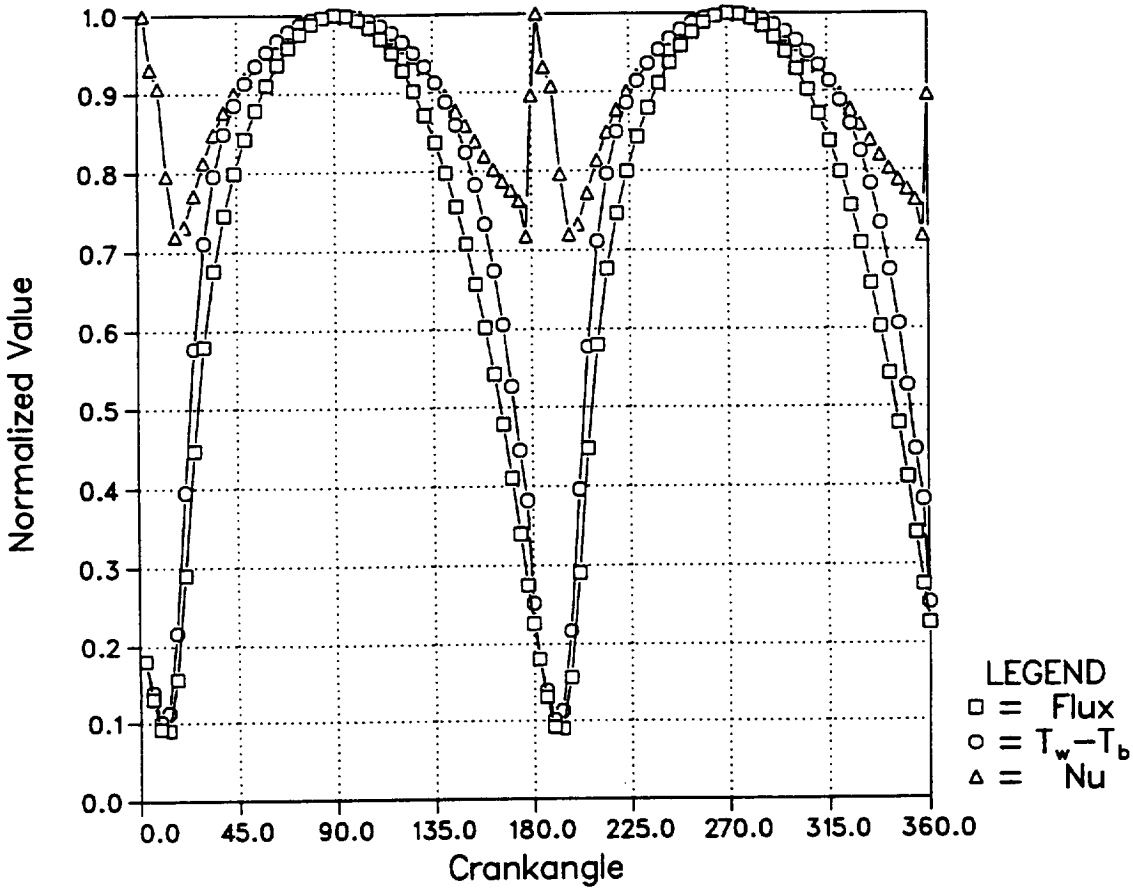

Figure 5.16: Phase comparison between heat transfer quantities at the axial middle of the pipe for $Va = 1$.

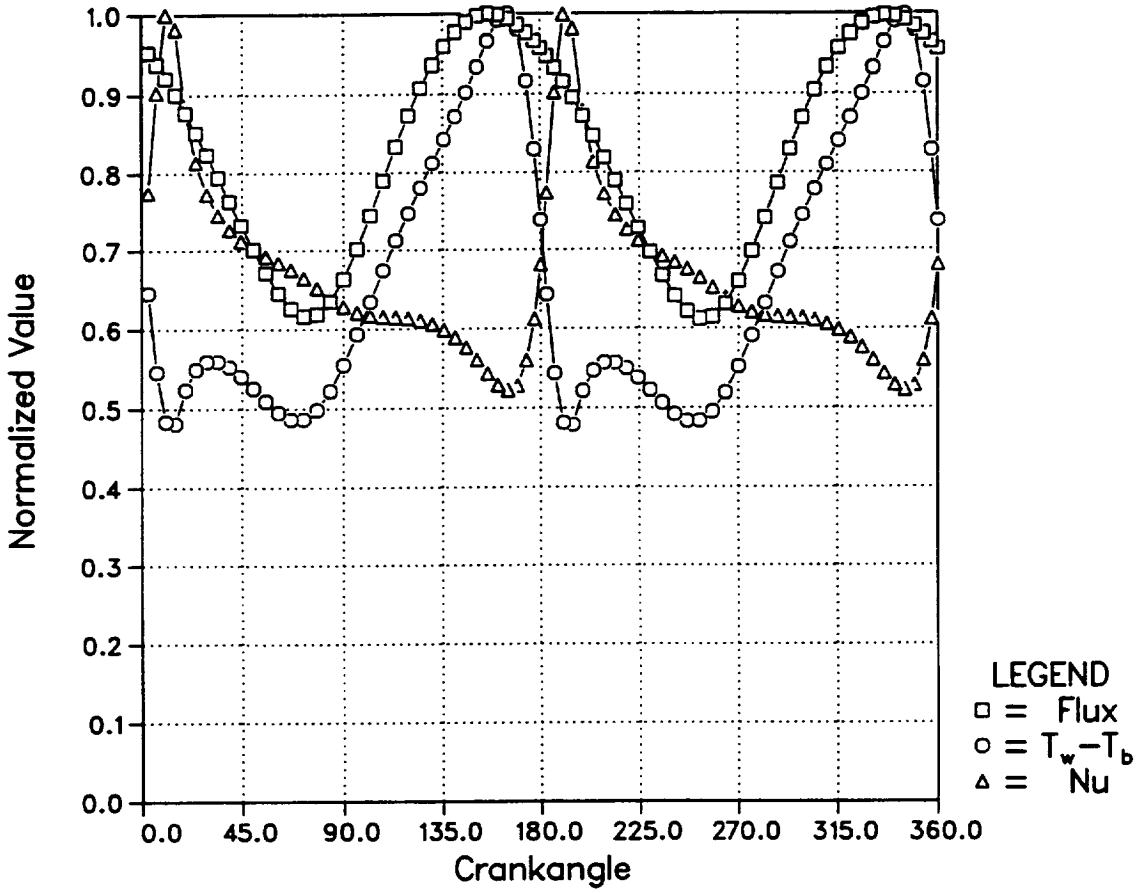

Figure 5.17: Phase comparison between heat transfer quantities at the axial middle of the pipe for $Va = 30$.

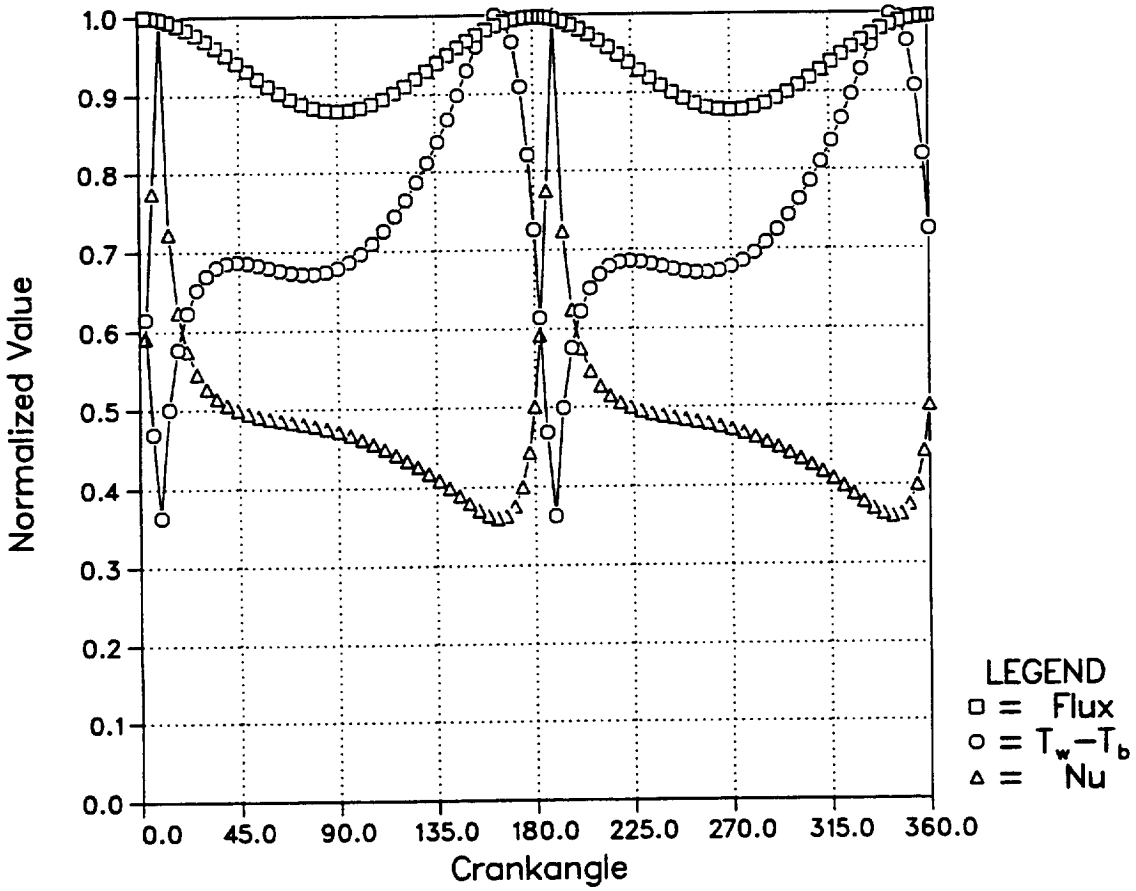

Figure 5.18: Phase comparison between heat transfer quantities at the axial middle of the pipe for $Va = 100$.

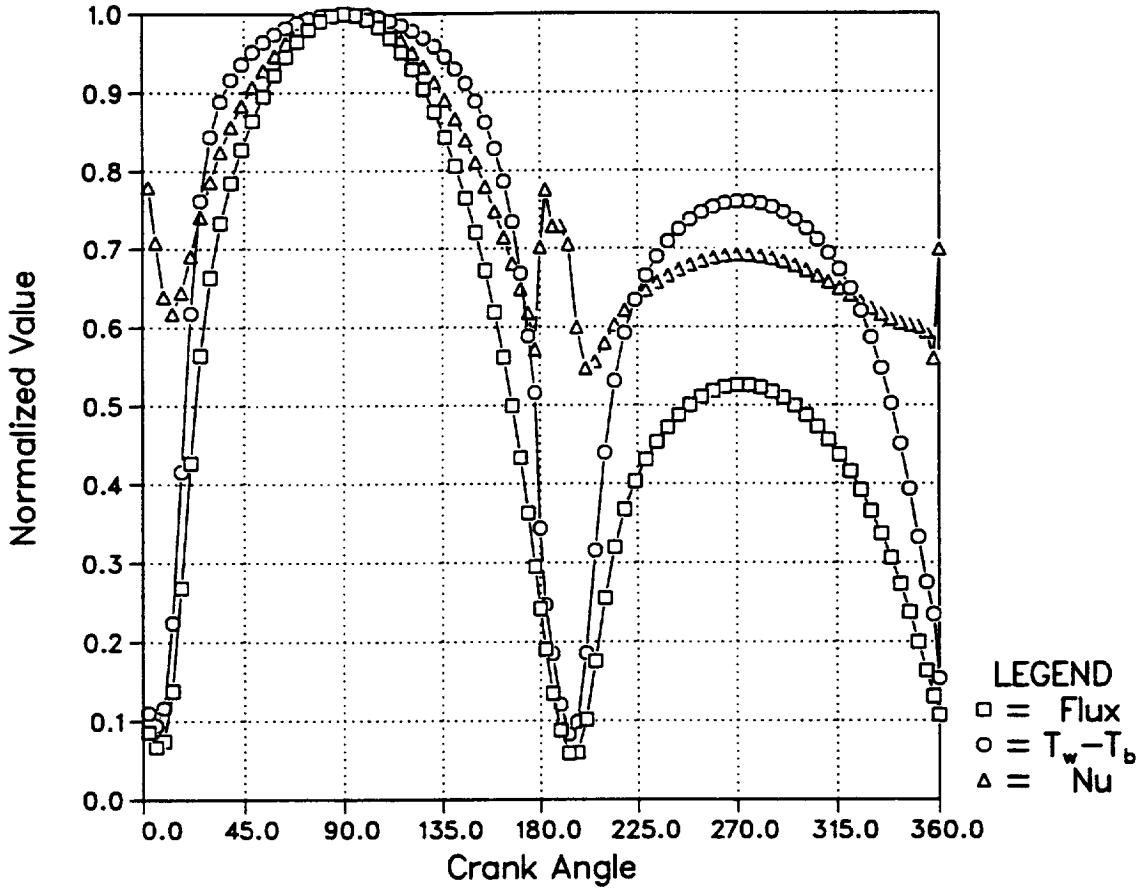

Figure 5.19: Phase comparison between heat transfer quantities at x/D = 10.4 for $Va = 1$.

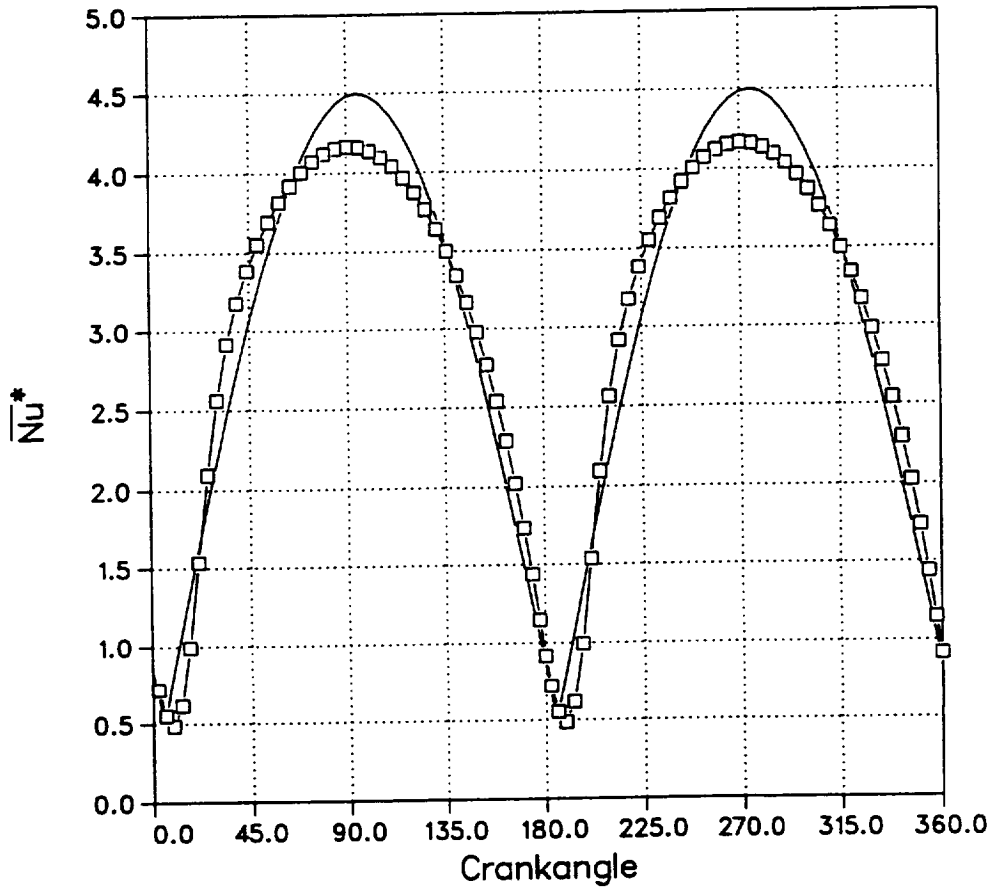

Figure 5.20: Axial-averaged Nusselt number based on T_w - T_{in} for $Va = 1$.

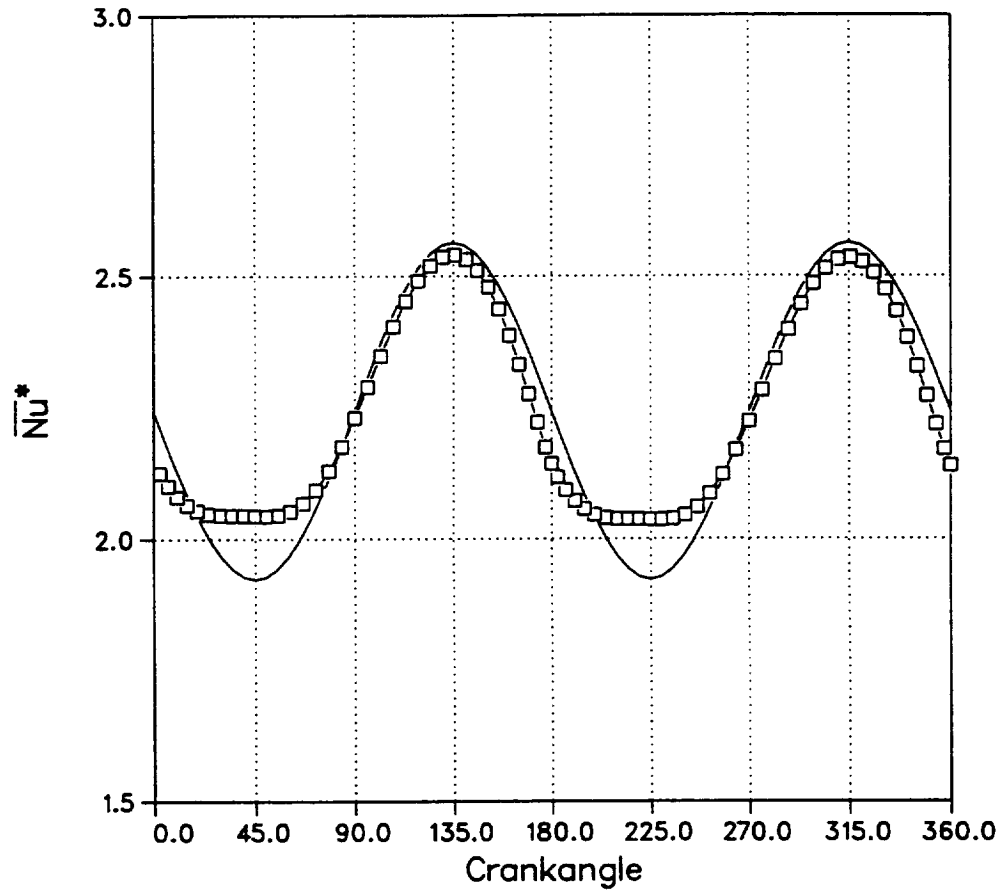

Figure 5.21: Axial-averaged Nusselt number based on T_w - T_{in} for $Va = 30$.

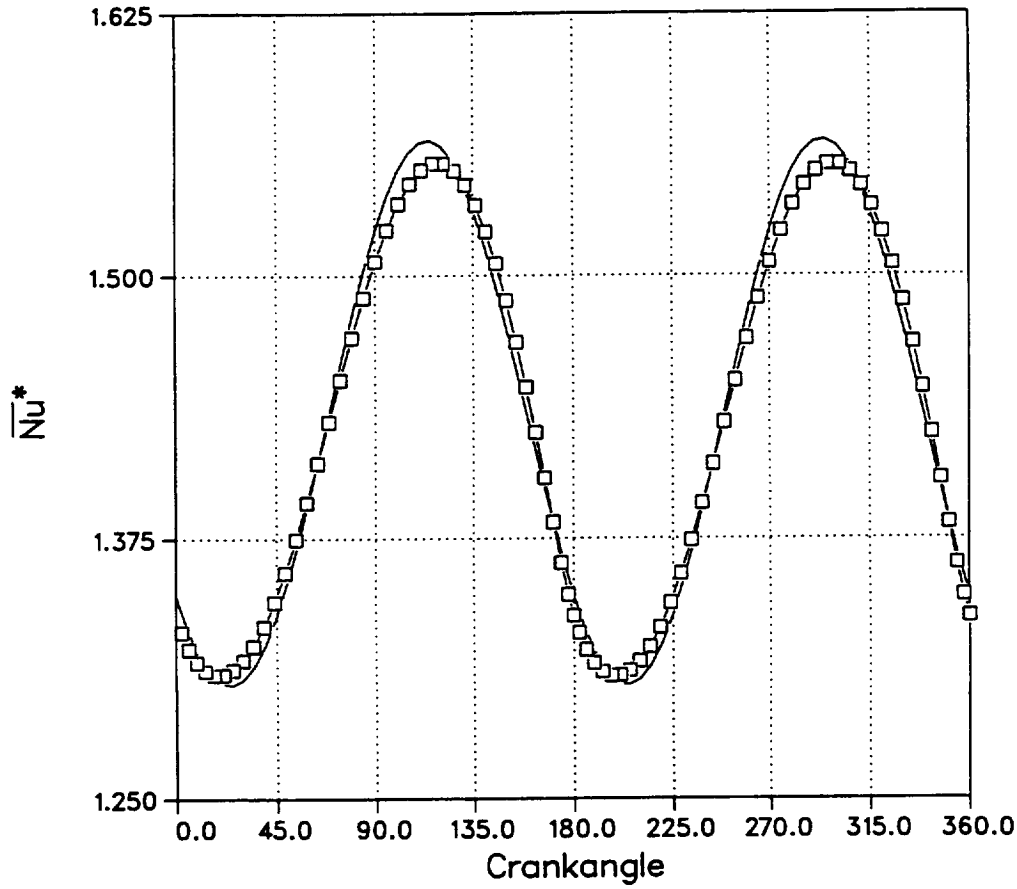

Figure 5.22: Axial-averaged Nusselt number based on T_w - T_{in} for $Va = 100$.

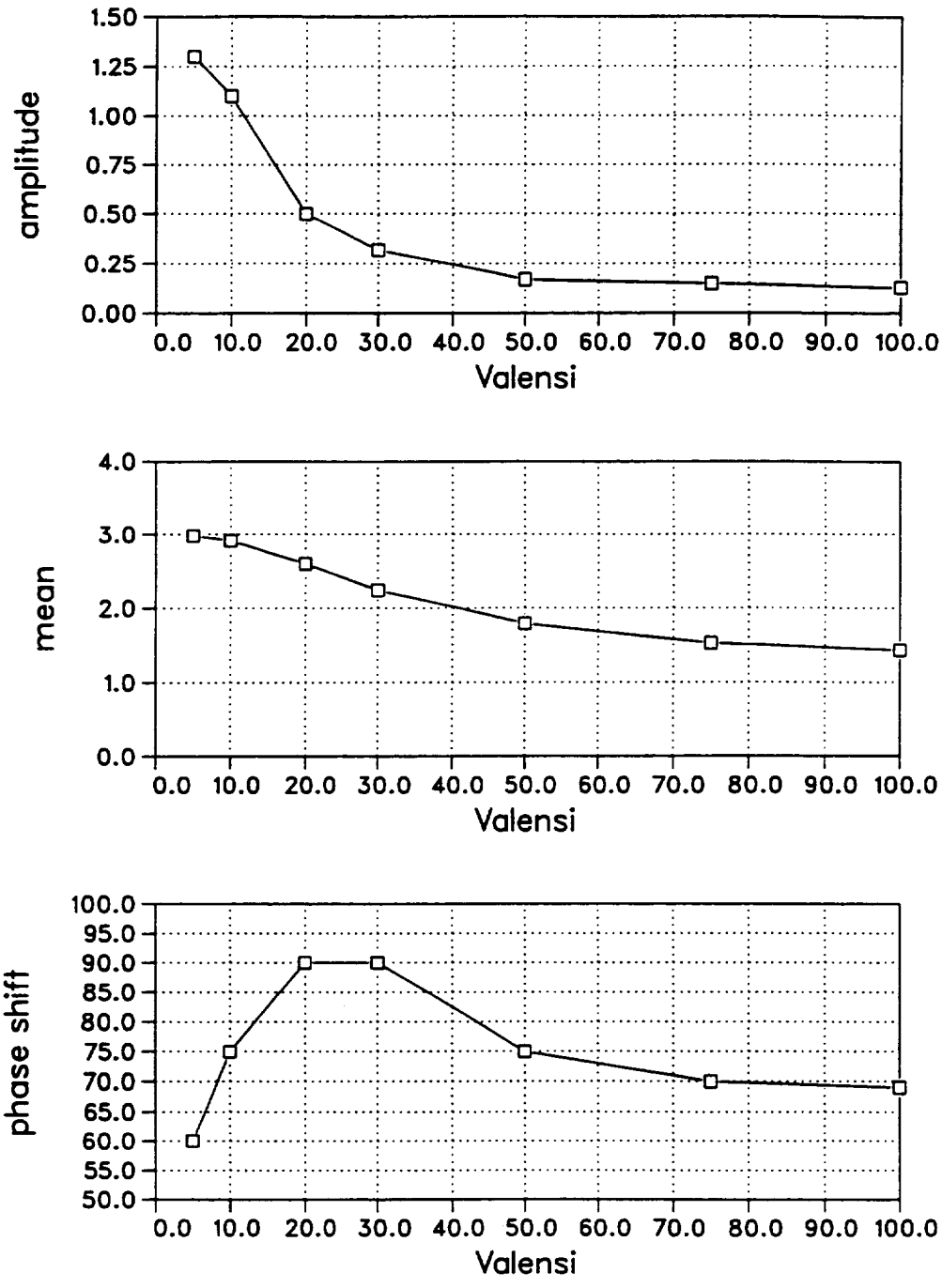

Figure 5.23: Amplitude, mean and phase shift for the laminar Nusselt number correlation as a function of Va .

Chapter 6

The Turbulent Heat Transfer Solution

In this chapter the heat transfer results for turbulent flow will be presented. The steady results will be examined in order to verify the computer program. The unsteady results will then be studied to determine the effect of flow oscillation on the heat transfer in the presence of transition, turbulence and relaminarization.

6.1 Fully Developed Turbulent Heat Transfer

The axial variation of the Nusselt number in developing turbulent flow is shown in figure 6.1 for Reynolds numbers of 10000 and 50000. The calculations are based on a pipe with $L/D = 100$ and a uniform inlet velocity profile. The inlet turbulence intensity is 5%. Grid sizes of 32 by 42 and 32 by 52 were used for $Re = 10000$ and 50000, respectively. The results are normalized against the Gnielinski correlation reported by Kakac, et al. (1987). This correlation is suitable for the ranges $2300 \leq Re \leq 5 * 10^6$ and $0.5 \leq Pr \leq 2000$, with errors on the order of 5% for modest Pr and 10% for larger Pr. The behavior of the two curves differs near the inlet of the pipe. For $Re = 10000$ Nu tends to drop below Nu_{fd} near the inlet. This is due to the specification of the turbulence kinetic energy and dissipation rate at the

inflow boundary, combined with the uniform inlet velocity profile and the modest Re. As the flow enters the pipe, the velocity gradient over the most of the pipe cross section is zero, resulting in zero turbulence generation. Turbulence is once again generated as the velocity profile develops. After a few diameters the level of Nu is within 0.7% of Nu_{fd} . This effect can also be observed when $Re = 50000$, but is barely visible in figure 6.1. The computed value of Nu for $Re = 50000$ is 4.0% high. It is not obvious whether the errors are due to the fully developed correlation or the computer model, but the differences are slight. The numerical results can be brought into agreement with the correlation by increasing the turbulent Prandtl number Pr_t, which was assigned the uniform value of 0.9 for this calculation. This level of agreement can be considered as validation of the model for steady flow heat transfer.

6.2 Heat Transfer in Turbulent Oscillating Pipe Flow

The treatment used to study the turbulent oscillating heat transfer problem is similar to that used in Chapter 5 for the laminar case, except that the Reynolds averaged energy equation (2.44) is used. A pipe is fitted with expansion and contraction end regions whose outer diameter is adiabatic. The pipe walls and the shoulders of the expansion and contraction end regions are set to a uniform hot temperature, while the inflow is set to a uniform cold temperature. The expansion and contraction regions are each 10 pipe diameters long. The L/D ratio for the model is 60. See figure 2.1. The flow and oscillation rates are given by $Re_{max} = 12000$ and $Va = 80$. These operating conditions match those of the heater section of the SPRE engine.

The dimensionless temperature profiles at the axial middle of the pipe ($x/D = 30$) at select crank angles during the first half of the flow cycle are shown in figures

6.2 through 6.5 for Va = 40, 60, 80 and 100. These figures show that the level of temperature at the axial middle of the pipe increases with Va. This is caused by the decreased convection which occurs as oscillation frequency is increased. The same effect was observed in figures 5.3 through 5.5 for laminar flow. The sequence of events that produces the temperature profiles shown in figure 6.2 can be described as follows. The fluid at the axial middle of the pipe at 30° crank angle has been in the pipe since prior to the last flow reversal and so has a fairly high temperature. The same is true at 58.7°, so the temperature rises further. By 90° crank angle fluid from outside the pipe has reached the axial middle of the pipe, causing the temperature to drop. The temperatures continue to drop until very nearly 180° crank angle, when convection is small and the temperatures within the pipe rise almost exponentially. For the given values of Re_{max}, Va and L/D, the amplitude ratio A_r for figure 6.2 is 2.5, showing that a significant amount of fluid is convected through the pipe during each half cycle. The amplitude ratio decreases in proportion as Va increases. In figure 6.3 A_r is reduced to 1.67 when Va is 60. As a result, cool fluid is only just beginning to arrive at the axial middle of the pipe by 90° crank angle. Similar conclusions can be drawn from figures 6.4 and 6.5 for Va = 80 and 100 and A_r = 1.25 and 1.0, respectively.

The temperature contours within the pipe at select times during the first half cycle are shown in figures 6.6 through 6.9 for Va = 40, 60, 80 and 100. The radial dimension of each subplot has been stretched by a factor of 10 for clarity. The top of each subplot represents the pipe wall, where heat is introduced, while the bottom represents the pipe axis. The flow is from left to right in all subplots except the last, which represents bulk flow reversal. The temperature contours during the second half of the cycle are mirror images of those shown for the first. In figure 6.6 the temperature contours show a behavior similar to that of figure 5.7 for the laminar

case. Starting with the subplot for 30° crank angle, the progression of the fluid to the right can be seen. The warmest fluid is near the left end, having spent part of the last cycle being heated inside the pipe. As the cycle continues, this fluid is swept to the right, followed by cooler fluid. The very warmest slug of fluid which is seen in the pipe at 58.7° crank angle is swept out of the pipe prior to 90° crank angle.

The temperature contours behave in a similar manner for Va = 60, 80 and 100, but the warm slug of fluid persists in the pipe for an increasing portion of the cycle. For the Va = 100 case, A_r is 1.0. The fluid near the axis moves faster than the bulk fluid, but figure 6.9 shows that the warm slug only just has time to reach the end of the pipe before flow reversal in the Va = 100 case. The results for Va = 60 and 80 are intermediate between those for Va = 40 and 100.

The cycle-averaged dimensionless bulk temperature variation along the pipe is shown in figure 6.10 for Va = 40, 60, 80 and 100. The trend with increasing Va is the same as in the laminar case, shown in figure 5.9. As Va increases and the convective effect decreases, the fluid temperature must rise in order to move heat in the axial direction by means of diffusion. Figure 6.10 gives an indication of the net effectiveness of diffusion over a complete oscillating flow cycle.

The Nusselt number along the pipe wall at select crank angles during the first half cycle is shown in figures 6.11 through 6.14 for Va = 40, 60, 80 and 100. The flow is from left to right. Each curve is normalized by the Nusselt number for fully-developed turbulent heat transfer (Nu_{fd}) at the corresponding instantaneous Reynolds number (Re). The developing temperature field near the pipe entrance creates a Nusselt number which is well above the fully-developed value. The Nusselt number then drops and levels off as the end effect diminishes. The effect of oscillation appears in the change in the level of Nu during the cycle. For crank angles

early in the cycle, the flow retains a laminar-like character, with little turbulent cross-stream transport. As a result, Nu drops below Nu_{fd}. As the flow increases, transition occurs and Nu rises. During deceleration, turbulence developed at peak flow persists and maintains a high cross-stream transport, boosting Nu above Nu_{fd}. This explanation needs further discussion for the case when $Va = 100$. In this case the rate of oscillation is sufficiently high that the flow retains some turbulent character at 30° crank angle. This turbulence is still in the process of decaying from the peak levels which occurred during the last cycle. On the other hand, transition to turbulence in the present cycle is delayed by the acceleration effect until just after 60° crank angle, giving Nu a laminar-like behavior for 58.7°. This sequence of events is also observed in the behavior of the friction coefficient, shown in figures 4.11 through 4.14.

Figures 6.15 through 6.18 show the axial-averaged Nu over one flow cycle for $Va = 40$, 60, 80 and 100. There are two cycles of heat transfer in each flow cycle since the heat transfer does not depend on the axial direction of flow. The Nusselt number is normalized against Nu_{fd} at the corresponding Re. Nu is particularly large near flow reversal due to circulation caused by the oscillating flow effect. Nu drops below Nu_{fd} early in the cycle due to the acceleration damping effect. Nu rises above Nu_{fd} later as discussed in conjunction with figures 6.11 through 6.14 above. Notice that the minimum of each curve falls lower and occurs later as Va increases, once again due to acceleration damping of turbulence.

The Nusselt numbers presented in figures 6.11 through 6.18 are based on the definition used in equation (5.5)

$$Nu = \frac{hD}{k}$$

The heat transfer coefficient is given by equation (5.6)

$$h = \frac{q}{T_w - T_b}$$

The bulk (velocity-area weighted) temperature for incompressible, constant property flow is defined by equation (5.7)

$$T_b = \frac{\int |u(r)|\, T\, r\, dr}{\int |u(r)|\, r\, dr}$$

As was seen in the laminar cases, the wall heat flux q, the temperature difference T_w - T_b and the Nusselt number Nu vary in a complicated fashion over the course of the oscillating flow cycle. Figures 6.19 through 6.22 show the phase relationship between the flux, T_w - T_b, and Nu over one flow cycle at the axial middle of the pipe for Va = 40, 60, 80 and 100. Three features in these figures will be discussed further:

1. the sudden change in behavior of T_w - T_b and Nu near flow reversal

2. the phase shift between the three curves

3. the sharp rise in flux after each flow reversal.

The behavior of T_w - T_b and Nu near flow reversal is an unsteady effect. As the bulk flow rate approaches zero near flow reversal, the convection has a diminished effect on the heat transfer problem. At flow reversal, the heat transfer is nearly reduced to a transient conduction problem, for which an exponential behavior is expected. If the flow were to remain at rest after completing a number of cycles, the value of T_w - T_b would exponentially approach zero as the fluid absorbed heat from the wall. Soon after flow reversal, the convection again becomes important, imparting a behavior which is periodic due to the prescribed bulk flow boundary condition. The value of Nu near flow reversal also reflects this unsteady effect.

The peak in the curve T_w - T_b lags the peak flux by roughly 20° to 40° as Va increases from 40 to 100. This is also an unsteady effect. As the heat flux at the wall changes, T_b cannot respond instantaneously, due to thermal inertia. The peak value of Nu, based on the ratio of flux to T_w - T_b, leads the flux by roughly 15° to 50°. Moreover, the behavior of Nu is not sinusoidal. This effect can be seen in a test case which considers the ratio of two sinusoidal functions separated by a small phase difference. Figure 6.23 shows three functions A, B, and C, given by

$$A = 2 + sin(\theta) \tag{6.1}$$

$$B = 2 + sin(\theta + \phi) \tag{6.2}$$

$$C = A/B \tag{6.3}$$

where ϕ gives the phase shift between A and B. In this test case, functions A, B and C may be considered analogues to the heat flux, T_w - T_b, and Nu, respectively, of figures 6.19 through 6.22. As shown in figure 6.23, function C leads both A and B and is not sinusoidal. The function C reaches its peak roughly 80° after each valley, with the next valley following 100° later. This phase shift effect also causes a non-sinusoidal Nu when Nu is based on a flux and temperature difference which are out of phase. The phase shift between Nu and flux can be eliminated by using T_w - T_{in} instead of T_w - T_b in the definition of Nu. This causes Nu to have the same behavior as flux since T_w - T_{in} is a constant.

The sudden rise in flux after flow reversal is due to transition to turbulence. This rise occurs from roughly 35° to 50° crank angle after flow reversal for Va ranging from 40 to 100. Figure 6.24 shows the turbulent kinetic energy profiles for select crank angles at the axial middle of the pipe when $Va = 80$. The turbulent kinetic energy rises sharply near the wall at about 45°, demonstrating that the rise in flux

near that crank angle is due to transition. The same transition also occurs at 225° in the second half of the flow cycle for $Va = 80$.

As was seen in the laminar case in chapter 5, the temporal and spatial variation of Nu seen in figures 6.11 through 6.22 is far too complicated to reduce to a function of axial position and time as

$$Nu = Nu(x,t)$$

Once again an alternate definition of Nu will be used along with axial averaging in order to produce a more tractable expression for the oscillating heat transfer. The pipe inlet temperature T_{in} will be used in place of T_b in the temperature difference, relieving the engine modeler of the need to specify the complicated variation of the bulk temperature. The inlet and outlet fluid temperatures will be available from the performance code to be used (iteratively) as an input to the heat transfer calculation. The end effects can be accounted for implicitly by the use of axial averaging. The resulting correlation for Nu will be restricted to a given L/D ratio but will still be a function of time. This is acceptable for the purpose of building a Stirling engine performance code once the heat exchanger tube has been selected. (Cost, weight, configuration and space constraints may be just as important as the heat transfer performance.) When the redefined Nusselt number is averaged over the length of the pipe ($\overline{Nu^*}$) we find the behavior shown in figures 6.25 through 6.28.

Figure 6.25 shows the predicted variation of $\overline{Nu^*}$ over one flow cycle for $Va = 40$. The prediction is shown in square symbols. A curve fit is also plotted using the equation

$$\overline{Nu^*} = 10.0 * sin\,(2 * (crank\ angle - 68°)) + 14.93 \qquad (6.4)$$

Both the numerical prediction and the curve fit have a cycle-averaged $\overline{Nu^*}$ of 14.93.

The curve fit was established by adjusting the amplitude, phase shift and vertical offset to produce the same cycle-averaged value and the best qualitative agreement with the computed curve.

Figure 6.26 shows the variation of $\overline{Nu^*}$ over one flow cycle for $Va = 60$. For this case the following sinusoidal curve fit was selected

$$\overline{Nu^*} = 7.5 * sin\,(2 * (crank\ angle - 78°)) + 12.58 \tag{6.5}$$

The cycle-averaged value is 12.58.

Figure 6.27 shows the variation of $\overline{Nu^*}$ over one flow cycle for $Va = 80$. The curve fit is given by

$$\overline{Nu^*} = 5.5 * sin\,(2 * (crank\ angle - 88°)) + 9.72 \tag{6.6}$$

The cycle-averaged value is 9.72.

Figure 6.28 shows the variation of $\overline{Nu^*}$ over one flow cycle for $Va = 100$. The curve fit is given by

$$\overline{Nu^*} = 4.1 * sin\,(2 * (crank\ angle - 85°)) + 8.17 \tag{6.7}$$

The cycle-averaged value is 8.17.

Figures 6.25 through 6.28 show that, unlike the more conventional Nusselt number defined by equations (5.5) through (5.7), $\overline{Nu^*}$ decreases with increasing Va. This clearly illustrates the reduced effectiveness of axial convective transport as the oscillation rate increases. At very high rates of oscillation the axial transport is primarily due to diffusion which has been enhanced through interaction with the oscillating flow field. The axial heat flux under these conditions may be substantially larger than in the case of pure conduction, but will nevertheless be smaller than if steady pipe flow were allowed to occur.

The variation of the amplitude, mean and phase shift (relative to the bulk flow) of $\overline{Nu}^*$ with Va is shown in figure 6.29. This figure may be used as a means of interpolating the turbulent $\overline{Nu}^*$ correlation (equations (6.4) through (6.7)) for oscillation rates in the range $40 \leq Va \leq 100$.

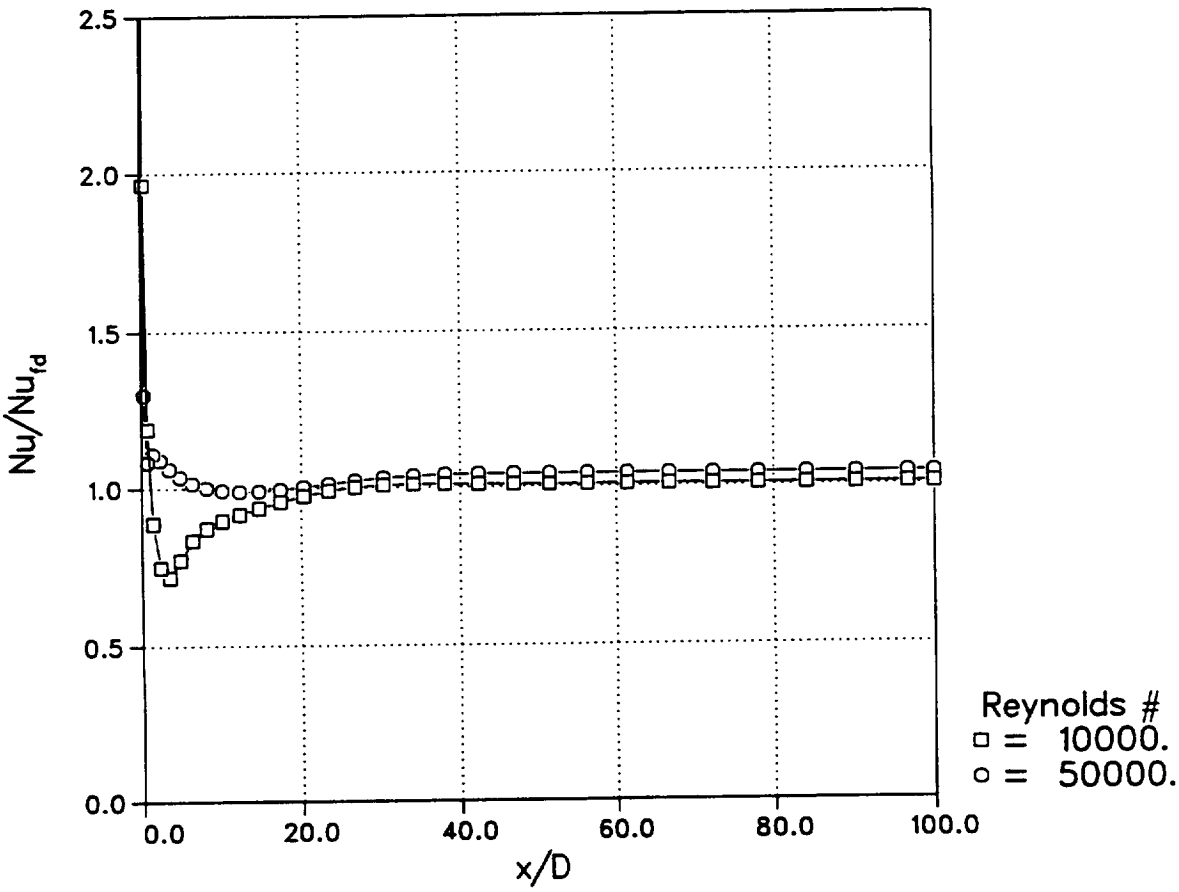

Figure 6.1: Nusselt number in developing turbulent flow.

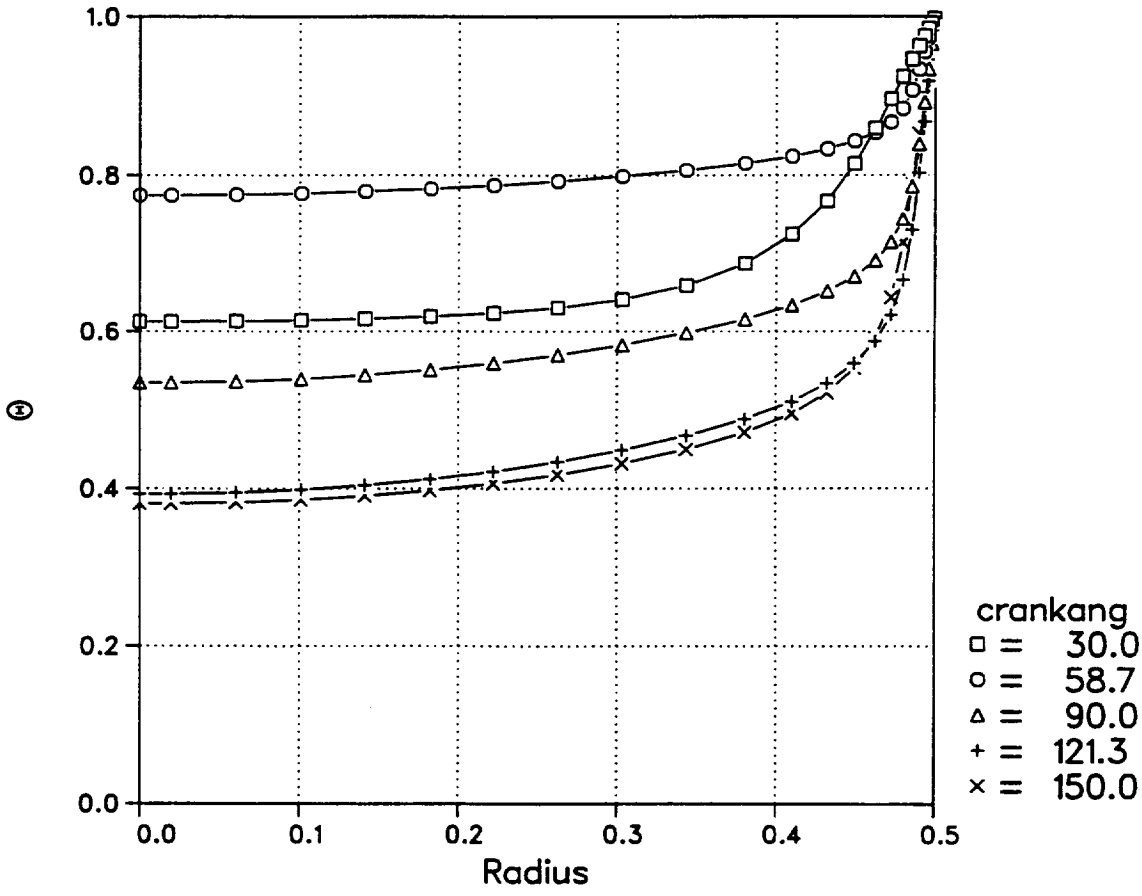

Figure 6.2: Temperature profiles at the axial middle of the pipe for $Va = 40$.

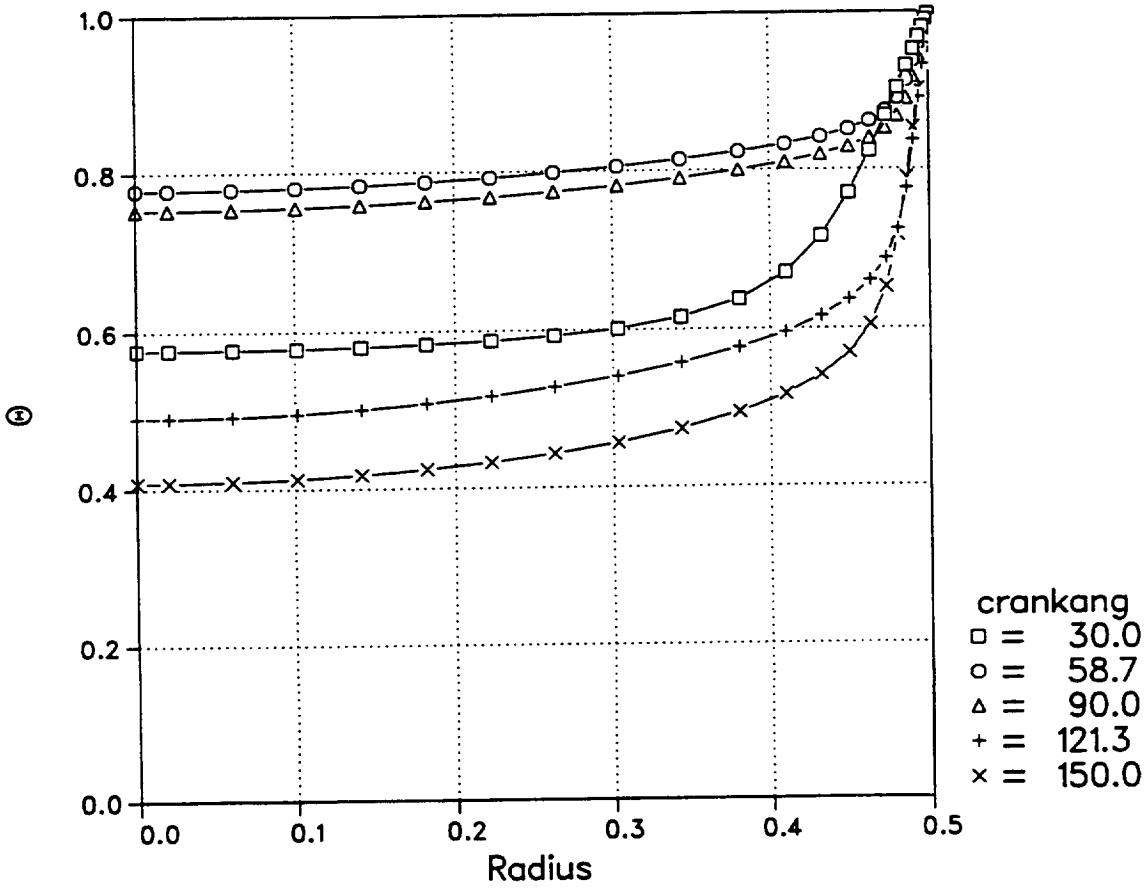

Figure 6.3: Temperature profiles at the axial middle of the pipe for $Va = 60$.

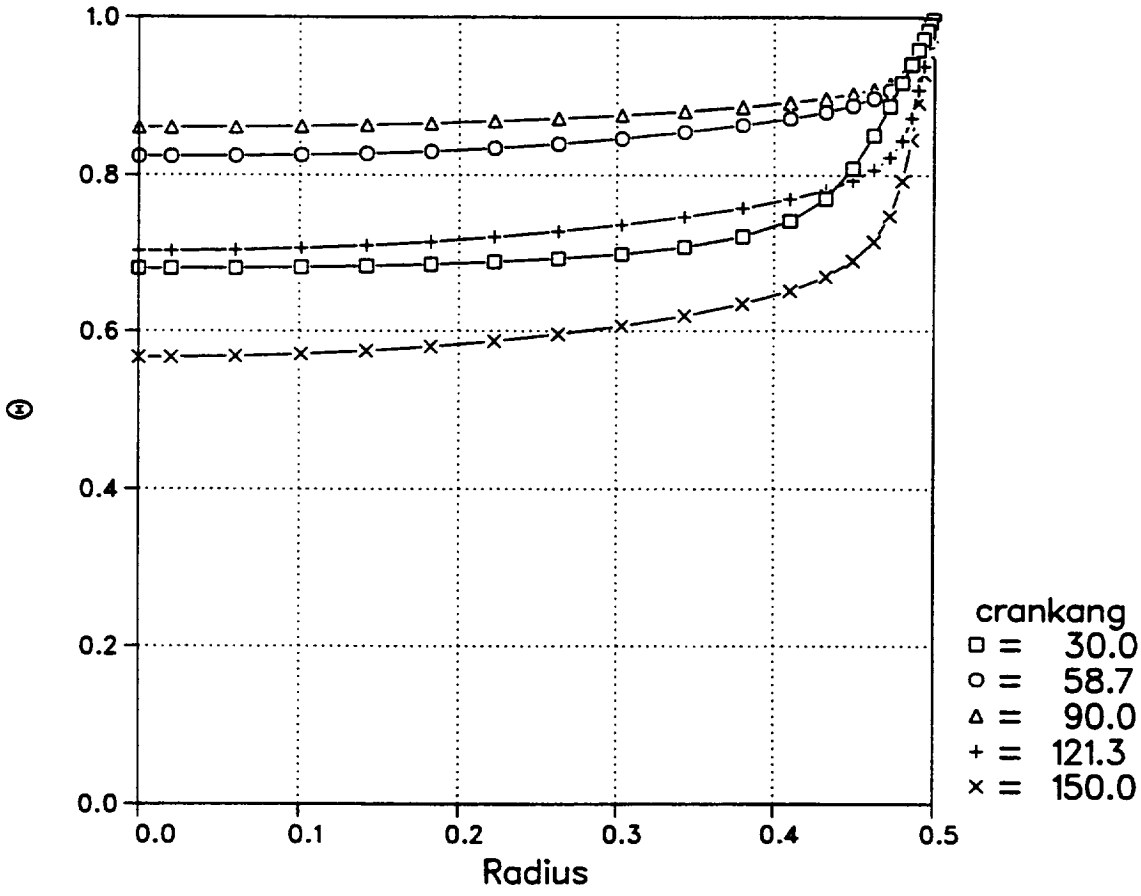

Figure 6.4: Temperature profiles at the axial middle of the pipe for $Va = 80$.

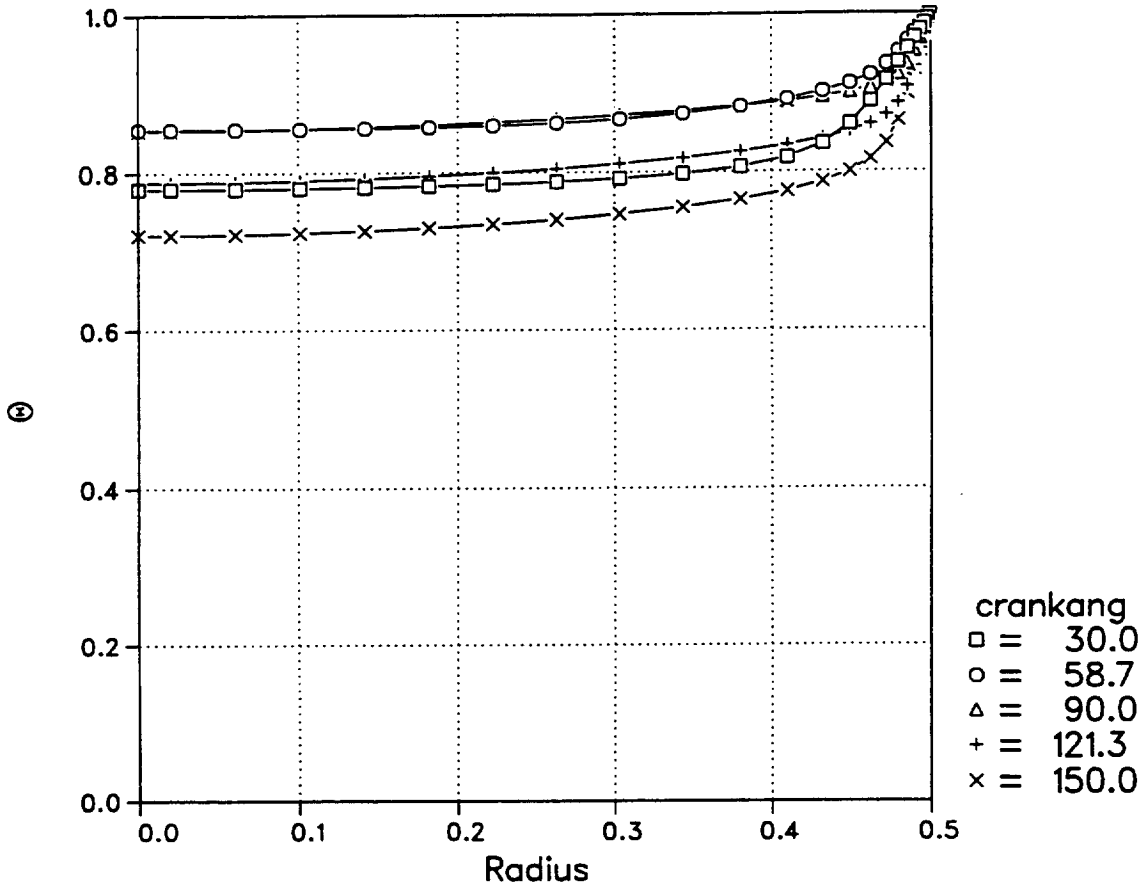

Figure 6.5: Temperature profiles at the axial middle of the pipe for $Va = 100$.

C-3.

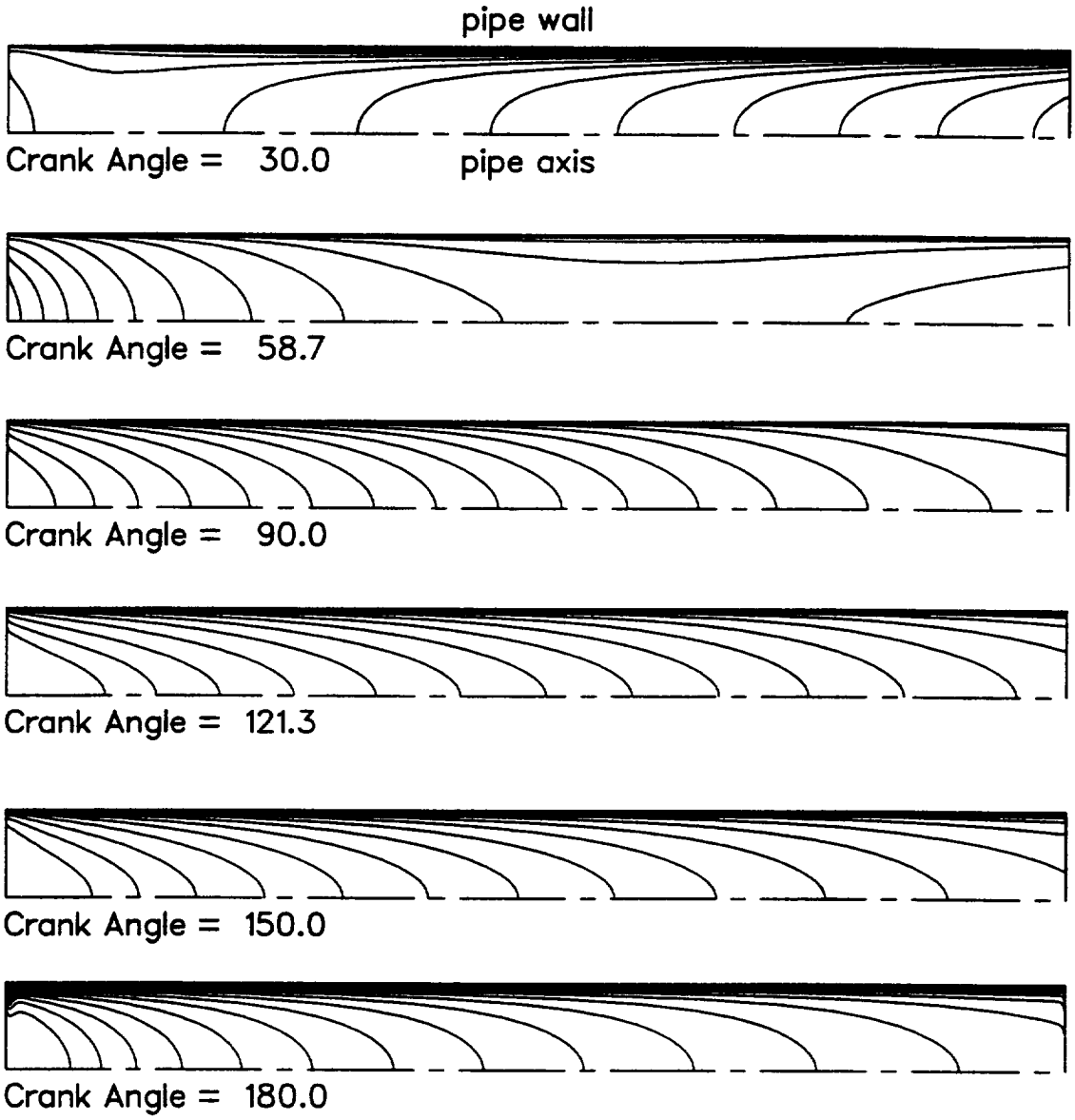

Figure 6.6: Temperature contours within pipe during first half cycle for $Va = 40$.

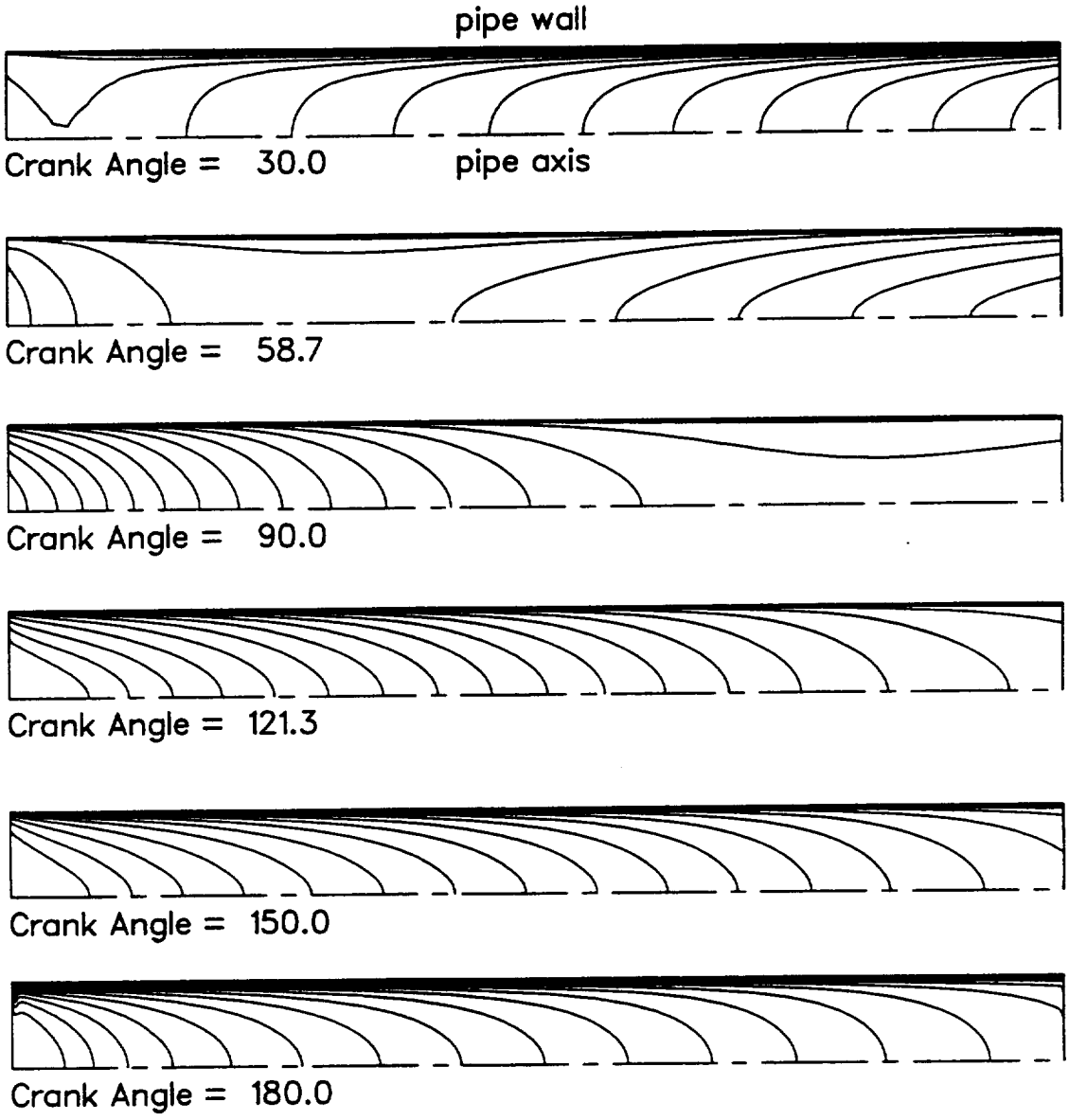

Figure 6.7: Temperature contours within pipe during first half cycle for $Va = 60$.

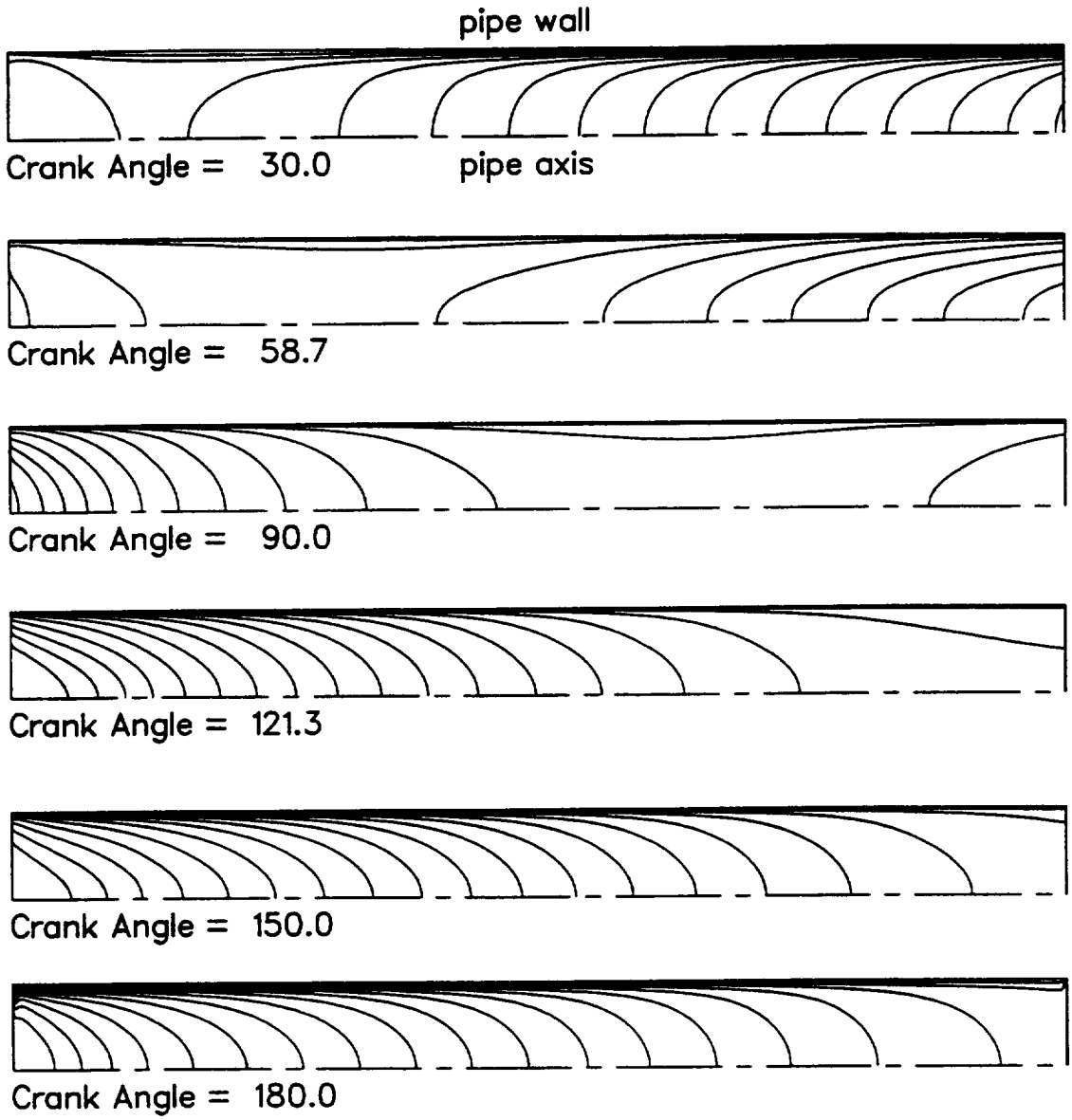

Figure 6.8: Temperature contours within pipe during first half cycle for $Va = 80$.

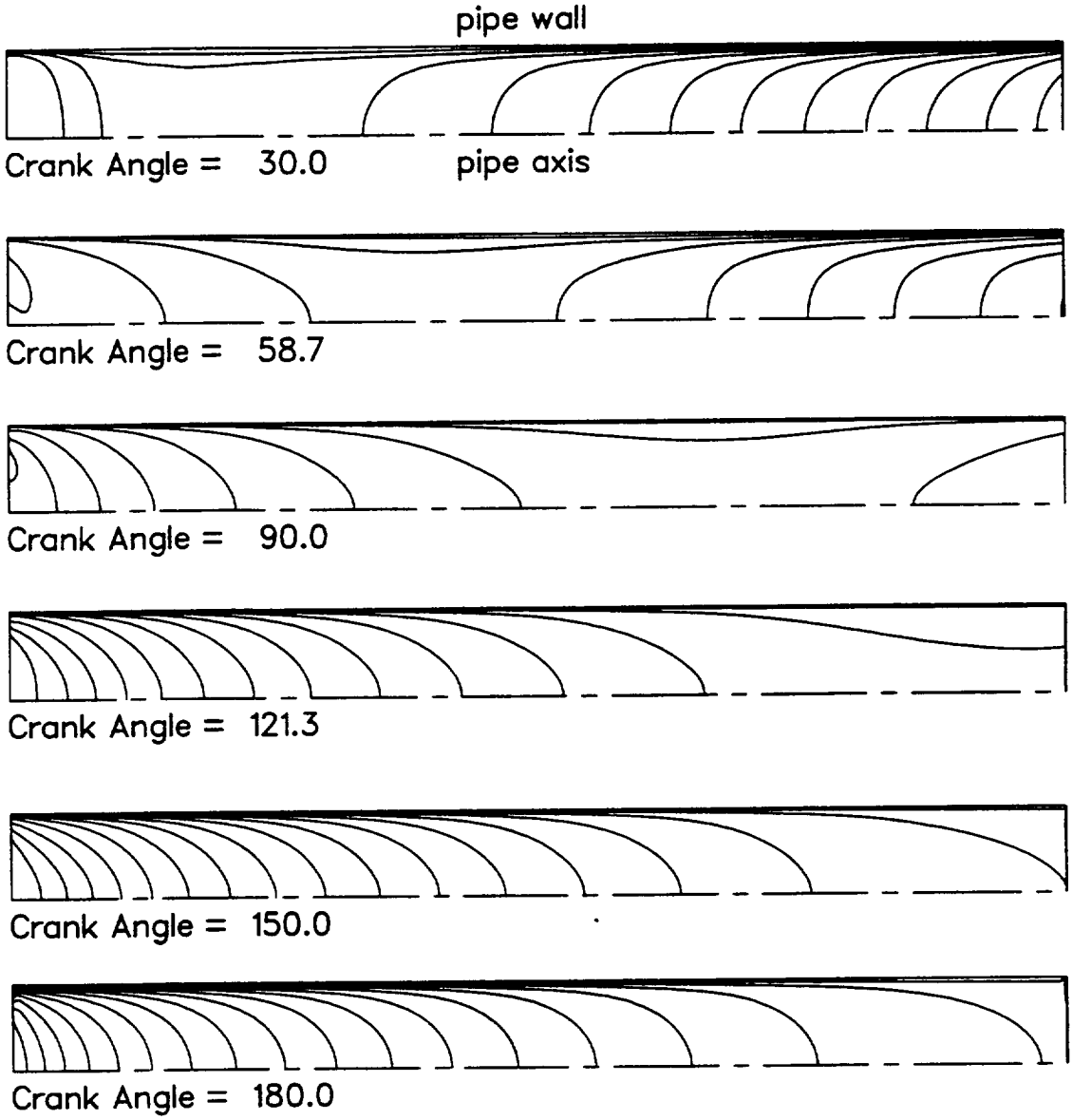

Figure 6.9: Temperature contours within pipe during first half cycle for $Va = 100$.

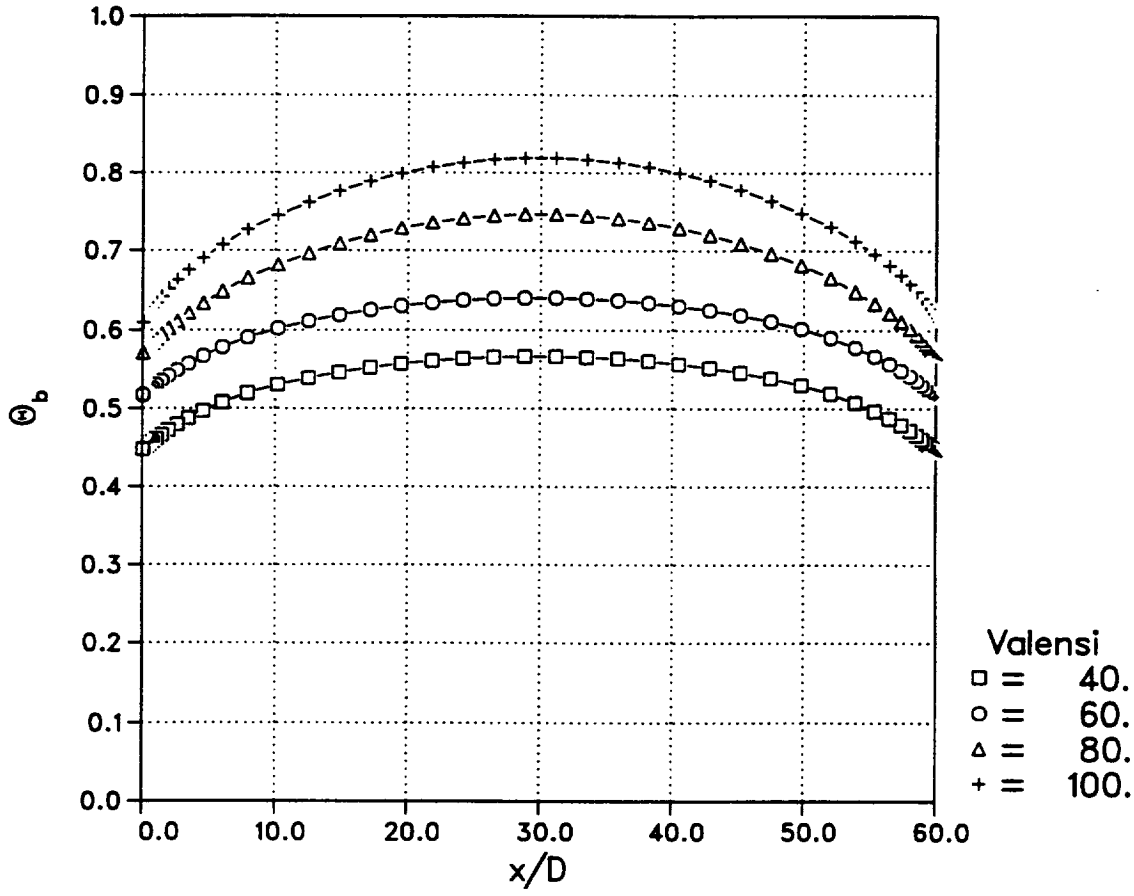

Figure 6.10: Cycle-averaged dimensionless bulk temperature for Va = 40, 60, 80 and 100.

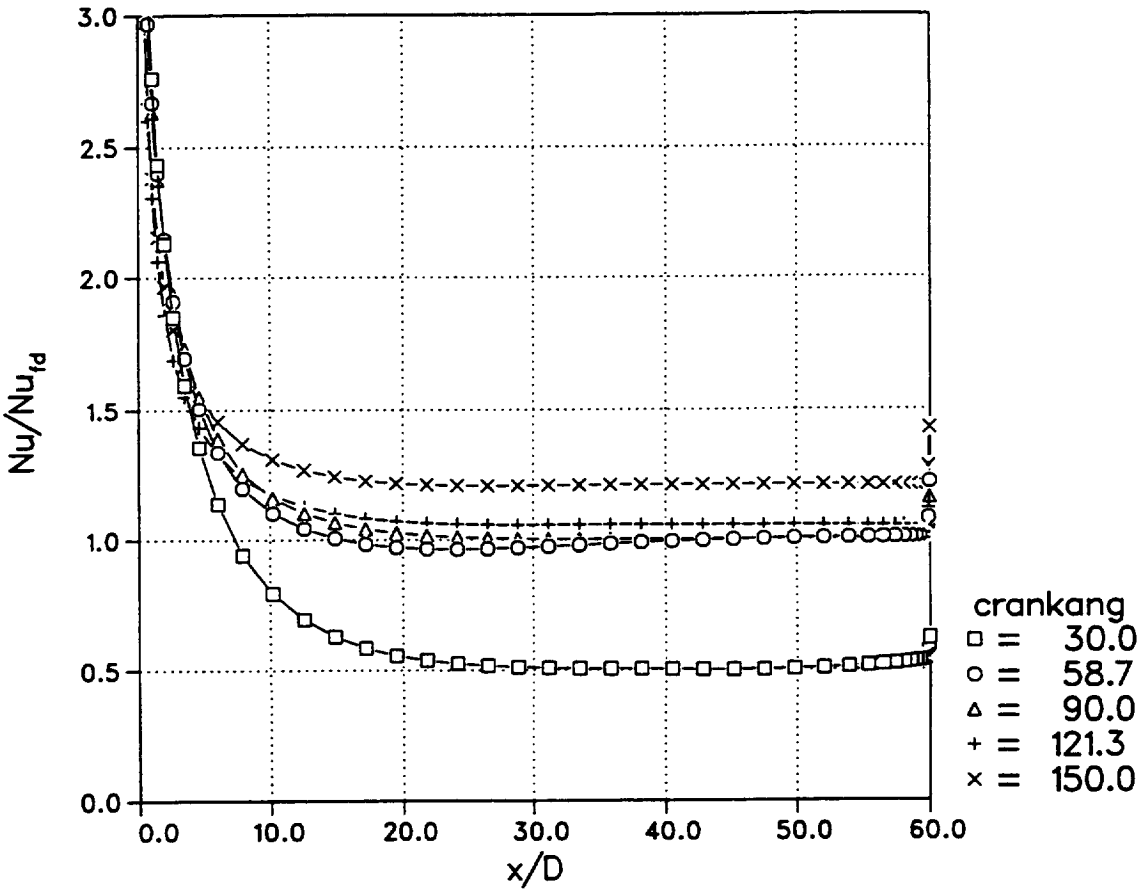

Figure 6.11: Nusselt number versus axial position during the first half cycle for $Va = 40$.

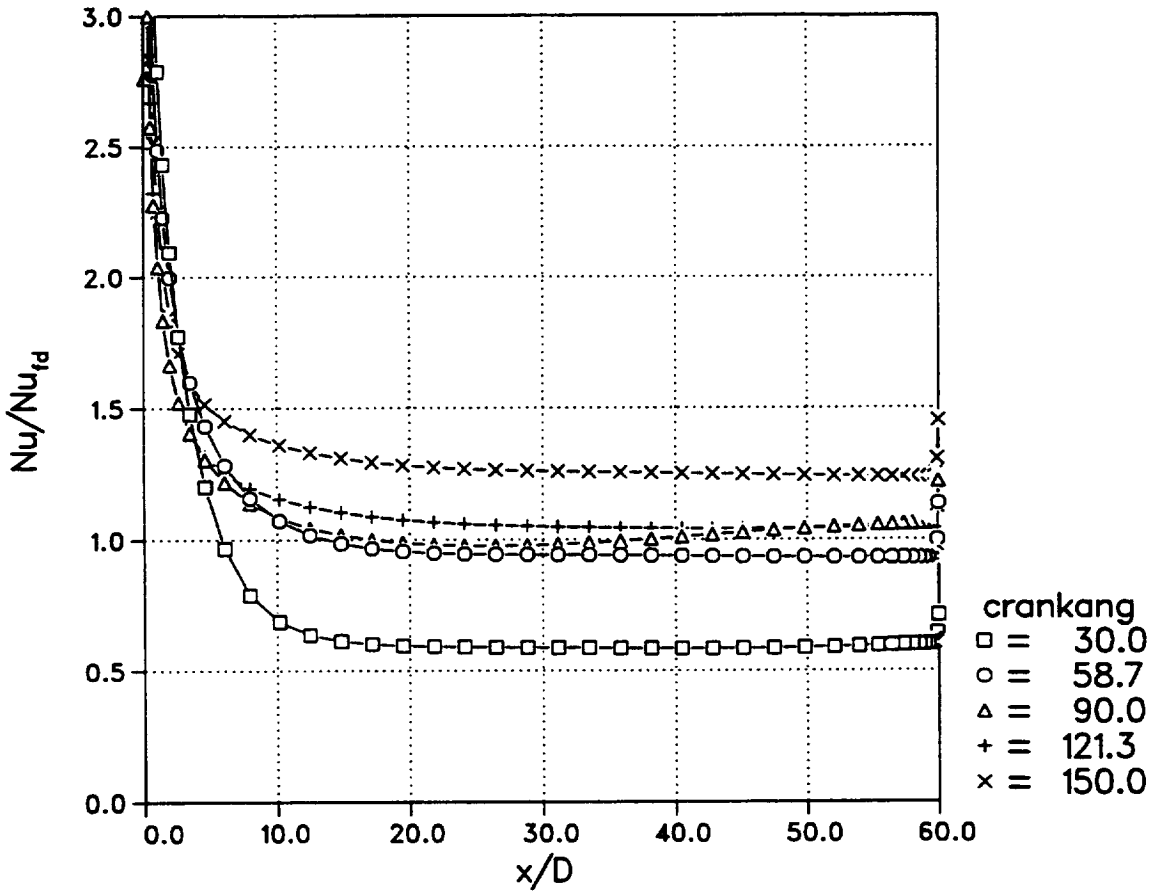

Figure 6.12: Nusselt number versus axial position during the first half cycle for Va = 60.

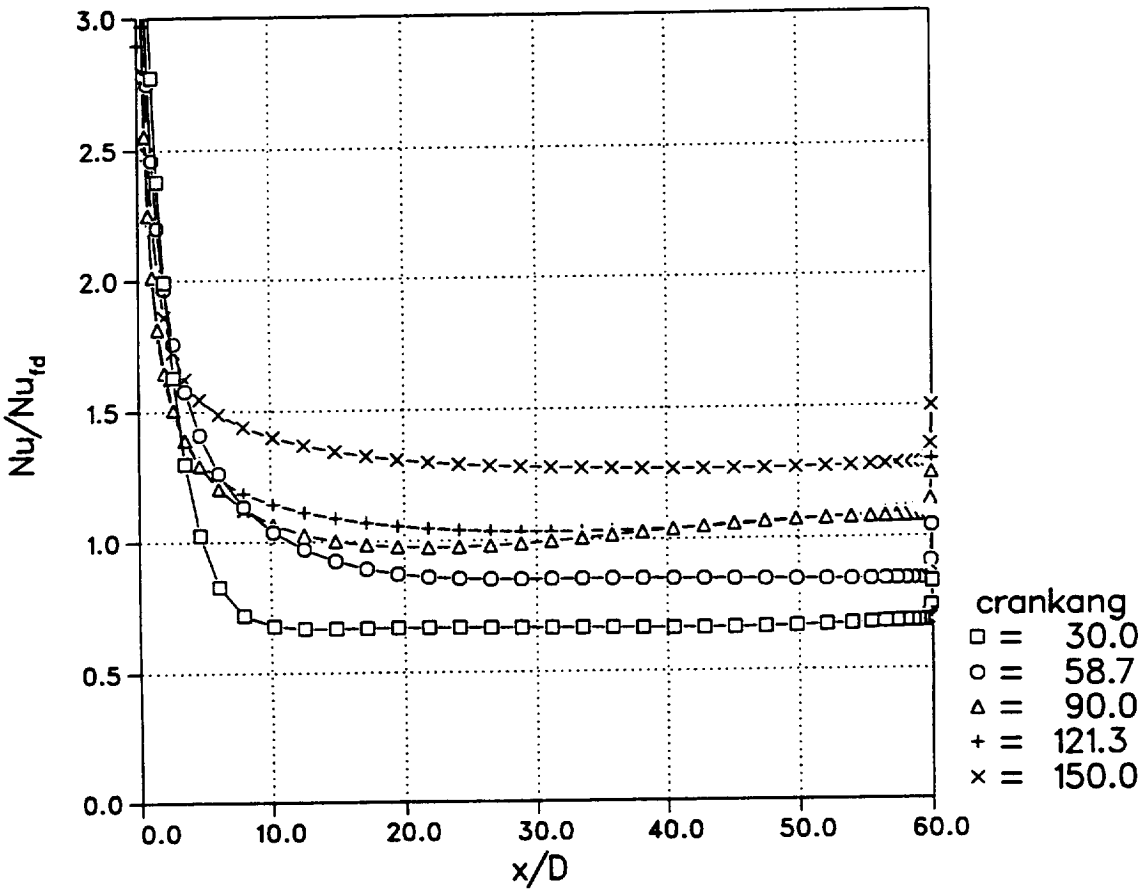

Figure 6.13: Nusselt number versus axial position during the first half cycle for Va = 80.

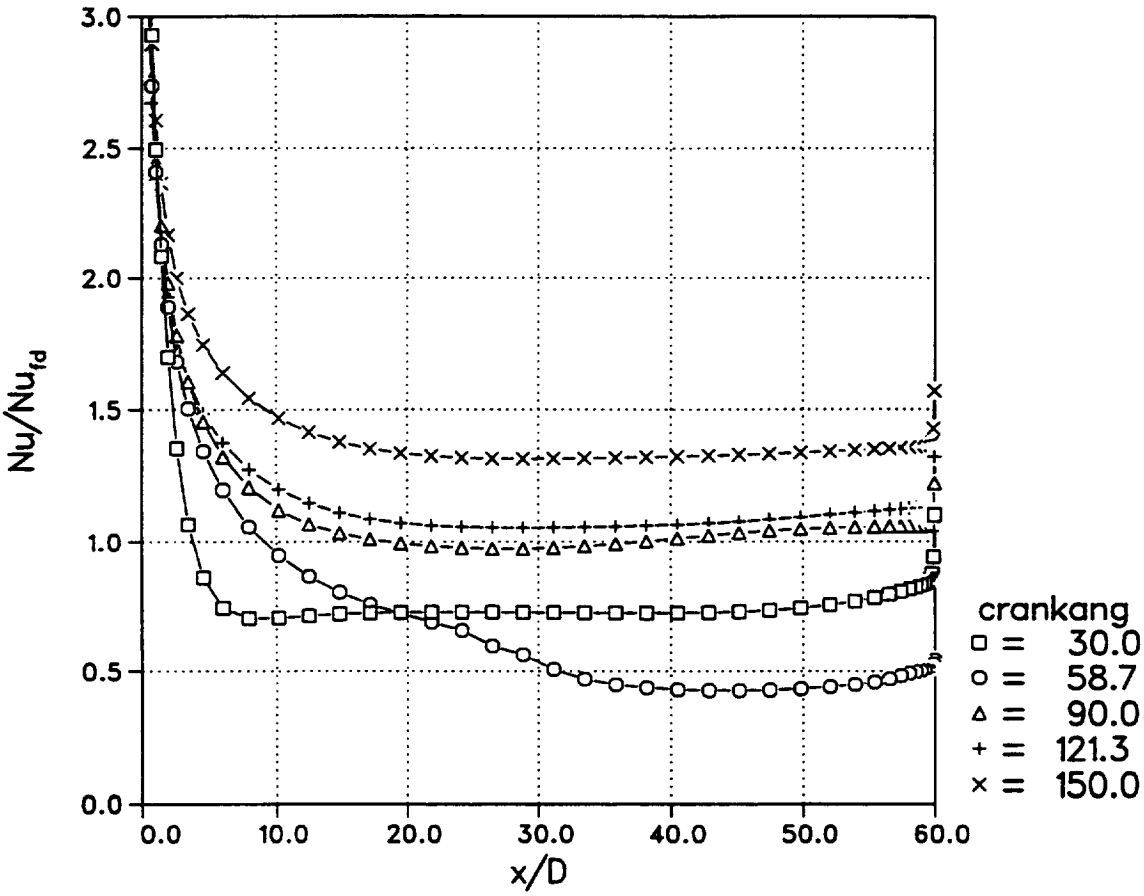

Figure 6.14: Nusselt number versus axial position during the first half cycle for Va = 100.

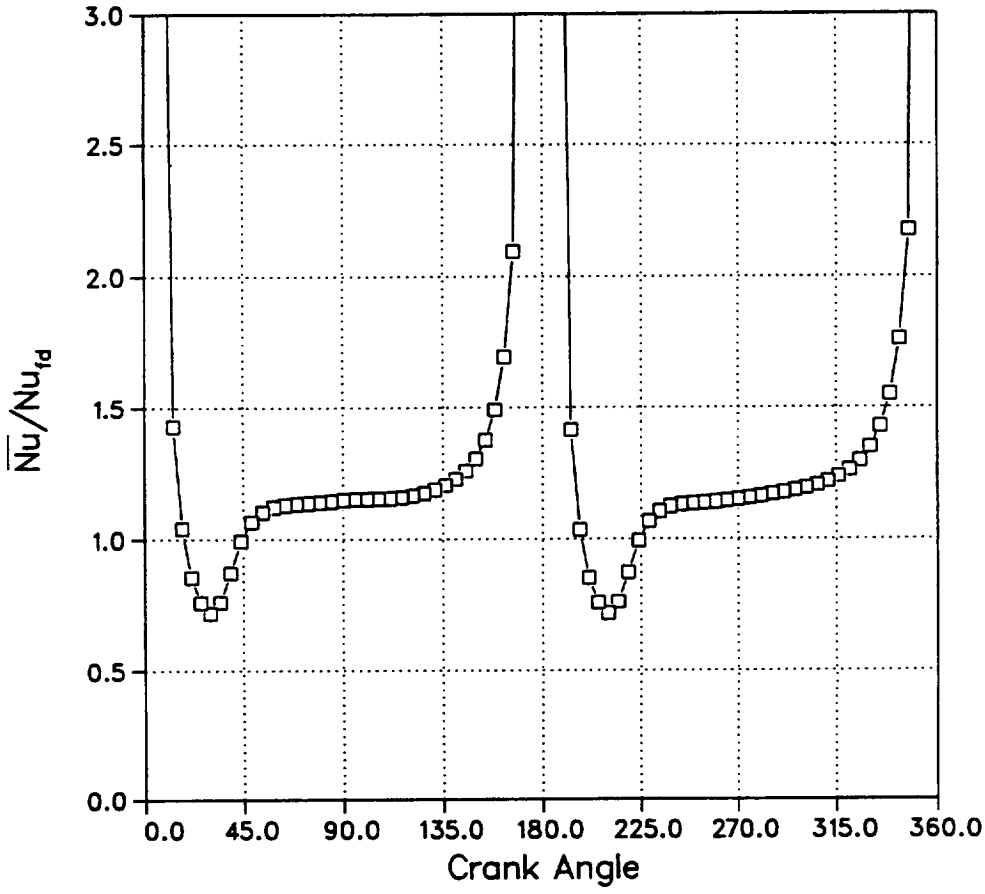

Figure 6.15: Axial-averaged Nusselt number variation during the cycle for $Va = 40$.

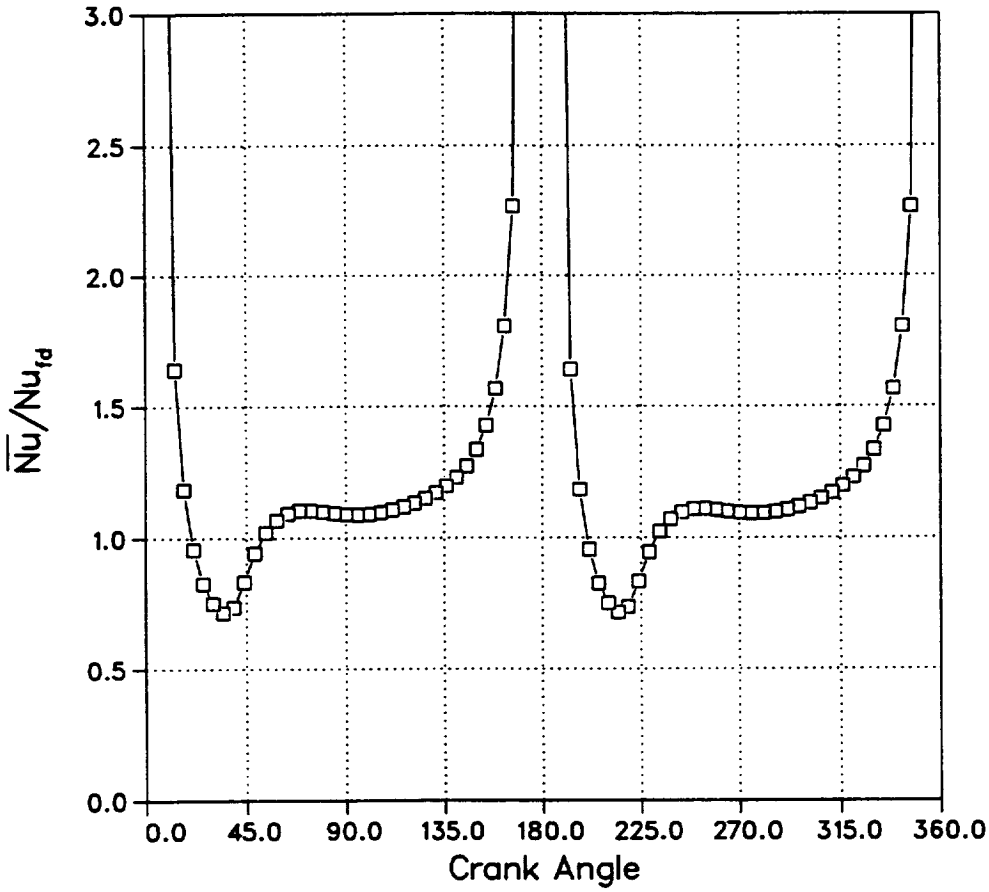

Figure 6.16: Axial-averaged Nusselt number variation during the cycle for $Va = 60$.

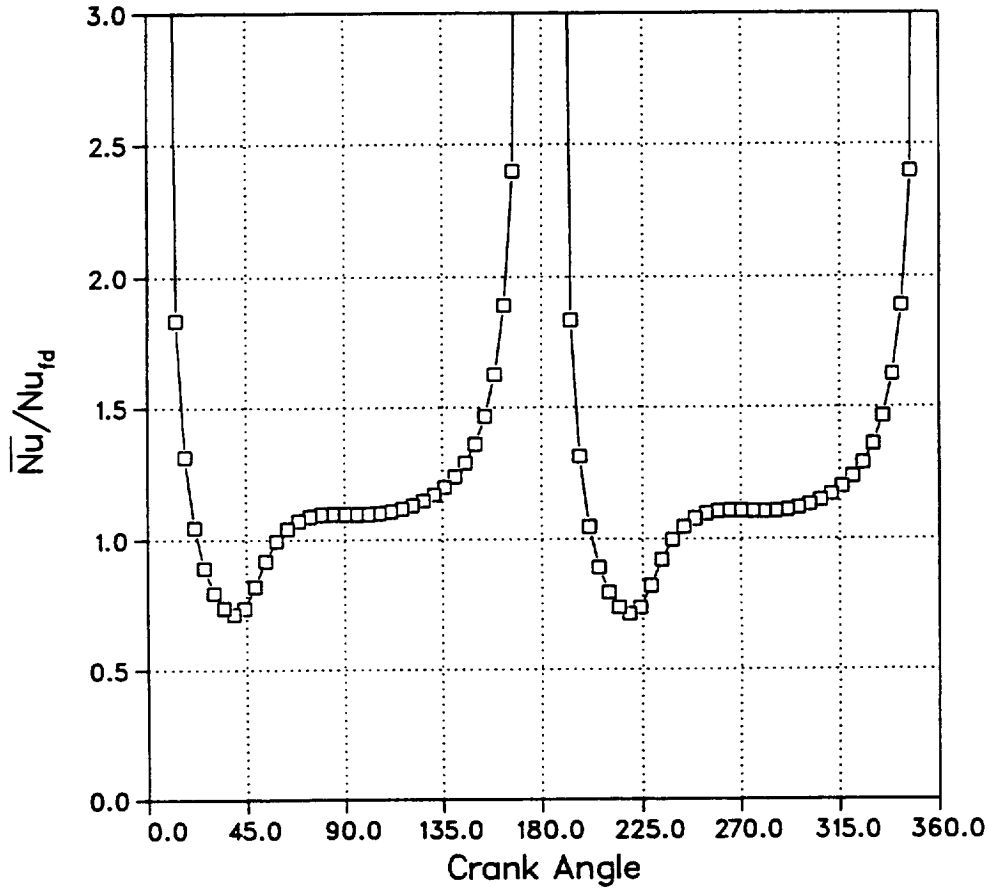

Figure 6.17: Axial-averaged Nusselt number variation during the cycle for $Va = 80$.

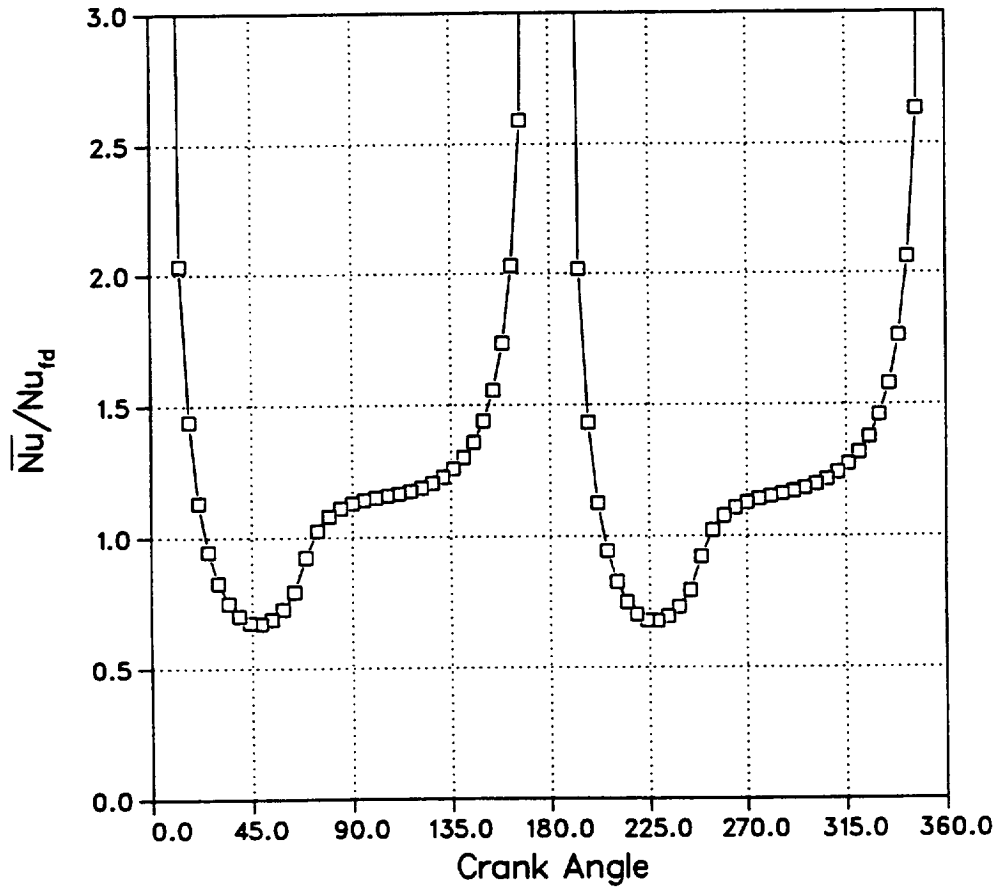

Figure 6.18: Axial-averaged Nusselt number variation during the cycle for $Va = 100$.

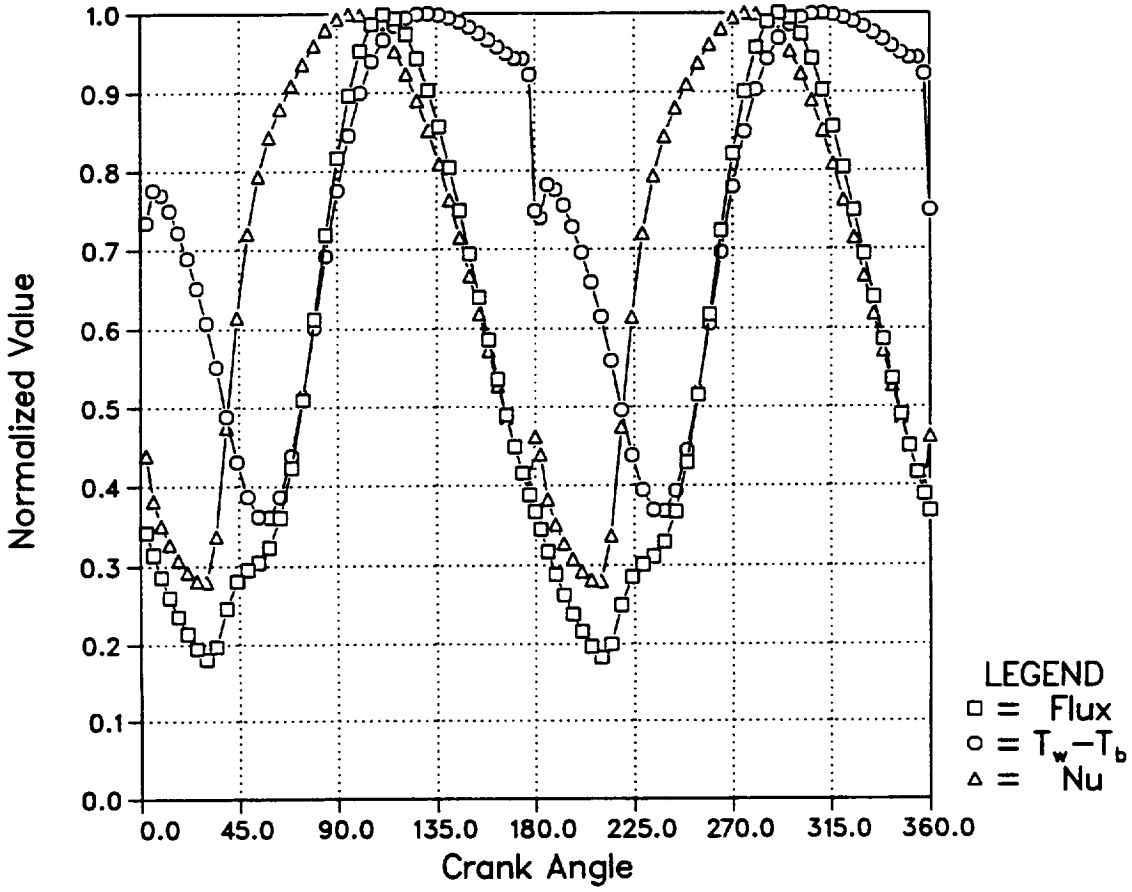

Figure 6.19: Phase comparison between heat transfer quantities at the axial middle of the pipe for $Va = 40$.

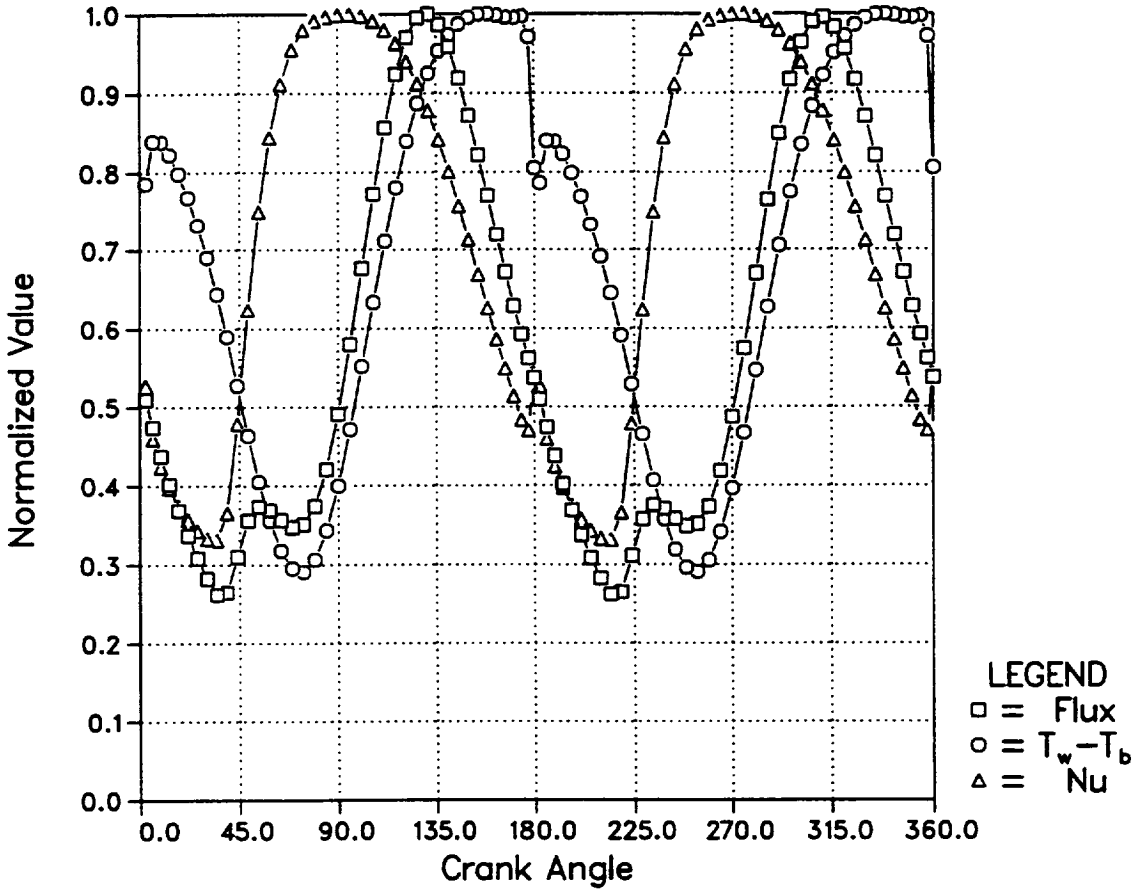

Figure 6.20: Phase comparison between heat transfer quantities at the axial middle of the pipe for $Va = 60$.

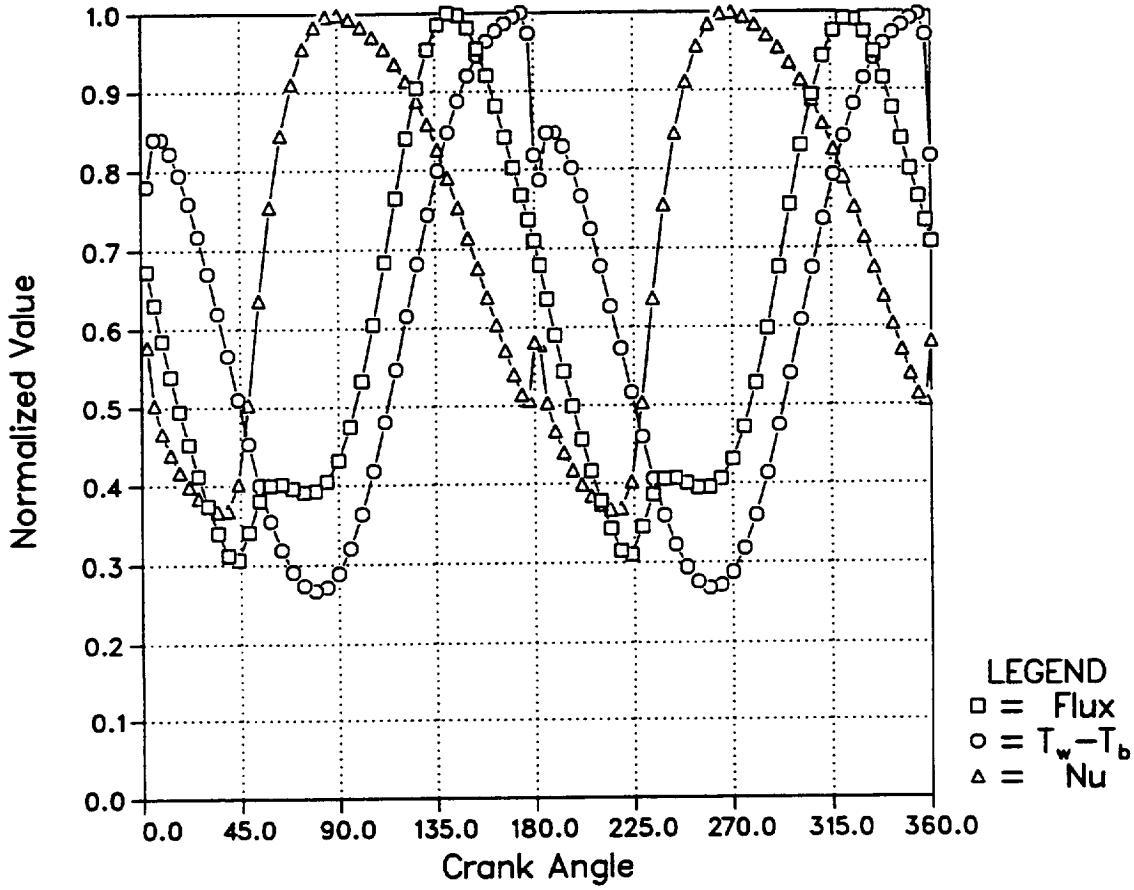

Figure 6.21: Phase comparison between heat transfer quantities at the axial middle of the pipe for $Va = 80$.

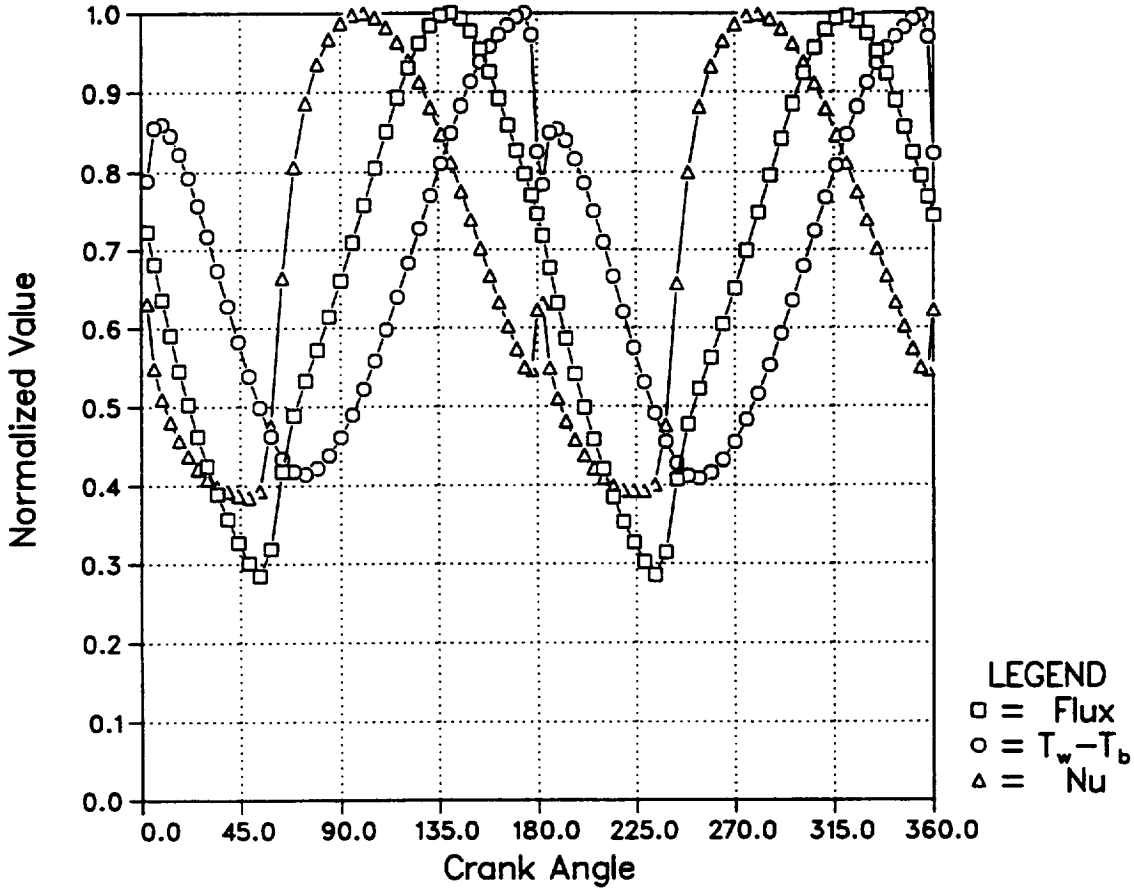

Figure 6.22: Phase comparison between heat transfer quantities at the axial middle of the pipe for $Va = 100$.

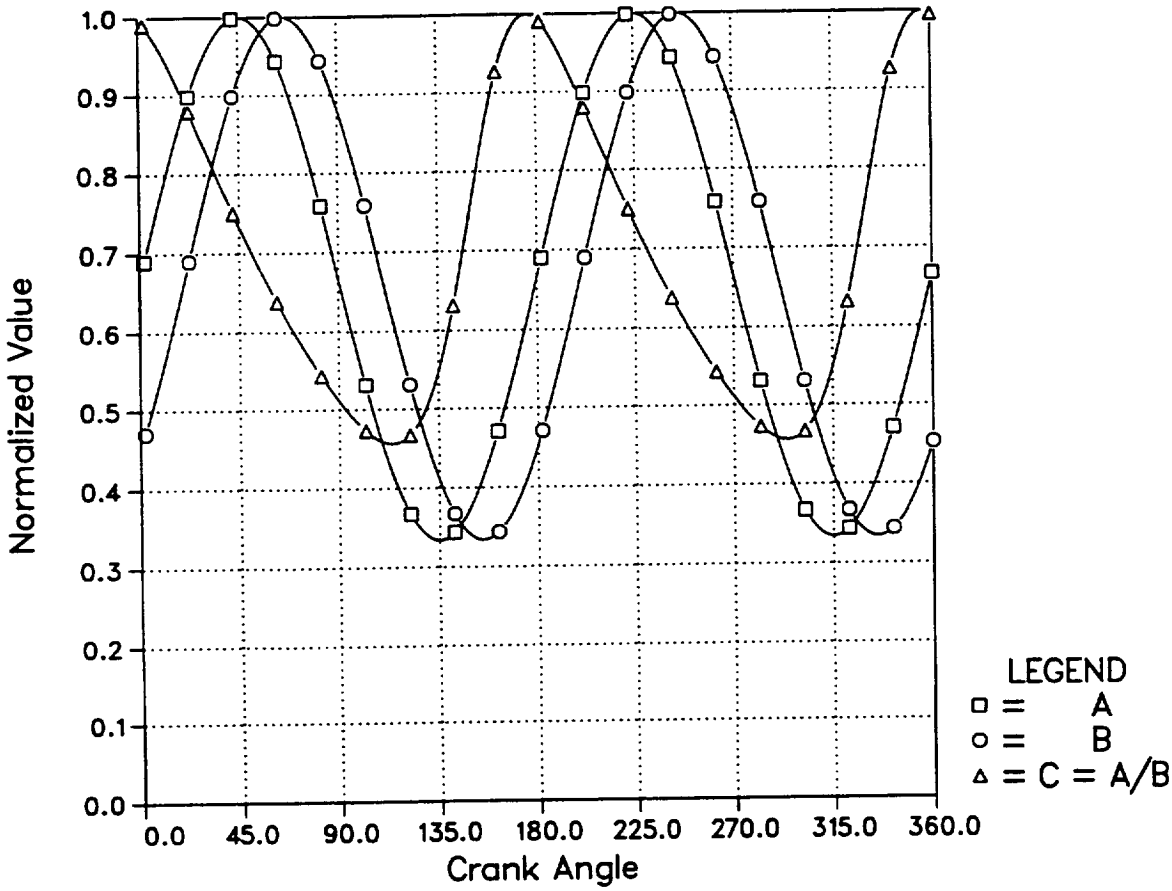

Figure 6.23: Phase comparison between test functions.

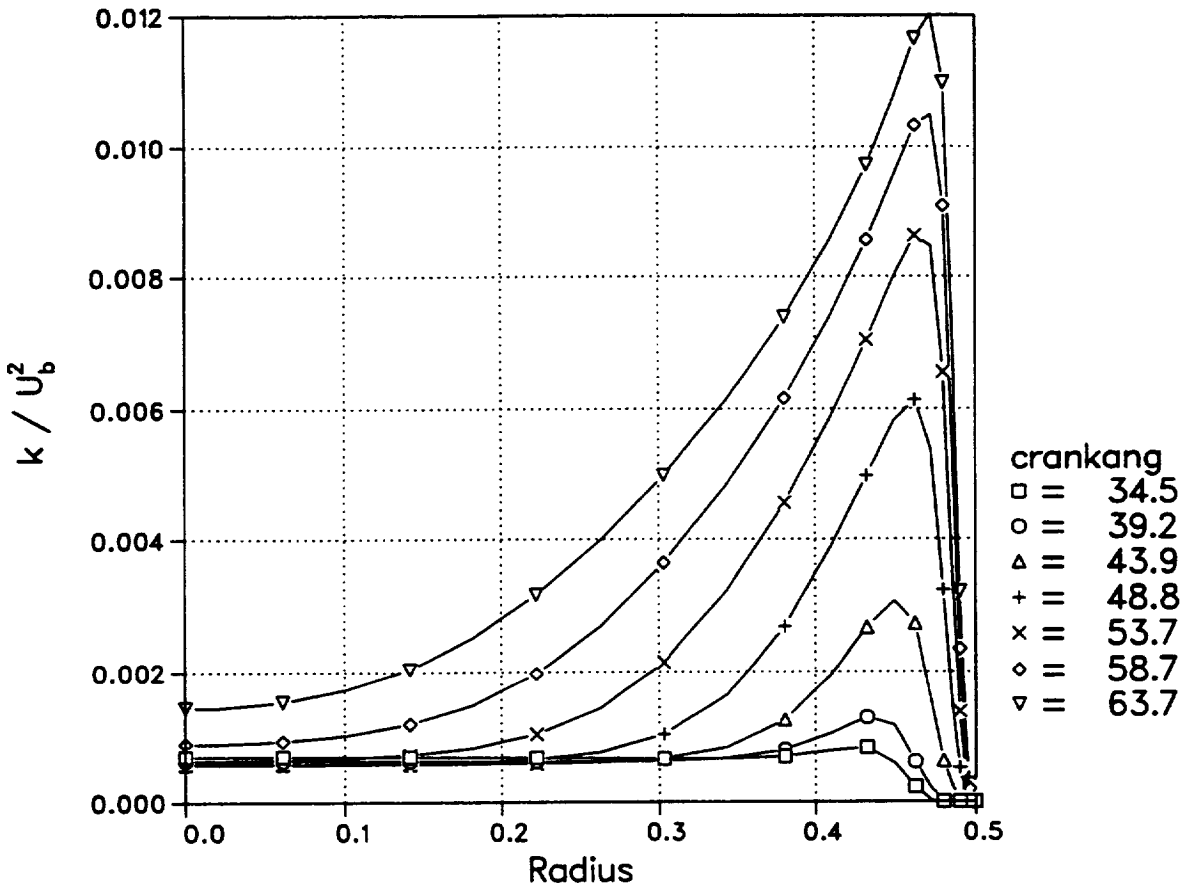

Figure 6.24: Turbulent kinetic energy profiles at the axial middle of the pipe during transition, for $Va = 80$.

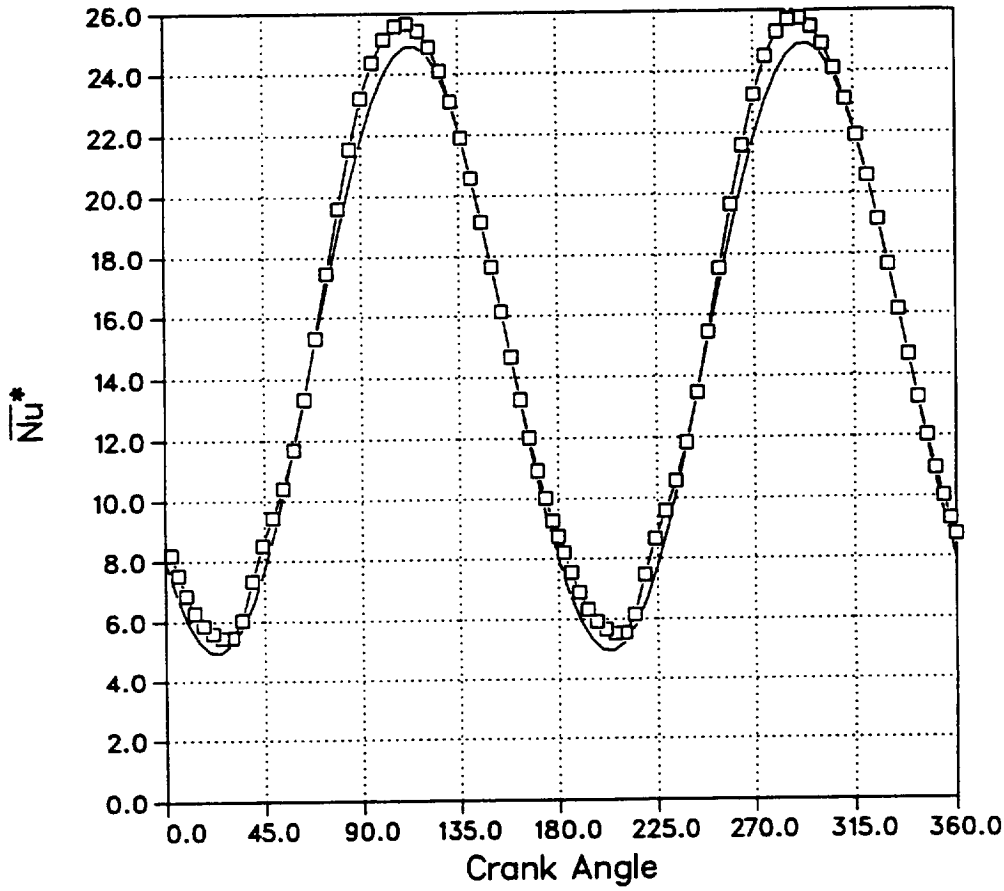

Figure 6.25: Axial-averaged Nusselt number based on T_w - T_{in} for $Va = 40$.

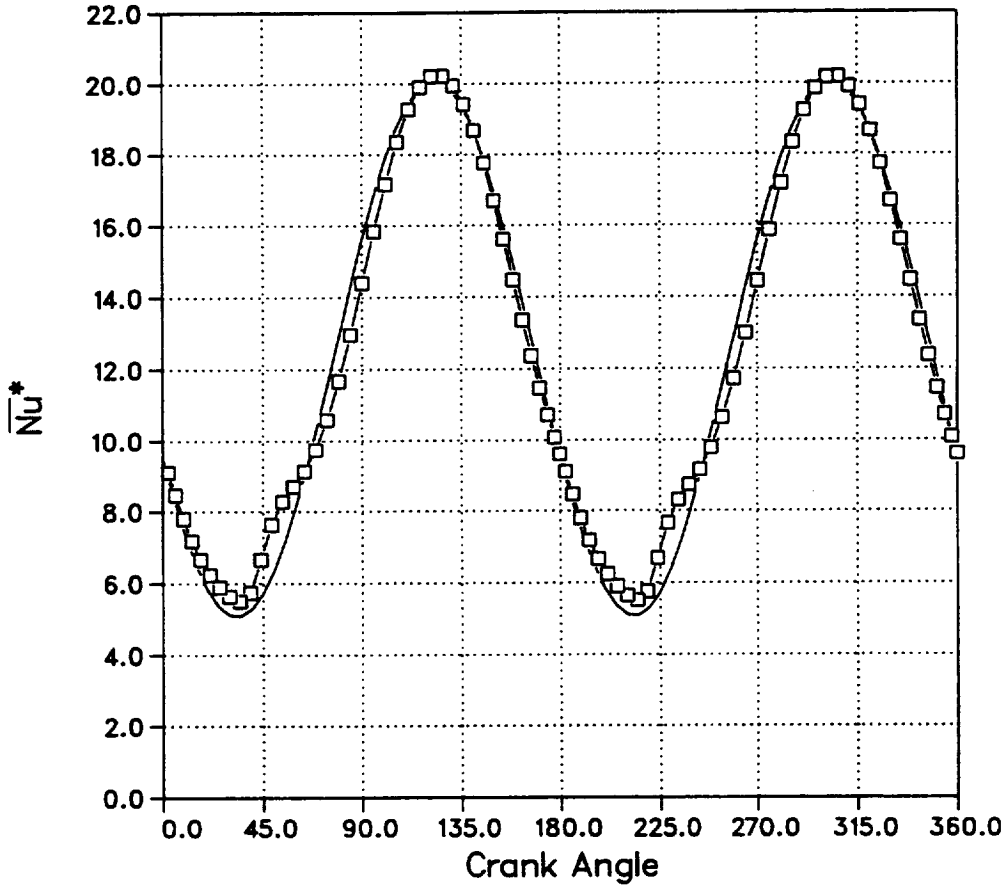

Figure 6.26: Axial-averaged Nusselt number based on T_w - T_{in} for $Va = 60$.

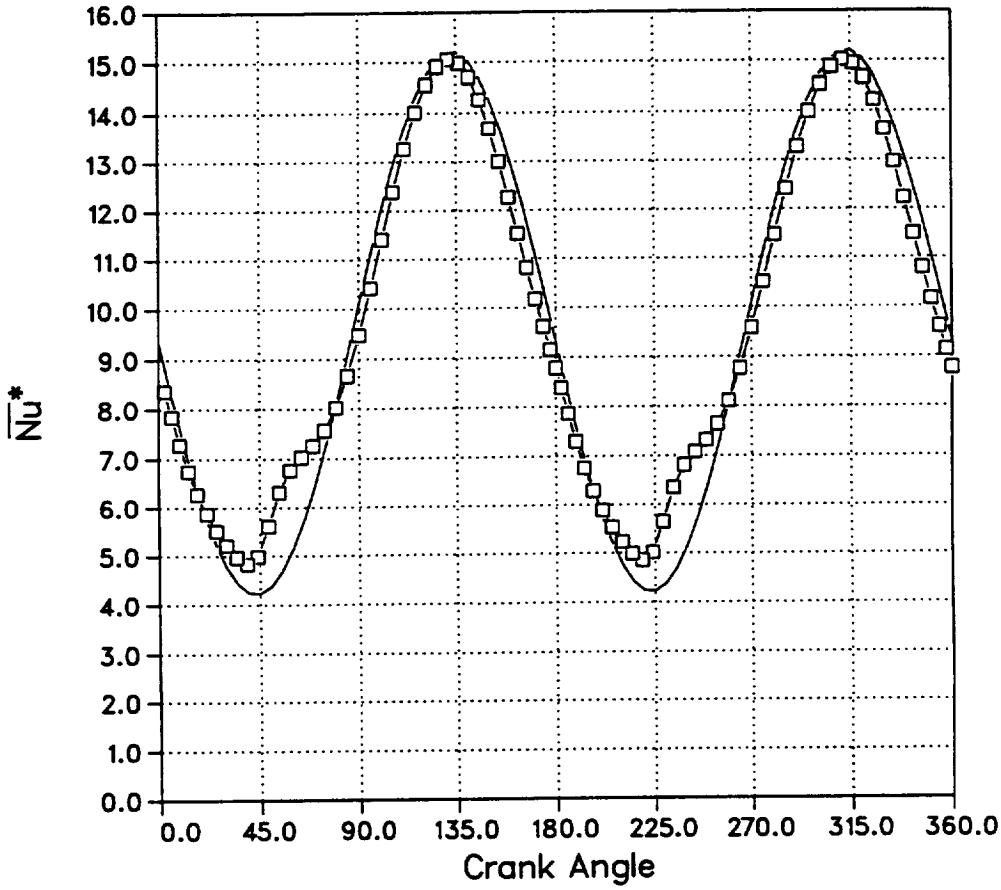

Figure 6.27: Axial-averaged Nusselt number based on T_w - T_{in} for $Va = 80$.

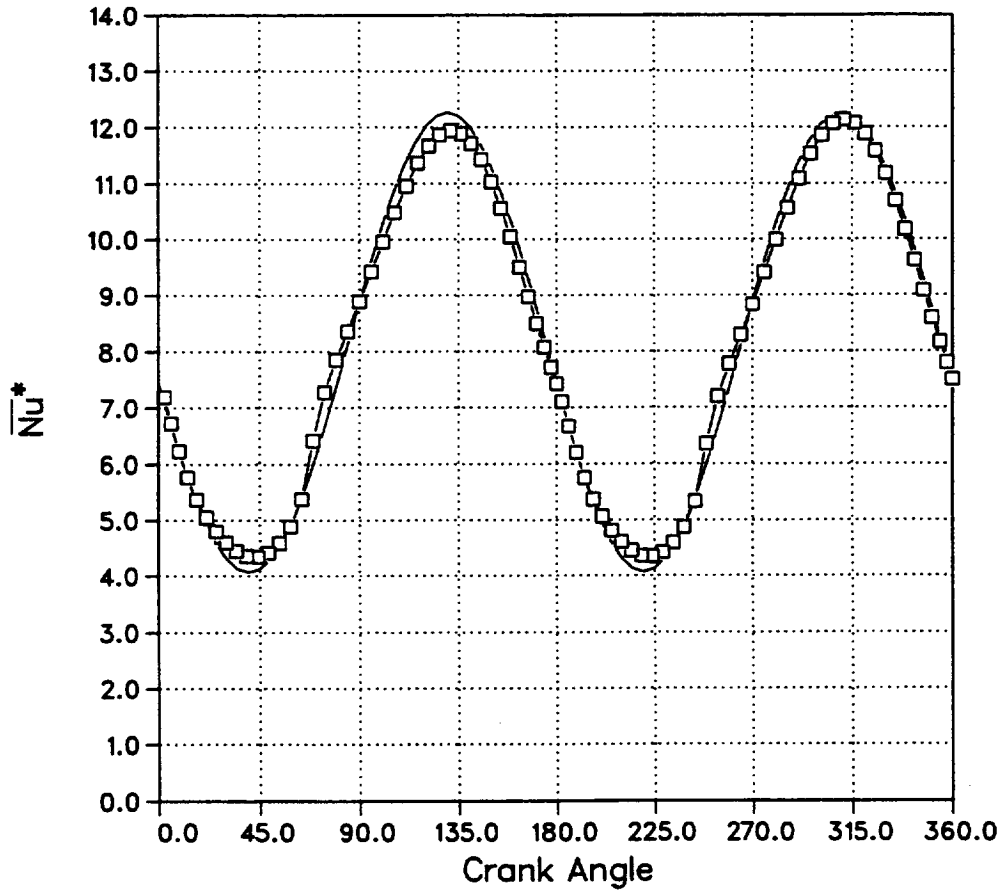

Figure 6.28: Axial-averaged Nusselt number based on T_w - T_{in} for $Va = 100$.

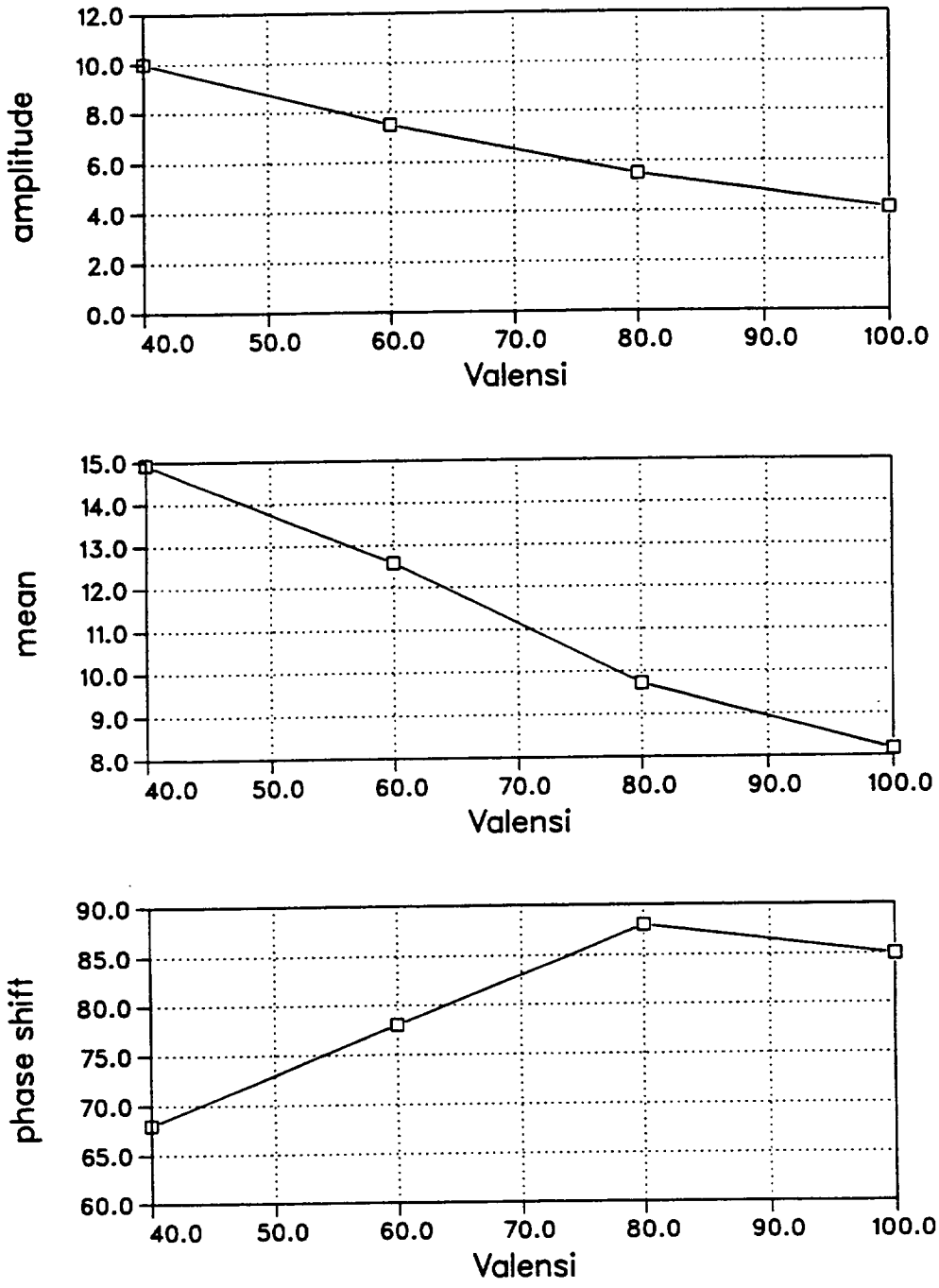

Figure 6.29: Amplitude, mean and phase shift for the turbulent Nusselt number correlation as a function of Va.

Chapter 7

Concluding Remarks

7.1 Summary and Conclusions

1. A literature survey shows that sufficient experimental data is available for validation of numerical flow and transition predictions.

2. Only limited data is available for validation of heat transfer results. The data is not suitable for comparison with the present work due to differences in the end conditions.

3. The Low Reynolds Number k-ϵ turbulence model of Lam-Bremhorst (1981) predicts transition and relaminarization of the flow, but not at the same times observed during experiments. Previously proposed modifications to this turbulence model were examined, and found to be physically incompatible with oscillating flows (flows with reversal). The model does not produce the experimentally observed convection of large turbulent slugs.

4. The two time scale turbulence model of Kim (1992) produces results which are similar to the Lam-Bremhorst model. No improvement was found in terms of transition, relaminarization or the convection of turbulent slugs.

5. The High Reynolds Number RNG-based k-ϵ model of Yakhot and Smith

(1992) provides modest improvements over Lam-Bremhorst for steady pipe flow, but cannot be applied to oscillating flow due to limitations of the wall functions boundary treatment. An extension of the Yakhot and Smith model to low Reynolds numbers was devised, but produced results nearly indistinguishable from Lam-Bremhorst, from whom the low Reynolds number functions were borrowed. The rigorously derived Low Reynolds Number RNG model of Yakhot and Orszag (1986) is not yet fully described in the literature, and was not tested.

6. The heat transfer predictions show that the wall heat flux and bulk temperature are out of phase with the bulk flow rate (and each other). The temperature difference exhibits complicated behavior near bulk flow reversal due to the momentary "conduction-like" nature of the heat transfer problem in the absence of (significant) convection.

7. A Nusselt number based on the flux and bulk temperature is even less well behaved than the bulk temperature, with non-sinusoidal variation throughout the cycle and strong dependence on end effects.

8. A newly defined Nusselt number based on the pipe inlet temperature instead of the bulk temperature is proposed. Also, axial averaging of this Nusselt number produces a more tractable expression for the oscillating heat transfer.

7.2 Contributions of This Work

This work is the first of which the author is aware which provides an investigation and results for the following:

1. Detailed numerical predictions for turbulent and transitional oscillating pipe flow with complicated end geometries.

2. Application of the Kim two time scale turbulence model to highly unsteady flow.

3. Numerical predictions for the variation of the Nusselt number along the pipe and throughout the oscillating flow cycle.

4. A proposed modification to the Nusselt number, producing a form which is more readily applied to Stirling engine design.

7.3 Suggestions for Further Research

The following items deserve further attention during future research:

1. When available, the Low Reynolds Number version of the RNG-based k-ϵ model should be applied to the oscillating flow and heat transfer problem to determine whether it yields improvements over the Lam-Bremhorst model.

2. The parametric range of this study should be expanded to ensure the results are applicable to a broader range of oscillating flow and heat transfer problems.

3. The geometry and boundary conditions should be adjusted to produce results which may be compared against the newly available experimental heat transfer data of Simon and Qiu (1993).

4. The variation of the turbulent Prandtl number should be accounted for using the expression of Yakhot, et al. (1987) which gives Pr_t as a function of the turbulent viscosity.

5. The effects of temperature-dependent properties should be captured by introducing thermally expandable effects into the numerical procedure.

References

Ahn, K.H., Ibrahim, M.B. (1992): "Laminar/Turbulent Oscillating Flow in Circular Pipes," *International Journal of Heat and Fluid Flow,* Vol. 13, pp. 340-346.

Bennethum, J.E., Laymac, T.D., Johansson, L.N., Godett, T.M. (1991): "The Detroit Diesel Corporation / Stirling Thermal Motors, Inc. Program to Develop Stirling Based Commercial Products," Proceedings of the 26^{th} Intersociety Energy Conversion Engineering Conference, pp. 198-204.

Cairelli, J.E., Swec, D.M., Wong, W.A., Doeberling, T.J., Madi, F.J. (1991): "Update on Results of SPRE Testing at NASA Lewis, " Proceedings of the 26^{th} Intersociety Energy Conversion Engineering Conference, pp. 217-222.

Chan, K.W., Baird, M.H.I. (1974): "Wall Friction in Oscillating Liquid Columns," *Chemical Engineering Science,* Vol. 29, pp. 2093-2099.

Chen, C.J., Singh, K. (1990): "Development of a Two-Scale Turbulence Model and Prediction of Buoyant Shear Flows," in **Heat Transfer in Turbulent Flow,** Amano, R.S., Crawford, M.E., Anand, N.K., (ed.) ASME.

Cho, H.W., Hyun, J.M. (1990): "Numerical Solutions of Pulsating Flow and Heat Transfer Characteristics in a Pipe," *International Journal of Heat and Fluid Flow,* Vol. 11, pp. 321-330.

Dec, J.E., Keller, J.O. (1989): "Pulse Combustor Tail-Pipe Heat Transfer Dependence on Frequency, Amplitude and Mean Flow Rate," *Combustion and Flame,* Vol. 77, pp. 359-374.

Dec, J.E., Keller, J.O., Arpaci, V.S. (1992): "Heat Transfer Enhancement in the Oscillating Turbulent Flow of a Pulse Combustor Tail Pipe," *International Journal of Heat and Mass Transfer,* Vol. 35, pp. 2311-2325.

De Graaff, P.J. (1991): "A Multicylinder Free-Piston Stirling Engine for Application in Stirling-Electric Drive Systems," Proceedings of the 26^{th} Intersociety Energy Conversion Engineering Conference, pp. 205-210.

Dochat, G. (1990): "Free-Piston Space Stirling Technology Program," Proceedings of the 25^{th} Intersociety Energy Conversion Engineering Conference, pp. 219-223.

Drake, D.G. (1965): "On the Flow in a Channel due to a Periodic Pressure Gradient," *Quarterly Journal of Mechanics and Applied Mathematics,* Vol. 18, pp. 1-10.

Faghri, M., Javdani, K., Faghri, A. (1979): "Heat Transfer with Laminar Pulsating Flow in a Pipe," *Letters in Heat and Mass Transfer,* Vol. 6, pp. 259-270.

Fauvel, O.R., Walker, G., Reader, G.T. (1990): "Excitation of a Fluidyne Tuning Line," Proceedings of the 25^{th} Intersociety Energy Conversion Engineering Conference, pp. 315-318.

Fishler, L.S., Brodkey, R.S. (1991): "Transition, Turbulence and Oscillating Flow in a Pipe - A Visual Study," *Experiments in Fluids,* Vol. 11, pp. 388-398.

Friedman, G. (1991): "Experimental Investigation of Fluid Mechanics on Oscillating Flow," Masters Thesis, Department of Mechanical Engineering, University of Minnesota, Minneapolis, Minnesota.

Gaver, D.P., Grotberg, J.B. (1986): "An Experimental Investigation of Oscillating Flow in a Tapered Channel," *Journal of Fluid Mechanics,* Vol. 172, pp. 47-61.

Goldwater, B. (1990): "Free-Piston Stirling Engines: for Space, Earth and Ocean Applications, " Proceedings of the 25^{th} Intersociety Energy Conversion Engineering Conference, pp. 324-330.

Hanjalic, K., Launder, B.E. (1980): "Sensitizing the Dissipation Equation to Irrotational Strains," *Journal of Fluids Engineering,* Vol. 102, pp. 34-40.

Hanjalic, K., Launder, B.E., Schiestel, R. (1980): "Multiple-Time-Scale Concepts in Turbulence Modeling," in **Turbulent Shear Flows II,** Bradbury, L.J.S., Durst, F., Launder, B.E., Schmidt, F.W., Whitelaw, J., (ed.) Springer.

Hargreaves, C.M. (1991): **The Philips Stirling Engine,** Wiley.

Harlow, F.H., Nakayama, P.I. (1967): "Turbulent Transport Equations," *Physics of Fluids,* Vol. 10, pp. 2323-2332.

Hino, M., Sawamoto, M., Takasu, S. (1976): "Experiments on Transition to Turbulence in an Oscillatory Pipe Flow," *Journal of Fluid Mechanics,* Vol. 75, pp. 193-207.

Ibrahim, M., Kannapareddy, M., Tew, R.C., Dudenhoefer, J.E. (1991): "Instantaneous Heat Transfer Coefficient based upon Two-Dimensional Analysis of Stirling Space Engine Components," Proceedings of the 26^{th} Intersociety Energy Conversion Engineering Conference, Vol. 6 pp. 149-159.

Ibrahim, M., Hashim, W., Tew, R.C., Dudenhoefer, J.E. (1992): "Heat Transfer in Oscillating Flows with Sudden Change in Cross Section," Proceedings of the 27^{th} Intersociety Energy Conversion Engineering Conference, Vol. 5 pp. 503-508.

Ibrahim, M. (1993): "Development of Multi-Dimensional Stirling Engine Code," August Progress Report on NASA Grant NAG 3-955.

Iguchi, M., Park, G., Akao, F., Yamamoto, F. (1992): "A Study on Velocity Profiles of Developing Laminar Oscillatory Flows in a Square Duct," *JSME International Journal, Series II* Vol. 35, pp. 158-164.

Incropera, F.P., DeWitt, D.P. (1985): **Fundamentals of Heat and Mass Transfer,** Wiley.

Jeong, E.S. (1991): "Heat Transfer with Oscillating Pressure in Reciprocating Machinery," Ph.D. Thesis, Department of Mechanical Engineering, Massachusetts Institute of Technology, Cambridge, Massachusetts.

Jones, W.P., Launder, B.E. (1972): "The Prediction of Laminarization with a Two-Equation Model of Turbulence," *International Journal of Heat and Mass Transfer,* Vol. 15, pp. 301-314.

Kakac, S., Shah, R.K., Aung, W. (1987): **Handbook of Single-Phase Convective Heat Transfer,** Wiley.

Kays, W.M., Crawford, M.E. (1980): **Convective Heat and Mass Transfer,** McGraw-Hill.

Kim, S.W., Chen, C.P. (1989): "A Multiple-Time-Scale Turbulence Model Based on Variable Partitioning of the Turbulent Kinetic Energy Spectrum," *Numerical Heat Transfer* **B**, Vol. 16, pp. 193-211.

Kim, S.W. (1990): "Near-Wall Turbulence Model and its Application to Fully Developed Turbulent Channel and Pipe Flows," *Numerical Heat Transfer* **B**, Vol. 17, pp. 101-122.

Kim, S.W. (1991): "Calculation of Divergent Channel Flows with a Multiple-Time-Scale Turbulence Model," *AIAA Journal,* Vol. 29, pp. 547-554.

Kim, S.W. (1992): "Low Re Multiple-Time-Scale Turbulence Model and Calculations of Steady and Pulsating Shear Layers," NASA Contractor Report 189176.

Koehler, W.J. (1990): "Numerical Prediction of Turbulent Oscillating Flow and Associated Heat Transfer," Ph.D. Thesis, Department of Mechanical Engineering, University of Minnesota, Minneapolis, Minnesota.

Lam, C.K.G., Bremhorst, K. (1981): " A Modified Form of the k-ϵ Model for Predicting Wall Turbulence," *Journal of Fluids Engineering,* Vol. 103, pp. 456-460.

Laufer, J. (1953): "The Structure of Turbulence in Fully Developed Pipe Flow," NACA Report 1174.

Launder, B.E., Spalding, D.B. (1972): **Lectures in Mathematical Models of Turbulence,** Academic Press.

Launder, B.E., Spalding, D.B. (1974): "The Numerical Computation of Turbulent Flows," *Computer Methods in Applied Mechanics and Engineering,* Vol. 3, pp. 269-289.

Launder, B.E. (1989): "Second-Moment Closure: Present ... and Future?," *International Journal of Heat and Fluid Flow,* Vol. 10, pp. 282-300.

Lee, K.P. (1983): "A Simplistic Model of Cyclic Heat Transfer Phenomena in Closed Spaces," Proceedings of the 18^{th} Intersociety Energy Conversion Engineering Conference, pp. 720-723.

Liao, N.S., Wang, C.C., Hong, J.T. (1985): "An Investigation of Heat Transfer in Pulsating Turbulent Pipe Flow," in **Fundamentals of Forced and Mixed Convection,** ASME HTD Vol. 42, pp. 53-60.

Liou, W.W., Shih, T.H. (1993): "A Multiple-Scale Model for Compressible Turbulent Flows," NASA Technical Memorandum 106072.

Mankbadi, R.R., Mobark, A. (1991): "Quasi-Steady Turbulence Modeling of Unsteady Flows," *International Journal of Heat and Fluid Flow,* Vol. 12, pp. 122-129.

Mansour, N.N., Kim, J., Moin, P. (1989): "Near-Wall k-ϵ Turbulence Modeling," *AIAA Journal,* Vol. 27, pp. 1068-1073.

McComb, W.D. (1990): **The Physics of Fluid Turbulence,** Oxford.

Moin, P. (1991): "Toward Large Eddy and Direct Simulation of Complex Turbulent Flows," *Computer Methods in Applied Mechanics and Engineering,* Vol. 87, pp. 329-334.

Ohmi, M., Iguchi, M., Kakehashi, K., Masuda, T. (1982): "Transition to Turbulence and Velocity Distribution in an Oscillating Pipe Flow," *Bulletin of the JSME,* Vol. 25, pp. 365-371.

Park, J.R.S., Baird, M.H.I. (1970): "Transition Phenomena in an Oscillating Manometer," *Canadian Journal of Chemical Engineering,* Vol. 48, pp. 491-495.

Patankar, S.V. (1980): **Numerical Heat Transfer and Fluid Flow,** Hemisphere.

Patankar, S.V., Spalding, D.B. (1967): **Heat and Mass Transfer in Boundary Layers,** Intertext.

Patel, V.C., Rodi, W., Scheuerer, G. (1985): "Turbulence Models for Near-Wall and Low Reynolds Number Flows: A Review," *AIAA Journal,* Vol. 23, pp. 1308-1319.

Reichardt, H. (1951): "Vollstandige Darstellung der Turbulenten Geshwindigkeitsverteilung in Glatten Leitungen ," *Zeitschrift fur angewandte Mathematik und Mechanik,* Vol. 31, pp. 208-219.

Richardson, E.G., Tyler, E. (1929): "The Transverse Velocity Gradient near the Mouths of Pipes in which an Alternating Continuous Flow of Air is Established," *The Proceedings of the Physical Society,* Vol. 42, pp. 1-15.

Schetz, J.A. (1984): **Foundations of Boundary Layer Theory,** Prentice-Hall.

Schlichting, H. (1979): **Boundary-Layer Theory,** McGraw-Hill.

Schmidt, R.C., Patankar, S.V. (1988): "Two-Equation Low-Reynolds Number Turbulence Modeling of Transitional Boundary Layer Flow Characteristic of Gas Turbine Blades," NASA Contractor Report 4145.

Sergeev, S.I. (1966): "Fluid Oscillations in Pipes at Moderate Reynolds Numbers," *Fluid Dynamics,* Vol. 1, pp. 121-122.

Seume, J. (1988): "An Experimental Investigation of Transition in Oscillating Pipe Flow," Ph.D. Thesis, Department of Mechanical Engineering, University of Minnesota, Minneapolis, Minnesota.

Sexl, T. (1930): "Uber den von E. G. Richardson Entdeckten 'Annulareffeckt' ," *Zeitschrift fur Physik,* Vol. 61, pp. 349-362.

Siegel, R. (1987): "Influence of Oscillation-Induced Diffusion on Heat Transfer in a Uniformly Heated Channel," *Journal of Heat Transfer,* Vol. 109, pp. 244-247.

Simon, T.W., Ibrahim, M., Kannapareddy, M., Johnson, T., Friedman, G. (1992): "Transition of Oscillatory Flow in Tubes: An Empirical Model for Application to Stirling Engines," *Proceedings of the* 27^{th} *Intersociety Energy Conversion Engineering Conference,* Vol. 5, pp. 495-502.

Simon, T.W., Qiu, S, (1993): "Investigation of Heat Transfer and Hydrodynamics of Oscillating Flows," July Progress Report on NASA Grant NAG 3-598.

Smith, J.L., Lienhard, J.H., Tziranis, A.K., Ho, Y. (1992): "M.I.T. Stirling-Cycle Heat Transfer Apparatus," *Proceedings of the* 27^{th} *Intersociety Energy Conversion Engineering Conference,* Vol. 5, pp. 509-516.

Sparrow, E.M., Patankar, S.V. (1977): "Relationship Among Boundary Conditions and Nusselt Numbers for Thermally Developed Duct Flows," *Journal of Heat Transfer,* Vol. 99, pp. 483-485.

Speziale, C.G., Abid, R., Anderson, E.C. (1990): "A Critical Evaluation of Two-Equation Models for Near Wall Turbulence," AIAA Paper 90-1481.

Tang, X., Cheng, P. (1993): "Correlations of the Cycle-Averaged Nusselt Number in a Periodically Reversing Pipe Flow," *International Communications in Heat and Mass Transfer,* Vol. 20, pp. 161-172.

Tew, R.C., Thieme, L.G., Dudenhoefer, J.E. (1990): "Recent Stirling Loss-Understanding Results," *Proceedings of the* 25^{th} *Intersociety Energy Conversion Engineering Conference,* Vol. 5, pp. 377-385.

Tew, R.C., Geng, S.M. (1992): "Overview of NASA Supported Stirling Thermodynamic Loss Research," *Proceedings of the* 27^{th} *Intersociety Energy Conversion Engineering Conference,* Vol. 5, pp. 489-494.

Tu, S.W., Ramaprian, B.R. (1983): "Fully Developed Periodic Turbulent Pipe Flow. Part 1. Main Experimental Results and Comparison With Predictions," *Journal of Fluid Mechanics,* Vol. 137, pp. 31-58.

Uchida, S. (1956): "The Pulsating Viscous Flow Superposed on the Steady Laminar Motion of Incompressible Fluid in a Circular Pipe," *Zeitschrift fur angewandte Mathematik und Physik,* Vol. 7, pp. 403-422.

Walker, G., Senft, J.R. (1985): **Free Piston Stirling Engines,** Springer-Verlag.

Wallace, D.A., Noble, J.E., Emigh, S.G., Ross, B.A., Lehmann, G.A. (1991): "Final Design of a Free-Piston Hydraulic Advanced Stirling Conversion System," Proceedings of the 26^{th} Intersociety Energy Conversion Engineering Conference, pp. 349-354.

West, C.D. (1986): **Principles and Applications of Stirling Engines,** Van Nostrand Reinhold.

White, F.M. (1974): **Viscous Fluid Flow,** McGraw-Hill.

Wilcox, D.C. (1988): " Reassessment of the Scale-Determining Equation for Advanced Turbulence Models," *AIAA Journal,* Vol. 26, pp. 1299-1310.

Wong, W.A., Cairelli, J.E., Swec, D.M., Doeberling, T.J., Lakatos, T.F., Madi, F.J. (1992): "NASA Lewis Stirling SPRE Testing and Analysis with Reduced Number of Cooler Tubes, " Proceedings of the 27^{th} Intersociety Energy Conversion Engineering Conference, pp. 443-448.

Yang, Z., Shih, T.H. (1992): "A New Time Scale Based k-ϵ Model for Near Wall Turbulence," NASA Technical Memorandum 105768.

Yakhot, V., Orszag, S.A. (1986): " Renormalization Group Analysis of Turbulence. I. Basic Theory," *Journal of Scientific Computing,* Vol. 1, pp. 3-51.

Yakhot, V., Orszag, S.A., Yakhot, A. (1987): "Heat Transfer in Turbulent Fluids - I. Pipe Flow," *International Journal of Heat and Mass Transfer,* Vol. 30, pp. 15-22.

Yakhot, V., Orszag, S.A.,Thangam, S., Gatski, T.B., Speziale, C.G. (1992): " Development of Turbulence Models for Shear Flows by a Double Expansion Technique," *Physics of Fluids* **A**, Vol. 4, pp. 1510-1520.

Yakhot, V., Smith, L.M. (1992): " The Renormalization Group, The ϵ-Expansion, and Derivation of Turbulence Models," *Journal of Scientific Computing,* Vol. 7, pp. 35-61.

Zhang, J., Kurzweg, U. (1991): "Numerical Simulation of Time-Dependent Heat Transfer in Oscillating Pipe Flow," *Journal of Thermophysics,* Vol. 5, pp. 401-406.

Zhu, H., Liu, S. (1991): "Numerical Simulation of Transitional Flow and Heat Transfer in a Smooth Pipe," *International Journal of Heat and Mass Transfer,* Vol. 34 pp. 2475-2482.

REPORT DOCUMENTATION PAGE

Form Approved
OMB No. 0704-0188

1. AGENCY USE ONLY (Leave blank)	2. REPORT DATE	3. REPORT TYPE AND DATES COVERED
	December 1995	Final Contractor Report

4. TITLE AND SUBTITLE
Numerical Prediction of Turbulent Oscillating Flow and Heat Transfer in Pipes With Various End Geometries

5. FUNDING NUMBERS
WU-233-02-0B
G-NAG3-1024

6. AUTHOR(S)
Kirk LeRoi Oseid

7. PERFORMING ORGANIZATION NAME(S) AND ADDRESS(ES)
University of Minnesota
111 Church Street S.E.
Minneapolis, Minnesota 55455

8. PERFORMING ORGANIZATION REPORT NUMBER
E-9983

9. SPONSORING/MONITORING AGENCY NAME(S) AND ADDRESS(ES)
National Aeronautics and Space Administration
Lewis Research Center
Cleveland, Ohio 44135-3191

10. SPONSORING/MONITORING AGENCY REPORT NUMBER
NASA CR-198416

11. SUPPLEMENTARY NOTES
This report was submitted as a dissertation in partial fulfillment of the requirements for the degree Doctor of Philosophy to the University of Minnesota, Minneapolis, Minnesota. S.V. Patanker, Principal Investigator. Project manager, Roy C. Tew, Power Technology Division, organization code 5460, (216) 433-8471.

12a. DISTRIBUTION/AVAILABILITY STATEMENT
Unclassified - Unlimited
Subject Categories 34 and 64

This publication is available from the NASA Center for Aerospace Information, (301) 621-0390.

12b. DISTRIBUTION CODE

13. ABSTRACT ***(Maximum 200 words)***

Unsteady flow is present in man, machine and nature. The flow of blood in arteries and capillaries in the human body is pulsatile- composed of a mean flow superposed with an oscillating component. The tides that wash in and out of rivers, harbors and estuaries are unsteady flows with very long periods of oscillation. Many engineering devices employ pulsatile and oscillating flow. Pulsating flow is defined here as a periodic flow with a net displacement of fluid over each flow cycle. Oscillating flow is defined as a periodic flow with a zero mean over each cycle. The subject of this thesis is oscillating flow and heat transfer in pipes which make up the heater and cooler sections of the NASA Space Power Research Engine (SPRE) currently under development. This engine uses the Stirling cycle as the thermal energy converter in a power plant for future space applications. The information presented in this thesis will of course be applicable to the design of many types of machinery which employ oscillating flow and heat transfer.

14. SUBJECT TERMS	15. NUMBER OF PAGES
Oscillating flow; Heat transfer; Numerical prediction	229
	16. PRICE CODE: A11

17. SECURITY CLASSIFICATION OF REPORT	18. SECURITY CLASSIFICATION OF THIS PAGE	19. SECURITY CLASSIFICATION OF ABSTRACT	20. LIMITATION OF ABSTRACT
Unclassified	Unclassified	Unclassified	